IODINE CYCLING IN MODERN AND ANCIENT MARINE OXYGEN DEPLETED ZONES: CONSTRAINTS FROM OBSERVATIONS, EARTH SYSTEM MODELING, AND EXPERIMENTS

By

Keyi Cheng

A DISSERTATION

Submitted to
Michigan State University
in partial fulfillment of the requirements
for the degree of

Earth and Environmental Sciences — Doctor of Philosophy

2025

ABSTRACT

Iodine is a redox sensitive element that transforms between its two stable forms—iodate (IO_3^-) and iodide (I^-)—depending on the redox state of the seawater. Because only the oxidized form of iodine, IO_3^-, incorporated into the carbonate lattice that is precipitated from seawater, iodine to calcium (I/Ca) ratios in marine carbonates are therefore used as a paleoredox proxy. However, the current understanding towards mechanisms of IO_3^- redox transformations is limited, hindering redox interpretations based on the I/Ca proxy. The overall goal of this dissertation is to understand the redox cycling of iodine in marine low-O_2 settings and hence provide insights for quantitative redox reconstruction based on secular variation of I/Ca records.

Chapter 2 focuses on the iodine cycle in modern marine low-O_2 settings. Samples were collected from two modern anoxic basins: the Baltic Sea and Siders Pond. Iodine speciation was measured, including IO_3^-, I^-, dissolved organic iodine (DOI) and total dissolved iodine (TI) of these samples. IO_3^- was depleted in both the anoxic basins, and was even low within the surface layer where dissolved O_2 was saturated. In addition, non-conservative features were observed throughout the water column. A significant I^- flux from the sediments contributed to excessive iodine observed in the bottom of Siders Pond. In the Baltic Sea, net I^- removal from the water column near the chemocline was observed. The causation of such I^- removal requires further investigation. The decoupling of IO_3^- and O_2 in relatively small water bodies in the surface anoxic basins indicates IO_3^- accumulation requires ventilation within the oxygenated open ocean waters.

Chapter 3 calibrates the iodine cycle built into an Earth System model (cGENIE). Four processes were simulated: IO_3^- uptake and release of I^- through the biological pump, the reduction in ambient IO_3^- to IO_3^- in the water column, and the re-oxidation of I^- to IO_3^-. New I^- oxidation and IO_3^- reduction parameters were incorporated into cGENIE. The model performance was evaluated

against both modern and paleo-observations. The iodine cycle parameterizations optimized through model-data comparison replicates the general trends of iodine speciation gradients, including the zonal surface distribution, depth profiles, and oxygen-deficient zones (ODZs). The best-performing parameters were selected to simulate IO_3^- distribution in a Cretaceous model configuration as a case study. The broad match between the simulated IO_3^- and the carbonate I/Ca observation emphasizes the potential of using these parameters to interpreting and constraining redox variation in past oceans.

Chapter 4 provides insights into the secular variation of marine IO_3^- through Earth history. Two approaches were conducted targeting understanding IO_3^- accumulation in seawater: (1) microbial IO_3^- reduction experiment under low but controlled O_2, and (2) Earth System modelling. The model bacterial strain *Shewanella oneidensis* MR-1 started reducing IO_3^- when dissolved O_2 in its medium decreased to 0.1μM. This O_2 threshold provides the minimum estimate of dissolved O_2 in association with the first appearance of IO_3^- accumulation in seawater during the Great Oxygenation Event (GOE). Earth system modelling indicates that IO_3^- accumulation in the surface ocean is a function of atmospheric O_2 and ocean nutrient levels (PO_4). A low I/Ca baseline in the Proterozoic could be best explained as the combined results of low atmospheric O_2 (< 3% present atmospheric level, PAL) and low PO_4 (< 10% present ocean level, POL). The transition of the low I/Ca baseline from the Proterozoic low levels to the modern-like values observed throughout the Paleozoic may require shifts in both oxygenation and nutrient availability. Together, this chapter demonstrates that changes in IO_3^- steady-state values through Earth history reflects fundamental changes in the Earth System, including O_2 and other non-redox factors that have been previously overlooked.

This dissertation is dedicated to my parents, Mr. Jianbo Cheng and Ms. Yangqun Yu, for their unconditional support and love throughout my life.

ACKNOWLEDGEMENTS

I started my PhD program at MSU in August 2019 and it has been five and a half years since I settled in East Lansing. During these years, I have built a deep connection with people here, as well as the campus and the city.

Firstly, I want to acknowledge my advisor, Dr. Dalton Hardisty. I am impressed by your insights into the field of paleoceanography. Instead of assigning missions, you gave me opportunities to discover previously overlooked points on my own while also encouraging me to explore these questions with a diverse set of skills. While encouraging me to conduct research independently, you were also an accessible advisor, always ready to provide feedback. Our chats about science always sparked ideas that eventually blossomed into brilliant discussions in the manuscript. I also appreciate your support when I encountered racism on campus. The chats in the office as well as the short walk to the fountain truly helped ease my stress. I'm proud to be a "seasick oceanographer" in your group.

I also want to thank the rest of my committee, Dr. Tyrone Rooney, Dr. Matthew Schrenk, and Dr. Jay Zarnetske for guiding my research. Tyrone, thanks for leading me into the world of Python. The coding skills I developed in your class enabled me to process large volumes of data generated by the model. Also, I like your jokes although I couldn't fully comprehend some of those. Matt, thanks for your guidance in microbiology. Without your help, I wouldn't be able to complete the culture experiment, which was also my favorite chapter in the dissertation. I also remember how you encouraged me to pursue academic positions when I was doubting myself during the annual progress report, thank you. Jay, you always provide insights from an angle that I previously overlooked. I always remember your advice during the comprehensive exam: never ignore equations in manuscripts. Your guidance has been crucial in helping me conduct more robust research.

I had a great time with friends in the EES department, including my lab mate Alexi Schnur, Kirsten Fentzke, as well as folks on the third floor of Giltner and across the street in the Nat Sci Building. Alexi, I always enjoy chitchatting about everything in the office, on the trail to the Engineering Building, and in the dining halls. My days on campus would be so tedious without you being around. You are my best lab mate as well as my best friend. You are so close to finishing the dissertation, so hang in there! Also wish you the best in your future life and career.

I have also met a group of nice folks through the past five years. Dr. Yuqian Zhang, Yongqing Ye, Junyi Han, Lu Zhang, Yanzeng Li, Qiyang Lin, Yue Zhang, Xinyi He, Rusin Shen, Yurong Zhang, Dr. Fan Wang, Zhuoran Zhang, Shuqi Wang, Yunyang Zhang, Meicheng Shen, Yue'an Qiu, Xinming Deng, and many others—knowing each of you has deepened my connection to East Lansing. It was you who brought color to my life and supported me through the challenging moments during the pandemic and other difficult times. I will always cherish the joyful times we shared in East Lansing, in Sleeping Bear Dunes, on Mackinac Island, in Glacier National Park, in Nevada, and in Peru.

I want to thank my parents, Mr. Jianbo Cheng and Mrs. Yangqun Yu. Although you are thousands of miles away on the other side of the planet, I know you have always kept me in your thoughts. It was your unconditional love and support that gave me the confidence to overcome all the challenges I have faced, and those I will face in the future. I love you, mom and dad.

I also want to express my appreciation to my girlfriend—Xiumin (Mia) Cai. You joined me in the last half-year of my journey in East Lansing—it was short, but you made that time shine. We shared joyful moments admiring the beauty of sunsets, foliage, mountains, snow, and campfires, not just in Michigan but across the continent. In fact, simply staying with you—no matter what we do or where we are—is always enjoyable. Thank you for being my harbor. I love you.

Finally, but not least, I want to thank my little fluffy roommate, Wally the tabby cat. Thanks for staying aside and purring. You might not understand what I have typed, but all you need to know is I will never leave you behind.

As I stated in my defense, pursuing on scientific goals was not only my only reason for coming to Michigan, but also to experience a diverse culture and a variety of ways of life. Thanks to those great people (and four-legged friends) I met, I had an unforgettable time at MSU. It is this experience that has also fueled my ambition to explore not only the frontiers of science, but also the vast world beyond. I did it and Go Green!

TABLE OF CONTENTS

LIST OF ABBREVIATIONS

ODZ	Oxygen Deficient Zone
IO_3^-	Iodate
I^-	Iodide
DOI	Dissolved Organic Iodide
TI	Todal Dissolved Iodine
I/Ca	Iodine-to-Calcium ratio
H_2S	Hydrogen Sulfide
NH_4^+	Ammonium
NO_3^-	Nitrate
NO_2^-	Nitrite
O_2	Oxygen
PO_4	Phosphate
GOE	Great Oxygenation Event
NOE	Neoproterozoic Oxygenation Event
PAL	Present Atmospheric Level
POL	Present Oceanic Level
OOE	Ocean Oxygenation Events
OAE	Ocean Anoxic Events
ROC	Receivers Characteristics Curve
AUC	Area Under Curve
TPR	True Positive Rate
FPR	False Positive Rate

CHAPTER 1: INTRODUCTION

1.1 Background and rationale

Free oxygen (O_2) is a vital element that supports the metabolism of complex eukaryotic organisms, especially animals on Earth (Ward and Brownlee, 2000). Aerobic respiration, which utilizes O_2 as the terminal electron acceptor to oxidize organic compounds, releases significantly more energy relative to other forms of respiration, as demonstrated by its highest Gibbs free energy yield (Canfield and Thamdrup, 2009). Such a leap in energy availability associated with aerobic metabolism in mitochondria facilitates the larger genome sizes in eukaryotic cells and hence laid the foundation for complexity of eukaryotes and the emergence of multicellular organisms (Lane and Martin, 2010). However, instead of being constant, the O_2 abundance in the atmosphere, rather evolved from an anoxic state to the modern oxygen-rich state over the last 4.5 billion years (e.g., Lyons et al., 2014). Accurately constraining atmospheric O_2 therefore serves a necessary component of understanding the interplay between the atmospheric and oceanic oxygenation and the biological evolution.

Traditionally, oxygen has been attributed as a driving factor of the evolution of eukaryotic species due to the broad temporal coincidence between the oxygenation events and diversification of fossil records (Canfield et al., 2007; Sahoo et al., 2012; Dahl et al., 2010; Xiao et al., 1998). However, recently the idea that oxygen played an essential role in evolution—especially in the evolution of metazoans—has been intensely debated (Cole et al., 2020). In contrast to the classic view that the origin of complex forms of animals requires a certain threshold of dissolved oxygen, a new opinion has been proposed that the early animals, such as sponges, were able to withstand much lower oxygen levels—perhaps even low to sub-μM levels (Mills and Canfield, 2014). Although controversial, there are geochemical, molecular biological and fossil evidence indicating

that the earliest animals originated, or even diversified during the Cryogenian (~700 - 800Ma), before the Ediacaran, when the Neoproterozoic Oxidation Event occurred (Love et al., 2009; Erwin et al., 2011; Dohrmann and Wörheide, 2017; Neuweiler et al., 2009). Furthermore, in contrast to the view that the appearance of abundant oxygen was a prerequisite for the evolution of animals, there is a possibility that the shallow ocean oxygenation during the Neoproterozoic was instead actually the result from increased organic matter remineralization depth caused by the origin of animals (Butterfield, 2009; Mills and Canfield, 2014; Erwin and Tweedt, 2012) or eukaryotic phytoplankton (Lenton et al., 2014). Indeed, a long-term hinderance to address these competing hypotheses is limited by quantitative constraints on surface oxygen levels across the Proterozoic broadly, which inhibits direct comparisons between oxygen availability and proposed metabolic demands as well as the timing of evolutionary appearances and changes in specific oxygen concentrations.

During the past 4.5 billion years the Earth system had undergone a remarkable transition of the atmospheric O_2 baseline, evolving from an undetectable level ($<10^{-5}$ present atmospheric level, PAL) to the modern state (1 PAL, 21% atm) through a series of stepwise oxygenation events (Lyons et al., 2014, 2021, 2024) (Figure 1.1). The first milestone of atmospheric oxygenation took place between 2.45-2.32 billion years ago (Ga) during the Great Oxygenation Event (GOE). This event marked an irreversible rise in atmospheric O_2 to levels of 10^{-5} to 10^{-3} PAL, as first evidenced by disappearance of mass independent fractionation of sulfur (MIF-S) signals in sedimentary rocks (Farquhar and Wing, 2003; Farquhar et al., 2000). A low baseline of atmospheric O_2 between 0.1% to 1% PAL persisted through the Earth's middle age between ~1.8-0.8 Ga was evidenced by oxidative chromium weathering recorded in shale chromium isotopic signals ($\delta^{53}Cr$) (Lyons et al., 2014; Cole et al., 2016; Gilleaudeau et al., 2016; Canfield et al., 2018). The second milestone of

oxygenation occurred during the later stages of the Proterozoic (Neoproterozoic Oxygenation Event, NOE) between 1.0-0.55 Ga (D. E. Canfield, 1998). Iron speciation in deep sea sediments and the enrichment in redox-sensitive metals (e.g., uranium, molybdenum, and vanadium) in anoxic shales suggest the existence of large reservoirs in oxidized forms of these elements was maintained by widespread oxidation in the ocean (Canfield et al., 2007; Sahoo et al., 2012). Traditionally, the NOE represents the second stepwise transition, marking the atmospheric O_2 close to the modern level (e.g., Lyons et al., 2014). However, recent re-examination of these geochemical signals has argued that oxygenation during the Late Proterozoic, even in the Early Paleozoic, was rather limited, likely below 10% PAL (Sperling et al., 2015; Ostrander et al., 2023b; Zhang et al., 2018; Wallace et al., 2017).

A third milestone has been proposed to have occurred during the Paleozoic (Figure 1.1), marking the final breakthrough of atmospheric O_2 level from the low Precambrian ceiling to approximating to the modern. The timing of this event varies depends on different proxies as well as Earth System models used, but there is a general agreement that it occurred during the Silurian-Devonian Periods (Krause et al., 2018; Wallace et al., 2017). The evolution of large vascular land plants has been hypothesized to have driven this third atmospheric oxygenation by enhancing burial of organic carbon (in lignin) in terrestrial settings (Algeo et al., 1995; Algeo and Ingall, 2007; Wallace et al., 2017).

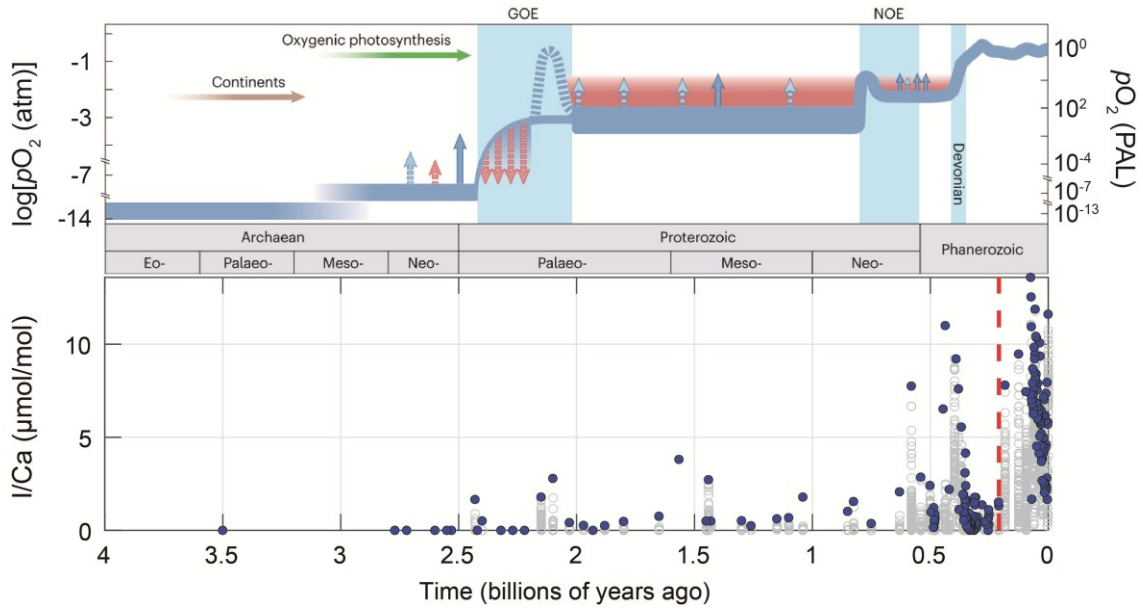

Figure 1.1. Secular evolution of Earth's atmospheric O_2 (upper panel) and carbonate I/Ca records (lower panel) averaged in 1 million year-bin intervals. The blue curve represents the long-term O_2 evolution, while the red shadow shows an alternative higher pO_2 estimation using a numeric model (Daines et al., 2017). Three oxygenation events are highlighted as GOE, NOE, and the Devonian event. Blue arrows represent transient increases in $pO2$ reflected by geochemical evidence. The red arrows marks the short-term fluctuations in O_2 that were accompanied with the GOE (Lyons et al., 2024). The blue dots represent the highest I/Ca values for each interval. The redline marks the transition of I/Ca from the Precambrian baseline to the modern-like baseline (Hardisty and Lau, 2025).

The redox state of the Earth's Ocean also evolved along with the oxygenation of the atmosphere. However, direct constraints for dissolved O_2 levels in the ocean remain more qualitative than quantitative, especially for periods in the Precambrian. It is widely accepted that the majority of the early ocean was ferruginous (anoxic with Fe(II) present) with interspersed euxinic conditions (anoxic with sulfide present) regions, overlain by a thin layer of weakly oxygenated seawater in the surface (Lyons et al., 2014). In contrast to the overall low O_2 in the surface ocean beneath the weakly oxygenated atmosphere 'oxygen oases' likely existed (Reinhard et al., 2016; Reinhard and Planavsky, 2022). Oxygen oases are regions with sufficient nutrient supplies supporting elevated photosynthetic primary productivity and have the potential to accumulate dissolved O_2 significantly higher than those dictated by seawater-air equilibrium.

Oxygen oases might have been sanctuaries for early multicellular eukaryotic organisms even animals, in which dissolved O_2 can reach to ~10 μM, supporting metabolic requirements (Reinhard et al., 2016). The limited oxygenation state in the surface ocean might have persisted throughout the Proterozoic and Early Paleozoic (Sperling et al., 2015; Planavsky et al., 2016; Liu et al., 2021; Hardisty et al., 2017). Completion of deep ocean oxygenation, which is regarded as the milestone of ocean oxygenation, likely occurred during the Late Paleozoic (Wallace et al., 2017; Lu et al., 2018). As the deep ocean anoxia gradually diminished, more niches were created and hence laid the foundation for biodiversification (Edwards et al., 2017; Edwards, 2019; Lindskog et al., 2023; Kozik et al., 2023). This transition also signifies a shift from the 'OOE state', characterized by a broadly anoxic ocean with episodic ocean oxygenation events (OOEs), to the 'OAE state', where the ocean became predominantly oxygenated with episodic ocean anoxic events (OAEs) (Hardisty and Lau, 2025). In addition to previous research outlining the broad patterns of ocean oxygenation, there is a growing need for quantitatively constraining local/regional seawater oxygenation, not only to bridge the gaps in our understanding of marine oxygenation, but also to explore the co-evolution of life and the Earth system.

The ratio of iodine to calcium (I/Ca or I/(Ca+Mg) considering dolomitization) in marine carbonates has been recently regarded as a potential proxy for oxygenation in the surface ocean at local or regional scales (Hardisty et al., 2017; Zhou et al., 2015; Hardisty et al., 2014; Edwards et al., 2018; Liu et al., 2020, 2019; Lu et al., 2020, 2016, 2018; He et al., 2022; Lu et al., 2010; Zhou et al., 2014; Bowman et al., 2020; Pohl et al., 2021; Wei et al., 2021; Ding et al., 2022; Shang et al., 2019; Uahengo et al., 2020; Yu et al., 2022; Fang et al., 2024; Tang et al., 2023). The geochemical basis of using the I/Ca paleoredox proxy lies in iodine's redox sensitivity. Its two thermodynamically stable forms in the ocean, iodate (IO_3^-) and iodide (I^-), shift between each other

according to the redox state of the seawater (Wong and Brewer, 1977; Luther et al., 1995). The redox potential of IO_3^-/ I^- and O_2/ H_2O reactions in seawater are much closer compared to those of other redox sensitive elements (e.g., uranium, iron, and molybdenum), making iodine speciation theoretically more sensitive to O_2 variation (Rue et al., 1997; Cutter et al., 2018). In the modern ocean, the relative abundance of iodine species is generally redox-dependent (Figure 1.2). Specifically, IO_3^- is usually dominant in oxygenated parts of the ocean, while in oxygen deficient zones (ODZs) or below the chemocline of anoxic basins, IO_3^- is commonly reduced to I^- (e.g., Rue et al., 1997; Farrenkopf and Luther, 2002; Cutter et al., 2018; Chance et al., 2014; Moriyasu et al., 2023, 2020; Rapp et al., 2019; Chapman, 1983; Luther and Campbell, 1991; Wong and Brewer, 1977; Truesdale et al., 2013). Importantly, IO_3^- incorporates into the carbonate lattice whilst I^- does not, enabling the estimation of IO_3^- in ancient seawater via I/Ca hosted in carbonates, which can be used for redox interpretation (Lu et al., 2010; Zhou et al., 2014; Hashim et al., 2022; Podder et al., 2017; Kerisit et al., 2018; Zhang et al., 2013). In addition, I/Ca provides the most conservative minimum estimation of oxygenation, as post-depositional alterations selectively removes IO_3^- from carbonate lattice, thereby lowering the primary signal of I/Ca (Hardisty et al., 2017; Hashim et al., 2022).

The well-known secular trend of I/Ca throughout Earth history showing IO_3^- accumulation generally matches with the progress of atmospheric oxygenation (Figure 1.1). However, the details of oxygenation reflected by I/Ca remain unclear. For example, the first appearance of non-zero IO_3^- in seawater, signaling the initiation of the oxidative iodine cycle, corresponds to the atmospheric oxygenation during the GOE (Hardisty et al., 2014). Following the GOE, I/Ca remained at a low baseline close to 0.5 μmol/mol through the Proterozoic to the Early Paleozoic, punctuated by transient higher values indicating temporal limited oxygenation (Hardisty et al.,

2017; Liu et al., 2020; Shang et al., 2019)(Figure 1.1). However, the level of atmospheric and oceanic O_2 necessary to enable this first IO_3^- appearance, as well as sustaining a low Proterozoic baseline level of IO_3^- accumulation has not yet been well quantified. That is, better constraining oxygenation in the ancient ocean is hindered by poor knowledge of the iodine cycling in low O_2 conditions, as well as mechanisms contributing to IO_3^- accumulation in seawater.

The overall goal of this dissertation is to better understand iodine redox cycling in low O_2 environments to assist quantitative paleoredox reconstruction. These constraints have implications for the roles of secular O_2 variation, if any, in the origin of eukaryotes and the development of multicellularity on Earth. Specifically, I investigate iodine redox cycling in the modern ocean **using insights from the present as a key to unlock the questions to Earth's past**. I integrate constraints from seawater samples collected from modern anoxic basins (Chapter 2), Earth System modeling (Chapter 3), and microbial incubation experiments (Chapter 4), together to interpret the secular variation of atmospheric O_2, as well as ocean oxygenation, as informed by existing I/Ca records. The hypotheses tested in this dissertation not only provide new insights to coevolution of the Earth surface oxygenation and life in the past, but also assist in understanding the potential distribution of complex life in the Universe, which fits within the scope of the Evolution of Advanced Life emphasized by the NASA Exobiology Program. In the next section (Section 1.2), I introduce more specific objectives of Chapters 2-4.

1.2 Objectives of this dissertation

Chapters 2-4 are inspired by these important questions that ultimately point to quantitatively reconstructing redox conditions in the atmosphere and the ocean through Earth's history: (1) how does IO_3^- accumulate in surface water above the chemocline in a redox stratified basin? (2) Can incorporation of the iodine cycle into an Earth System model (cGENIE) that is

calibrated against modern observations and field-based experimental constraints improve paleo-applications to reconstruct near-surface redox? (3) What is the O_2 threshold for microbial IO_3^- reduction? And (4) combining the insights from questions 1-3, what is the secular redox landscape in the ocean and the atmosphere based on existing I/Ca compilations?

In Chapter 2, I analyzed iodine speciation in samples collected from the Baltic Sea and Siders Pond. Despite their differences in spatial extent, both the basins share the same hydrographic character—redox stratified water column divided by the upper, oxygenated layer and the deeper, anoxic layer (Truesdale et al., 2013; Ostrander et al., 2023a; Caraco, 1986). This redox stratification serves as an analogue to Earth's early oceans, offering insights into the iodine redox cycling processes during the Proterozoic Eon. Importantly, the redox proximity between iodine and manganese (Mn) and nitrogen (N) in seawater hints at the possibility that these elemental cycles interplay with iodine redox cycling across the chemocline. Laboratory experiments have shown that Mn species, dissolved Mn(II) and mineral phase Mn oxides can abiotically reduce IO_3^- and oxidize I^-, respectively (Anschutz et al., 2000; Fox et al., 2009). In addition, some strains of bacteria that are capable of oxidizing Mn(II) and ammonium, also exhibit the ability to oxidize I^- (Li et al., 2014; Hughes et al., 2021). The redox interactions between iodine and these elements are, however, rarely examined. In this chapter, I hypothesize that due to the significant difference between kinetics of IO_3^- reduction (in the scale of hours) compared to I^- re-oxidation (in the scale of years) leads to a net removal of IO_3^- in the surface layer under prolonged, stagnant stratification, even when the layer remains saturated with O_2. In another words, IO_3^- accumulation in the surface water relies on replenishment from the oligotrophic open ocean, where O_2 is above the reduction threshold and photosynthetic assimilation is minimal.

If this hypothesis is correct, IO_3^- may serve as regional, even sub-global scale redox indicator, which is further supported by observations of mixed IO_3^- signal from several major water masses of the Pacific Ocean within a relative small area in the Eastern Tropical North Pacific (ETNP) (Hardisty et al., 2021). Redox reconstruction based on I/Ca therefore requires a comprehensive approach. This includes consideration of not only the iodine biogeochemical cycle itself, but also seawater circulation patterns that must be coupled to dynamic bathymetric configurations of targeted time slices in the past.

In Chapter 3, I work on improving and calibrating the iodine cycle that has been preliminarily built in the cGENIE Earth System Model (Lu et al., 2018). cGENIE is a classification of 'Earth system model with intermediate complexity' (EMIC) designed for simulating a range of biogeochemical and physical processes in the ocean with a balance of detail and computational efficiency. This makes it particularly suitable for modeling ancient ocean conditions, allowing researchers to explore the interactions between geochemical cycles through large numbers of sensitivity analyses (Ridgwell et al., 2007). The iodine cycle in cGENIE includes four processes: (1) IO_3^- reduction in the water column, (2) I^- oxidation (also in the water column), (3) photosynthetic IO_3^- uptake (and assumed intercellular reduction to I^-), and (4) I^- release to seawater during the remineralization of organic matter. Based upon the previous research by Lu et al., (2018), I evaluate the performance of alternative scenarios which might be more suitable for simulating the anoxia-dominated ancient ocean. The parameters associated with these iodine oxidation-reduction scenarios are against the IO_3^- and I^- concentrations observed in the modern-day ocean. The combination of parameters that not only reach the best overall replication of observations, but also correctly simulate iodine gradients (i.e., depth profiles, ODZ features, and meridional distributions), are further tested against I/Ca measurements made on Cretaceous carbonates. I

hypothesize that if there are one or more parameter combinations that performed well in replicating both modern ocean iodine distribution as well as Cretaceous I/Ca, the iodine cycle built in cGENIE has the potential of simulating the marine iodine cycle to help interpret and constrain the redox evolution of past oceans.

Chapter 4 focuses on providing direct O_2 constraints from secular I/Ca variation via two approaches: (1) microbial incubation experiments that aim at finding the O_2 threshold for IO_3^- reduction and (2) constraining oxygenation and nutrient levels in the ancient ocean, using cGENIE iodine cycle calibrated in Chapter 3. Specifically, recent studies has demonstrated that IO_3^- can be reduced by bacteria, including genus *Shewanella sp.*, *Roseovarius sp.*, *Notoacmeibacter sp.*, and *Aliiroseovarius sp*. (Farrenkopf et al., 1997; Jiang et al., 2023; Kine et al., 2024; Toporek et al., 2019; Shin et al., 2022). In this Chapter, I incubate bacteria *Shewanella oneidensis* MR-1 in M5 minimal medium amended with IO_3^-, and test its ability to reduce IO_3^- under various low-O_2 levels. In addition, I conduct sensitivity analysis by varying atmospheric O_2 and ocean water PO_4 levels to constrain the conditions that are required to accumulate different levels of IO_3^- in the ocean. Together, these approaches provide constraints on the minimum extent of ocean oxygenation that allowed the initial appearance of I/Ca in rock records, as well as the O_2 and nutrient requirements for the Proterozoic low I/Ca baseline and the Paleozoic high I/Ca baseline (Figure 1.1). By comparison between these boundary conditions, we could potentially understand the driving factor behind such baseline transitions, and hence provide temporal constraints on the completion of deep ocean oxygenation.

REFERENCES

Algeo, T. J. and Ingall, E.: Sedimentary Corg:P ratios, paleocean ventilation, and Phanerozoic atmospheric pO2, Palaeogeogr. Palaeoclimatol. Palaeoecol., 256, 130–155, https://doi.org/10.1016/j.palaeo.2007.02.029, 2007.

Algeo, T. J., Berner, R. A., Maynard, J. B., and Scheckler, S. E.: Late Devonian oceanic anoxic events and biotic crisis: "rooted'' in the evolution of vascular land plants?," GSA Today, 5, 1995.

Anschutz, P., Sundby, B., Lefrancois, L., Luther, G. W., and Mucci, A.: Interactions between metal oxides and species of nitrogen and iodine in bioturbated marine sediments, Geochim. Cosmochim. Acta, 64, 2751–2763, 2000.

Bowman, C. N., Lindskog, A., Kozik, N. P., Richbourg, C. G., Owens, J. D., and Young, S. A.: Integrated sedimentary, biotic, and paleoredox dynamics from multiple localities in southern Laurentia during the late Silurian (Ludfordian) extinction event, Palaeogeogr. Palaeoclimatol. Palaeoecol., 553, 109799, https://doi.org/10.1016/j.palaeo.2020.109799, 2020.

Butterfield, N. J.: Oxygen, animals and oceanic ventilation: An alternative view, Geobiology, 7, 1–7, https://doi.org/10.1111/j.1472-4669.2009.00188.x, 2009.

Canfield, D. E. and Thamdrup, B.: Towards a consistent classification scheme for geochemical environments, or, why we wish the term "suboxic" would go away: Editorial, Geobiology, 7, 385–392, https://doi.org/10.1111/j.1472-4669.2009.00214.x, 2009.

Canfield, D. E., Poulton, S. W., and Narbonne, G. M.: Late-Neoproterozoic deep-ocean oxygenation and the rise of animal life, Science (80-.)., 315, 92–95, https://doi.org/10.1126/science.1135013, 2007.

Canfield, D. E., Zhang, S., Frank, A. B., Wang, X., Wang, H., Su, J., Ye, Y., and Frei, R.: Highly fractionated chromium isotopes in Mesoproterozoic-aged shales and atmospheric oxygen, Nat. Commun., 9, 1–11, https://doi.org/10.1038/s41467-018-05263-9, 2018.

Caraco, N.: Phosphorus, Iron, and Carbon Cycling in a Salt Stratified Coastal Pond, Boston University, 1–213 pp., 1986.

Chance, R., Baker, A. R., Carpenter, L., and Jickells, T. D.: The distribution of iodide at the sea surface, Environ. Sci. Process. Impacts, 16, 1841–1859, https://doi.org/10.1039/c4em00139g, 2014.

Chapman, P.: Changes in iodine speciation in the Benguela current upwelling system, Deep Sea Res. Part A, Oceanogr. Res. Pap., 30, 1247–1259, https://doi.org/10.1016/0198-0149(83)90083-3, 1983.

Cole, D. B., Reinhard, C. T., Wang, X., Gueguen, B., Halverson, G. P., Gibson, T., Hodgskiss, M. S. W., Mckenzie, N. R., Lyons, T. W., and Planavsky, N. J.: A shale-hosted Cr isotope

record of low atmospheric oxygen during the Proterozoic, Geology, 44, 555–558, 2016.

Cole, D. B., Mills, D. B., Erwin, D. H., Sperling, E. A., Porter, S. M., Reinhard, C. T., and Planavsky, N. J.: On the co-evolution of surface oxygen levels and animals, Geobiology, 18, 260–281, https://doi.org/10.1111/gbi.12382, 2020.

Cutter, G. A., Moffett, J. G., Nielsdóttir, M. C., and Sanial, V.: Multiple oxidation state trace elements in suboxic waters off Peru: In situ redox processes and advective/diffusive horizontal transport, Mar. Chem., 201, 77–89, https://doi.org/10.1016/j.marchem.2018.01.003, 2018.

D. E. Canfield: A new model for Proterozoicocean chemistry, Nature, 396, 1–4, 1998.

Dahl, T. W., Hammarlund, E. U., Anbar, A. D., Bond, D. P. G., Gill, B. C., Gordon, G. W., Knoll, A. H., Nielsen, A. T., Schovsbo, N. H., and Canfield, D. E.: Devonian rise in atmospheric oxygen correlated to the radiations of terrestrial plants and large predatory fish, Proc. Natl. Acad. Sci. U. S. A., 107, 17911–17915, https://doi.org/10.1073/pnas.1011287107, 2010.

Ding, Y., Sun, W., Liu, S., Xie, J., Tang, D., Zhou, X., Zhou, L., Li, Z., Song, J., Li, Z., Xu, H., Tang, P., Liu, K., Li, W., and Chen, D.: Low oxygen levels with high redox heterogeneity in the late Ediacaran shallow ocean: Constraints from I/(Ca + Mg) and Ce/Ce* of the Dengying Formation, South China, Geobiology, 20, 790–809, https://doi.org/10.1111/gbi.12520, 2022.

Dohrmann, M. and Wörheide, G.: Dating early animal evolution using phylogenomic data, Sci. Rep., 7, 1–6, https://doi.org/10.1038/s41598-017-03791-w, 2017.

Edwards, C. T.: Links between early Paleozoic oxygenation and the Great Ordovician Biodiversification Event (GOBE): A review, Palaeoworld, 28, 37–50, https://doi.org/10.1016/j.palwor.2018.08.006, 2019.

Edwards, C. T., Saltzman, M. R., Royer, D. L., and Fike, D. A.: Oxygenation as a driver of the Great Ordovician Biodiversification Event, Nat. Geosci., 10, 925–929, https://doi.org/10.1038/s41561-017-0006-3, 2017.

Edwards, C. T., Fike, D. A., Saltzman, M. R., Lu, W., and Lu, Z.: Evidence for local and global redox conditions at an Early Ordovician (Tremadocian) mass extinction, Earth Planet. Sci. Lett., 481, 125–135, https://doi.org/10.1016/j.epsl.2017.10.002, 2018.

Erwin, D. H. and Tweedt, S.: Ecological drivers of the Ediacaran-Cambrian diversification of Metazoa, Evol. Ecol., 26, 417–433, https://doi.org/10.1007/s10682-011-9505-7, 2012.

Erwin, D. H., Laflamme, M., Tweedt, S. M., Sperling, E. A., Pisani, D., and Peterson, K. J.: The Cambrian conundrum: Early divergence and later ecological success in the early history of animals, Science (80-.)., 334, 1091–1097, https://doi.org/10.1126/science.1206375, 2011.

Fang, H., Fralick, P., Ramsay, B., Tang, D., and Riding, R.: Non-zero I/(Ca + Mg) recorded in Archean and Paleoproterozoic shallow marine Ca-carbonate sediments, Precambrian Res.,

405, 107350, https://doi.org/10.1016/j.precamres.2024.107350, 2024.

Farquhar, J. and Wing, B. A.: Multiple sulfur isotopes and the evolution of the atmosphere, 213, 1–13, https://doi.org/10.1016/S0012-821X(03)00296-6, 2003.

Farquhar, J., Bao, H., and Thiemens, M.: Atmospheric Influence of Earth ' s Earliest Sulfur Cycle, Science (80-.)., 289, https://doi.org/10.1126/science.289.5480.756, 2000.

Farrenkopf, A. M. and Luther, G. W.: Iodine chemistry reflects productivity and denitrification in the Arabian Sea: Evidence for flux of dissolved species from sediments of western India into the OMZ, Deep. Res. Part II Top. Stud. Oceanogr., 49, 2303–2318, https://doi.org/10.1016/S0967-0645(02)00038-3, 2002.

Farrenkopf, A. M., Dollhopf, M. E., Chadhain, S. N., Luther, G. W., and Nealson, K. H.: Reduction of iodate in seawater during Arabian Sea shipboard incubations and in laboratory cultures of the marine bacterium Shewanella putrefaciens strain MR-4, Mar. Chem., 57, 347–354, https://doi.org/10.1016/S0304-4203(97)00039-X, 1997.

Fike, D. A., Grotzinger, J. P., Pratt, L. M., and Summons, R. E.: Oxidation of the Ediacaran ocean, Nature, 444, 744–747, https://doi.org/10.1038/nature05345, 2006.

Fox, P. M., Davis, J. A., and Luther, G. W.: The kinetics of iodide oxidation by the manganese oxide mineral birnessite, Geochim. Cosmochim. Acta, 73, 2850–2861, https://doi.org/10.1016/j.gca.2009.02.016, 2009.

Gilleaudeau, G. J., Frei, R., Kaufman, A. J., Kah, L. C., Azmy, K., Bartley, J. K., Chernyavskiy, P., and Knoll, A. H.: Oxygenation of the mid-Proterozoic atmosphere: Clues from chromium isotopes in carbonates, Geochemical Perspect. Lett., 2, 178–187, https://doi.org/10.7185/geochemlet.1618, 2016.

Grotzinger, J. P., Fike, D. A., and Fischer, W. W.: Enigmatic origin of the largest-known carbon isotope excursion in Earth's history, Nat. Geosci., 4, 285–292, https://doi.org/10.1038/ngeo1138, 2011.

Hardisty, D. S. and Lau, K. V: Ocean redox evolution past and present, in: Treatise on geochemistry (3rd Edition), edited by: Anbar, A. D. and Weis, D., Elsevier Science, 245–296, 2025.

Hardisty, D. S., Lu, Z., Planavsky, N. J., Bekker, A., Philippot, P., Zhou, X., and Lyons, T. W.: An iodine record of Paleoproterozoic surface ocean oxygenation, Geology, 42, 619–622, https://doi.org/10.1130/G35439.1, 2014.

Hardisty, D. S., Lu, Z., Bekker, A., Diamond, C. W., Gill, B. C., Jiang, G., Kah, L. C., Knoll, A. H., Loyd, S. J., Osburn, M. R., Planavsky, N. J., Wang, C., Zhou, X., and Lyons, T. W.: Perspectives on Proterozoic surface ocean redox from iodine contents in ancient and recent carbonate, Earth Planet. Sci. Lett., 463, 159–170, https://doi.org/10.1016/j.epsl.2017.01.032, 2017.

Hardisty, D. S., Horner, T. J., Evans, N., Moriyasu, R., Babbin, A. R., Wankel, S. D., Moffett, J. W., and Nielsen, S. G.: Limited iodate reduction in shipboard seawater incubations from the Eastern Tropical North Pacific oxygen deficient zone, Earth Planet. Sci. Lett., 554, 116676, https://doi.org/10.1016/j.epsl.2020.116676, 2021.

Hashim, M. S., Burke, J. E., Hardisty, D. S., and Kaczmarek, S. E.: Iodine incorporation into dolomite: Experimental constraints and implications for the iodine redox proxy and Proterozoic Ocean, Geochim. Cosmochim. Acta, 338, 365–381, https://doi.org/10.1016/j.gca.2022.10.027, 2022.

He, R., Limburg, K. E., Walther, B. D., Samson, M. A., and Lu, Z.: Iodine content of fish otoliths in species found in diverse habitats, Environ. Biol. Fishes, 105, 351–367, https://doi.org/10.1007/s10641-022-01228-6, 2022.

Hughes, C., Barton, E., Hepach, H., Chance, R., Wadley, M. R., Pickering, M. D., Hogg, K., Pommerening-r, A., Stevens, D. P., and Jickells, T. D.: Oxidation of iodide to iodate by cultures of marine ammonia-oxidising bacteria, Mar. Chem., 234, 1–7, https://doi.org/10.1016/j.marchem.2021.104000, 2021.

Jiang, Z., Cui, M., Qian, L., Jiang, Y., Shi, L., Dong, Y., Li, J., and Wang, Y.: Abiotic and Biotic Reduction of Iodate Driven by Shewanella oneidensis MR-1, Environ. Sci. Technol., 57, 19817–19826, https://doi.org/10.1021/acs.est.3c06490, 2023.

Kerisit, S. N., Smith, F. N., Saslow, S. A., Hoover, M. E., Lawter, A. R., and Qafoku, N. P.: Incorporation Modes of Iodate in Calcite, Environ. Sci. Technol., 52, 5902–5910, https://doi.org/10.1021/acs.est.8b00339, 2018.

Kine, K., Yamamura, S., and Amachi, S.: Iodate reduction by marine aerobic bacteria, Front. Microbiol., 15, 1–8, https://doi.org/10.3389/fmicb.2024.1446596, 2024.

Kozik, N. P., Young, S. A., Ahlberg, P., Lindskog, A., and Owens, J. D.: Progressive marine oxygenation and climatic cooling at the height of the Great Ordovician Biodiversification Event, Glob. Planet. Change, 227, 104183, https://doi.org/10.1016/j.gloplacha.2023.104183, 2023.

Krause, A. J., Mills, B. J. W., Zhang, S., Planavsky, N. J., Lenton, T. M., and Poulton, S. W.: Stepwise oxygenation of the Paleozoic atmosphere, Nat. Commun., 9, 1–10, https://doi.org/10.1038/s41467-018-06383-y, 2018.

Lane, N. and Martin, W.: The energetics of genome complexity, Nature, 467, 7–12, https://doi.org/10.1038/nature09486, 2010.

Lenton, T. M., Boyle, R. A., Poulton, S. W., Shields-Zhou, G. A., and Butterfield, N. J.: Co-evolution of eukaryotes and ocean oxygenation in the Neoproterozoic era, Nat. Geosci., 7, 257–265, https://doi.org/10.1038/ngeo2108, 2014.

Li, H., Daniel, B., Creeley, D., Grandbois, R., Zhang, S., Xu, C., Ho, Y., and Schwehr, K. A.: Superoxide Production by a Manganese-Oxidizing Bacterium Facilitates Iodide Oxidation,

Appl. Environ. Microbiol., 80, 2693–2699, https://doi.org/10.1128/AEM.00400-14, 2014.

Lindskog, A., Young, S. A., Bowman, C. N., Kozik, N. P., Newby, S. M., Eriksson, M. E., Pettersson, J., Molin, E., and Owens, J. D.: Oxygenation of the Baltoscandian shelf linked to Ordovician biodiversification, Nat. Geosci., 16, 1047–1054, https://doi.org/10.1038/s41561-023-01287-z, 2023.

Liu, A., Tang, D., Shi, X., Zhou, X., Zhou, L., Shang, M., Li, Y., and Fang, H.: Mesoproterozoic oxygenated deep seawater recorded by early diagenetic carbonate concretions from the Member IV of the Xiamaling Formation, North China, Precambrian Res., 341, 105667, https://doi.org/10.1016/j.precamres.2020.105667, 2020.

Liu, J., Luo, G., Lu, Z., Lu, W., Qie, W., Zhang, F., Wang, X., and Xie, S.: Intensified Ocean Deoxygenation During the end Devonian Mass Extinction, Geochemistry, Geophys. Geosystems, 20, 6187–6198, https://doi.org/10.1029/2019GC008614, 2019.

Liu, X. M., Kah, L. C., Knoll, A. H., Cui, H., Wang, C., Bekker, A., and Hazen, R. M.: A persistently low level of atmospheric oxygen in Earth's middle age, Nat. Commun., 12, 1–7, https://doi.org/10.1038/s41467-020-20484-7, 2021.

Love, G. D., Grosjean, E., Stalvies, C., Fike, D. A., Grotzinger, J. P., Bradley, A. S., Kelly, A. E., Bhatia, M., Meredith, W., Snape, C. E., Bowring, S. A., Condon, D. J., and Summons, R. E.: Fossil steroids record the appearance of Demospongiae during the Cryogenian period, Nature, 457, 718–721, https://doi.org/10.1038/nature07673, 2009.

Lu, W., Ridgwell, A., Thomas, E., Hardisty, D. S., Luo, G., Algeo, T. J., Saltzman, M. R., Gill, B. C., Shen, Y., Ling, H. F., Edwards, C. T., Whalen, M. T., Zhou, X., Gutchess, K. M., Jin, L., Rickaby, R. E. M., Jenkyns, H. C., Lyons, T. W., Lenton, T. M., Kump, L. R., and Lu, Z.: Late inception of a resiliently oxygenated upper ocean, Science (80-.)., 361, 174–177, https://doi.org/10.1126/science.aar5372, 2018.

Lu, W., Rickaby, R. E. M., Hoogakker, B. A. A., Rathburn, A. E., Burkett, A. M., Dickson, A. J., Martínez-Méndez, G., Hillenbrand, C. D., Zhou, X., Thomas, E., and Lu, Z.: I/Ca in epifaunal benthic foraminifera: A semi-quantitative proxy for bottom water oxygen in a multi-proxy compilation for glacial ocean deoxygenation, Earth Planet. Sci. Lett., 533, 116055, https://doi.org/10.1016/j.epsl.2019.116055, 2020.

Lu, Z., Jenkyns, H. C., and Rickaby, R. E. M.: Iodine to calcium ratios in marine carbonate as a paleo-redox proxy during oceanic anoxic events, Geology, 38, 1107–1110, https://doi.org/10.1130/G31145.1, 2010.

Lu, Z., Hoogakker, B. A. A., Hillenbrand, C.-D., Zhou, X., Thomas, E., Gutchess, K. M., Lu, W., Jones, L., and Rickaby, R. E. M.: Oxygen depletion recorded in upper waters of the glacial Southern Ocean, Nat. Commun., 7, 1–8, https://doi.org/10.1038/ncomms11146, 2016.

Luther, G. W. and Campbell, T.: Iodine speciation in the water column of the Black Sea, Deep Sea Res. Part A. Oceanogr. Res. Pap., 38, S875–S882, https://doi.org/10.1016/s0198-0149(10)80014-7, 1991.

Luther, G. W., Wu, J., and Cullen, J. B.: Redox Chemistry of Iodine in Seawater, 135–155, https://doi.org/10.1021/ba-1995-0244.ch006, 1995.

Lyons, T. W., Reinhard, C. T., and Planavsky, N. J.: The rise of oxygen in Earth's early ocean and atmosphere, Nature, 506, 307–315, https://doi.org/10.1038/nature13068, 2014.

Lyons, T. W., Diamond, C. W., Planavsky, N. J., Reinhard, C. T., and Li, C.: Oxygenation, Life, and the Planetary System during Earth's Middle History: An Overview, Astrobiology, 21, 906–923, https://doi.org/10.1089/ast.2020.2418, 2021.

Lyons, T. W., Tino, C. J., Fournier, G. P., Anderson, R. E., Leavitt, W. D., Konhauser, K. O., and Stüeken, E. E.: Co-evolution of early Earth environments and microbial life, Nat. Rev. Microbiol., 22, 572–586, https://doi.org/10.1038/s41579-024-01044-y, 2024.

Mills, D. B. and Canfield, D. E.: Oxygen and animal evolution: Did a rise of atmospheric oxygen "trigger" the origin of animals?, BioEssays, 36, 1145–1155, https://doi.org/10.1002/bies.201400101, 2014.

Moriyasu, R., Evans, N., Bolster, K. M., Hardisty, D. S., and Moffett, J. W.: The Distribution and Redox Speciation of Iodine in the Eastern Tropical North Pacific Ocean, Global Biogeochem. Cycles, 34, 0–3, https://doi.org/10.1029/2019GB006302, 2020.

Moriyasu, R., Bolster, K. M., Hardisty, D. S., Kadko, D. C., Stephens, M. P., and Moffett, J. W.: Meridional Survey of the Central Pacific Reveals Iodide Accumulation in Equatorial Surface Waters and Benthic Sources in the Abyssal Plain Global Biogeochemical Cycles, Global Biogeochem. Cycles, 37, 1–15, https://doi.org/10.1029/2021GB007300, 2023.

Neuweiler, F., Turner, E. C., and Burdige, D. J.: Early Neoproterozoic origin of the metazoan clade recorded in carbonate rock texture, Geology, 37, 475–478, https://doi.org/10.1130/G25621A.1, 2009.

Ostrander, C. M., Nielsen, S. G., Gadol, H. J., Villarroel, L., Wankel, S. D., Horner, T. J., Blusztajn, J., and Hansel, C. M.: Thallium isotope cycling between waters , particles , and sediments across a redox gradient, Geochim. Cosmochim. Acta, 348, 397–409, https://doi.org/10.1016/j.gca.2023.03.028, 2023a.

Ostrander, C. M., Bjerrum, C. J., Ahm, A. S. C., Stenger, S. R., Bergmann, K. D., El-Ghali, M. A. K., Harthi, A. R., Aisri, Z., and Nielsen, S. G.: Widespread seafloor anoxia during generation of the Ediacaran Shuram carbon isotope excursion, Geobiology, 1–15, https://doi.org/10.1111/gbi.12557, 2023b.

Planavsky, N. J., Cole, D. B., Reinhard, C. T., Diamond, C., and Love, G. D.: No evidence for high atmospheric oxygen levels 1 , 400 million years ago, 113, 2550–2551, https://doi.org/10.1073/pnas.1601925113, 2016.

Podder, J., Lin, J., Sun, W., Botis, S. M., Tse, J., Chen, N., Hu, Y., Li, D., Seaman, J., and Pan, Y.: Iodate in calcite and vaterite: Insights from synchrotron X-ray absorption spectroscopy and first-principles calculations, Geochim. Cosmochim. Acta, 198, 218–228,

https://doi.org/10.1016/j.gca.2016.11.032, 2017.

Pohl, A., Lu, Z., Lu, W., Stockey, R. G., Elrick, M., Li, M., Desrochers, A., Shen, Y., He, R., Finnegan, S., and Ridgwell, A.: Vertical decoupling in Late Ordovician anoxia due to reorganization of ocean circulation, Nat. Geosci., 14, 868–873, https://doi.org/10.1038/s41561-021-00843-9, 2021.

Rapp, I., Schlosser, C., Barraqueta, J. M., Wenzel, B., Lüdke, J., and Scholten, J.: Controls on redox-sensitive trace metals in the Mauritanian oxygen minimum zone, Biogeosciences, 16, 4157–4182, 2019.

Reinhard, C. T. and Planavsky, N. J.: The History of Ocean Oxygenation, Ann. Rev. Mar. Sci., 14, 331–353, https://doi.org/10.1146/annurev-marine-031721-104005, 2022.

Reinhard, C. T., Planavsky, N. J., Olson, S. L., Lyons, T. W., and Erwin, D. H.: Earth's oxygen cycle and the evolution of animal life, Proc. Natl. Acad. Sci. U. S. A., 113, 8933–8938, https://doi.org/10.1073/pnas.1521544113, 2016.

Ridgwell, A., Hargreaves, J. C., Edwards, N. R., Annan, J. D., Lenton, T. M., Marsh, R., Yool, A., and Watson, A.: Marine geochemical data assimilation in an efficient Earth system model of global biogeochemical cycling, Biogeosciences, 4, 87–104, https://doi.org/10.5194/bg-4-87-2007, 2007.

Rue, E. L., Smith, G. J., Cutter, G. A., and Bruland, K. W.: The response of trace element redox couples to suboxic conditions in the water column, Deep. Res. Part I Oceanogr. Res. Pap., 44, 113–134, https://doi.org/10.1016/S0967-0637(96)00088-X, 1997.

Sahoo, S. K., Planavsky, N. J., Kendall, B., Wang, X., Shi, X., Scott, C., Anbar, A. D., Lyons, T. W., and Jiang, G.: Ocean oxygenation in the wake of the Marinoan glaciation, Nature, 489, 546–549, https://doi.org/10.1038/nature11445, 2012.

Shang, M., Tang, D., Shi, X., Zhou, L., Zhou, X., Song, H., and Jiang, G.: A pulse of oxygen increase in the early Mesoproterozoic ocean at ca. 1.57–1.56 Ga, Earth Planet. Sci. Lett., 527, 115797, https://doi.org/10.1016/j.epsl.2019.115797, 2019.

Shin, H. D., Toporek, Y., Mok, J. K., Maekawa, R., Lee, B. D., Howard, M. H., and DiChristina, T. J.: Iodate Reduction by Shewanella oneidensis Requires Genes Encoding an Extracellular Dimethylsulfoxide Reductase, Front. Microbiol., 13, 1–11, https://doi.org/10.3389/fmicb.2022.852942, 2022.

Sperling, E. A., Wolock, C. J., Morgan, A. S., Gill, B. C., Kunzmann, M., Halverson, G. P., Macdonald, F. A., Knoll, A. H., and Johnston, D. T.: Statistical analysis of iron geochemical data suggests limited late Proterozoic oxygenation, Nature, 523, 3–6, https://doi.org/10.1038/nature14589, 2015.

Tang, D., Fang, H., Shi, X., Liang, L., Zhou, L., Xie, B., Huang, K., Zhou, X., Wu, M., and Riding, R.: Mesoproterozoic Molar Tooth Structure Related to Increased Marine Oxygenation, J. Geophys. Res. Biogeosciences, 128, 1–18, https://doi.org/10.1029/2022jg007077, 2023.

Toporek, Y. J., Mok, J. K., Shin, H. D., Lee, B. D., Lee, M. H., and DiChristina, T. J.: Metal Reduction and Protein Secretion Genes Required for Iodate Reduction by Shewanella oneidensis, Appl. Environ. Microbiol., 85, 1–13, https://doi.org/10.1128/AEM.02115-18, 2019.

Truesdale, V. W., Nausch, G., and Waite, T. J.: The effects of the 2001 Barotropic intrusion of bottom-water upon the vertical distribution of inorganic iodine in the Gotland Deep, Cont. Shelf Res., 55, 155–167, https://doi.org/10.1016/j.csr.2013.01.005, 2013.

Uahengo, C. I., Shi, X., Jiang, G., and Vatuva, A.: Transient shallow-ocean oxidation associated with the late Ediacaran Nama skeletal fauna: Evidence from iodine contents of the Lower Nama Group, southern Namibia, Precambrian Res., 343, 105732, https://doi.org/10.1016/j.precamres.2020.105732, 2020.

Wallace, M. W., Hood, A., Shuster, A., Greig, A., Planavsky, N. J., and Reed, C. P.: Oxygenation history of the Neoproterozoic to early Phanerozoic and the rise of land plants, Earth Planet. Sci. Lett., 466, 12–19, https://doi.org/10.1016/j.epsl.2017.02.046, 2017.

Ward, P. D. and Brownlee, D.: Rare Earth, Copernicus, New York, https://doi.org/10.1007/b97646, 2000.

Wei, B., Tang, D., Shi, X., Lechte, M., Zhou, L., Zhou, X., and Song, H.: A Pulsed Oxygenation in Terminal Paleoproterozoic Ocean: Evidence From the Transition Between the Chuanlinggou and Tuanshanzi Formations, North China, Geochemistry, Geophys. Geosystems, 22, 1–23, https://doi.org/10.1029/2020GC009612, 2021.

Wong, G. T. F. and Brewer, P. G.: The marine chemistry of iodine in anoxic basins, Geochim. Cosmochim. Acta, 41, 151–159, https://doi.org/10.1016/0016-7037(77)90195-8, 1977.

Xiao, S., Zhang, Y., and Knoll, A. H.: Three-dimensional preservation of algae and animal embryos in a neoproterozoic phosphorite, Nature, 391, 553–558, https://doi.org/10.1038/35318, 1998.

Yu, Y., Chen, Y., Li, D., and Su, J.: A transient oxygen increase in the Mesoproterozoic ocean at ∼1.44 Ga: Geochemical evidence from the Tieling Formation, North China Platform, Precambrian Res., 369, 106527, https://doi.org/10.1016/j.precamres.2021.106527, 2022.

Zhang, F., Xiao, S., Kendall, B., Romaniello, S. J., Cui, H., Meyer, M., Gilleaudeau, G. J., Kaufman, A. J., and Anbar, A. D.: Extensive marine anoxia during the terminal ediacaran period, Sci. Adv., 4, https://doi.org/10.1126/sciadv.aan8983, 2018.

Zhang, S., Xu, C., Creeley, D., Ho, Y. F., Li, H. P., Grandbois, R., Schwehr, K. A., Kaplan, D. I., Yeager, C. M., Wellman, D., and Santschi, P. H.: Iodine-129 and iodine-127 speciation in groundwater at hanford site, U.S.: Iodate incorporation into calcite", Environ. Sci. Technol., 47, 13205–13206, https://doi.org/10.1021/es4046132, 2013.

Zhou, X., Thomas, E., Rickaby, R. E. M., Winguth, A. M. E., and Lu, Z.: I/Ca evidence for upper ocean deoxygenation during the PETM, Paleoceanography, 29, 964–975,

https://doi.org/10.1002/2014PA002702, 2014.

Zhou, X., Jenkyns, H. C., Owens, J. D., Junium, C. K., Zheng, X. Y., Sageman, B. B., Hardisty, D. S., Lyons, T. W., Ridgwell, A., and Lu, Z.: Upper ocean oxygenation dynamics from I/Ca ratios during the Cenomanian-Turonian OAE 2, Paleoceanography, 30, 510–526, https://doi.org/10.1002/2014PA002741, 2015.

CHAPTER 2: IODINE CYCLING IN MARINE ANOXIC BASINS: EXAMPLES FROM THE BALTIC SEA AND SIDERS POND

2.1 Abstract

Iodine in the ocean is redox sensitive and therefore its relative speciation distribution is thought to be dependent on the O_2 concentration in seawater. While the oxidized iodate (IO_3^-) is observed to become depleted relative to the reduced iodide (I^-) in modern and ancient low oxygen settings, the mechanisms and relationship with oxygen, if any, remain unclear. To provide constraints on potential O_2 controls on the iodine biogeochemical cycle, we collected samples and investigated iodine cycling in two modern anoxic systems: Siders Pond and the Baltic Sea. Like other stratified euxinic systems, iodide increases, and IO_3^- declines at or below the chemocline of both systems. Both basins, however, have complex patterns between iodine species that are decoupled from O_2, likely reflecting the unique hydrological and biogeochemical conditions of these stratified systems. Our findings reveal that, beyond redox conditions, a combination of factors including sea water renewal, freshwater input, density-stratification, phytoplankton reduction, benthic fluxes and reactive metal species, together exert influences on iodine speciation in anoxic basins. Notably, we observe significant IO_3^- depletion in the fully oxygenated surface layers of both systems, a phenomenon uncommonly reported elsewhere. In both basins, the surface water has an elevated (low IO_3^-) freshwater component, hence newly introduced (high IO_3^-) seawater must sink below the chemocline, limiting direct supply of IO_3^- to the surface. Based on our findings, O_2 and IO_3^- are likely to be decoupled in restricted basins and therefore, carbonate associated IO_3^- redox proxy records from such environments in deep time may be biased. Further, our study provides evidence that elevated surface IO_3^- accumulation in ancient oceans likely requires atmospheric O_2 to be sufficient for oxidizing underlying pelagic seawater.

2.2 Introduction

Iodine (I) speciation in the ocean is redox sensitive. In seawater, the iodine shifts between its oxidized form, iodate (IO_3^-), and the reduced form, iodide (I^-) depending on the redox state of the seawater. The ocean is one of the largest reservoirs of iodine on the surficial Earth, to which iodine is introduced from atmospheric deposition and freshwater, and the sink of oceanic iodine is emission into the atmosphere and sedimentation (Muramatsu and Wedepohl, 1998). Due to the long residence time in the ocean (~300 kyrs; Broecker and Peng, 1983), the total dissolved inorganic iodine has relatively constant concentrations across the ocean around 450nM (Elderfield and Truesdale, 1980; Truesdale et al., 2000; Chance et al., 2014). Despite the overall stable total dissolved iodine concentration, processes such as sedimentary benthic flux and primary productivity, either introduce or remove iodine from seawater. As a biophilic element, iodine is assimilated by phytoplankton, causing ~50nM net depletion of total dissolved iodine in the surface ocean (Schnur et al., 2024; Chance et al., 2014; Rue et al., 1997; Elderfield and Truesdale, 1980; Campos et al., 1996). Iodine associated with organics are delivered to the sediments, where iodine (in the form of I^-) is preferentially removed from organic particles during diagenesis and accumulates at near the sediment-water interface (Kennedy and Elderfield, 1987a; Scholz et al., 2024; Price and Calvert, 1973; Ullman and Aller, 1985; Martin et al., 1993). Resulting benthic fluxes of iodine could be upwelled into the overlying water column, causing excessive total iodine in seawater above ~450nM, which has been commonly observed globally in oxygen deficient zones (ODZ) (Moriyasu et al., 2020; Scholz et al., 2024; Cutter et al., 2018; Chapman, 1983; Farrenkopf et al., 1997).

As a redox sensitive element, IO_3^- is commonly observed to be reduced to I^- in marine low oxygen settings, such as ODZs and anoxic basins (Truesdale et al., 2000; Rue et al., 1997;

Farrenkopf and Luther, 2002; Wong and Brewer, 1977; Cutter et al., 2018; Moriyasu et al., 2020; Truesdale et al., 2013; Rapp et al., 2020, 2019). The redox potential for the IO_3^-/I^- reaction is close to that of O_2/H_2O, making iodine a sensitive tracer of seawater deoxygenation (Rue et al., 1997; Cutter et al., 2018). Because IO_3^- is preferentially incorporated into the calcite and dolomite lattice (Lu et al., 2010, Hashim et al., 2022), I/Ca in ancient carbonate traces the variation of IO_3^-, and hence provides a redox proxy for seawater in the deep time, covering the interval from Archean through Cenozoic (Lu et al., 2010; Hardisty et al., 2014; Zhou et al., 2015; Lu et al., 2016; Edwards et al., 2018; Lu et al., 2018; Bowman et al., 2020; Pohl et al., 2021; Wei et al., 2021; Ding et al., 2022; Shang et al., 2019; Liu et al., 2020; Fang et al., 2022; Uahengo et al., 2020; Yu et al., 2022; Tang et al., 2023).

Despite the widespread application of I/Ca in paleoceanography, the understanding of IO_3^--O_2 interaction in modern seawater is not fully clear, thus hindering quantitative redox reconstructions based on the I/Ca proxy. Field and laboratory experiments suggested that IO_3^- is dissimilatory reduced in anoxic seawater by reductases produced by bacteria (Farrenkopf et al., 1997; Reyes-Umana et al., 2021), or via abiotic pathways through reaction with Fe(II) or reduced sulfur (Councell et al., 1997; Jiang et al., 2023; Zhang and Whitfield, 1986). The IO_3^--O_2 data compilation from the modern open ocean ODZs show that IO_3^- reduction may not occur until a very low O_2 threshold, perhaps below 1μM (Cutter et al., 2018; Rue et al., 1997; Farrenkopf and Luther, 2002; Chapman, 1983; Moriyasu et al., 2020). However, more limited IO_3^- reduction is observed in some ODZs, probably due to processes such as large scale water mass mixing, or limited organic matter as a substrate for microbial activities (Hardisty et al., 2021; Cutter et al., 2018; Moriyasu et al., 2020). This inconsistency between limited IO_3^- reduction in the ODZ complicates the exploration of the redox requirement for IO_3^- reduction. On the other hand, anoxic

basins, with limited water mass mixing, more stable anoxia below the oxycline, and high organic matter deposition, provide an ideal marine setting for exploring the IO_3^- reduction mechanisms. Disproportionate from its importance, the iodine speciation measurements from anoxic basins are rare, and most of them are published more than 20 years ago (Truesdale et al., 2013; Wong et al., 1985; Emerson et al., 1979; Luther and Campbell, 1991; Ullman et al., 1990; Wong and Brewer, 1977; Shi et al., 2023).

Due to the proximity of their redox potentials in the seawater, iodine redox transformations might be influenced by manganese (Mn) and nitrogen (N) species (Rue et al., 1997). It has been suggested that the dissolved Mn species, such as Mn(II), are capable of reducing iodine in shallow marine sediments (Anschutz et al., 2000). Conversely, some Mn oxide minerals are able to oxidize I^- to iodine intermediates, and eventually to IO_3^- in some experiments (Fox et al., 2009; Szlamkowicz et al., 2022). Previous studies indicated that the microbes oxidizing or reducing Mn also contribute to iodine redox reactions, hinting at the close relationship between I and Mn in biogeochemical pathways (Farrenkopf et al., 1997; Li et al., 2014a). Similarly, some ammonia (NH_3) oxidizing bacteria has been observed to oxidize I^- to IO_3^- in laboratory conditions (Hughes et al., 2021). The nitrite (NO_2^-) and I^- maxima exhibit a close distribution within the ODZ and in anoxic basins may also indicate that the conditions required to reduce N and I species are proximal (Cutter et al., 2018; Truesdale et al., 2013; Moriyasu et al., 2020). However, the redox interaction between I, N and Mn, in an anoxic basin remains unclear.

To understand seawater iodine redox cycling across the redox ladder (from oxic to sulfidic) in detail, as well as to provide constraints for redox reconstruction with I/Ca proxy, we collected and measured iodine speciation from two stratified euxinic marine basins, the Baltic Sea and Siders Pond.

2.3 Sampling locations

2.3.1 The Baltic Sea

The Baltic Sea is an intra-continental sea which is separated from the North Sea. The Danish Straits connect the Baltic Sea and the North Sea through the Kattegat and Skagerrak (Figure 2.1). The Darss Sill between the Arkona Basin and the Kattegat Sea is shallow, with an average depth <20m, even less than 10m at the Gedser Reef (Lemke et al., 1994). To the east of the Darss Sill, a series of sub-basins—the Arkona Basin, the Bornholm Basin, the Gotland Deep, Fårö Deep, and the Landsort Deep—forms the deeper parts of the Baltic Sea, among which the latter three represent the deepest areas of the Baltic Sea. This unique geographic and bathymetric setting limits the seawater exchange between the Baltic Sea and the North Atlantic, causing the restriction of the deep waterbody within the Baltic Sea, leading to anoxia and even the accumulation of hydrogen sulfide (euxinia).

The Baltic Sea collects freshwater from a catchment that is 4.3 times larger than the sea's surface area. The excess freshwater input results in the fjordic circulation in the Baltic Sea. The lower density "freshwater"—with the salinity close to 8.5 PSU—circulates in the surface, while the heavier saline water is separated in the bottom, causing a strong halocline in between (Voipio, 1981) (Table 2.1). The strong water column stratification causes anoxia and even euxinia in the bottom of some sub-basins. Different from a permanent anoxic basin, the water column stratification in the Baltic Sea is dynamic, controlled by saline water renewal through baroclinic and barotropic flows. The baroclinic flow occurs during calm periods and is driven by the salinity gradient between the Baltic Sea and the North Sea. About 500km^3 of mixed seawater from the North Sea and the fresher surface water of the Baltic Sea flows into the deep Baltic Sea annually (Voipio, 1981). This gentle inflow is usually not strong enough to renew the deep water below the

chemocline in the Baltic Sea. Instead, it interleaves in the halocline. The barotropic inflows (Major Baltic Inflows, MBIs), caused by specific air circulation patterns over the North Atlantic and the Europe, are the only known mechanism that introduces saline, O_2-abundant seawater into the bottom of the Baltic basins (Mohrholz et al., 2015). An MBI event has the potential to oxidize the deep Baltic water in the short-term (Mohrholz et al., 2015). For example, during the relatively largwe MBI in 1993-1994, no sulfidic water was observed for about 4 months (Neretin et al., 2003). However, since the MBIs import large quantity of high salinity seawater, the water column stratification is enhanced after the MBIs, intensifying the deep water anoxia in the long-term.

The Gotland Deep is one of the deepest sub-basins in the Baltic Sea, with the maximum depth close to 250m (Dellwig et al., 2010). The water column redox stratification is dynamic due to the occasional occurrence of MBIs, contributing to the relative shorter water residence time (20-100 years, Reissmann et al., 2009) compared to strongly stratified basins (i.e. the Black Sea). This dynamic redox stratification results in active Mn-Fe-P cycling across the chemocline in the Gotland Deep (Neretin et al., 2003; Dellwig et al., 2010).

2.3.2 Siders Pond

Siders Pond is a meromictic coastal pond in southern Cape Cod and close to downtown Falmouth, Massachusetts, USA. Salt water enters the pond at an estimated annual rate of 0.15×10^6 m^3 through the Fresh River connecting the pond with the Vineyard Sound during high tides. The annual fresh water in flow is close to 1×10^6 m^3, through groundwater, precipitation, run-off from the residential area and a stream connecting the Shiverick Pond at ~300m northeast to the Siders Pond (Caraco, 1986; Ostrander et al., 2023).

The maximum depth of the Siders Pond is ~15m. The salinity gradient across the water column in the Siders Pond results in stratification. The chemocline varies between 3-6m, above

which the dissolved O_2 in the surface is commonly higher than 300µM, and drops to close to 0 in the bottom of the pond. Below the oxycline, ammonium (NH_4^+) and hydrogen sulfide (H_2S) accumulate (Ostrander et al., 2023).

2.4 Methods

2.4.1 Sample collection

The Baltic Sea samples were collected from 6 stations in the Gotland Deep, 1 station from the adjacent Fårö Deep, during the R/V Elizabeth Mann Borgese EMB276 cruise in September 2021 (Figure 2.1). Seawater was collected onboard through Niskin bottles mounted on a CTD rosette (conductivity-temperature-depth profiler). The samples were filtered using 0.2µm with Sterivex filters and collected in 125ml or 60ml amber Nalgene bottles once on deck and were frozen immediately afterwards for preservation (Campos, 1997). Basic hydrographic data, including dissolved O_2, salinity, turbidity were measured by CTD instrument package Sea-Bird SBE 911plus and are available at BCO-DMO data repository (https://www.bco-dmo.org/dataset/935118). Nutrient data, including PO_4, NO_3^-, NO_2^-, NH_4^+, H_2S, and total sulfides, were measured onboard using the PUMP-CTD-System coupled with an SBE 911plus package, and is available at BCO-DMO data repository (https://www.bco-dmo.org/dataset/934904).

The Siders Pond samples were collected and filtered on four sampling days of July 17, September 19, November 6, 2020 and July 31, 2021 using the same method described in Ostrander et al., (2023) (Figure 2.1). Basic hydrological properties including pH, salinity, and DO were measured before collecting the samples with a YSI-multi-probe system (Ostrander et al., 2023). The samples for iodine were filtered at 0.2µm with Sterivex filters and collected in 125ml or 60ml amber Nalgene bottles and were frozen immediately afterwards for preservation (Campos, 1997).

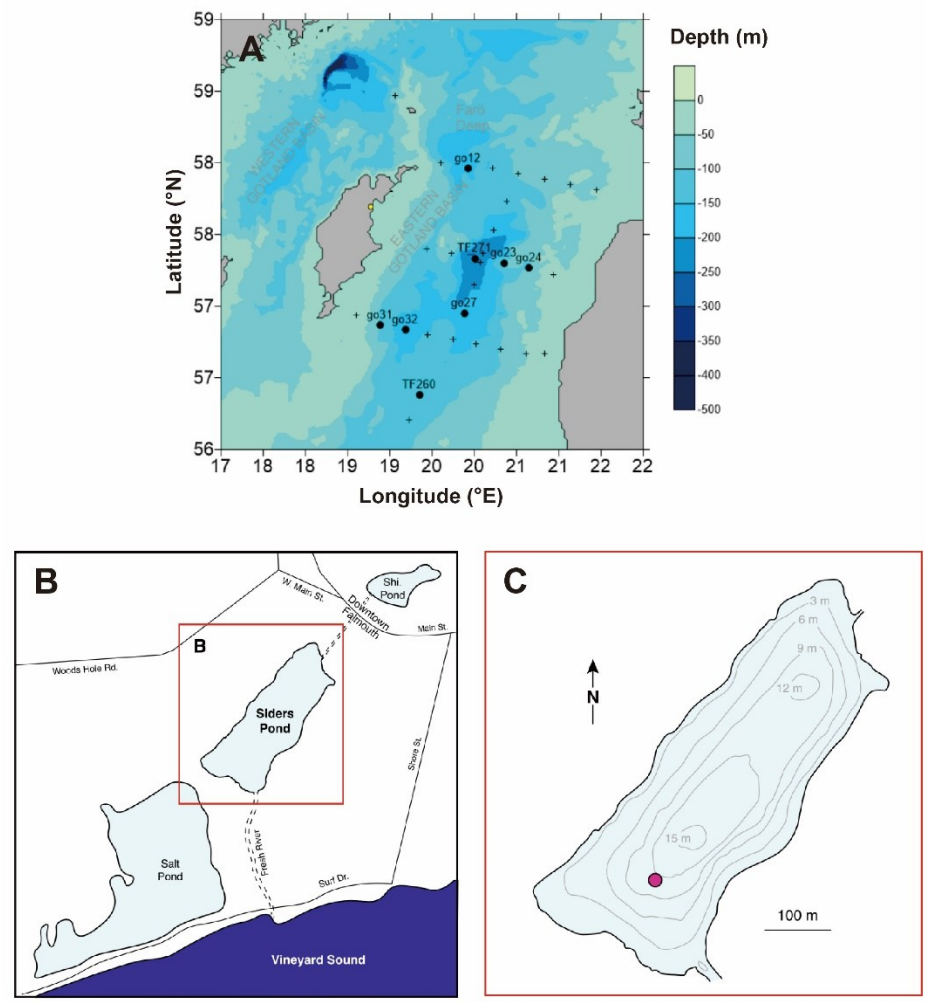

Figure 2.1. (A) The sampling stations of EMB276 cruise in the Baltic Sea (Voss et al., 2021). (B) Location of Siders Pond. (C) Bathymetry map and the sampling location of water sample collection in Siders Pond, modified from Ostrander et al., (2023).

2.4.2 Analytical methods

2.4.2.1 Ion Chromatography

We used a well-established ion chromatographic method to separate iodine speciation, including IO_3^-, I^-, dissolved organic iodine (DOI), and total iodine (TI) from natural water samples (Hou et al., 2013, 2001; Hardisty et al., 2021, 2020; Moriyasu et al., 2023; Reifenhäuser and Heumann, 1990; Hou et al., 1999; Ştreangă et al., 2024; Schnur et al., 2024). Glass columns for separating iodine species were washed by ultra-pure water (resistivity 18.2 MΩ.cm) produced from

the Milli-Q water purification system, followed by packing with PYREX glass wools and 1ml of AG1-X8 anion exchange resin. Before running any samples, the cleaning step using the same procedure of iodine speciation separation (replacing the sample with ultra-pure water) was applied to the columns and resins to remove any preexisting iodine contamination. We tested and verified that the reused resin does not induce notable cross- contamination between the samples.

During the chromatography procedure, the I^- fraction is specifically adsorbed onto the surface of the resin and is eluted following the addition of a 2M HNO_3 (Fisher Scientific, TraceMetal^{TM} Grade)- 18% (v/v) tetramethylammonium hydroxide (TMAH, Fisher Scientific) mixture solution. The eluent containing IO_3^- and DOI fractions (eluded with seawater and with 0.2 M KNO_3, respectively) were collected separately during the elution steps prior to the I^- collection. Once the DOI and IO_3^- were separately collected, they were externally reduced to I^- by the addition of concentrated hydrochloride acid (HCl, Fisher Scientific) and sodium metabisulfite ($Na_2S_2O_5$, VWR Analytical) (Hardisty et al., 2020; Hou et al., 1999, 2009). The treated eluent was left overnight for reaction and was processed through the same chromatographic procedure to collect the I^- derived from the IO_3^- and DOI fractions. For independent measurement of total dissolved iodine (TI) and quality control, a separate split of seawater samples was pre-treated with HCl/$Na_2S_2O_5$ and subsequently processed through the same chromatographic method.

For quality control, a 200ppb I^- solution, which was gravimetrically diluted from the Inorganic Ventures© 1000±4ug/ml I^- ICP-MS standard solution in 1% tetraethyl ammonium (TEA), was processed through chromatography alongside the seawater samples to estimate the yield of I^-, DOI and TI fractions. Similarly, for estimating the yield of IO_3^- reduction and column separation, a 200ppb KIO_3 solution dissolved from gravimetrically weighed solid KIO_3 powder (Fisher Science Education) was reduced and chromatographically processed. For monitoring

contamination, ultra-pure water was processed through the columns. Among each set of seawater samples (11 samples) which were processed at the same time, one of them was randomly selected as a replicate.

2.4.2.2 ICP-MS

The eluents from the chromatography were collected in Savillex PFA Teflon vials and then diluted 20 times (0.2M HNO_3-0.9% TMAH) before instrumental analysis. The iodine concentrations were measured using a Thermo Scientific iCAP Q triple-quadrupole inductively coupled plasma mass spectrometer (ICP-MS-TQ) using Qtegra software version 2.10.3324.131 in both single-quad (SQ) and triple-quad (TQ) mode with O_2 reaction cell gas. The samples were introduced into the ICP-MS via a Teledyne Cetac ASX-520 autosampler. We used 5ppb internal standard solution diluted from 1001±3ug/ml indium (In) in 2% HNO_3, 999±5ug/ml Rhodium (Rh) in 15% HCl, and 1000±4ug/ml Cesium 0.1% HNO_3 (Cs) elemental standards from Inorganic Ventures© to calibrate the intensity of iodine. The internal standard was either spiked into each sample or was introduced into the ICP-MS after being mixed with sample within an inline mixing chamber.

2.4.2.3 Spectrophotometer

We also conducted shipboard measurements of IO_3^- with a Thermo Scientific GENESYS 180 UV-Vis Spectrophotometer aboard the R/V Elizabeth Mann Borgese using the method established by Jickells et al., (1988). To each sample of 2.5 ml filtered seawater, 62.5 µL of 1.5 M sulfamic acid was added and allowed to react for 2.5 minutes to remove potential nitrite interference. After the reaction, 187.5 µL of 10% (w/v) potassium iodide and 375 µL of DI water were added, allowing the formation of triiodide (I_3^-) during a 2-minute reaction. The IO_3^- was quantified by measuring the absorbance at 350 nm.

2.5 Results

2.5.1 Chromatography method quality control

Our chromatography method separates all iodine speciation—IO_3^-, I^-, DOI—in a sample, and then we measure them separately. To validify the accuracy of this method, a second fraction of each sample was treated to determine the total dissolved iodine (TI). The sum of IO_3^-, I^-, DOI of each sample overall matches with the TI (Figure 2.2), indicating our chromatography-ICPMS method is generally accurate.

We additional note that the select samples measured for IO_3^- via the spectrophotometric approach yielded IO_3^- below detection. This result is generally consistent with the low IO_3^- concentrations measured via IC-ICPMS for most samples, but also likely indicates the presence of potential interferences common from this technique (Jones et al., 2023).

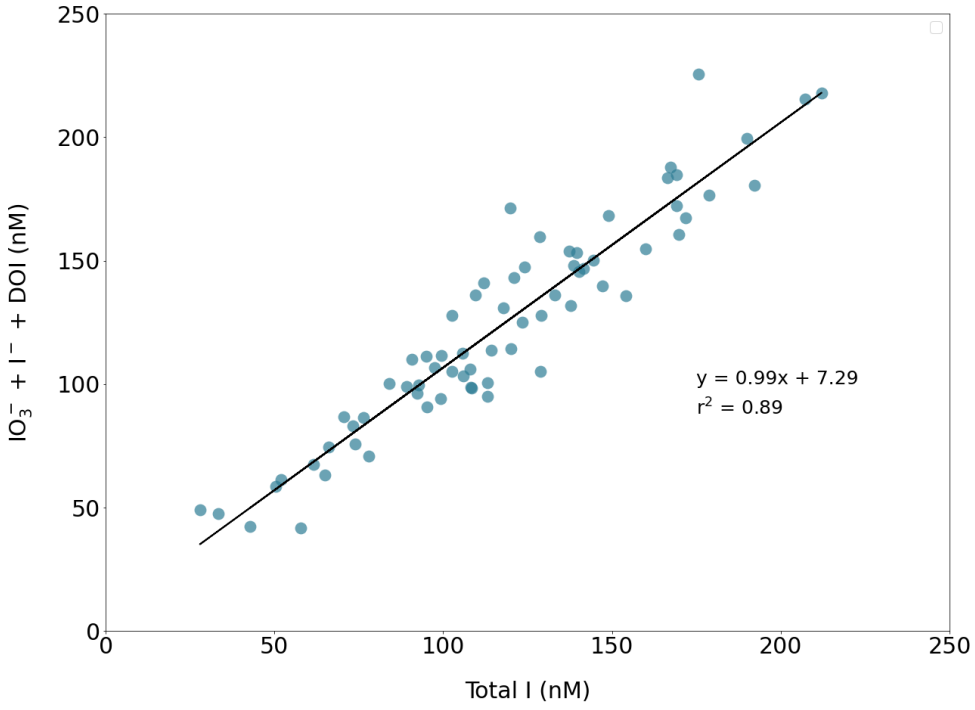

Figure 2.2. Comparison of the sum of IO_3^-, I^- and DOI with independently purified and measured total dissolved I, as a quality control of both chromatographic yield and ICPMS measurement.

2.5.2 The hydrography and iodine distribution in the Baltic Sea

The water column in the Baltic Sea is strongly stratified vertically. Based on the variation of O_2 and H_2S, the basic redox structure in the Baltic Sea can be divided into three layers: oxic zone, chemocline, and the euxinic zone.

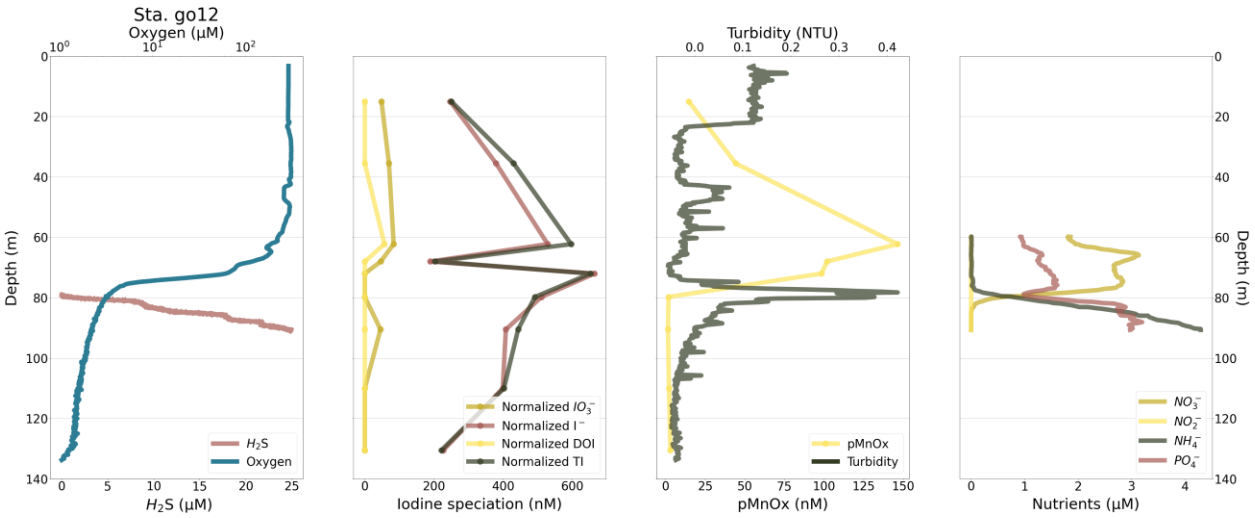

Figure 2.3. Geochemical depth profiles at Fårö Deep. Dissolved O_2, salinity and turbidity are adopted from BCO-DMO data repository (https://www.bco-dmo.org/dataset/935118). The PO_4, NO_3^-, NO_2^-, NH_4^+, and H_2S data are adopted from BCO-DMO data repository (https://www.bco-dmo.org/dataset/934904).

2.5.2.1 The oxic zone

The oxic zone is at the surface of the Baltic Sea, of which the water is well oxygenated, and has low salinity below 8 PSU (Table 2.2). Since the concentration of dissolved iodine in freshwater is usually less than 10% of those in seawater (Moran et al., 2002), we report our iodine measurements after being normalized by salinity to minimize the effect of dilution and allow for comparison between stations and to previous work (Figures 2.3-2.6). The depth of the lower boundary of the oxic zone is generally uniform across all sampling stations in the central Baltic Sea at ~40m, marked by the initial decline of the O_2 concentration (Figures 2.3-2.5). The relative abundance of IO_3^- and I^- in the oxic zone is unique compared to that at other open ocean or anoxic basin sites. The salinity normalized IO_3^- in the surface water column is close to, or lower than

100nM, significantly lower than that observed in the open ocean (~250nM, e.g. Moriyasu et al., 2020). I^- is the dominant species in the oxic zone, of which salinity-normalized concentration is significantly higher than IO_3^-, even when the O_2 is ~300μM. The normalized total I at some depths in some stations in the Fårö Deep (go12, Figure 2.3), Gotland Deep (go27, go32, Figure 2.4), and close to the Latvian coast (go24, Figure 2.5) are significantly lower than the global average value.

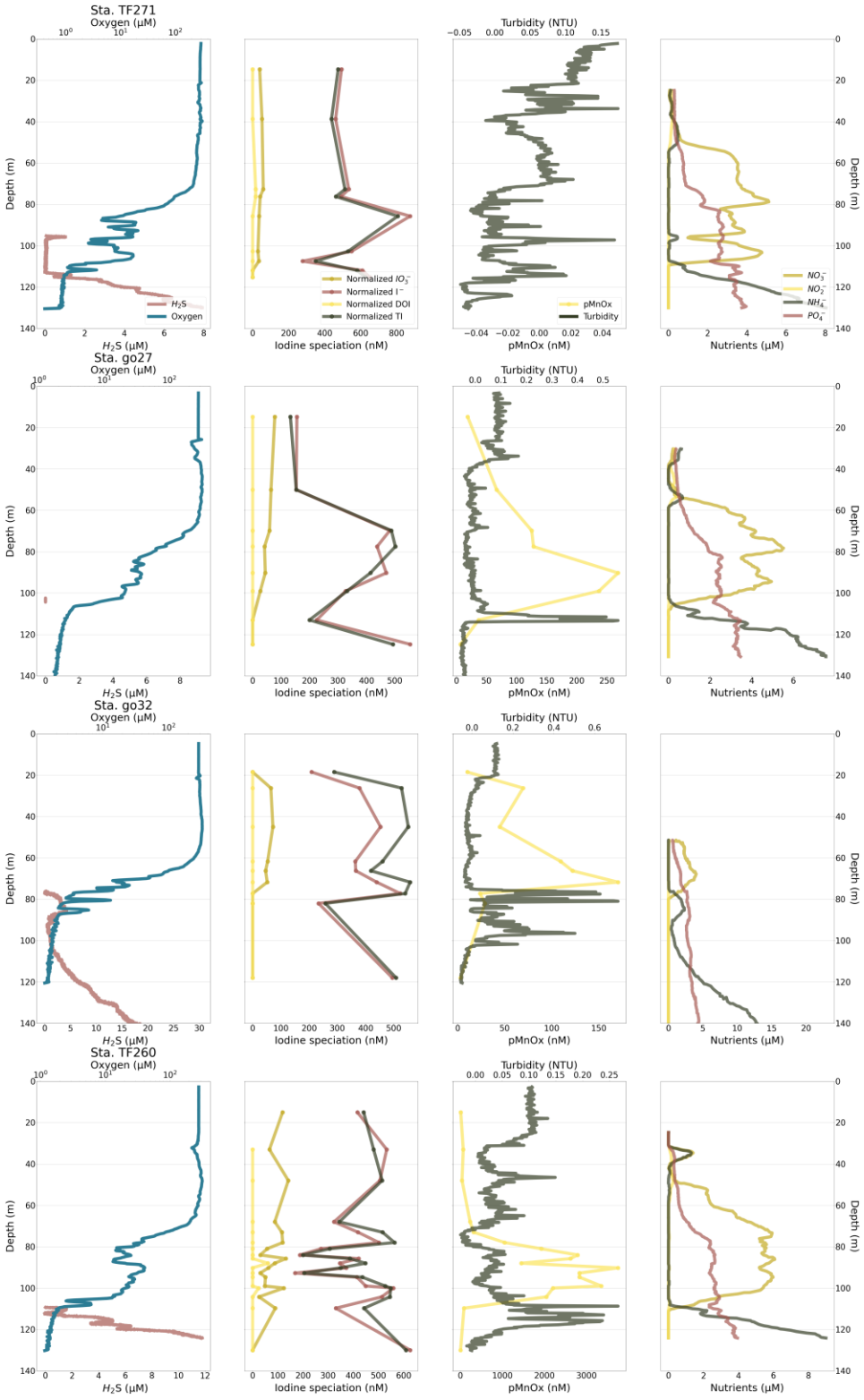

Figure 2.4. Geochemical depth profiles of redox (dissolved O_2, and H_2S), iodine speciation (IO_3^-, I^-, DOI, and TI), particles (Turbidity and Mn-oxides particles (pMnOx)), as well as nutrients (nitrate (NO_3^-), nitrite (NO_2^-), ammonium (NH_4^+), and phosphorate (PO_4)) at the central Gotland

Figure 2.4 (cont'd).
Deep stations. Dissolved O_2, salinity and turbidity are adopted from BCO-DMO data repository (https://www.bco-dmo.org/dataset/935118). The PO_4, NO_3^-, NO_2^-, NH_4^+, and H_2S data are adopted from BCO-DMO data repository (https://www.bco-dmo.org/dataset/934904).

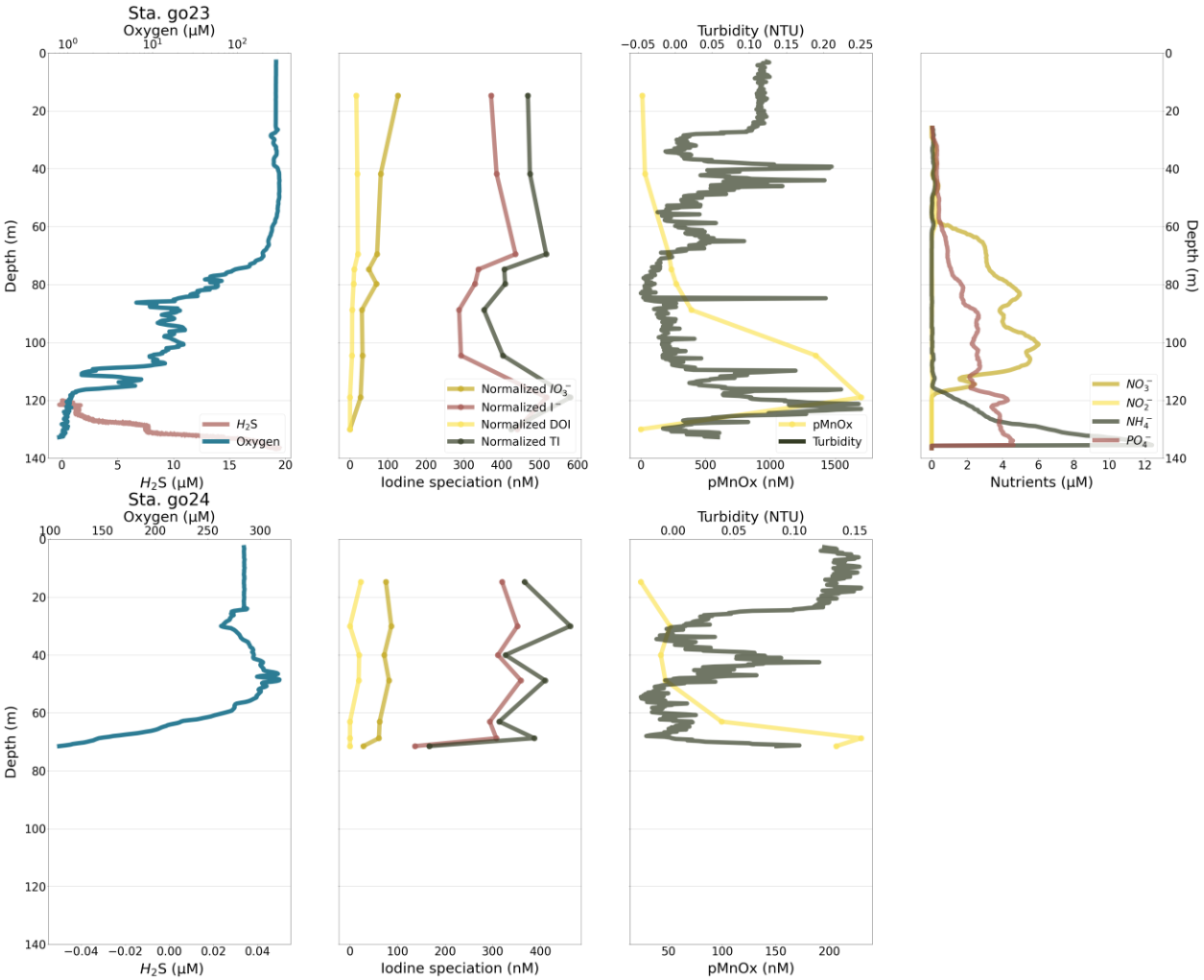

Figure 2.5. Geochemical depth profiles of redox (dissolved O_2, and H_2S), iodine speciation (IO_3^-, I^-, DOI, and TI), particles (Turbidity and Mn-oxides particles (pMnOx)), as well as nutrients (nitrate (NO_3^-), nitrite (NO_2^-), ammonium (NH_4^+), and phosphorate (PO_4)) at the east Gotland Deep, close to the coast. Note that there is no H_2S data measured from go24 station. Dissolved O_2, salinity and turbidity are adopted from BCO-DMO data repository (https://www.bco-dmo.org/dataset/935118). The PO_4, NO_3^-, NO_2^-, NH_4^+, and H_2S data are adopted from BCO-DMO data repository (https://www.bco-dmo.org/dataset/934904).

2.5.2.2 The chemocline

The chemocline in the Baltic Sea is marked by the dissolved O_2 concentration from initial decrease at the bottom of the oxic zone until O_2 reaches the detection limit of the O_2 sensor (1µM).

The lower boundary of the chemocline is between 100-120m in most of the stations (Figures 2.4, 2.5), except the Fårö Deep station go12 which has the narrowest chemocline between 40-75m (Figure 2.3). In the chemocline, the redox state of the seawater varies dramatically, controlling the speciation of O, I, manganese (Mn), nitrogen (N), phosphorus (P), and sulfur (S).

In the chemocline of the central Baltic Sea, the O_2 profiles in the chemocline exhibit two distinct features: 1) sharp decrease at 60-80m, followed by 2) oscillation around several tens of micromolar at the bottom of the chemocline (Figures 2.4, 2.5). While the normalized IO_3^- decreases subtly, the normalized I^- exhibits non-conservative features in the chemocline, with large fluctuations between the average seawater value (~500nM) and significantly depleted values (200-300nM). The only appearance of excess iodine occurs in the lower chemocline of the TF271 station, showing I^- close to 800nM. Interestingly, some iodine depletion corresponds to the variation in particle abundance, represented by Mn-oxides (pMnOx) or turbidity (stations go27, go32, TF260, go24). In particular, the detailed high resolution depth profile in the chemocline in TF260 shows a clear inversion relationship between I^- and MnOx (Figure 2.4). In addition, among all the chemocline samples we analyzed, none of them has higher IO_3^- than I^-. The NO_3^- shows a maximum in the chemocline.

2.5.2.3 The euxinic zone

The euxinic zone is characterized by the appearance of H_2S and NH_4 in the water column, where dissolved O_2 is below the detection limit. We only sampled the upper portion of the euxinic zone and did not sample the full depth profile to the bottom. At the boundary between the chemocline and the euxinic zone, some samples from stations go12, TF260, and go32 show low but detectable IO_3^-, but decrease to zero at deeper depths where higher H_2S concentrations occur (Figures 2.3-2.5). The highest turbidity across the sampling depths can also be observed in the

upper euxinic zone. The NO_3^- is reduced to NH_4^- in the euxinic zone. Also, PO_4^- starts to accumulate in the anoxic water.

2.5.3 The hydrography and iodine distribution in Siders Pond

The water column in Siders Pond is also redox stratified according to the variation of O_2 and H_2S in depth profiles (Figure 2.6). Although the bottom depth is much shallower than the Baltic Sea, similar stratification of the oxic zone, chemocline, and euxinic zone exist in Siders Pond. Note that for Siders Pond, the full suite of DOI, IO_3^-, I^- and TI were not measured.

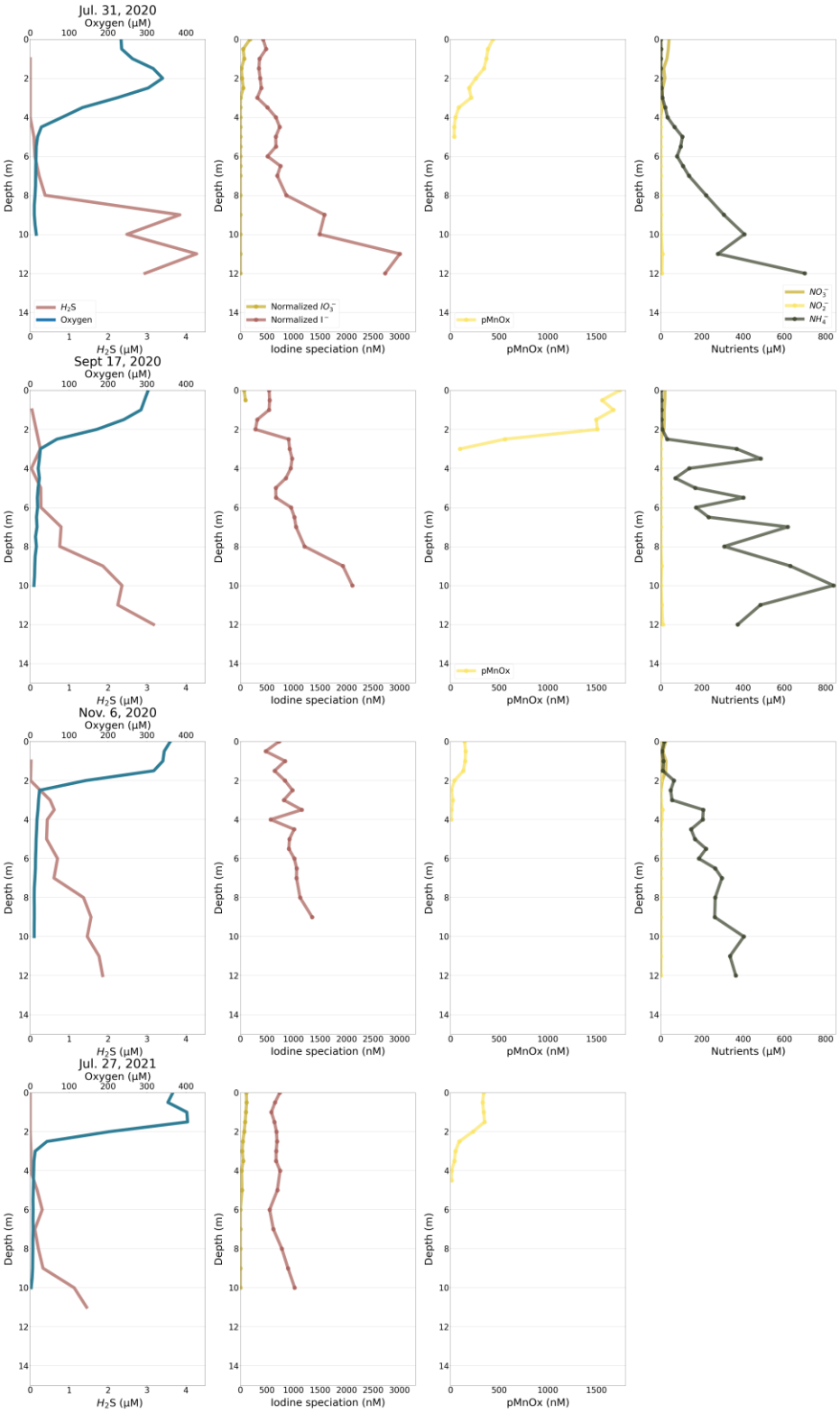

Figure 2.6. Geochemical depth profiles from Siders Pond. Note that IO_3^- is depleted in the surface oxygenated layer (0-3m) and I^- increases with depth.

2.5.3.1 The oxic zone

The oxic zone in the Siders Pond is in the upper 2 meters, marked by high dissolved O_2 above 200 μM and low sulfide. Like the Baltic Sea, the salinity normalized IO_3^- in the surface of Siders Pond among all the sampling dates are depleted relative to the open ocean surface measurements, close to 100nM. Nevertheless, the normalized I^- in the Siders Pond surface water is close to, or even higher than the average seawater value. Another different feature from the Baltic Sea is that the MnOx particles are enriched in the surface of the Siders Pond (Figure 2.6).

2.5.3.2 The chemocline

The chemocline in the Siders Pond is between 2-3 meters and characterized by a sharp decrease in dissolved O_2 in the water column. Some temporal variations can be observed among the four sampling dates. In two of the summer sampling dates in July 2020 and 2021, the O_2 reaches maximum at the top chemocline (Figure 2.6). A thicker chemocline can be observed on July 31st, 2020, during which it spans across 2-5 meters. The thicker chemocline does not reflect a systematic seasonality because such feature is not observed the following summer.

The IO_3^- in the chemocline of the Siders Pond decreases gradually with O_2, usually lower than 100nM. The I^- shows an overall increase, despite some oscillations. It is notable that I^- is significantly higher than the average seawater value, reaching over 600nM. In addition, the IO_3^- decrease (<100nM) does not count for the I^- increase in the chemocline (>200nM), indicating an additional source of I^- apart from the net transformation from IO_3^- to I^- (Figure 2.6). Unlike the Baltic Sea, the MnOx maximum does not exist in the chemocline of the Siders Pond. Instead, MnOx decreases with O_2, accompanied by the gradual increase of NH_4^+.

2.5.3.3 The euxinic zone

While the chemocline was sampled in detail for the Baltic Sea, and only the onset of euxinic zone only partially sampled, we sampled the euxinic zone of Siders Pond in detail all the way to the bottom. The euxinic zone in Siders Pond is below 4 meters, characterized by the appearance of H_2S and low O_2 (Figure 2.6). The O_2 below 4 meters maintains 10-20μM, which represent the detection limit of the PAR sensor. There is detectable IO_3^- in the upper euxinic zone until it is fully reduced at ~6m as H_2S increases. In the euxinic zone, I^- keeps increasing above 1000nM at depth despite minor oscillations (Figure 2.6). The particulate MnOx is not measurable in the euxinic zone. We note that the I^- depth profile shows a similar increasing trend with depth between sampling events, but that the maximum I^- differs widely between the events, indicating a strong temporal cycle.

2.6 Discussion

Our iodine speciation profiles from the Baltic Sea and Siders Pond exhibit two distinct shared features: 1). Depleted IO_3^- in oxygenated surface layer; 2). Non-conservative (net addition or removal) of total iodine, particularly within or below the oxycline. We interpret these phenomena as the result of the pathway(s) of seawater renewal and dynamics of vertical mixing through the water column. Below, we discuss these regional drivers in detail, as well as their broader implications for iodine cycling in marine low oxygen environments in both modern and ancient anoxic settings.

2.6.1 Depleted surface IO_3^- in a stratified basin

The redox potential of IO_3^-/I^- transformation lies proximal to the "upper side" of the redox ladder, largely overlapping with redox potential (pε) ranges of O_2/H_2O and Mn(IV)/Mn(III) couples (Rue et al., 1997; Cutter et al., 2018). Therefore, significant IO_3^- accumulation is common

in highly oxygenated water across global marine environments (Figure 2.7). In contrast, the samples from the oxygenated surface layers in the Baltic Sea and Siders Pond exhibits depleted IO_3^-, which has been rarely observed previously (e.g., Rue et al., 1997; Farrenkopf et al., 2002, Cutter et al., 2018; Moriyasu et al., 2020, 2023). Such a decoupling between IO_3^- and O_2 hints that there may be factors beyond in situ redox conditions that impact IO_3^- accumulation in the water column. Here we discuss these factors through investigating the sources and sinks of the IO_3^- reservoirs in the Baltic Sea and Siders Pond.

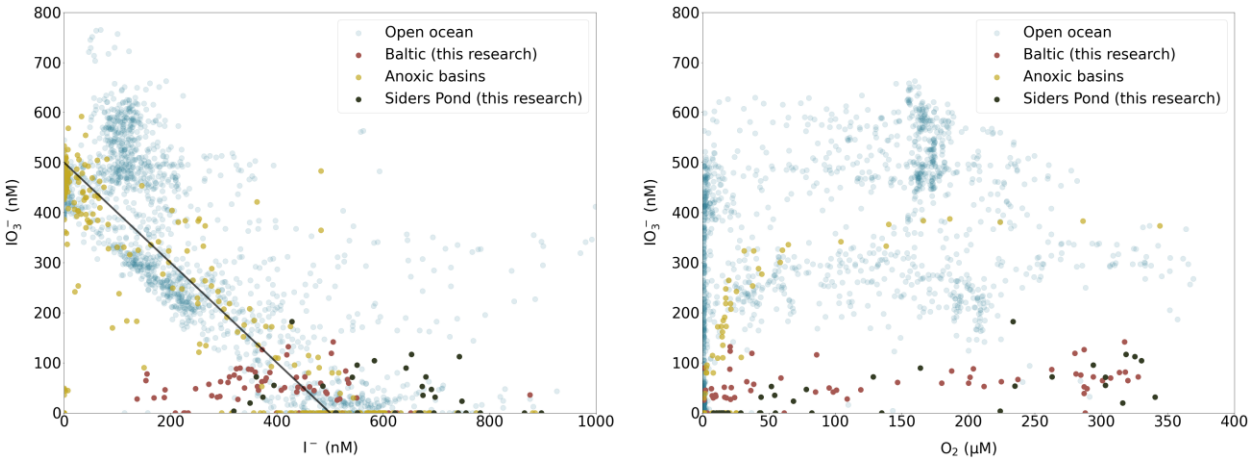

Figure 2.7. The relationship of IO_3^- with I^- and O_2 in the Baltic Sea, Siders Pond, open ocean ODZs (Rue et al., 1997; Farrenkopf and Luther, 2002; Cutter et al., 2018; Moriyasu et al., 2020; Chapman, 1983; Rapp et al., 2019, 2020), and in other marine anoxic basins (Emerson et al., 1979; Luther and Campbell, 1991; Luther and Cole, 1988; Ullman et al., 1990; Wong and Brewer, 1977). Note that IO_3^- in the Baltic Sea and the Siders Pond are significantly lower than other locations. The iodine measurements in anoxic basins are salinity-normalized.

2.6.1.1 Methodological considerations

We first consider sources of analytical uncertainty that may contribute to our observations. In particular, we highlight that for the chromatographic column separation, it is inevitable that some of the iodine speciation (especially IO_3^-) is lost during the AG1-X8 chromatography process, resulting in recovery rates less than 100% (Hou et al., 2001; Hardisty et al., 2020; Hou et al., 2007). To verify our observations of low IO_3^-, we performed 4 independent checks on IO_3^- concentrations:

(1) potassium iodate standards of known concentration were put through the column procedure alongside our samples; (2) total iodine was determined independently and compared to the sum of the IO_3^-, DOI, and I^-; (3) total iodine from our Baltic study is compared to a previous Baltic study; (4) we analyzed IO_3^- with an independent spectrophotometric procedure.

First, in order to assess the potential for low IO_3^- recovery during column separation, we calculated column recovery yields via adding 200 ppb IO_3^- solutions through the chromatography process, followed by mass balance calculation comparing the mass of IO_3^- recovered in eluent against the initial mass before the process. The IO_3^- recoveries for our samples are 82% - 109%, with most >90% (Tables 2.1, 2.3). This is a slightly wider range but comparable with previous reported values of 90% - 100% (Hou et al., 2001, 2007). These recovery standards were processed alongside each column set and the results were used to correct unknowns. Thus, while we recognize potential uncertainty, our methodological approach is unlikely to explain low IO_3^- yields.

Second, we compared independent measures of total iodine to the sum of iodate, iodide, and DOI (Figure 2.2). The results demonstrate overall general agreement and confirm that iodide is the dominant iodine species controlling total iodine variations in profiles. Third, we compared our total iodine measurements from the Baltic to that of previous Baltic depth profiles also from the same location (Gotland Deep) measured with a voltametric method (Figure 2.8)(Truesdale et al., 2013). While our iodine speciation results differ and observations of non-conservative processes below the chemocline do not overlap (discussed in detail in later sections), our baseline measurements of total dissolved iodine in the Baltic above the chemocline have general agreement with that from Truesdale et al., (2013). Given method differences and spatiotemporal differences between the 2 studies, the total iodine comparison provides further support that IO_3^- is not significantly underestimated.

Lastly, another line of evidence supporting *in situ* IO_3^- depletion in the Baltic Sea comes from ship-board measurements of IO_3^- spectrophotometrically. For this method, standard additions of potassium IO_3^- to samples were used for standard calibrations. This included the addition of IO_3^- concentrations up to ~1000nM to the samples that are collected above the chemocline. However, most of the samples with standard addition from stations TF260, TF271, go12 and go23 show significantly lower IO_3^- concentrations relative to the expected added value. The removal of added IO_3^- during standard additions inhibited use of the spectrophotometric method for IO_3^- quantification but also suggests that there might be trace amounts of reductants inhibiting *in situ* IO_3^- accumulation in the surface Baltic waters, which will be addressed later in 5.1.3. We note that this phenomenon has been observed during standard additions to samples from the oxygen minimum zones of the Arabian Sea and Eastern Tropical North Pacific (Moriyasu et al., 2020; Farrenkopf and Luther, 2002).

While we provide several independent checks on IO_3^-, we highlight that there is uncertainty in quantifying DOI. Notably, in an estuarine system, DOI could represent a significant proportion of total dissolved iodine (Wong and Cheng, 1998). However, one reason for uncertainty in its distribution and abundance is because of a lack of DOI standards for method assessment and limited direct measurement techniques. Current analysis methods of DOI require either quantitatively oxidizing it to IO_3^- by UV radiation (Jones et al., 2023; Wong and Cheng, 1998; Jones et al., 2024) or reduction to I^- with strong reductants (sodium bisulfite) (Hardisty et al., 2020). For the method used in this study, there is uncertainty regarding yields during column chromatographic separation of DOI. Some approaches assume a DOI fraction similar to that here (Schnur et al., 2024; Hou et al., 1999), while other studies using our same chromatographic approach combined the DOI and IO_3^- pools into a pool assumed to a single pool representing IO_3^-

(Ştreangă et al., 2023). For this reason, it is possible that there are significant organic iodine size fractions or recalcitrant phases which are not accounted for in our or other studies. Therefore, it is possible that DOI is an important overlooked iodine fraction in our study. Future studies are expected to resolve the quality of DOI recovery for the chromatography method in order to provide a more complete measure of DOI and hence total iodine measurements in estuarine systems.

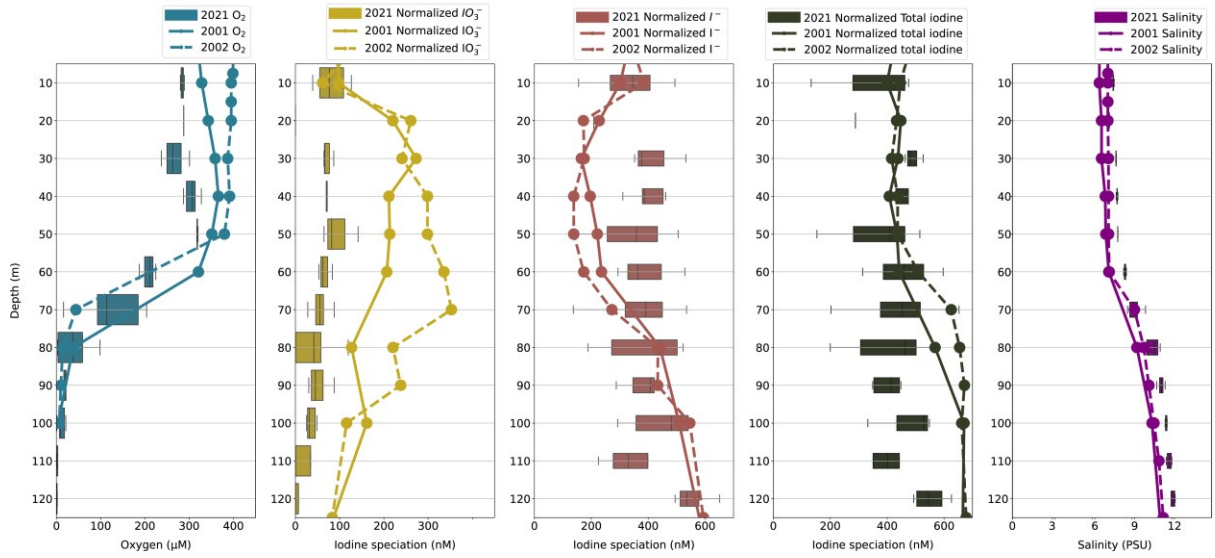

Figure 2.8. The comparison of O_2 iodine speciation, and salinity in the Baltic Sea between this study (2021) and previous depth profiles sampled in 2001 and 2002 (Truesdale et al., 2013). Note that for our study, the 9 depth profiles are binned to the depths matching that of Truesdale et al., (2013) and the concentrations represented here through box and whisker plots showing overall range, median, and quartiles.

2.6.1.2 Iodate sources: Salinity and hydrographic impacts on iodine

Compared to other stratified anoxic marine basins, such as Saanich Inlet (Emerson et al., 1979) and Cariaco Basin (Wong and Brewer, 1977), IO_3^- concentrations above the anoxic water column in the Baltic Sea and Siders Pond are significantly lower (Figure 2.9). In each of these stratified basins, iodine speciation and abundance are controlled by redox conditions, but variations in salinity are also an important factor. The Baltic Sea, to a large extent, is an estuarine system since it accepts ~400 km^3/yr freshwater from the North European catchments (Voipio,

1981). Among all the sources of water, fully oxygenated seawater from the North Sea and the Atlantic carries the majority of IO_3^- that is introduced into the Baltic Sea (Truesdale et al., 2013) and the Siders Pond. These sources can have up to 500 nM IO_3^- (Chance et al., 2014; Hou et al., 2007). Other freshwater sources like river water and rain water are dominated by I^-, but their total iodine concentrations are relatively negligible, typically below 50 nM (Moran et al., 2002). For these reasons, iodine measurements are commonly normalized by salinity in order to allow for comparison across salinity gradients locally and between global localities. For example, the surface salinity of other anoxic estuaries like the Saanich Inlet, Cariaco Basin, and the Black Sea are ~29.5 PSU (Emerson et al., 1979), ~36.8 PSU (Wong and Brewer, 1977), and ~18.3 PSU (Wong and Brewer, 1977, Luther and Campbell, 1991), respectively, while that of Siders Pond and the Baltic Sea are 6-10 PSU and ~7.5 PSU, respectively. We also notice that, however, IO_3^- does not always follow conservative mixing in low salinity (< 18 PSU) waters, as reported by Luther et al., (1991) and confirmed in this study (Figure 2.13). We propose that this deviation of IO_3^- from linearity with salinity resulted from *in situ* reduction in freshwater environments, as discussed in later sections.

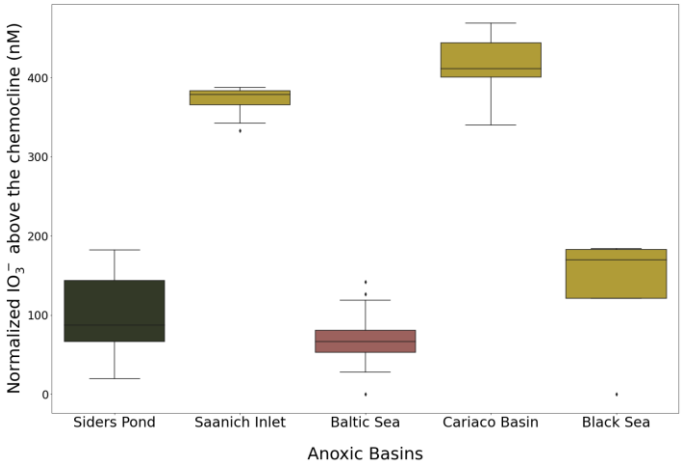

Figure 2.9. Salinity-normalized IO_3^- above the chemocline in Siders Pond (This study), Saanich Inlet (Emerson et al., 1979), the Baltic Sea (This study), Cariaco Basin (Wong and Brewer, 1977), and the Black Sea (Luther and Campbell, 1991; Wong and Brewer, 1977).

In addition to salinity, the hydrography of estuary systems—like the Baltic Sea and Siders Pond—also influences circulation patters that impact the distribution of IO_3^- and iodide. For the Baltic, the seawater from the North Sea renews the Baltic water through two pathways: relatively less intense but continuous baroclinic inflow and stronger barotropic inflow during special large scale air circulation pattern over the North Atlantic Ocean and Europe (MBIs)(Voipio, 1981; Reissmann et al., 2009; Elken and Matthäus, 2008) (Figure 2.10). The former interleaves in the halocline/chemocline (Truesdale et al., 2013), while the latter is strong enough to penetrate below the chemocline and briefly oxygenate the formally sulfidic water (Mohrholz et al., 2015; Schmale et al., 2016). Through both types of inflows, oxygenated seawater containing IO_3^- is introduced into or below the chemocline, before being advected or diffused upwards into the surface layer. Such bottom-bearing IO_3^- renewal in the Baltic Sea is similar to that in the Black Sea, in which all the Mediterranean seawater through the Bosphorus is renewed into the anoxic intermediate water before entering the surface layers through upward advection (Truesdale et al., 2001). Siders Pond operates on a much smaller scale but is similar. Like the silled passages separating the North Sea and the Baltic Sea, the local Fresh River serves as the pathway through which seawater from Vineyard Sound enters Siders Pond (Caraco, 1986; Ostrander et al., 2023) (Figure 2.10).

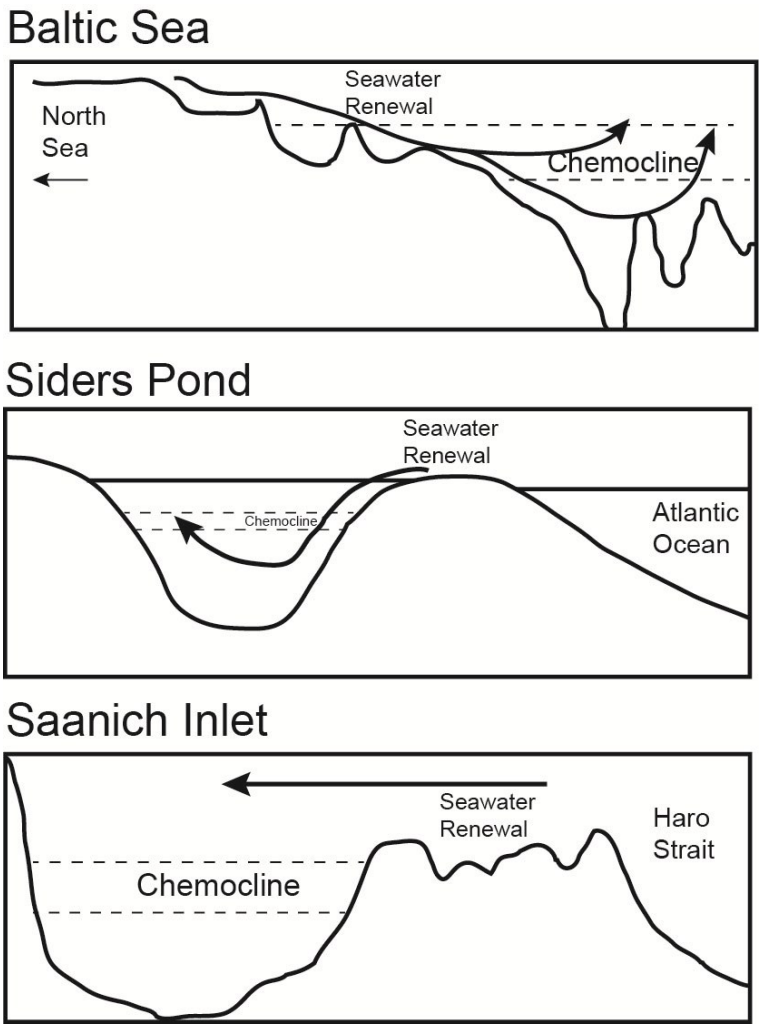

Figure 2.10. Unscaled schematic diagrams of IO_3^- renewal pathways into the surface layer of the Baltic Sea (Truesdale et al., 2013), Siders Pond, and Saanich Inlet (Gargett et al., 2003; Soetaert et al., 2022). The pathways of seawater-derived IO_3^- renewal and subsequent upward diffusion and oxidation within the surface layer are represented by the arrows.

Under suboxic/anoxic conditions, the introduced IO_3^- is reduced to I^-, which takes place perhaps even rapidly within between several hours by microbial-induced reduction (Farrenkopf et al., 1997; Jiang et al., 2023; Councell et al., 1997) or interaction with sulfide (Councell et al., 1997; Zhang and Whitfield, 1986). Consequently, IO_3^- sources into these anoxic basins are reduced rapidly to I^- under the chemocline before being transported to the surface water column. Accumulation of IO_3^- in the surface water of anoxic basins therefore depends on the *in situ* oxidation rate of I^- as well as the residence time of the surface layer—i.e., the residence time of

the water body must be long enough to allow I^- oxidation to occur. Contrary to rapid reduction, the oxidation from I^- to IO_3^- has much slower kinetics (Tsunogai, 1971; Hardisty et al., 2020; Truesdale et al., 2001; He et al., 2013; Schnur et al., 2024; Moriyasu et al., 2023), which hinders IO_3^- accumulation in the surface layer. The residence time of water above the chemocline in the Black Sea and the Baltic Sea is ~18.5 years and ~30 years (Truesdale et al., 2001; Reissmann et al., 2009). Comparatively, the open ocean residence time of I^- is ~40 years, which has been observed as well as validated through Earth System Model (Tsunogai, 1971; Lu et al., 2018, Cheng et al., 2024). Even in the open ocean, surface IO_3^- accumulation may be closely tied to rates of mixing between IO_3^- rich deep waters and surface waters hosting IO_3^- reduction during primary productivity (Chance et al., 2014). The short residence time of surface waters relative to the oxidation rate of I^- may also explain the low IO_3^- in surface Black Sea. Similarly, the overall lower IO_3^- in the surface of Siders Pond could also be the result from short waterbody lifetime of 2 years (Caraco, 1986; Ostrander et al., 2023), which is also far shorter than I^- oxidation rates in the open ocean.

Notably, while the surface IO_3^- accumulation is impacted by the slow oxidation kinetics of I^-—which are primarily sourced from freshwater and underlying anoxic deep water—compared to the residence time of surface water—other factors likely plays a role too in surface IO_3^- depletion. Specifically, while the concentration of some other redox-sensitive elements scale to the basin's residence time (e.g., molybdenum; Algeo and Lyons, 2006), IO_3^- does not show a straightforward relationship when comparing a range of stratified anoxic basins (Figure 2.9). For example, Saanich Inlet has relatively high IO_3^- within surface waters thus that the basin is relatively less restricted and therefore receives more frequent IO_3^- inputs from normal marine waters relative to other sources, which outpaces IO_3^- reduction. In the Black Sea, the residence time is longer, yet IO_3^-

concentrations are still low. We therefore suggest that *in situ* processes may also play an important role in IO_3^- availability in surface waters of stratified basins.

2.6.1.3 Potential sinks of IO_3^- in the surface layer of a stratified basin

In-situ reduction within the surface layer could resolve the observation of extra depleted IO_3^- in the Baltic Sea. Reduction can be driven by phytoplankton as well as bacteria and inorganic reactions. The latter two are expected in anoxic deep waters of stratified basins but have been uncommonly documented before in oxic surface waters.

Primary producers in the euphotic zone (e.g. phytoplankton) reduce IO_3^- to I^- through photosynthetic assimilation (Elderfield and Truesdale, 1980) or dissimilatory reduction during cell senescence (Hepach et al., 2020). The photosynthetic assimilation incorporates IO_3^- into organic matter following a "Redfield-ratio" stoichiometry with I:C ratios close to the order of 10^{-4} mol/mol (Elderfield and Truesdale, 1980; Chance et al., 2010). Such a process is followed by I^- releasement back to ambient water during cell senescence and organic matter remineralization (Wong et al., 1985, 2002; Bluhm et al., 2010; Carpenter et al., 2021; Hepach et al., 2020). Observations of iodine speciation from oxic ocean waters also display IO_3^- depletion in the euphotic zone (Tsunogai, 1971; Elderfield and Truesdale, 1980; Wong et al., 1985; Rue et al., 1997; Moriyasu et al., 2023; Chance et al., 2010). The seasonality covariation between chlorophyll-a maxima and IO_3^- minima during the summertime algal bloom revealed by Chance et al., (2010) provide a more explicit connection between primary production and surface IO_3^- reduction. Additionally, vertical correlation between fluorescence (a measure of chlorophyll) and I^- below the fluorescence maximum (but not above) also points out the role of primary productivity in reducing IO_3^- (Moriyasu et al., 2023). In the Baltic Sea, annual-averaged chlorophyll-a is overall higher than that in the Black Sea (Sea-viewing Wide Field-of-view Sensor (SeaWiFS) Level-2 Ocean Color Data, version R2018.8) (Figure 2.12),

indicating high primary productivity of an already low IO_3^- pool probably also explains the lower IO_3^- in the surface Baltic Sea.

Multiple factors could impact I^- accumulation via surface IO_3^- reduction, including phytoplankton composition, mixed layer depth, and temperature (Chance et al., 2014). For example, vertical mixing is important. Within open ocean meridional transects there is lower accumulation of I^- at high latitudinal stations with higher primary productivity yet less stratification. Low latitude surface waters accumulate higher I^- given stronger temperatural controlled stratification, and hence less frequent IO_3^- sourced from underlying IO_3^-rich waters (Moriyasu et al., 2023). In addition, variations in the ability of organisms to reduce IO_3^- have been reported previously, with the dinoflagellate *Amphidinium carterae* showing the highest capacity for this process (Wong et al., 2002). The ability of IO_3^- assimilation/reduction also varies in dependence of phytoplankton growth phase. Phytoplankton cells deplete IO_3^- faster during the log stage than the stationary and the senescent stages (Wong et al., 2002). Future studies should include detailed time series sampling of iodine speciation, alongside with recordings of phytoplankton composition and physiology, to quantitatively assess the phytoplankton-mediated IO_3^- removal from the Baltic and other water columns.

As mentioned before, low salinity (<10 PSU, Table 2.2) indicates freshwater significantly contributes to water masses in the surface of the Baltic Sea, while its dilution effect does not readily explain the salinity-normalized IO_3^- depletion either in the surface Baltic Sea or Siders Pond (Figure 2.13). Such non-conservative surface IO_3^- depletion is not unique, as it is also observed in the Chesapeake Bay and Yangtze River estuaries (Lin, 2023; Luther et al., 1991; Wong and Cheng, 2008). For example, in the Chesapeake Bay, IO_3^- was not detectable at salinities <21 PSU and dissolved organic iodine makes up significant iodine fraction (Luther et al., 1991). A decrease in

dissolved IO_3^-/I^- ratio is also reported in near-shore stations in the Arctic Ocean (Zhang et al., 2023), suggesting dissolved organic matter (DOM) sourced from the river water enhanced IO_3^- reduction. Indeed, humic substance near or within the sediments have been proposed to reduce IO_3^- in oxygenated Pacific bottom water followed by incorporation into organic molecules (Francois, 1987). This same mechanism seems plausible for IO_3^- in the surface Baltic water since the sea receives 0.33 Tmol/yr riverine DOM load plus 4.2 Tmol/yr marine DOM from primary producer (Hoikkala et al., 2015). However, near undetectable levels of DOI from the Gotland Deep (Figure 2.4) do not support the existence of a significant organic-bond iodine reservoir; however, as we noted before, the DOI approach used here has not been properly calibrated against standards with known DOI.

In addition to phytoplankton and riverine DOM, here we propose inorganic reductants are a possible factor contributing to in situ IO_3^- reduction in the surface Baltic Sea. As previously mentioned in 5.1.1, the addition of 1000 nM IO_3^- into the surface samples was immediately reduced in shipboard experiment (Table 2.5). Such experiment implies the existence of reductants in the surface water reducing IO_3^- through rapid inorganic reactions (Councell et al., 1997; Ullman et al., 1990; Zhang and Whitfield, 1986). Sulfide in the surface seawater originates from hydrolysis of carbonyl sulfide from phytoplankton, usually in the concentration of pico-molar (Cutter et al., 1999; Walsh et al., 1994). Although previous studies have pointed out that sulfides have short residence time in oxygenated seawater, around 20 minutes (Qstlund and Alexander, 1963), I^- as the residual product of the reaction, persists due to its long residence time. Another source of surface sulfides might be from the euxinic layer. The dynamic vertical physical mixing across the chemocline in the Baltic Sea has the potential to ephemerally upwell higher concentrations of sulfides into the surface layer (Schmale et al., 2016). We hypothesize that the occasional upwelling of small-scale

water mass containing nano-molar or even micro-molar level sulfides might penetrate in the surface layer and result in significant IO_3^- depletion. In the light of observation of IO_3^- reduction, a detailed study of sulfide cycling, especially in the surface layer, is needed in the future.

2.6.1.4 Dynamic water column caused by Major Baltic Inflows

Our iodine measurement across the Baltic chemocline are not the first. Truesdale et al., (2013) published iodine redox profiles in the Gotland Deep collected in summer 2001 and spring 2002, spanning an MBI event that took place in winter 2001 (Figure 2.11). Notably, Truesdale found that IO_3^- increased following the MBI. Compared to our profiles, the depth profiles two decades ago have higher IO_3^- accumulation above the chemocline regardless of whether it is before or after the 2001 MBI event (Figure 2.8). We hypothesize that weak water column mixing and length of time since a major MBI resulted in inhibited IO_3^- input and generation in the Baltic Sea during our sampling (Figure 2.11). Thus, the relative differences in IO_3^- concentrations from the 3 sampling time periods may be best explained by the differences in water column stratification, hence reflecting ventilation with the ocean water from the North Atlantic.

In addition to acting as a direct source of IO_3^-, the overall dynamic water column after an MBI, characterized by uplift of the chemocline (Truesdale et al., 2013) and enhanced vertical mixing (Reissmann et al., 2009; Schmale et al., 2016), which introduce reactive metal (Manganese) and nitrogen species in the upper water column, might assist *in situ* IO_3^- formation. This explanation appears plausible in the light that the peak of IO_3^- accumulation occurred in the oxycline in Truesdale's 2002 profile (Figure 2.8), where the reactive metal species, such as Mn(III)-L and MnOx, is likely present (Dellwig et al., 2010, 2012). Under regular seawater pH values (>7.0), I^- oxidation through direct reaction with Mn-oxides seems unlikely, as both thermodynamics calculation and experiment argue that this reaction requires acidic conditions

(Luther, 2023; Fox et al., 2009). Nevertheless, it is possible that the upwelling of reduced Mn and N species offers a habitat for microorganisms which can oxidize these compounds. Recent microbial cultures have shown that Mn-oxidizing bacteria *Roseobacter sp.* AzwK-3b as well as ammonia-oxidizing bacteria *Nitrosomonas sp.* Nm51 and *Nitrosoccocus oceani* Nc10 are capable of oxidizing I^-, probably through producing strong oxidants such as reactive oxygen species (ROS) (Hughes et al., 2021; Li et al., 2014b). However, *Roseobacter sp.* does not activate I^- oxidation until Mn oxidation is completed, and superoxide produced by these organism might produce iodine intermediates instead of full oxidation to IO_3^- (Luther et al., 1995; Li et al., 2014b). We note that current knowledge is limited in understanding the mechanisms of IO_3^- formation in the modern ocean, and thus untangling the factors that promote or inhibit IO_3^- accumulation in the Baltic Sea during these two periods that are characterized by different hydrographic features requires detailed investigation into not only iodine cycling itself, but also other elemental geochemical cycles and microbial communities.

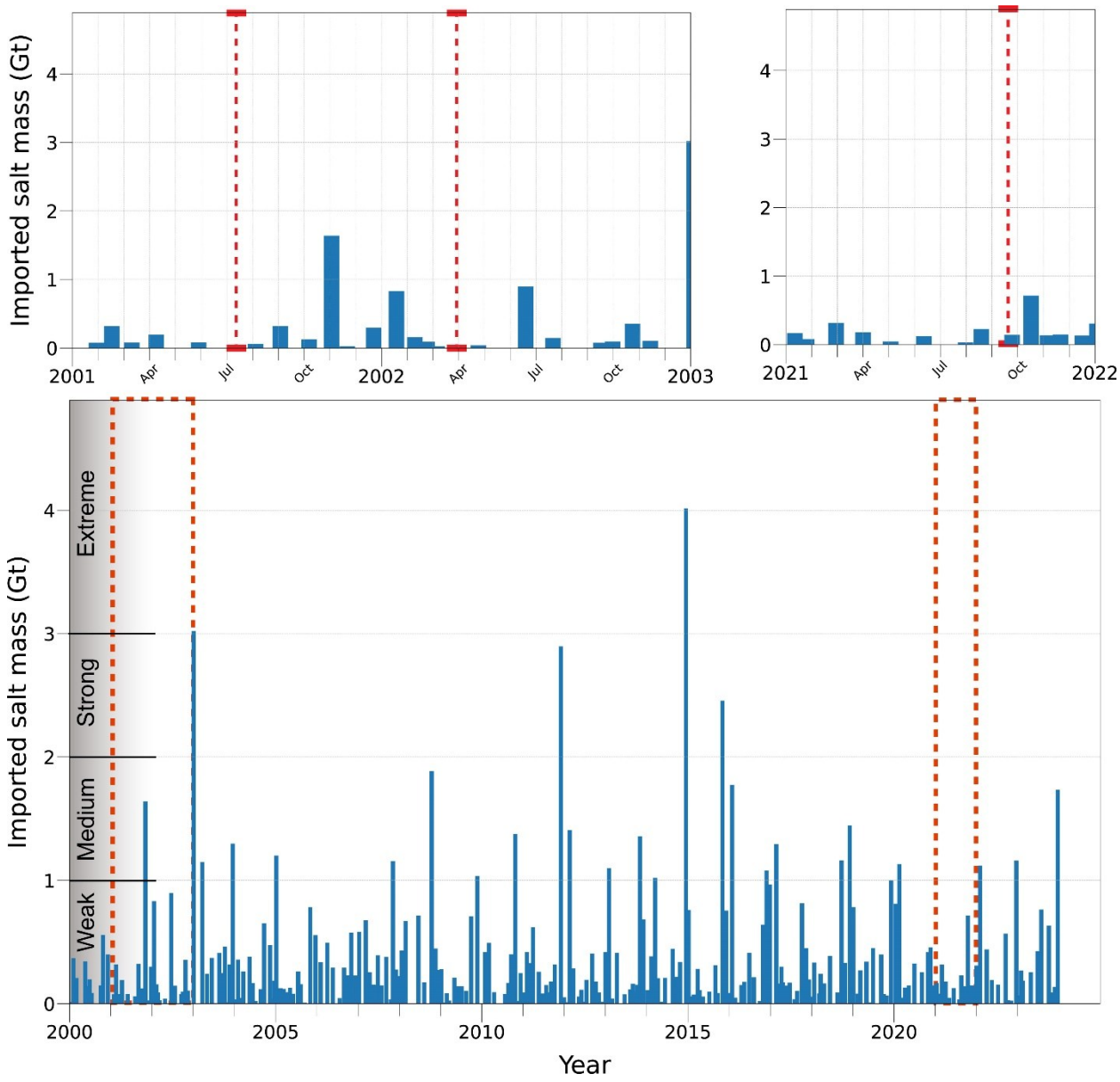

Figure 2.11. The time series of intensity (Gt of salt intrusion) of Major Baltic Inflow events through 2000-2023. Two sampling intervals of 2001-2002 and 2021 are highlighted by the dashed red box. Each sampling cruise is marked by the red dashed line. Data from E.U. Copernicus Marine Service Information (CMEMS).

2.6.2 Non-conservative iodine speciation within the chemocline

The ocean's long residence time results in relatively constant total dissolved iodine at around 450-500nM (Broecker and Peng, 1983; Elderfield and Truesdale, 1980; Truesdale et al., 2000; Chance et al., 2014), in which net transformation between IO_3^- and I^- is dominant. In contrast

to open ocean water reported previously (e.g. Rue et al., 1997), iodine depth profiles in Siders Pond and the Baltic Sea exhibit non-conservative behaviour, showing excess and depletion, respectively (Figures 2.3-2.6).

Salinity normalized total iodine in Siders Pond progressively increases from slightly above ocean average values to over 1000nM towards the bottom (Figure 2.6), indicating the excessive iodine likely originated from benthic flux and affects the entire water column. Iodine is assimilated by primary producers and incorporated into particulate organic matter (POM) followed by sinking towards the sediments (Elderfield and Truesdale, 1980). Beneath anoxic bottom water, POM accumulates and degrades during early diagenesis at the surface sediments and releases I^- (Scholz et al., 2024; Price and Calvert, 1973; Cutter et al., 2018; Francois, 1987). As such, a benthic flux accounting for excessive I^- is commonly observed across the marine ODZs and anoxic basins (Chapman, 1983; Moriyasu et al., 2020; Farrenkopf and Luther, 2002; Ullman et al., 1990; Wong and Brewer, 1977; Luther and Campbell, 1991; Wong et al., 1985). This same explanation likely also explains excess I^- in Siders Pond. We further note that there is a strong temporal component, as the degree of excess I^- accumulation varied widely between sampling events. Further evidence for an organic source for excess I^- comes from comparison of I^- to ammonia and H_2S, which show a positive correlation in depth profiles (Figure 2.6). Ammonia is also sourced from organic remineralization (Anschutz et al., 2000; Scholz et al., 2024) and H_2S may play a role in the release of iodide from organics (Francois, 1987).

It is surprising that excess I^- is not a more widely observed feature in the Baltic. One explanation may be that our study focused on the oxic and suboxic regions and does not include high-resolution sampling within the euxinic zone. Similar to our explanation for excess I^- in Siders Pond, benthic fluxes carrying iodine accumulated at sediment-water interface into the water

column by upward transportation might be expected in euxinic waters (Wong and Brewer, 1977; Luther and Campbell, 1991). While such features are uncommonly observed during our sampling period, there are occasional occurrences of excessive iodine across the chemocline of TF271 and go12 stations (Figures 2.2, 2.3). Such mid-depth iodine enrichment is unlikely to originate directly from the underlying sediments beneath the sampling station; otherwise, a progressive increase in total iodine should be expected, similar to the trend observed in Siders Pond (Figure 2.6). Rim currents laterally transporting benthic chemical signals, such as I^-, are known in the Baltic (Elken and Matthäus, 2008) and may also be an explanation. For example, rim currents may explain O_2 variations within the suboxic regions sampled at high resolution in this study. That said, while lateral transport of excessive iodine from sediments at the rim of basins is possible, we note that the excess iodine features are not associated with other clear chemical signals and similar features are not observed across adjacent stations in the Gotland Basin (Figure 2.3). Another possible source includes *in situ* iodine introduction from the remineralization of sinking organic matter accumulated at the boundary between low- and high-density waters (pycnocline) (Wong et al., 1985). Such mid-depth total iodine enrichments, as well as I^- enrichments were also reported in the Cariaco Basin and the Orca Basin, close to the pycnocline (Wong and Brewer, 1977; Wong et al., 1985).

Iodine speciation in the Baltic Sea more commonly exhibits depletion of total iodine rather than excess (Figures 2.2-2.5). Most of the total iodine depletion is driven by low I^- values, occurring either in surface (stations go12, go27, go32) or within the chemocline at all the stations. We propose that these observations could be explained by an undercharacterized role of organic iodine or through assimilation and sorption processes. In the case of organic iodine, as mentioned earlier in section 2.7.1.1, it is possible that recalcitrant phases or size fractions not easily reduced

are not captured via our approach. The pathway for elevated DOI in suboxic zones could be through the formation of reactive iodine intermediates related to oxidation via reactive oxygen species (Bielski et al., 1985; Buxton et al., 1988; Liu et al., 2001) or manganese cycling (Fox et al., 2009; Szlamkowicz et al., 2022; Kennedy and Elderfield, 1987a, b), as discussed by Luther, (2023). Iodine intermediates such as HOI or I_2 can react with dissolved organics to form DOI (e.g., Hardisty et al., 2020; Luther et al., 1995; Truesdale and Luther, 1995). While speculative, this hypothesis requires some combination of higher I^- oxidation rates to intermediates (not fully to IO_3^-) and dissolved organic titrants of the oxidation products.

Interestingly, depleted iodine species (including IO_3^-, I^-, and DOI) corresponds to enrichment of Mn-oxides (MnOx) within the chemocline, particularly in the high-resolution depth profile at station TF260 (Figure 2.4). Such correlation therefore suggests the possibility that MnOx particles adsorb iodine species in the water column. The proximity of redox potential between Mn and I in seawater provides thermodynamic basis for Mn species to participate in iodine speciation changes (Rue et al., 1997; Cutter et al., 2018). Previous experiments have demonstrated that birnessite (δ-MnO_2) could to oxidize I^- to IO_3^- through two step pathway as well as adsorb the intermediate form, molecular iodine (Fox et al., 2009). However, such a pathway is most efficient in acidic solutions and becomes almost negligible when pH exceeds above 6.25. Another MnOx species, γ-MnO_2, has the highest efficiency of adsorbing I^- among MnO_2 with different crystal structures (Wang et al., 2022). γ -MnO_2 also remains reactive, although less so in lower pH, to a pH of 9.6 (Wang et al., 2022). This pH range already envelopes the pH range of the Baltic Sea water (Müller, 2018). More evidence, from shipboard incubation with MnOx, as well as from determining the structure of MnOx present in the Baltic Sea, would assist in elucidating whether MnOx contributes to iodine absorption.

2.6.3 Implications to I/Ca proxy application in paleoceanography.

Successful application of the I/Ca paleoredox proxy requires a necessary assumption that IO_3^- exclusively accumulates in highly oxygenated seawater and vice versa. Recently published data from modern low-O_2 marine settings, nevertheless, demonstrate that such a positive relationship between IO_3^- and O_2 is not always consistent. The decoupling between IO_3^- and O_2 involves two aspects in modern ocean: 1) IO_3^- accumulation in the core of some ODZs (Cutter et al., 2018; Moriyasu et al., 2020), and 2) IO_3^- depletion in highly oxygenated water above the chemocline in anoxic basins. Our findings in Siders Pond and the Baltic Sea, together with previous measurements from the Black Sea, propose caution to I/Ca redox application in restricted basins. For example, surface seawater, over a shallowed chemocline which developed during Phanerozoic ocean anoxic events (OAE) (e.g., He et al., 2022; Liu et al., 2019; Pohl et al., 2021; Zhou et al., 2015) might have very low IO_3^- which is recorded by low carbonate I/Ca values despite being locally saturated by O_2 under fully oxygenated atmosphere. Such "false negative signals" for local surface water conditions still have implications for local/regional stratification and should be considered when using I/Ca to trace early ocean oxygenation. We recommend that, prior to conducting paleoredox reconstructions using I/Ca, the paleogeographic setting of the host carbonates should be carefully examined to exclude samples deposited in restricted basins.

As discussed in Section 2.7.1, depleted IO_3^- in high O_2 seawater requires special hydrological settings where the inflow of ocean water directly enters below the chemocline, which has resulted from low salinity water in the surface layer. As a contrast, the surface layer in the Cariaco Basin has similar density with nearby ocean water, and therefore receives IO_3^- directly through horizontal advection (Truesdale et al., 2001). In this case, IO_3^- is the dominant iodine species in the surface layer (Figure 2.9). Modern marine carbonate factories are located exclusively

in salinities close to or exceeding average seawater (Reijmer, 2021). If this mechanism of carbonate formation applied to the ancient ocean, a density-stratified basin like the Baltic Sea or the Black Sea would be unlikely to precipitate carbonates that are suitable for I/Ca analysis. Therefore, most ancient carbonate I/Ca measurements are likely not impacted by density stratification. Instead, early diagenesis of carbonate is more likely to decrease I/Ca values and causing the false negative signals of oxygenation (Hardisty et al., 2017; Hashim et al., 2022).

Another concern regarding the application of I/Ca as a redox proxy arises from the potential impact of riverine DOM flux on seawater iodine speciation. Observation of IO_3^- reduction in the surface of the Central Arctic Ocean, where salinities are close to the ocean mean values, suggests that freshwater-originated DOM has the potential to be transported across the salinity gradients on a scale as extensive as the entire ocean basin (Zhang et al., 2023). If this scenario also applies to the deep time, it is possible for low I/Ca to be recorded in carbonates even formed in relative higher salinity. For example, hypothesized large DOM pools for the Neoproterozoic might explain low I/Ca across this interval, as IO_3^- formation might be prevented by the titration of iodine intermediates with organic carbon to form DOI (Truesdale and Luther, 1995). This might also explain elevated I/Ca during negative carbon isotope excursions possibly driven by oxidation of marine DOM (Dodd et al., 2023).

Another broader implication of this study is that relatively high surface ocean IO_3^-, and thus high I/Ca, might require a well-ventilated global ocean, even if the atmosphere is fully oxygenated. For example, recent model analyses demonstrate that Paleozoic oceans may have maintained widespread anoxia—even after the rise of atmospheric pO_2 to modern levels—due to stratification and resulting ocean circulation enhanced by certain paleogeographies (Pohl et al., 2022). The I/Ca record supports this possibility, as its baseline remains low through the Paleozoic

(Lu et al., 2018). The Baltic Sea might act as an analogue for the overall ventilation process. In this scenario, elevated pelagic IO_3^- is mostly formed over longer timescales (decades) during deep ocean circulation within oxygenated waters and is the main supply of elevated IO_3^- in marine surface waters (e.g., Cheng et al., 2024). These high salinity open ocean waters are the main supply of elevated IO_3^- to anoxic marine basins today (e.g., Cariaco Basin). However, in the Baltic and Siders Pond surface waters, the supply of IO_3^- from open ocean waters is limited and passes through reducing waters before upwelling to the surface, thus maintaining overall low IO_3^-. In this way, regardless of local redox conditions, elevated surface water IO_3^- may indicate a source of broadly oxygenated water masses with the potential for iodide oxidation over long-timescales. There is even some support for this in the open ocean. Within open ocean meridional transects there is lower accumulation of I^- at high latitudinal stations with higher primary productivity with less temperature stratification, and hence a supply of deep water IO_3^- to replenish that in surface waters where IO_3^- is actively reduced by phytoplankton (Chance et al., 2014; Moriyasu et al., 2023). On the other hand, low latitude surface waters accumulate higher I^- and lower IO_3^- given stronger temperature-controlled stratification, and hence less frequent IO_3^- supply from underlying IO_3^- rich waters. Within this context, periods of elevated I/Ca through Earth history may require decreased ocean redox stratification broadly, and not just locally oxygenated seawater.

2.7 Conclusion

We have collected and measured iodine speciation from two modern anoxic basins, Siders Pond and the Baltic Sea. Two distinct features are found in the iodine depth profiles: 1) IO_3^- is depleted in fully oxygenated surface layer even after being normalized for salinity, and 2) non-conservative I^- concentrations within and below the chemocline. We interpret that depleted IO_3^- in the surface of both basins is the combined results from seawater sourced IO_3^- introduction beneath the

chemocline due to low density surface water, phytoplankton assimilation, and possible adsorption and reduction by riverine DOM. Our measurements, compared together with previous reports of iodine speciation from the same area by Truesdale et al., (2013), suggest that intense water column stratification during long-term stagnation period possibly enhanced IO_3^- reduction in the surface layer in the Baltic Sea. Further, iodine species are non-conservative in both anoxic basins. In Siders Pond, excessive I^- is observed towards the sediments, indicating the existence of a benthic flux. Net removal of iodine is prominent in the Baltic Sea water column, especially within the chemocline. We hypothesize that reactive metal species, such as MnOx, might contributes to iodine adsorption from seawater.

The IO_3^--O_2 decouple like that observed in Siders Pond and the Baltic Sea would likely result in a false negative signal of oxidation via the I/Ca paleoredox proxy. A restricted anoxic basin could host depleted IO_3^- in fully oxygenated surface water body and hence record low I/Ca values in carbonates due to fjordic circulation and imbalance between rapid IO_3^- reduction and sluggish I^- oxidation. Therefore, caution should be taken when applying carbonate I/Ca strictly as a local paleoredox proxy. Successful redox interpretation based on I/Ca proxy hence depends on careful reconstruction of paleoceanographic properties, including primary productivity, freshwater flux, as well as the degree of basin restriction.

REFERENCES

Anderson, J. J. and Devol, A. H.: Deep water renewal in Saanich Inlet, an intermittently anoxic basin, Estuar. Coast. Mar. Sci., 1, 1–10, https://doi.org/10.1016/0302-3524(73)90052-2, 1973.

Anschutz, P., Sundby, B., Lefrancois, L., Luther, G. W., and Mucci, A.: Interactions between metal oxides and species of nitrogen and iodine in bioturbated marine sediments, Geochim. Cosmochim. Acta, 64, 2751–2763, 2000.

Bielski, B. H. J., Cabelli, D. E., Arudi, R. L., and Ross, A. B.: Reactivity of HO2/O2− Radicals Radicals in Aqueous Solution, J. Phys. Chem. Ref. Data, 14, 1041–1100, 1985.

Bluhm, K., Croot, P., Wuttig, K., and Lochte, K.: Transformation of iodate to iodide in marine phytoplankton driven by cell senescence, Aquat. Biol., 11, 1–15, https://doi.org/10.3354/ab00284, 2010.

Bowman, C. N., Lindskog, A., Kozik, N. P., Richbourg, C. G., Owens, J. D., and Young, S. A.: Integrated sedimentary, biotic, and paleoredox dynamics from multiple localities in southern Laurentia during the late Silurian (Ludfordian) extinction event, Palaeogeogr. Palaeoclimatol. Palaeoecol., 553, 109799, https://doi.org/10.1016/j.palaeo.2020.109799, 2020.

Broecker, W. S. and Peng, T. H.: Tracers in the Sea., Lamont-Doherty Geological Observatory, Columnbia University, New York, https://doi.org/10.1016/0016-7037(83)90075-3, 1983.

Buxton, G. V, Greenstock, C. L., Helman, W. P., and Ross, A. B.: Critical Review of rate constants for reactions of hydrated electrons, hydrogen atoms and hydroxyl radicals (· OH/ · O − in Aqueous Solution , J. Phys. Chem. Ref. Data, 17, 513–886, 1988.

Campos, M. L. A. M.: New approach to evaluating dissolved iodine speciation in natural waters using cathodic stripping voltammetry and a storage study for preserving iodine species, Mar. Chem., 57, 107–117, https://doi.org/10.1016/S0304-4203(96)00093-X, 1997.

Campos, M. L. A. M., Farrenkopf, A. M., Jickells, T. D., and Luther, G. W.: A comparison of dissolved iodine cycling at the Bermuda Atlantic Time-series station and Hawaii Ocean Time-series station, Deep. Res. Part II Top. Stud. Oceanogr., 43, 455–466, https://doi.org/10.1016/0967-0645(95)00100-x, 1996.

Caraco, N.: Phosphorus, Iron, and Carbon Cycling in a Salt Stratified Coastal Pond, Boston University, 1–213 pp., 1986.

Carpenter, L. J., Chance, R. J., Sherwen, T., Adams, T. J., Ball, S. M., Evans, M. J., Hepach, H., Hollis, L. D. J., Hughes, C., Jickells, T. D., Mahajan, A., Stevens, D. P., Tinel, L., and Wadley, M. R.: Marine iodine emissions in a changing world, Proc. R. Soc. A Math. Phys. Eng. Sci., 477, https://doi.org/10.1098/rspa.2020.0824, 2021.

Chance, R., Weston, K., Baker, A. R., Hughes, C., Malin, G., Carpenter, L., Meredith, M. P.,

Clarke, A., Jickells, T. D., Mann, P., and Rossetti, H.: Seasonal and interannual variation of dissolved iodine speciation at a coastal Antarctic site, Mar. Chem., 118, 171–181, https://doi.org/10.1016/j.marchem.2009.11.009, 2010.

Chance, R., Baker, A. R., Carpenter, L., and Jickells, T. D.: The distribution of iodide at the sea surface, Environ. Sci. Process. Impacts, 16, 1841–1859, https://doi.org/10.1039/c4em00139g, 2014.

Chapman, P.: Changes in iodine speciation in the Benguela current upwelling system, Deep Sea Res. Part A, Oceanogr. Res. Pap., 30, 1247–1259, https://doi.org/10.1016/0198-0149(83)90083-3, 1983.

Cheng, K., Ridgwell, A., and Hardisty, D. S.: Characterizing the marine iodine cycle and its relationship to ocean deoxygenation in an Earth System model, Biogeosciences, 21, 4927–4949, 2024.

Councell, T. B., Landa, E. R., and Lovley, D. R.: Microbial reduction of iodate, Water. Air. Soil Pollut., 100, 99–106, 1997.

Cutter, G. A., S. Walsh, R., and Silva De Echols, C.: Production and speciation of hydrogen sulfide in surface waters of the high latitude north Atlantic Ocean, Deep. Res. Part II Top. Stud. Oceanogr., 46, 991–1010, https://doi.org/10.1016/S0967-0645(99)00013-2, 1999.

Cutter, G. A., Moffett, J. G., Nielsdóttir, M. C., and Sanial, V.: Multiple oxidation state trace elements in suboxic waters off Peru: In situ redox processes and advective/diffusive horizontal transport, Mar. Chem., 201, 77–89, https://doi.org/10.1016/j.marchem.2018.01.003, 2018.

Daines, S. J., Mills, B. J. W., and Lenton, T. M.: Atmospheric oxygen regulation at low Proterozoic levels by incomplete oxidative weathering of sedimentary organic carbon, Nat. Commun., 8, 1–11, https://doi.org/10.1038/ncomms14379, 2017.

Dellwig, O., Leipe, T., Ma, C., Glockzin, M., Pollehne, F., Schnetger, B., Yakushev, E. V, and Bo, M. E.: A new particulate Mn – Fe – P-shuttle at the redoxcline of anoxic basins, 74, 7100–7115, https://doi.org/10.1016/j.gca.2010.09.017, 2010.

Dellwig, O., Schnetger, B., Brumsack, H. J., Grossart, H. P., and Umlauf, L.: Dissolved reactive manganese at pelagic redoxclines (part II): Hydrodynamic conditions for accumulation, J. Mar. Syst., 90, 31–41, https://doi.org/10.1016/j.jmarsys.2011.08.007, 2012.

Deuser, W. G.: Cariaco trench: Oxidation of organic matter and residence time of anoxic water, Nature, 242, 601–603, https://doi.org/10.1038/242601b0, 1973.

Ding, Y., Sun, W., Liu, S., Xie, J., Tang, D., Zhou, X., Zhou, L., Li, Z., Song, J., Li, Z., Xu, H., Tang, P., Liu, K., Li, W., and Chen, D.: Low oxygen levels with high redox heterogeneity in the late Ediacaran shallow ocean: Constraints from I/(Ca + Mg) and Ce/Ce* of the Dengying Formation, South China, Geobiology, 20, 790–809, https://doi.org/10.1111/gbi.12520, 2022.

Dodd, M. S., Shi, W., Li, C., Zhang, Z., Cheng, M., Gu, H., Hardisty, D. S., Loyd, S. J., Wallace, M. W., Hood, A., Lamothe, K., Mills, B. J. W., Poulton, S. W., and Lyons, T. W.: Uncovering the Ediacaran phosphorus cycle, Nature, 618, 974–980, https://doi.org/10.1038/s41586-023-06077-6, 2023.

Edwards, C. T., Fike, D. A., Saltzman, M. R., Lu, W., and Lu, Z.: Evidence for local and global redox conditions at an Early Ordovician (Tremadocian) mass extinction, Earth Planet. Sci. Lett., 481, 125–135, https://doi.org/10.1016/j.epsl.2017.10.002, 2018.

Elderfield, H. and Truesdale, V. W.: On the biophilic nature of iodine in seawater, Earth Planet. Sci. Lett., 50, 105–114, https://doi.org/10.1016/0012-821X(80)90122-3, 1980.

Elken, J. and Matthäus, W.: Assessment of Climate Change for the Baltic Sea Basin, Springer Berlin Heidelberg, https://doi.org/10.1007/978-3-540-72786-6, 2008.

Emerson, S., Cranston, R. E., and Liss, P. S.: Redox species in a reducing fjord: equilibrium and kinetic considerations, Deep Sea Res. Part A, Oceanogr. Res. Pap., 26, 859–878, https://doi.org/10.1016/0198-0149(79)90101-8, 1979.

Fang, H., Tang, D., Shi, X., Zhou, L., Zhou, X., Wu, M., Song, H., and Riding, R.: Early Mesoproterozoic Ca-carbonate precipitates record fluctuations in shallow marine oxygenation, Precambrian Res., 373, 106630, https://doi.org/10.1016/j.precamres.2022.106630, 2022.

Farrenkopf, A. M. and Luther, G. W.: Iodine chemistry reflects productivity and denitrification in the Arabian Sea: Evidence for flux of dissolved species from sediments of western India into the OMZ, Deep. Res. Part II Top. Stud. Oceanogr., 49, 2303–2318, https://doi.org/10.1016/S0967-0645(02)00038-3, 2002.

Farrenkopf, A. M., Dollhopf, M. E., Chadhain, S. N., Luther, G. W., and Nealson, K. H.: Reduction of iodate in seawater during Arabian Sea shipboard incubations and in laboratory cultures of the marine bacterium Shewanella putrefaciens strain MR-4, Mar. Chem., 57, 347–354, https://doi.org/10.1016/S0304-4203(97)00039-X, 1997.

Fox, P. M., Davis, J. A., and Luther, G. W.: The kinetics of iodide oxidation by the manganese oxide mineral birnessite, Geochim. Cosmochim. Acta, 73, 2850–2861, https://doi.org/10.1016/j.gca.2009.02.016, 2009.

Francois, R.: The influence of humic substances on the geochemistry of iodine in nearshore and hemipelagic marine sediments, Geochim. Cosmochim. Acta, 51, 2417–2427, https://doi.org/10.1016/0016-7037(87)90294-8, 1987.

Gargett, A. E., Stucchi, D., and Whitney, F.: Physical processes associated with high primary production in Saanich Inlet , British Columbia, Esruarine, Coast. Shelf Sci., 56, 1141–1156, https://doi.org/10.1016/S0272-7714(02)00319-0, 2003.

Hardisty, D. S., Lu, Z., Planavsky, N. J., Bekker, A., Philippot, P., Zhou, X., and Lyons, T. W.: An iodine record of Paleoproterozoic surface ocean oxygenation, Geology, 42, 619–622,

https://doi.org/10.1130/G35439.1, 2014.

Hardisty, D. S., Lu, Z., Bekker, A., Diamond, C. W., Gill, B. C., Jiang, G., Kah, L. C., Knoll, A. H., Loyd, S. J., Osburn, M. R., Planavsky, N. J., Wang, C., Zhou, X., and Lyons, T. W.: Perspectives on Proterozoic surface ocean redox from iodine contents in ancient and recent carbonate, Earth Planet. Sci. Lett., 463, 159–170, https://doi.org/10.1016/j.epsl.2017.01.032, 2017.

Hardisty, D. S., Horner, T. J., Wankel, S. D., Blusztajn, J., and Nielsen, S. G.: Experimental observations of marine iodide oxidation using a novel sparge-interface MC-ICP-MS technique, Chem. Geol., 532, 119360, https://doi.org/10.1016/j.chemgeo.2019.119360, 2020.

Hardisty, D. S., Horner, T. J., Evans, N., Moriyasu, R., Babbin, A. R., Wankel, S. D., Moffett, J. W., and Nielsen, S. G.: Limited iodate reduction in shipboard seawater incubations from the Eastern Tropical North Pacific oxygen deficient zone, Earth Planet. Sci. Lett., 554, 116676, https://doi.org/10.1016/j.epsl.2020.116676, 2021.

Hashim, M. S., Burke, J. E., Hardisty, D. S., and Kaczmarek, S. E.: Iodine incorporation into dolomite: Experimental constraints and implications for the iodine redox proxy and Proterozoic Ocean, Geochim. Cosmochim. Acta, 338, 365–381, https://doi.org/10.1016/j.gca.2022.10.027, 2022.

He, P., Hou, X., and Aldahan, A.: Iodine isotopes species fingerprinting environmental conditions in surface water along the northeastern Atlantic Ocean, Sci. Rep., 3, 1–9, https://doi.org/10.1038/srep02685, 2013.

He, T., Newton, R. J., Wignall, P. B., Reid, S., Dal, J., Takahashi, S., Wu, H., Todaro, S., Di, P., Randazzo, V., Rigo, M., and Dunhill, A. M.: Shallow ocean oxygen decline during the end-Triassic mass extinction, Glob. Planet. Change, 210, 103770, https://doi.org/10.1016/j.gloplacha.2022.103770, 2022.

Hepach, H., Hughes, C., Hogg, K., Collings, S., and Chance, R.: Senescence as the main driver of iodide release from a diverse range of marine phytoplankton, Biogeosciences, 17, 2453–2471, https://doi.org/10.5194/bg-17-2453-2020, 2020.

Hoikkala, L., Kortelainen, P., Soinne, H., and Kuosa, H.: Dissolved organic matter in the Baltic Sea, J. Mar. Syst., 142, 47–61, https://doi.org/10.1016/j.jmarsys.2014.10.005, 2015.

Hou, X., Dahlgaard, H., Rietz, B., Jacobsen, U., Nielsen, S. P., and Aarkrog, A.: Determination of chemical species of iodine in seawater by radiochemical neutron activation analysis combined with ion-exchange preseparation, Anal. Chem., 71, 2745–2750, https://doi.org/10.1021/ac9813639, 1999.

Hou, X., Dahlgaard, H., and Nielsen, S. P.: Chemical speciation analysis of 129I in seawater and a preliminary investigation to use it as a tracer for geochemical cycle study of stable iodine, Mar. Chem., 74, 145–155, https://doi.org/10.1016/S0304-4203(01)00010-X, 2001.

Hou, X., Aldahan, A., Nielsen, S. P., Possnert, G., Nies, H., and Hedfors, J.: Speciation of 129I and 127I in seawater and implications for sources and transport pathways in the North Sea, Environ. Sci. Technol., 41, 5993–5999, https://doi.org/10.1021/es070575x, 2007.

Hou, X., Aldahan, A., Nielsen, S. P., and Possnert, G.: Time Series of 129I and 127I Speciation in Precipitation from Denmark, Environ. Sci. Technol., 43, 6522–6528, 2009.

Hou, X., Povinec, P. P., Zhang, L., Shi, K., Biddulph, D., Chang, C., Fan, Y., Golser, R., Hou, Y., and Jes, M.: Iodine-129 in Seawater Off shore Fukushima: Distribution, Inorganic Speciation, Sources, and Budget, Environ. Sci. Technol., 47, 3091–3098, 2013.

Hughes, C., Barton, E., Hepach, H., Chance, R., Wadley, M. R., Pickering, M. D., Hogg, K., Pommerening-r, A., Stevens, D. P., and Jickells, T. D.: Oxidation of iodide to iodate by cultures of marine ammonia-oxidising bacteria, Mar. Chem., 234, 1–7, https://doi.org/10.1016/j.marchem.2021.104000, 2021.

Jiang, Z., Cui, M., Qian, L., Jiang, Y., Shi, L., Dong, Y., Li, J., and Wang, Y.: Abiotic and Biotic Reduction of Iodate Driven by Shewanella oneidensis MR-1, Environ. Sci. Technol., 57, 19817–19826, https://doi.org/10.1021/acs.est.3c06490, 2023.

Jickells, T. D., Boyd, S. S., and Knap, A. H.: Iodine Cycling in the Sargasso Sea and the B e r m u d a Inshore Waters, Mar. Chem., 24, 61–82, 1988.

Jones, M. R., Chance, R., Dadic, R., Hannula, H., May, R., Ward, M., and Carpenter, L. J.: Environmental iodine speciation quantification in seawater and snow using ion exchange chromatography and UV spectrophotometric detection, Anal. Chim. Acta, 1239, 340700, https://doi.org/10.1016/j.aca.2022.340700, 2023.

Jones, M. R., Chance, R., Bell, T., Jones, O., Loades, D. C., May, R., Tinel, L., Weddell, K., Widdicombe, C., and Carpenter, L. J.: Iodide, iodate & dissolved organic iodine in the temperate coastal ocean, Front. Mar. Sci., 11, 1–18, https://doi.org/10.3389/fmars.2024.1277595, 2024.

Kennedy, H. A. and Elderfield, H.: Iodine diagenesis in non-pelagic deep-sea sediments, Geochim. Cosmochim. Acta, 51, 2505–2514, 1987a.

Kennedy, H. A. and Elderfield, H.: Iodine diagenesis in pelagic deep-sea sediments, Geochim. Cosmochim. Acta, 51, 2489–2504, 1987b.

de La Cuesta, J. L. and Manley, S. L.: Iodine assimilation by marine diatoms and other phytoplankton in nitrate-replete conditions, Limnol. Oceanogr., 54, 1653–1664, https://doi.org/10.4319/lo.2009.54.5.1653, 2009.

Lemke, W., Kuijpers, A., Hoffmann, G., Milkert, D., and Atzler, R.: The Darss Sill, hydrographic threshold in the southwestern Baltic: Late Quaternary geology and recent sediment dynamics, Cont. Shelf Res., 14, 847–870, https://doi.org/10.1016/0278-4343(94)90076-0, 1994.

Li, H., Daniel, B., Creeley, D., Grandbois, R., Zhang, S., Xu, C., Ho, Y., and Schwehr, K. A.: Superoxide Production by a Manganese-Oxidizing Bacterium Facilitates Iodide Oxidation, Appl. Environ. Microbiol., 80, 2693–2699, https://doi.org/10.1128/AEM.00400-14, 2014a.

Li, H. P., Daniel, B., Creeley, D., Grandbois, R., Zhang, S., Xu, C., Ho, Y. F., Schwehr, K. A., Kaplan, D. I., Santschi, P. H., Hansel, C. M., and Yeager, C. M.: Superoxide production by a manganese-oxidizing bacterium facilitates iodide oxidation, Appl. Environ. Microbiol., 80, 2693–2699, https://doi.org/10.1128/AEM.00400-14, 2014b.

Lin, J.: Dissolved iodine in the Changjiang River Estuary, China, Water Sci. Technol., 88, 1267–1279, https://doi.org/10.2166/wst.2023.263, 2023.

Liu, A., Tang, D., Shi, X., Zhou, X., Zhou, L., Shang, M., Li, Y., and Fang, H.: Mesoproterozoic oxygenated deep seawater recorded by early diagenetic carbonate concretions from the Member IV of the Xiamaling Formation, North China, Precambrian Res., 341, 105667, https://doi.org/10.1016/j.precamres.2020.105667, 2020.

Liu, J., Algeo, T. J., Qie, W., and Saltzman, M. R.: Intensified oceanic circulation during Early Carboniferous cooling events: Evidence from carbon and nitrogen isotopes, Palaeogeogr. Palaeoclimatol. Palaeoecol., 531, 0–1, https://doi.org/10.1016/j.palaeo.2018.10.021, 2019.

Liu, Q., Schurter, L. M., Muller, C. E., Aloisio, S., Francisco, J. S., and Margerum, D. W.: Kinetics and Mechanisms of Aqueous Ozone Reactions with Bromide, Sulfite, Hydrogen Sulfite, Iodide, and Nitrite Ions, Inorg. Chem., 40, 4436–4442, 2001.

Lu, W., Ridgwell, A., Thomas, E., Hardisty, D. S., Luo, G., Algeo, T. J., Saltzman, M. R., Gill, B. C., Shen, Y., Ling, H. F., Edwards, C. T., Whalen, M. T., Zhou, X., Gutchess, K. M., Jin, L., Rickaby, R. E. M., Jenkyns, H. C., Lyons, T. W., Lenton, T. M., Kump, L. R., and Lu, Z.: Late inception of a resiliently oxygenated upper ocean, Science (80-.)., 361, 174–177, https://doi.org/10.1126/science.aar5372, 2018.

Lu, Z., Jenkyns, H. C., and Rickaby, R. E. M.: Iodine to calcium ratios in marine carbonate as a paleo-redox proxy during oceanic anoxic events, Geology, 38, 1107–1110, https://doi.org/10.1130/G31145.1, 2010.

Lu, Z., Hoogakker, B. A. A., Hillenbrand, C.-D., Zhou, X., Thomas, E., Gutchess, K. M., Lu, W., Jones, L., and Rickaby, R. E. M.: Oxygen depletion recorded in upper waters of the glacial Southern Ocean, Nat. Commun., 7, 1–8, https://doi.org/10.1038/ncomms11146, 2016.

Luther, G. W.: Review on the physical chemistry of iodine transformations in the oceans, Front. Mar. Sci., 10, 1–16, https://doi.org/10.3389/fmars.2023.1085618, 2023.

Luther, G. W. and Campbell, T.: Iodine speciation in the water column of the Black Sea, Deep Sea Res. Part A. Oceanogr. Res. Pap., 38, S875–S882, https://doi.org/10.1016/s0198-0149(10)80014-7, 1991.

Luther, G. W. and Cole, H.: Iodine speciation in chesapeake bay waters, Mar. Chem., 24, 315–325, https://doi.org/10.1016/0304-4203(88)90039-4, 1988.

Luther, G. W., Ferdelman, T., Culberson, C. H., Kostka, J., and Wu, J.: Iodine Chemistry in the Water the Chesapeake Bay : Evidence Iodine Forms Column of for Organic, Esruarine, Coast. Shelf Sci., 32, 267–279, 1991.

Luther, G. W., Wu, J., and Cullen, J. B.: Redox Chemistry of Iodine in Seawater, Adv. Chem., 244, 135–155, 1995.

Martin, J. B., Gieskes, J. M., Torres, M., and Kastner, M.: Bromine and iodine in Peru margin sediments and pore fluids: Implications for fluid origins, Geochim. Cosmochim. Acta, 57, 4377–4389, https://doi.org/10.1016/0016-7037(93)90489-J, 1993.

Mohrholz, V., Naumann, M., Nausch, G., Krüger, S., and Gräwe, U.: Fresh oxygen for the Baltic Sea — An exceptional saline in fl ow after a decade of stagnation, J. Mar. Syst., 148, 152–166, https://doi.org/10.1016/j.jmarsys.2015.03.005, 2015.

Moran, J. E., Oktay, S. D., and Santschi, P. H.: Sources of iodine and iodine 129 in rivers, Water Resour. Res., 38, 24-1-24–10, https://doi.org/10.1029/2001wr000622, 2002.

Moriyasu, R., Evans, N., Bolster, K. M., Hardisty, D. S., and Moffett, J. W.: The Distribution and Redox Speciation of Iodine in the Eastern Tropical North Pacific Ocean, Global Biogeochem. Cycles, 34, 0–3, https://doi.org/10.1029/2019GB006302, 2020.

Moriyasu, R., Bolster, K. M., Hardisty, D. S., Kadko, D. C., Stephens, M. P., and Moffett, J. W.: Meridional Survey of the Central Pacific Reveals Iodide Accumulation in Equatorial Surface Waters and Benthic Sources in the Abyssal Plain Global Biogeochemical Cycles, Global Biogeochem. Cycles, 37, 1–15, https://doi.org/10.1029/2021GB007300, 2023.

Müller, J. D.: Ocean acidification in the Baltic Sea: involved processes, metrology of pH in brackish waters, and calcification under fluctuating conditions, 1–70 pp., 2018.

Muramatsu, Y. and Wedepohl, K. H.: The distribution of iodine in the Earth's crust, Chem. Geol., 147, 201–216, https://doi.org/10.1016/S0009-2541(98)00013-8, 1998.

Sea-viewing Wide Field-of-view Sensor (SeaWiFS) Level-2 Ocean Color Data, version R2018.8:

Neretin, L. N., Pohl, C., Jost, G., Leipe, T., and Pollehne, F.: Manganese cycling in the Gotland Deep, Baltic Sea, Mar. Chem., 82, 125–143, https://doi.org/10.1016/S0304-4203(03)00048-3, 2003.

Ostrander, C. M., Nielsen, S. G., Gadol, H. J., Villarroel, L., Wankel, S. D., Horner, T. J., Blusztajn, J., and Hansel, C. M.: Thallium isotope cycling between waters , particles , and sediments across a redox gradient, Geochim. Cosmochim. Acta, 348, 397–409, https://doi.org/10.1016/j.gca.2023.03.028, 2023.

Pohl, A., Lu, Z., Lu, W., Stockey, R. G., Elrick, M., Li, M., Desrochers, A., Shen, Y., He, R., Finnegan, S., and Ridgwell, A.: Vertical decoupling in Late Ordovician anoxia due to reorganization of ocean circulation, Nat. Geosci., 14, 868–873, https://doi.org/10.1038/s41561-021-00843-9, 2021.

Pohl, A., Ridgwell, A., Stockey, R. G., Thomazo, C., Keane, A., Vennin, E., and Scotese, C. R.: Continental configuration controls ocean oxygenation during the Phanerozoic, Nature, 608, 523–527, https://doi.org/10.1038/s41586-022-05018-z, 2022.

Price, N. B. and Calvert, S. E.: The geochemistry of iodine in oxidised and reduced Recent marine sediments, Geochim. Cosmochim. Acta, 37, 2149–2158, 1973.

Qstlund, H. G. and Alexander, J.: Oxidation rate of sulfide in sea water, A preliminary study, J. Geophys. Res., 68, 3995–3997, 1963.

Rapp, I., Schlosser, C., Barraqueta, J. M., Wenzel, B., Lüdke, J., and Scholten, J.: Controls on redox-sensitive trace metals in the Mauritanian oxygen minimum zone, Biogeosciences, 16, 4157–4182, 2019.

Rapp, I., Schlosser, C., Browning, T. J., Wolf, F., Le Moigne, F. A. C., Gledhill, M., and Achterberg, E. P.: El Niño-Driven Oxygenation Impacts Peruvian Shelf Iron Supply to the South Pacific Ocean, Geophys. Res. Lett., 47, 0–3, https://doi.org/10.1029/2019GL086631, 2020.

Reifenhäuser, C. and Heumann, K. G.: Development of a definitive method for iodine speciation in aquatic systems, Fresenius. J. Anal. Chem., 336, 559–563, https://doi.org/10.1007/BF00331416, 1990.

Reijmer, J. J. G.: Marine carbonate factories: Review and update, Sedimentology, 68, 1729–1796, https://doi.org/10.1111/sed.12878, 2021.

Reissmann, J. H., Burchard, H., Feistel, R., Hagen, E., Lass, H. U., Mohrholz, V., Nausch, G., Umlauf, L., and Wieczorek, G.: Vertical mixing in the Baltic Sea and consequences for eutrophication - A review, Prog. Oceanogr., 82, 47–80, https://doi.org/10.1016/j.pocean.2007.10.004, 2009.

Reyes-Umana, V., Henning, Z., Lee, K., Barnum, T. P., and Coates, J. D.: Genetic and phylogenetic analysis of dissimilatory iodate-reducing bacteria identifies potential niches across the world's oceans, ISME J., 16, 38–49, https://doi.org/10.1038/s41396-021-01034-5, 2021.

Rue, E. L., Smith, G. J., Cutter, G. A., and Bruland, K. W.: The response of trace element redox couples to suboxic conditions in the water column, Deep. Res. Part I Oceanogr. Res. Pap., 44, 113–134, https://doi.org/10.1016/S0967-0637(96)00088-X, 1997.

Schmale, O., Krause, S., Holtermann, P., Power Guerra, N. C., and Umlauf, L.: Dense bottom gravity currents and their impact on pelagic methanotrophy at oxic/anoxic transition zones, Geophys. Res. Lett., 43, 5225–5232, https://doi.org/10.1002/2016GL069032, 2016.

Schnur, A. A., Sutherland, K. M., Hansel, C. M., and Hardisty, D. S.: Rates and pathways of iodine speciation transformations at the Bermuda Atlantic Time Series, Front. Mar. Sci., 10, 1–14, https://doi.org/10.3389/fmars.2023.1272870, 2024.

Scholz, F., Hardisty, D. S., and Dale, A. W.: Early Diagenetic Controls on Sedimentary Iodine Release and Iodine-To-Organic Carbon Ratios in the Paleo-Record, Global Biogeochem. Cycles, 38, e2023GB007919, https://doi.org/10.1029/2023GB007919, 2024.

Shang, M., Tang, D., Shi, X., Zhou, L., Zhou, X., Song, H., and Jiang, G.: A pulse of oxygen increase in the early Mesoproterozoic ocean at ca. 1.57–1.56 Ga, Earth Planet. Sci. Lett., 527, 115797, https://doi.org/10.1016/j.epsl.2019.115797, 2019.

Shi, Q., Kim, J. S., and Wallace, D. W.: Speciation of dissolved inorganic iodine in a coastal fjord : a time- series study from Bedford Basin , Nova Scotia , Canada, Front. Mar. Sci., 1–15, https://doi.org/10.3389/fmars.2023.1171999, 2023.

Ştreangă I-M, Repeta DJ, Blusztajn JS, Horner TJ (2024) Speciation and cycling of iodine in the subtropical North Paci fi c Ocean. *Frontiers in Marine Science* **10**, 1272968.

Soetaert, G., Hamme, R. C., and Raftery, E.: Renewal of seasonally anoxic Saanich Inlet is temporally and spatially dynamic, Front. Energy Res., 9, 1–17, https://doi.org/10.3389/fmars.2022.1001146, 2022.

Szlamkowicz, I. B., Fentress, A. J., Longen, L. F., Stanberry, J. S., and Anagnostopoulos, V. A.: Transformations and Speciation of Iodine in the Environment as a Result of Oxidation by Manganese Minerals, ACS Earth Sp. Chem., 6, 1948–1956, https://doi.org/10.1021/acsearthspacechem.1c00372, 2022.

Tang, D., Fang, H., Shi, X., Liang, L., Zhou, L., Xie, B., Huang, K., Zhou, X., Wu, M., and Riding, R.: Mesoproterozoic Molar Tooth Structure Related to Increased Marine Oxygenation, J. Geophys. Res. Biogeosciences, 128, 1–18, https://doi.org/10.1029/2022jg007077, 2023.

Truesdale, V. W. and Luther, G. W.: Molecular Iodine Reduction by Natural and Model Organic Substances in Seawater, Aquat. Geochemistry, 1, 89–104, 1995.

Truesdale, V. W., Bale, A. J., and Woodward, E. M. S.: The meridional distribution of dissolved iodine in near-surface waters of the Atlantic Ocean, Prog. Oceanogr., 45, 387–400, https://doi.org/10.1016/S0079-6611(00)00009-4, 2000.

Truesdale, V. W., Watts, S. F., and Rendell, A. R.: On the possibility of iodide oxidation in the near-surface of the Black Sea and its implications to iodine in the general ocean, Deep. Res. Part I, 48, 2397–2412, 2001.

Truesdale, V. W., Nausch, G., and Waite, T. J.: The effects of the 2001 Barotropic intrusion of bottom-water upon the vertical distribution of inorganic iodine in the Gotland Deep, Cont. Shelf Res., 55, 155–167, https://doi.org/10.1016/j.csr.2013.01.005, 2013.

Tsunogai, S.: Iodine in the deep water of the ocean, Deep. Res., 18, 913–919, 1971.

Uahengo, C. I., Shi, X., Jiang, G., and Vatuva, A.: Transient shallow-ocean oxidation associated with the late Ediacaran Nama skeletal fauna: Evidence from iodine contents of the Lower Nama Group, southern Namibia, Precambrian Res., 343, 105732,

https://doi.org/10.1016/j.precamres.2020.105732, 2020.

Ullman, J. and Aller, C.: The geochemistry of iodine in near-shore carbonate sediments, Geochim. Cosmochim. Acta, 49, 967–978, 1985.

Ullman, W. J., Luther, G. W., De Lange, G. J., and Woittiez, J. R. W.: Iodine chemistry in deep anoxic basins and overlying waters of the Mediterranean Sea, Mar. Chem., 31, 153–170, https://doi.org/10.1016/0304-4203(90)90036-C, 1990.

Voipio, A.: The Baltic Sea, Elsevier Scientific Pub. Co. ; Distributors for the U.S. and Canada, Elsevier/North-Holland, Amsterdam ; New York, 1981, pp 135, pp 132, pp 125, pp 130.

Voss, M., Burmeister, C., Cheng, K., Gentsch, K., Hansel, C., Hübner, V., Köhler, A., Kolbe, M., Ostrander, C., Pardis, W., Schulz-Vogt, H., and Taenzer, L.: Elisabeth Mann-Borgese Berichte, Cruise EMB276, Rostock-Rostock, 17.09.2021-29.09.2021 Table, 1–15 pp., https://doi.org/10.48433/cr_emb276, 2021.

Walsh, R. S., Cutter, G. A., Dunstan, W. M., Radford-Knoery, J., and Elder, J. T.: The biogeochemistry of hydrogen sulfide: Phytoplankton production in the surface ocean, Limnol. Oceanogr., 39, 941–948, https://doi.org/10.4319/lo.1994.39.4.0941, 1994.

Wang, N., Zhang, G., Xiong, R., Liu, R., Liu, H., and Qu, J.: Synchronous Moderate Oxidation and Adsorption on the Surface of γ-MnO2for Efficient Iodide Removal from Water, Environ. Sci. Technol., 56, 9417–9427, https://doi.org/10.1021/acs.est.2c01682, 2022.

Wegwerth, A., Plessen, B., Kleinhanns, I. C., and Arz, H. W.: Black Sea hydroclimate and coupled hydrology was strongly controlled by high-latitude glacial climate dynamics, Commun. Earth Environ., 2, 1–8, https://doi.org/10.1038/s43247-021-00129-3, 2021.

Wei, G. Y., Planavsky, N. J., He, T., Zhang, F., Stockey, R. G., Cole, D. B., Lin, Y. B., and Ling, H. F.: Global marine redox evolution from the late Neoproterozoic to the early Paleozoic constrained by the integration of Mo and U isotope records, Earth-Science Rev., 214, 103506, https://doi.org/10.1016/j.earscirev.2021.103506, 2021.

Wong, G. T. F. and Brewer, P. G.: The marine chemistry of iodine in anoxic basins, Geochim. Cosmochim. Acta, 41, 151–159, https://doi.org/10.1016/0016-7037(77)90195-8, 1977.

Wong, G. T. F. and Cheng, X.: Dissolved organic iodine in marine waters : Determination , occurrence and analytical implications, Mar. Chem., 59, 271–281, 1998.

Wong, G. T. F. and Cheng, X.: Dissolved inorganic and organic iodine in the Chesapeake Bay and adjacent Atlantic waters : Speciation changes through an estuarine system, Mar. Chem., 111, 221–232, https://doi.org/10.1016/j.marchem.2008.05.006, 2008.

Wong, G. T. F., Takayanagi, K., and Todd, J. F.: Dissolved iodine in waters overlying and in the Orca Basin, Gulf of Mexico, Mar. Chem., 17, 177–183, https://doi.org/10.1016/0304-4203(85)90072-6, 1985.

Wong, G. T. F., Piumsomboon, A. U., Dunstan, W. M., Wong, G. T. F., Piumsomboon, A. U., and Dunstan, W. M.: The transformation of iodate to iodide in marine phytoplankton cultures, Mar. Geol. Prog. Ser., 237, 27–39, 2002.

Yu, Y., Chen, Y., Li, D., and Su, J.: A transient oxygen increase in the Mesoproterozoic ocean at ~1.44 Ga: Geochemical evidence from the Tieling Formation, North China Platform, Precambrian Res., 369, 106527, https://doi.org/10.1016/j.precamres.2021.106527, 2022.

Zhang, J. and Whitfield, M.: KINETICS OF INORGANIC REDOX REACTIONS IN SEAWATER I . The reduction of iodate by bisulphide Micro-organisms play a dominant role in the diagenesis of organic-rich sediments . The oxidative breakdown of the organic matter , with the accom- panying reductio, Mar. Chem., 19, 121–137, 1986.

Zhang, L., Hou, X., Gwynn, J. P., Karcher, M., Chen, N., Fan, Y., and Liu, Q.: Spatial variation and species transformation of 129I and 127I in the Central Arctic Ocean, Earth Planet. Sci. Lett., 612, 118165, https://doi.org/10.1016/j.epsl.2023.118165, 2023.

Zhou, X., Jenkyns, H. C., Owens, J. D., Junium, C. K., Zheng, X. Y., Sageman, B. B., Hardisty, D. S., Lyons, T. W., Ridgwell, A., and Lu, Z.: Upper ocean oxygenation dynamics from I/Ca ratios during the Cenomanian-Turonian OAE 2, Paleoceanography, 30, 510–526, https://doi.org/10.1002/2014PA002741, 2015.

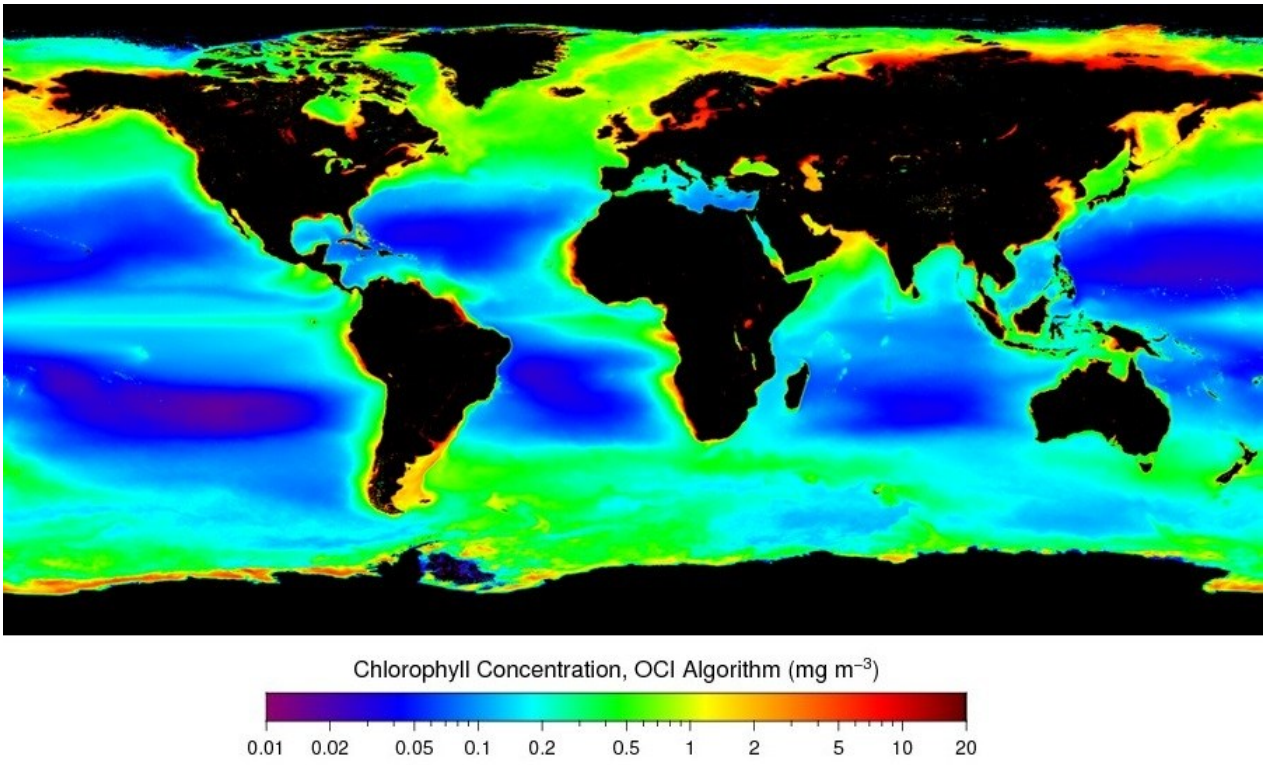

Figure 2.12. Composited global chlorophyll concentration measured by satellite Aqua/MODIS during July 2002-November 2023 (NASA Ocean Biology Processing Group, 2018).

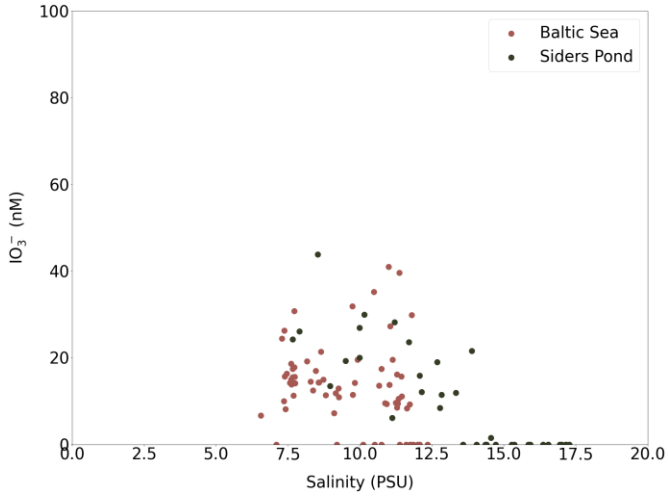

Figure 2.13. Salinity versus IO_3^- in the Baltic Sea and Siders Pond. Note that there is no linear relationship between Salinity and IO_3^-.

Table 2.1. Iodine speciation measurements of Baltic Sea samples using the chromatography and ICPMS method, including column recover rate and instrumental detection limit (D.L.).

Station	Latitude (°N)	Longitude (°E)	Depth (m)	IO_3^- (nM)	Recovery (%)	I^- (nM)	Recovery (%)	DOI (nM)	Recovery (%)	D.L. (nM)	Total I (nM)	Recovery (%)	D.L. (nM)
go32	56.8336	19.1831	18.50	0.00	106%	41.77	91%	0.00	102%	4.8	57.68	104%	7.00
			26.25	13.88	106%	81.16	91%	0.00	102%	4.8	113.18	104%	7.00
			45.00	15.62	106%	98.65	91%	0.00	102%	4.8	120.05	104%	7.00
			61.75	12.49	106%	85.73	91%	0.00	102%	4.8	108.41	104%	7.00
			66.25	11.83	106%	94.22	91%	0.00	102%	4.8	108.05	104%	7.00
			71.75	14.28	106%	121.45	91%	0.00	102%	4.8	154.20	104%	7.00
			77.25	0.00	106%	154.81	91%	0.00	102%	4.8	159.86	104%	7.00
			82.00	0.00	106%	70.61	91%	0.00	102%	4.8	77.89	104%	7.00
			118.00	0.00	106%	167.36	91%	0.00	102%	4.8	171.80	104%	7.00
go27	56.9504	19.8828	14.75	16.36	108%	32.70	92%	0.00	109%	2	27.92	107%	3.20
			50.00	14.11	108%	33.43	92%	0.00	109%	2	33.43	107%	3.20
			69.75	14.36	108%	116.38	92%	0.00	109%	2	117.76	107%	3.20
			77.50	11.50	108%	120.18	92%	0.00	109%	2	137.85	107%	3.20
			90.25	13.80	108%	145.94	92%	0.00	109%	2	128.62	107%	3.20
			99.00	8.57	108%	103.91	92%	0.00	109%	2	105.62	107%	3.20
			113.00	0.00	108%	74.57	92%	0.00	109%	2	66.16	107%	3.20
			124.75	0.00	108%	187.97	92%	0.00	109%	2	167.41	107%	3.20
TF271_E_GD	57.2007	20.0312	14.75	8.18	93%	103.25	97%	0.00	94%	3.2	99.37	93%	4.80
			38.75	11.32	93%	100.04	97%	0.00	94%	3.2	95.07	93%	4.80
			72.75	14.30	93%	129.22	97%	4.07	94%	3.2	124.04	93%	4.80
			76.25	10.95	93%	128.31	97%	4.40	94%	3.2	120.85	93%	4.80
			85.75	6.67	93%	161.61	97%	0.00	94%	3.2	148.95	93%	4.80
			102.75	9.46	93%	175.27	97%	0.00	94%	3.2	169.19	93%	4.80
			107.50	11.11	93%	89.39	97%	0.00	94%	3.2	113.07	93%	4.80
			112.00	0.00	93%	199.41	97%	0.00	94%	3.2	190.05	93%	4.80
			115.25	0.00	93%	215.41	97%	0.00	94%	3.2	207.13	93%	4.80
go12 Fårö	58.0004	19.8998	15.00	10.01	94%	51.19	101%	0.00	101%	7.6	51.92	98%	11.20
			35.50	14.95	94%	81.38	101%	0.00	101%	7.6	92.28	98%	11.20
			62.25	19.19	94%	121.72	101%	13.06	101%	7.6	137.30	98%	11.20
			68.00	11.42	94%	46.99	101%	0.00	101%	7.6	50.36	98%	11.20
			72.00	0.00	94%	172.10	101%	0.00	101%	7.6	169.10	98%	11.20
			79.75	0.00	94%	145.68	101%	0.00	101%	7.6	140.23	98%	11.20
			90.50	13.59	94%	122.49	101%	0.00	101%	7.6	133.15	98%	11.20
			110.00	0.00	94%	127.94	101%	0.00	101%	7.6	129.00	98%	11.20
			130.50	0.00	94%	75.81	101%	0.00	101%	7.6	74.00	98%	11.20

Table 2.1 (cont'd).

			14.75	15.71	97%	66.59	88%	4.71	100%	2	76.40	99%	3.00
			30.00	18.62	97%	75.49	88%	0.00	100%	2	99.27	99%	3.00
			40.00	15.50	97%	67.09	88%	4.12	100%	2	70.53	99%	3.00
go24	57.2674	20.6501	48.75	17.81	97%	78.15	88%	3.96	100%	2	89.20	99%	3.00
			63.00	14.53	97%	68.57	88%	0.00	100%	2	73.18	99%	3.00
			68.75	14.94	97%	75.64	88%	0.00	100%	2	95.28	99%	3.00
			71.50	7.20	97%	35.06	88%	0.00	100%	2	42.75	99%	3.00
			14.75	26.29	95%	77.36	94%	3.45	96%	1.2	97.53	96%	1.80
			41.75	17.49	95%	83.48	94%	4.17	96%	1.2	102.48	96%	1.80
			69.50	17.04	95%	104.11	94%	4.93	96%	1.2	123.37	96%	1.80
			74.75	12.93	95%	88.29	94%	2.86	96%	1.2	105.97	96%	1.80
go23	57.3003	20.3501	79.75	19.53	95%	92.04	94%	2.62	96%	1.2	114.32	96%	1.80
			88.75	9.57	95%	88.16	94%	1.77	96%	1.2	108.24	96%	1.80
			104.50	10.54	95%	93.55	94%	1.71	96%	1.2	128.86	96%	1.80
			119.00	9.23	95%	171.33	94%	0.00	96%	1.2	192.14	96%	1.80
			130.00	0.00	95%	150.09	94%	0.00	96%	1.2	144.58	96%	1.80
			15.00	24.45	84%	85.51	104%		104%	10.2	90.64	95%	10.20
			33.00	14.24	84%	113.65	104%	0.00	104%	10.2	102.56	95%	10.20
			48.00	30.82	84%	110.01	104%	0.00	104%	10.2	111.96	95%	10.20
			68.00	21.41	84%	78.81	104%	0.00	104%	10.2	83.95	95%	10.20
TF260	56.6334	19.5835	73.00	31.87	84%	114.78	104%	0.00	104%	10.2	141.54	95%	10.20
			78.00	35.24	84%	148.22	104%	0.00	104%	10.2	166.44	95%	10.20
			88.00	27.33	84%	107.88	104%	18.82	104%	10.2	139.51	95%	10.20
			100.00	39.58	84%	178.96	104%	7.63	104%	10.2	175.67	95%	10.20
			130.00	0.00	84%	217.90	104%	0.00	104%	10.2	212.09	95%	10.20
			81.00	17.44	108%	82.24	82%	0.00	84%	5.2	92.82	125%	7.80
			84.00	9.39	108%	57.92	82%	0.00	84%	5.2	61.55	125%	7.80
			85.75	40.98	108%	130.47	82%	0.00	84%	5.2	119.73	125%	7.80
			90.25	19.58	108%	116.55	82%	0.00	84%	5.2	109.46	125%	7.80
TF260	56.6334	19.5835	92.75	9.60	108%	53.45	82%	0.00	84%	5.2	64.86	125%	7.80
			94.75	16.17	108%	131.85	82%	0.00	84%	5.2	138.67	125%	7.80
			99.00	15.68	108%	144.90	82%	0.00	84%	5.2	169.86	125%	7.80
			104.25	8.32	108%	168.29	82%	0.00	84%	5.2	178.79	125%	7.80
			109.75	29.88	108%	109.81	82%	0.00	84%	5.2	147.17	125%	7.80

Table 2.2. Water column chemistry (dissolved O_2, salinity, and MnOx) of the Baltic Sea samples. The Dissolved O_2 and Salinity data were adopted from BCO-DMO data repository (https://www.bco-dmo.org/dataset/935118). The MnOx data were provided by Chadlin Ostrander.

Station	Latitude (°N)	Longitude (°E)	Depth (m)	O_2 (μM)	Salinity (PSU)	MnOx (nM)
go32	56.8336	19.1831	18.50	287.77	7.10	10.26
			26.25	300.85	7.62	69.53
			45.00	327.55	7.74	44.67
			61.75	211.60	8.37	109.47
			66.25	100.61	9.16	122.00
			71.75	16.26	9.82	170.45
			77.25	3.59	10.51	23.72
			82.00	2.52	10.74	29.06
			118.00	1.45	12.01	3.03
go27	56.9504	19.8828	14.75	280.93	7.46	18.53
			50.00	319.97	7.74	66.79
			69.75	199.99	8.57	125.06
			77.50	84.87	9.75	127.99
			90.25	36.36	11.03	268.74
			99.00	21.18	11.29	237.07
			113.00	2.57	11.76	36.69
			124.75	2.06	12.05	6.71
TF271_E_GD	57.2007	20.0312	14.75	286.87	7.42	
			38.75	286.95	7.70	
			72.75	179.77	8.58	
			76.25	98.34	9.26	
			85.75	9.82	6.55	
			102.75	7.95	11.32	
			107.50	7.10	11.45	
			112.00	2.92	11.60	
			115.25	0.94	11.74	
go12 Fårö	58.0004	19.8998	15.00	289.11	7.36	14.63
			35.50	306.97	7.61	44.21
			62.25	187.34	8.17	146.48
			68.00	118.95	8.81	101.88
			72.00	61.50	9.20	98.46
			79.75	3.36	10.12	1.81
			90.50	2.29	10.66	1.47
			110.00	1.58	11.38	2.12
			130.50	1.27	11.86	2.99
go24	57.2674	20.6501	14.75	284.38	7.39	23.99
			30.00	262.64	7.61	51.10

Table 2.2 (cont'd).

			40.00	293.82	7.66	42.63
			48.75	317.90	7.72	46.84
go24	57.2674	20.6501	63.00	224.62	8.28	99.25
			68.75	146.62	8.73	229.67
			71.50	108.83	9.10	206.44
			14.75	286.89	7.38	12.44
			41.75	313.52	7.67	32.69
			69.50	201.11	8.46	216.91
			74.75	95.17	9.25	236.58
go23	57.3003	20.3501	79.75	59.10	9.92	273.80
			88.75	16.73	10.88	390.17
			104.50	10.01	11.35	1351.49
			119.00	1.08	11.74	1701.00
			130.00	0.91	12.08	0.89
			15.00	280.13	7.29	9.59
			33.00	237.04	7.57	68.87
			48.00	317.27	7.72	39.96
			68.00	203.75	8.65	232.25
TF260	56.6334	19.5835	73.00	85.74	9.74	315.99
			78.00	37.00	10.48	1053.61
			88.00	20.45	11.05	1451.85
			100.00	20.81	11.37	2203.05
			130.00	1.25	12.36	4.77
			81.00	38.53	10.75	1926.84
			84.00	24.07	10.92	2788.84
			85.75	20.78	10.99	2617.44
			90.25	33.24	11.13	3749.66
TF260	56.6334	19.5835	92.75	18.13	11.24	2834.35
			94.75	21.61	11.29	2833.48
			99.00	6.73	11.45	3352.03
			104.25	1.13	11.63	2045.37
			109.75	0.91	11.80	85.95

Table 2.3. Iodine speciation measurements of Siders Pond samples using the chromatography and ICPMS method, including column recover rate and instrumental detection limit (D.L.).

Sampling Date	Depth (m)	Iodate (nM)	Recovery (%)	Iodide (nM)	Recovery (%)	DOI (nM)	Recovery (%)	D.L. (nM)	Total I (nM)	Recovery (%)	D.L. (nM)
7/31/2020	0			102.94	102%			2.90			
	0.5			122.88	102%			2.90			
	1			96.64	102%			2.90			
	1.5			109.47	102%			2.90			
	2			135.08	102%			2.90			
	2.5			154.17	102%			2.90			
	3			130.66	102%			2.90			
	3.5			211.51	102%			2.90			
	4			287.69	102%			2.90			
	4.5			320.87	102%			2.90			
	5			297.57	102%			2.90			
	5.5			300.60	102%			2.90			
	6			235.87	102%			2.90			
	6.5			352.15	102%			2.90			
	7			324.01	102%			2.90			
	8			418.21	99%			2.90			
	9			771.40	99%			2.90			
	10			721.71	99%			2.90			
	11			1433.53	99%			2.90			
	12			1307.45	99%			2.90			
9/17/2020	0	20.05	104%	152.3619933	84%	9.81	104%	10.20	205.67	95%	10.20
	0.5	26.91	104%	154.9866593	84%	0.00	104%	10.20	187.12	95%	10.20
	1			152.3733759	99%						
	1.5			91.64733989	99%						
	2			86.54352806	99%						
	2.5			296.4187815	99%						
	3			370.7381874	99%						

Table 2.3 (cont'd).

	3.5	409.2393424	99%
	4	406.1773463	99%
	4.5	373.4785258	99%
	5	298.3618831	100%
	5.5	307.1237831	100%
	6	440.5768886	100%
9/17/2020	6.5	477.1211312	100%
	7	493.715086	100%
	8	576.5315932	100%
	9	945.9042539	100%
	10	1028.077019	100%
	11	1048.775215	100%
	12	1178.067588	100%
	0	184.3370295	101%
	0.5	120.5738137	101%
	1	218.313314	101%
	1.5	168.2634987	101%
	2	255.3319735	101%
	2.5	383.9960666	101%
	3	335.0033286	101%
	3.5	485.0415912	101%
11/6/2020	4	240.3689628	101%
	4.5	433.2120796	101%
	5	399.557746	101%
	5.5	409.8623679	101%
	6	462.6812237	101%
	6.5	489.5486653	101%
	7	493.4421198	101%
	8	532.8004798	101%

Table 2.3 (cont'd)

11/6/2020	9			664.2726516	101%						
	10										
	11			710.6917532	101%						
	12			798.8414158	101%						
7/27/2021	0	24.31	97%	160.5300512	93%	0.00	94%	3.20	169.98	93%	4.80
	0.5	26.08	97%	145.2998071	93%	0.00	94%	3.20	174.99	93%	4.80
	1	29.96	94%	166.9499841	95%	10.66	96%	1.20	205.08	96%	1.80
	1.5	28.22	94%	202.7012212	95%	6.65	96%	1.20	240.84	96%	1.80
	2	23.65	101%	224.0403327	94%	12.49	95%	7.60	253.18	98%	11.20
	2.5	15.85	101%	234.8654746	94%	0.00	95%	7.60	251.79	98%	11.20
	3	12.12	89%	230.8075768	96%	0.00	100%	1.90	259.97	99%	2.90
	3.5	18.98	89%	240.3787833	96%	2.43	100%	1.90	182.22	99%	2.90
	4	8.41	89%	269.1341681	96%	2.34	100%	1.90	270.11	99%	2.90
	5	11.96	89%	261.7474195	96%	0.00	100%	1.90	286.42	99%	2.90
	6	0.00	91%	210.8564566	106%	0.00	102%	4.80	221.87	104%	7.00
	7	0.00	91%	246.1979916	106%	0.00	102%	4.80	251.32	104%	7.00
	8	0.00	92%	316.412527	108%	0.00	109%	2.00	289.47	107%	3.00
	9	0.00	92%	364.0214042	108%	0.00	109%	2.00	319.98	107%	3.00
	10	0.00	92%	414.5878552	108%	0.00	109%	2.00	378.53	107%	3.00
	11	0.00	0.80	259.293652	1.4			3.80			
	SP inlet	6.06	0.80	40.4670838	1.4			3.80			
	Spstream	11.75	0.80	68.40698984	1.4			3.80			

Table 2.4. Water column chemistry (dissolved O_2, salinity, and MnOx) of Siders Pond samples. Data was provided by Colleen Hansel.

Sampling Date	Depth (m)	Salinity (PSU)	Sulfides (μM)	NH_4^+ (μM)	O_2 (μM)	MnOx (nM)
7/31/2020	0	8.54	0.00	0.69	233.44	436.06
	0.5	8.97	0.00	1.69	235.00	384.31
	1	9.50	0.00	0.97	262.81	368.07
	1.5	11.12	0.00	0.78	315.94	343.63
	2	12.84	0.00	1.23	340.31	261.13
	2.5	13.89	0.00	4.41	303.13	189.71
	3	14.55	0.00	8.10	223.75	212.48
	3.5	14.72	0.00	21.50	134.69	85.16
	4	15.27	0.00	32.58	82.19	49.93
	4.5	15.37	0.00	66.98	28.75	37.98
	5	15.85	95.25	105.25	19.06	37.90
	5.5	15.92	0.00	97.05	15.63	0.00
	6	16.37	121.91	79.28	15.00	0.00
	6.5	16.55	0.00	107.98	14.38	0.00
	7	16.55	229.45	136.69	14.06	0.00
	8	17.16	384.24	220.07	12.50	0.00
	9	17.28	3846.83	306.18	10.63	0.00
	10	17.17	2483.26	405.96	15.63	0.00
	11	16.94	4278.20	277.47	0.00	0.00
	12	17.02	2950.78	698.47	0.00	0.00
9/17/2020	0	9.99		2.30	303.13	1737.44
	0.5	9.99		4.07	293.75	1557.12
	1	9.99	0.05	3.61	284.69	1673.61
	1.5	10.21		3.53	240.31	1497.31
	2	10.78		7.06	171.25	1508.71
	2.5	11.58		31.45	68.75	559.63
	3	14.17	0.26	368.60	26.25	97.18
	3.5	14.90		485.64	23.75	0.00
	4	15.19	0.03	137.96	20.63	0.00
	4.5	15.48		70.83	23.75	0.00
	5	15.89	0.27	167.22	20.31	0.00
	5.5	16.25		401.30	18.44	0.00
	6	16.38	0.28	170.66	19.06	0.00
	6.5	16.63		232.62	16.25	0.00
	7	16.72	0.79	616.44	17.50	0.00

Table 2.4 (cont'd).

	8	16.92	0.76	308.35	15.94	0.00
	9	17.39	1.87	628.49	11.88	0.00
9/17/2020	10	17.30	2.36	838.48	9.69	0.00
	11		2.25	483.91		
	12		3.17	373.76		
	0	8.98		16.77	360.00	144.01
	0.5	9.00		6.98	344.38	154.35
	1	9.21	0.02	13.00	340.94	149.78
	1.5	9.27		10.35	317.50	131.68
	2	10.80	0.01	64.19	142.81	40.86
	2.5	13.87		48.46	24.06	6.57
	3	14.54	0.51	54.80	21.56	23.33
	3.5	14.88	0.62	206.50	20.00	7.71
	4	14.96	0.44	203.80	17.50	7.06
	4.5	15.18		147.20	16.56	0.00
11/6/2020	5	15.35	0.42	166.06	15.31	0.00
	5.5	15.93		219.97	14.69	0.00
	6	16.16	0.70	184.93	13.75	0.00
	6.5	16.39		264.45	13.44	0.00
	7	16.56	0.61	296.79	12.19	0.00
	8	16.82	1.37	264.45	10.31	0.00
	9	17.44	1.56	261.75	10.63	0.00
	10	17.62	1.47	403.26	10.31	0.00
	11		1.77	335.88		
	12		1.86	364.18		
	0	7.67			325.00	
	0.5	7.90			318.44	
	1	10.16			330.00	
	1.5	11.20			163.75	
	2	11.70			128.44	
	2.5	12.08			78.13	
7/27/2021	3	12.15			54.38	
	3.5	12.68			51.88	
	4	12.78			68.44	
	5	13.33			44.06	
	6	13.58			43.75	
	7	14.05			42.81	
	8	14.36			43.44	

Table 2.4 (cont'd).

	9	14.40	54.69
	10	14.39	8.44
7/27/2021	11		
	SP inlet		
	Spstream		

CHAPTER 3: CHARACTERIZING THE MARING IODINE CYCLE AND ITS RELATIONSHIP TO OCEAN DEOXYGENATION IN AN EARTH SYSTEM MODEL

3.1 Abstract

Iodine abundance in marine carbonates (measured as an elemental ratio with calcium – I/Ca) is of broad interest as a proxy for local/regional ocean redox. This connection arises because the speciation of iodine in seawater – the balance between iodate (IO_3^-) and iodide (I^-) – is sensitive to the prevalence of oxic vs. anoxic conditions. However, although I/Ca ratios are increasingly commonly being measured in ancient carbonate samples, a fully quantitative interpretation of this proxy requires the availability of a mechanistic interpretative framework for the marine iodine cycle that can account for the extent and intensity of ocean deoxygenation in the past. Here we present and evaluate a representation of marine iodine cycling embedded in an Earth system model ('cGENIE') against both modern and paleo observations. In this framework, we account for IO_3^- uptake and release of I^- through the biological pump, the reduction of ambient IO_3^- to I^- in the water column, plus the re-oxidation of I^- to IO_3^-. We develop and test a variety of different plausible mechanisms for iodine reduction and oxidation transformation and contrast model projections against an updated compilation of observed dissolved IO_3^- and I^- concentrations in the present-day ocean.

By optimizing the parameters controlling previously proposed mechanisms involved in marine iodine cycling, we find that we can obtain broad matches to observed iodine speciation gradients in zonal surface distribution, depth profiles, and oxygen deficient zones (ODZs). However, we also identify alternative, equally well performing mechanisms which assume a more explicit mechanistic link between iodine transformation and environment – an ambiguity that highlights the need for more process-based studies on modern marine iodine cycling. Finally, to

help distinguish between competing representations of the marine iodine cycle and because our ultimate motivation is to further our ability to reconstruct ocean oxygenation in the geological past, we conducted 'plausibility tests' of different model schemes against available I/Ca measurements made on Cretaceous carbonates – a time of substantially depleted ocean oxygen availability compared to modern and hence a strong test of our model. Overall, the simultaneous broad match we can achieve between modelled iodine speciation and modern observations, and between forward-proxy modelled I/Ca and geological elemental ratios, supports the application of our Earth system modelling in simulating the marine iodine cycle to help interpret and constrain the redox evolution of past oceans.

3.2 Introduction

Dissolved Iodine (I) in seawater is redox sensitive and as such, is a potential invaluable delineator of past ocean deoxygenation. This arises directly from: (1) observations that the oxidized form of iodine (iodate, IO_3^-) is reduced to iodide (I^-) under low oxygen conditions, and (2) that IO_3^- in seawater is incorporated into carbonate lattice during precipitation in proportion to its seawater abundance (whilst I^- is not) (Lu et al., 2010; Zhang et al., 2013; Podder et al., 2017; Kerisit et al., 2018; Hashim et al., 2022). As a result, past ocean IO_3^- concentrations can be recorded in coeval carbonates as I/Ca ratios, with the potential for carbonate I/Ca to reflect the redox variation of the ancient seawater (Lu et al., 2010). Indeed, the I/Ca ratio in marine carbonates is already being applied widely as a paleoredox proxy, with studies employing it to explore variations in the dissolved oxygen ($[O_2]$) concentration of seawater throughout much of Earth history, from the Archean and through the Cenozoic (Lu et al., 2010, 2016, 2018; Hardisty et al., 2014; Zhou et al., 2015; Edwards et al., 2018; Shang et al., 2019; Bowman et al., 2020; Uahengo et al., 2020; Liu et al., 2020; Wei et al., 2021; Pohl et al., 2021; Ding et al., 2022; Yu et al., 2022;

Fang et al., 2022; Tang et al., 2023). However, realizing the full potential for I/Ca to provide critical insights into how the oxygenation of the ocean has evolve through time, as well as the causes and biological/ecological consequences of this, requires that we have an adequate understanding, not only of carbonate IO_3^- incorporation, but of the dynamics of the marine iodine cycle in general.

Considerable progress has been made over the past few decades towards the goal of understanding the marine iodine cycle. Iodine has a relatively long residence time in the ocean (~300 kyr; Broecker and Peng, 1983) leading to its concentration being relatively constant throughout the global ocean (at around 500 nM) (Elderfield & Truesdale, 1980; Truesdale et al., 2000; Chance et al., 2014). However, although the total concentration of dissolved iodine is relatively invariant, the two most abundant species of dissolved iodine in the ocean, IO_3^- and I^-, vary relative to each other depending on the environment. Today, IO_3^- is generally the dominant iodine species in oxygenated regions of the ocean where it represents total iodine nearly quantitatively below the euphotic zone. Within the euphotic zone, the concentration of I^- generally increases in association with release during phytoplankton growth and senescence (Hepach et al., 2020). Within ODZs, IO_3^- is reduced to I^- – but not always quantitatively so – and hence is present only at relatively low concentrations while I^- is abundant (Wong & Brewer, 1977; Rue et al., 1997; Truesdale et al., 2000; Farrenkopf & Luther, 2002; Truesdale et al., 2013; Cutter et al., 2018; Rapp et al., 2019; Moriyasu et al., 2020; Rapp et al., 2020).

Although IO_3^- is generally depleted in low-$[O_2]$ settings, the relationship between seawater $[O_2]$ and $[IO_3^-]$ is not simple and is not currently well understood. Recently published observations from ODZs in the ocean reveals that the relationship between dissolved $[O_2]$ and $[IO_3^-]$ is not linear, but instead it is possible that there is a certain $[O_2]$ or related redox threshold associated with triggering IO_3^- reduction (Chapman, 1983; Rue et al., 1997; Farrenkopf & Luther, 2002; Cutter et

al., 2018; Moriyasu et al., 2020). Dissimilatory IO_3^- reducing bacteria, as well as abiotic reduction with sulfide and dissolved Fe, have been identified within ODZs (Councell et al., 1997; Farrenkopf et al., 1997; Jiang et al., 2023). In addition, slow oxidation-reduction kinetics (Tsunogai, 1971; Hardisty et al., 2020; Schnur et al., 2024) imply the likelihood that in situ iodine signals could be integrated across large-scale physical oceanography processes – including ocean currents and mixing between water masses (Hardisty et al., 2021), and meaning that iodine speciation reflects regional rather than strictly *in situ* redox conditions (Lu et al., 2020a). Non-redox related processes, such as phytoplankton-mediated IO_3^- reduction and organic matter remineralization also exert controls on iodine speciation in the water column (Figure 3.1; Elderfield and Truesdale, 1980; Wong et al., 1985; Luther and Campbell, 1991; Hepach et al., 2020). Therefore, it is difficult to infer water column redox simply based on iodine speciation without considering these interacting physical and biological effects.

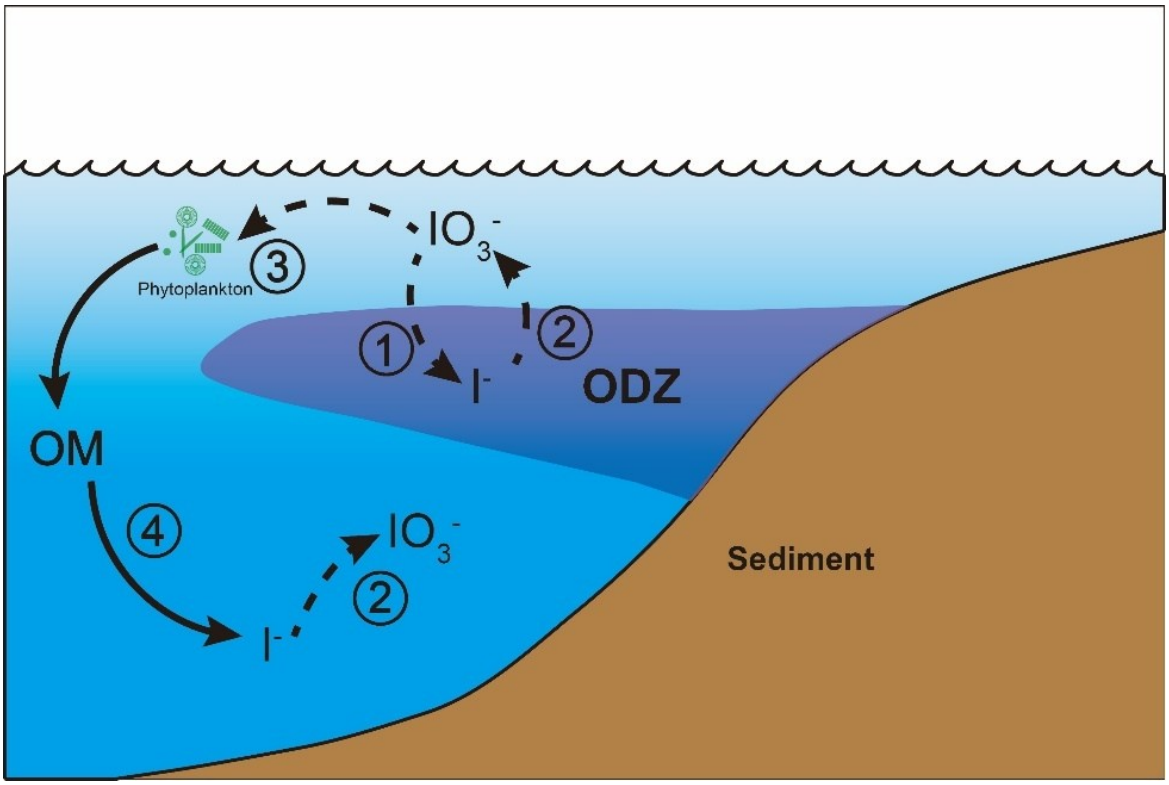

Figure 3.1. The iodine cycle in marine oxygen deficient zones (ODZ) in cGENIE including

Figure 3.1 (cont'd).
IO_3^- reduction to I^-, (2) re-oxidation of I^- to IO_3^-, (3) photosynthetic IO_3^- update by phytoplankton, and (4) I^- releasement from organic matter (OM) through remineralization. The detailed oxidation-reduction options are described in Section 3.2.2 and Table 3.1. Dashed arrows indicate variable processes during ensemble simulations.

Aside from the uncertainties associated with IO_3^- reduction, it is notable that the oxidants responsible for IO_3^- formation during I^- re-oxidation are currently unknown, only that it is unlikely to be free O_2, which is not thermodynamically favorable to oxidize I^- (Luther et al., 1995). A recent thermodynamic review indicates that reactive oxygen species (ROS) such as hydrogen peroxide and OH radicals can fully oxidize I^- to IO_3^-. Iodide oxidation to IO_3^- is a 6-electron transfer and other ROS, such as superoxide, are only thermodynamically favorable to catalyze partial oxidation to intermediates (Luther, 2023). These ROS species have heterogenous distributions and ambient ocean concentrations that are typically relatively low compared to iodine, supporting the likelihood of temporally or spatially isolated high I^- oxidation rates despite of overall extremely slow rates (Schnur et al., 2024). Additional support for spatially or temporally heterogenous I^- oxidation rates comes from recent experimental observations of IO_3^- production from I^- in nitrifying cultures (Hughes et al., 2021). Nitrification (oxidation of NH_4^+ to NO_2^- (and NO_3^-)) rates vary globally, with the highest values occurring in ODZs and the deep chlorophyl maximum (summarized in Table 2 of Hughes et al., 2021). Regardless, nitrification or other specific mechanisms have yet to be linked directly to I^- oxidation under normal marine conditions, leaving open the question of rates and locations of I^- oxidation.

Despite a growing understanding of I/Ca variations through geologic time, it remains challenging to determine the mechanisms responsible for controlling the spatiotemporal patterns of marine [IO_3^-] and how these are linked to seawater oxygen and there have only been a few attempts to date to model the marine iodine cycle. In a recent publication, a model was developed to simulate modern ocean surface I^- distributions, with the aim of being able to improve

tropospheric ozone models (Wadley et al., 2020). This particular model was based around a relatively high horizontal ocean resolution (1° grid size) with a 3-layer vertical upper water column. Iodine biogeochemical cycling was coupled with the nitrogen cycle, with the surface I^- distribution sensitive to biological and hydrological factors including primary productivity, I:C ratio, oxidation, mixed layer depth, advection, and freshwater flux. Because the Wadley et al., (2020) model was specifically focused on near-surface processes within the upper 500 m, it did not consider processes occurring within ODZs and hence is not directly applicable to questions concerning the controls on I/Ca ratios. In contrast, a second model-based study deliberately targeted paleoceanographic questions and incorporated an iodine cycle including redox-controlled biogeochemical reactions into the 'cGENIE' Earth system model (Lu et al., 2018). The advantage for paleo studies afforded by this particular approach is that the cGENIE model can take into account different continental configurations, non-modern atmospheric composition (pO_2, pCO_2), and other boundary conditions that may have differed on ancient Earth relative to today (Ridgwell et al., 2007; Reinhard et al., 2016; Remmelzwaal et al., 2019; Boscolo-Galazzo et al., 2021; Pohl et al., 2022; Reinhard & Planavsky, 2022).

Here, we calibrate the iodine cycle within the cGENIE Earth System model to provide a mechanistic framework for interpreting ancient I/Ca variations. In this study, we build on the work of Lu et al., (2018) and further develop and test a series of new potential parameterizations for water column iodine oxidation and reduction (in addition to reduction and transport associated with the biological pump). We also developed 3 criteria for assessing the model: (1) Statistical evaluation using the 'model skill score' (M-score) (Watterson, 1996) – a non-dimensional measure calculated using location-dependent comparisons between the model and an iodine ocean observation data compilation. (2) Graphical comparison of modeled and observed iodine across 3

illustrative iodine speciation gradients (depth profiles from multiple ocean basins, latitudinal transects of surface waters, and across transects of the Eastern Tropical North Pacific oxygen minimum zone (Moriyasu et al., 2020)). (3) Model applicability to ancient settings by comparing (also using the M-score) projections of ocean surface I/Ca with published I/Ca data from the Cretaceous (Zhou et al., 2015).

3.3 Model description

3.3.1 The cGENIE Earth system modelling framework

cGENIE is a class of model known as an 'Earth system model with intermediate complexity' (EMIC) – a global climate-carbon cycle model that simplifies one or more (typically physical climate) components of the Earth system. In the case of cGENIE, ocean circulation is solved for on a relatively low-resolution grid (here: an equal area 36×36 grid, which equates to 10° in longitude and latitude increments from 3° near the equator to 20° near the poles, and with 16 non-equally spaced vertical levels). This is coupled to a 2D energy-moisture-balance-model (EMBM) and a 2D dynamic-thermodynamic sea-ice model. The physics are described in (Edwards & Marsh, 2005; Marsh et al., 2011).

Representation of the primary factors controlling the oceanic iodine cycle – specifically, biological productivity, remineralization, and water column redox – follow Crichton et al., (2021). In this configuration, the rate of organic matter export from the ocean surface is calculated based on just a single nutrient (phosphate) control (together with modifiers reflecting ambient light, sea-ice cover, and temperature) and assumes a Redfield-ratio stoichiometry (1:106) with carbon (Figure 3.1). Organic matter is partitioned into particulate (POM) (33% of total export) and dissolved forms (DOM) (67%), with the former sinking down through the water column where it is progressively remineralized at a rate scaling with ambient temperature (described in Crichton et

al., 2021 and Boscolo-Galazzo et al., 2021). When dissolved oxygen nears depletion, sulphate (SO_4^{2-}) is assumed to be consumd as an electron acceptor to support the remineralization of organic matter (both POM and DOM). The rate of POM remineralization in the water column is governed only by ambient temperature which, in conjunction with a prescribed sinking rate, deterines the vertical distribution of solute release and oxidant consumption. The relative availablity of dissolved O_2 vs. SO_4^{2-} determines the proportion of organic matter degraded by each electron acceptor. In this, the relative consumption of SO_4^{2-} is goverened by a SO_4^{2-} half-saturation limitation term as well as a dissolved oxygen (O_2) inhibition term, while oxic resperation of organic matter is restricted by an [O_2] half-saturaion limitation term (described in Reinhard et al., 2020). Sulphate can hence be consumed even before dissolved oxygen can become fully depleted. For DOM, a decay constant (here: 0.5 years) determines the total fraction that is remineralized per unit time. It should be noted that currently, there is no published nitrogen cycle in the cGENIE model framework and we do not consider nitrate reduction as part of the redox cascade here.

3.3.2 Marine iodine cycling in cGENIE

In the cGENIE model, iodine is present in three reservoirs: IO_3^- and I^- in the water column, and I^- incorporated in POM (and DOM). We then consider four processes that transfer iodine between these reservoirs (summarized in Figure 3.1): (1) IO_3^- reduction in the water column, (2) I^- oxidation (also in the water column), (3) photosynthetic IO_3^- uptake (and assumed intercellular reduction to I^-), and (4) I^- release to seawater during the remineralization of POM (and DOM). As dissolved species, IO_3^- and I^- are physically transported and mixed through ocean circulation (as is I incorporated into DOM), whereas iodine in POM settles vertically through the water column. This is the same overall framework used by Lu et al., (2018). In this paper we re-assess this framework against an updated compilation of observed iodine speciation in the modern ocean and

develop and test alternative representations of IO_3^- reduction (process (1), 'threshold', 'inhibition', and 'reminSO4lifetime') and I^- re-oxidation (process (2), 'lifetime', 'Fennel', and 'reminO2lifetime'). Although we describe all 5 different parameterizations below for completeness and a number of different permutations of 3 IO_3^- reduction and 3 I^- re-oxidation processes (presented in S.I.), in this paper we will focus primarily on a single reduction parameterization ('threshold') in combination with the 3 different re-oxidation schemes.

3.3.2.1 IO_3^- reduction schemes

'threshold'. In the numerical scheme of Lu et al., (2018), when $[O_2]$ falls below a set concentration threshold, IO_3^- is immediately and quantitatively reduced to I^- (thereafter, we term this IO_3^- reduction parameterization 'threshold').

'inhibition'. The 'inhibition' scheme links the IO_3^- reduction rate with the ambient O_2 concentration. Following the formulation for the rate of SO_4^{2-} reduction in Reinhard et al., (2020), we apply an oxygen inhibition term governed by a half-saturation constant. In devising this scheme, we note that while IO_3^- reduction rates have been determined experimentally, the quantitative relationship with $[O_2]$ (or other parameters) is unknown. The IO_3^- reduction under 'inhibition' is mathematically described as:

$$d[IO_3^-]/dt = [IO_3^-] \times k_{red} \times \frac{k_{O_2}}{k_{O_2}+[O_2]} \quad (1)$$

in which k_{red} is the maximum first-order reduction rate of IO_3^-, and k_{O2} is the half-saturation constant of O_2.

'reminSO4lifetime'. Reduced sulfur (e.g. sulfides) is also suspected to play an important role in IO_3^- reduction in seawater, especially in the sulfidic zones (Wong & Brewer, 1977; Jia-zhong & Whitfield, 1986; Luther & Campbell, 1991; Truesdale et al., 2013). We therefore devise a scheme ('reminSO4lifetime') that scales a nominal 'lifetime' for IO_3^- with the rate of SO_4^{2-}

reduction in the model. This has the effect of increasing the rate of IO_3^- reduction (a shorter lifetime) under conditions of higher sulphate reduction rates and hence lower ambient oxygen concentrations and/or higher rates of organic matter degradation:

$$d[\mathrm{IO_3^-}]/dt = [IO_3^-] \times \frac{1}{\tau_{sul}} \times d[\mathrm{SO_4^{2-}}]/dt \quad (2)$$

in which τ_{sul} defines the rate constant parameter linking the IO_3^- and SO_4^{2-} reduction, while the $d[SO_4^{2-}]$ is amount of SO_4^{2-} reduced during each model timestep.

3.3.2.2 I^- oxidation schemes

'lifetime'. In Lu et al., (2018), I^- is oxidized to IO_3^- following first-order kinetics regardless of ambient O_2 (scheme 'lifetime'). In this scheme, I^- oxidation follows the first-order reaction kinetics:

$$d[\mathrm{I^-}]/dt = [\mathrm{I^-}] \times \frac{1}{\tau} \quad (3)$$

where τ is the lifetime of I^- in seawater.

'Fennel'. Given the overlapping redox potential between I and N (e.g. Rue et al., 1997; Cutter et al., 2018), we explore the potential for a link between areas of I^- and nitrification. To simulate this, we devise an alternative 'Fennel' scheme, in which I^- oxidation rates vary as a function of ambient O_2, increasing with ambient O_2 concentrations towards some hypothetical maximum value following Michaelis–Menten kinetics (Fennel et al., 2005). In Fennel et al., (2005), this parameterization was originally devised for ammonia reoxidation. The form of this response is defined by the maximum reaction rate and O_2 half-saturation constant (Fennel et al., 2005):

$$d[\mathrm{I^-}]/dt = [\mathrm{I^-}] \times k_{ox} \times \frac{[O_2]}{k_{fenn}+[O_2]} \quad (4)$$

in which k_{ox} defines the maximum rate constant of I^- oxidation, while k_{fenn} is the O_2 half-saturation constant.

'reminO2lifetime'. Finally, in 'reminO2lifetime', we associate I^- oxidation with O_2 consumption during remineralization. The logic behind this parameterization is the recent observation of I^- oxidation to IO_3^- catalyzed by bacteria, perhaps in association with ammonia oxidation (Hughes et al., 2021). Although the nitrogen cycle is not currently included in cGENIE, the NH_4^+ oxidation can be scaled to OM remineralization (Martin et al., 2019) and hence to O_2 consumption during remineralization. Under 'reminO2lifetime', the lifetime of I^- oxidation is inversely linked to O_2 consumption so that faster remineralization – which in the ocean leads to more intensive NH_4^+ oxidation – enhances I^- oxidation. This I^- oxidation scheme follow this equation:

$$d[\mathrm{I}^-]/dt = [\mathrm{I}^-] \times \frac{1}{\tau_{O2}} \times d[\mathrm{O}_2]/dt \quad (5)$$

where τ_{O2} is the rate constant parameter and $d[O_2]$ is the O_2 consumption during remineralization during a single timestep in the model.

3.3.2.3 Biological reduction pump

The final pair of coupled processes in the marine iodine cycle framework concerns the processing of iodine directly through the biological pump. Phytoplankton-absorbed iodine is stored in the cell as IO_3^-, I^-, or other forms, followed by release during senescence (Hepach et al., 2020). While there is some uncertainty as to whether IO_3^- reduction is assimilatory or dissimilatory (Hepach et al., 2020), we adopt a comparable approach to nitrogen cycling (sequence: NO_3^- uptake, N incorporation into organic matter, remineralization and release as the reduced NH_4^+ form). We assume that IO_3^- is assimilated by phytoplankton and incorporated into POM during photosynthesis (Elderfield & Truesdale, 1980) and released as I^- during remineralization and/or cell senescence (Wong et al., 1985, 2002; Hepach et al., 2020). cGENIE simulates these processes via an assumed 'Redfield-ratio' of iodine to carbon (I:C ratio) in OM. We note that while the value

of I:C can be adjusted in the model, it is currently assumed fixed in value throughout the ocean. We discuss the merits of an optimized and uniform I:C compared to variable I:C (e.g., Wadley et al., 2020) in more detail in the Discussion.

3.3.3 Model-data evaluation

For evaluating the marine iodine cycle in the cGENIE model, we compiled oceanic iodine observation data from the literature (Figure 3.2; Table 3.6). Our dataset builds on the compilation of Chance et al., (2019), which was used to calibrate the Wadley et al., (2020) model, but includes more recent publications (referenced in Table 3.6) and is also expanded to include the deep ocean and ODZ data. To avoid the influence of freshwater dilution and recycled iodine from the sedimentary flux, we applied a filter which only keeps the measurements with total iodine (or IO_3^- plus I^-) between 450 nM and 550 nM in the dataset. Note that the I^- measurements from the GP16 cruise in the ETSP are not included for the comparison because of potential method considerations (see Cutter et al., 2018 and Moriyasu et al., 2023). After filtering, the data were gridded to the cGENIE model grid (provided as .nc files in Supplementary Material).

We used the model skill measure (M-score) (Watterson, 1996) to assess the performance of the marine iodine cycle in cGENIE compared to the gridded data. For each iodine speciation (hereby IO_3^- and I^-), a M-score value is calculated through comparing gridded observations versus model results in each corresponding grid (Figure 3.2). The synthesized M-score for iodine of each model experiment is calculated through averaging those for both I^- and IO_3^-. The higher the M-score value the better the model-data performance.

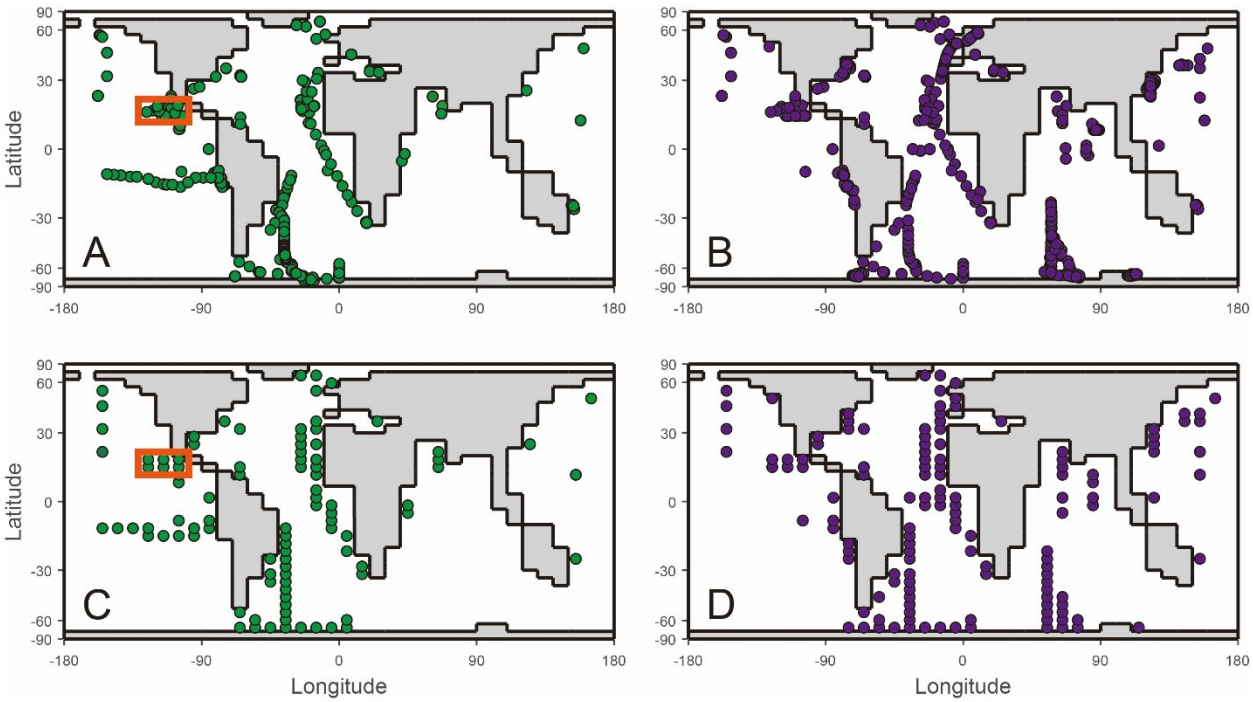

Figure 3.2. Ocean surface (uppermost ~81 m corresponding to the depth of the surface layer in the cGENIE model) sampling locations of IO_3^- (A) and I^- (B) field observations after data filtration for freshwater and sediment fluxes. The filtered observations were then gridded according to the cGENIE 36×36×16 framework for model-data comparison of IO_3^- (C) and I^- (D). The orange boxes in A and C highlight the grids of the oxygen deficient zone transect shown in Figure 3.7.

3.3.4 Sensitivity analyses and model implementation

Because the relative roles of IO_3^- reduction, I^- oxidation, and the shuttling of iodine through the biological pump are uncertain, we calibrate the parameters controlling these processes in cGENIE by creating an ensemble of different parameter value combinations controlling IO_3^- reduction and I^- oxidation in a 2D regularly spaced grid and then repeat the same 2D parameter ensemble for different assumptions regarding the biological pump (I:C) (Table 3.1, Figure 3.4). We focus on parameter ensembles testing the 3 different parameterizations for I^- oxidation (but only 'threshold' as the IO_3^- reduction parameterization) – 'lifetime-threshold', 'fennel-threshold', and 'reminO2lifetime-threshold'. (The results of 2 additional parameterization-combinations – 'lifetime-reminSO4lifetime', and 'lifetime-inhibition' are given in Table 3.3.) We discuss the reasons for selecting these specific parameterization-combinations in the Discussion

section. Finally, to explore whether the cGENIE model-simulated dissolved oxygen distribution imparts any particular bias to the tuned iodine cycle, we repeated the model ensembles for each of the 3 parameterization-combinations but continually restoring the 3D pattern of $[O_2]$ in the model to that of the World Ocean Atlas 18 (WOA18) climatology (Garcia *et al.*, 2018). The model ensembles are summarized in Table 3.1.

Each ensemble member was run for a total of 2,000 years and each starts from the same initial state, which was an experiment run for 10,000 years to equilibrium using a random set of iodine parameters within the ranges in Table 3.1. Running each ensemble member for 2000 years minimizes the CPU time but was also found to be more than sufficient to allow iodine inventories to equilibrate to new steady states. The output of each ensemble member is then statistically compared to our observational database.

3.3.5 Evaluation against geological observations

Parameter tuning, and the ability to reproduce modern observations, does not by itself offer any guarantee that spatial patterns are being simulated for the 'correct' mechanistic reason. This is even more pertinent in the context of the application of a modern-tuned model to paleoredox reconstruction. To quantify to what degree the calibrated parameterization-combinations for the modern marine iodine cycle have predictive power in the geological past, we carried out a deep-time plausibility test.

For the paleo plausibility test, we adopted the Cretaceous, pre-OAE2 (ca. 93 Ma) configuration (continental arrangement and ocean bathymetry, wind stress and velocity, and zonal average planetary albedo boundary conditions) of Monteiro et al., (2012). We choose this particular geological interval because the controls on ocean redox have been previously evaluated using the cGENIE model (Monteiro et al., 2012; Hülse et al., 2019), the oceanic conditions are much more

extensively dysoxic and anoxic than present-day and hence represent a relatively severe test of the model iodine cycle, and a number of I/Ca proxy measurements are available (Zhou et al., 2015). In order to evaluate the same configuration of the iodine cycle as optimized in this study, we also substituted the temperature-independent representation of biological export production and fixed remineralization profile of POM in the water column (i.e., Ridgwell et al., (2007)) for the temperature-dependent scheme of Crichton et al., (2021) used in our modern calibration. However, in substituting the biological pump scheme in the model we alter the ocean redox landscape compared with Monteiro et al., (2012). We therefore explore a range of different assumptions regarding the ocean PO_4 inventory at the time as a means of generating a range of different plausible states of ocean oxygenation. In this, we test: 0.2, 0.4, 0.6, 0.8, 1.0, and 1.5 times the mean modern concentration (2.15 mM). We run the model with each of the best-fit (highest M-score) sets of parameter values associated with the main 3 different parameterization-combinations (2 additional parameterization-combinations were run and are presented in SI), and for each of the varying PO_4 inventory assumptions, and for 10,000 years to steady-state. Major cation concentrations were adjusted to a value more representative of the earlier Cenozoic (18.2 mM [Ca^{2+}], 29.9 mM [Mg^{2+}]) (Panchuk et al., 2008) although that does not affect the calculation of carbonate I/Ca values. In the absence of independent constraints on the Cretaceous total dissolved iodine inventory, we assumed this to be modern (500 nM mean concentration).

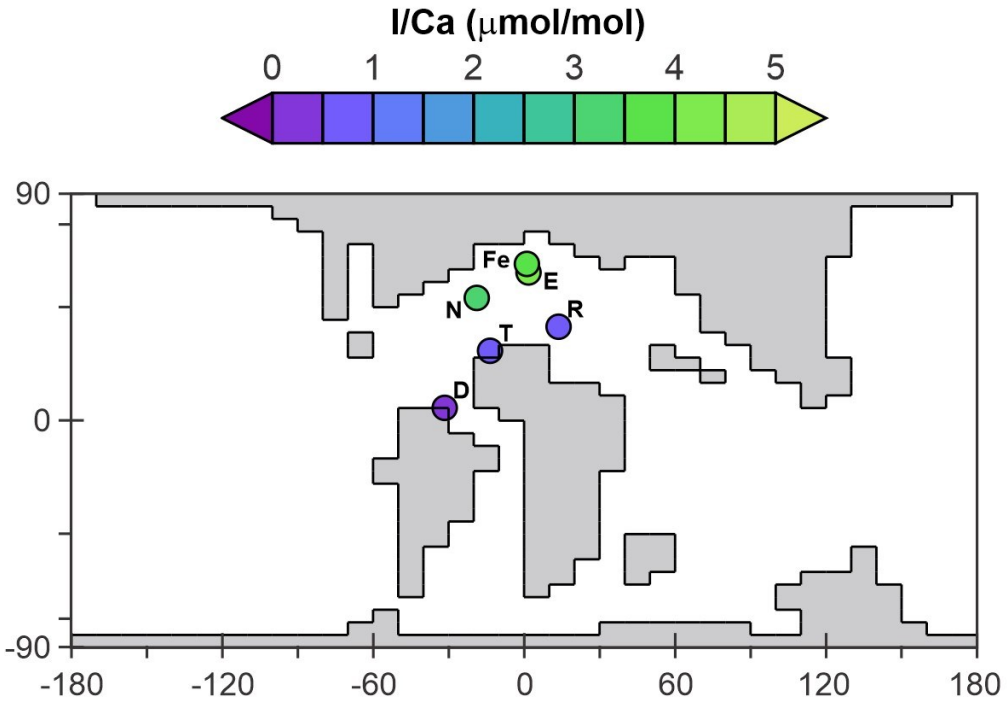

Figure 3.3. The continental setting during the Cretaceous OAE2 (Cenomanian - Turonian) in cGENIE. The colored dots represent averaged pre-OAE2 I/Ca measurements from each of the sections. D = Demerara Rise; E = Eastbourne; Fe = South Ferriby; N = Newfoundland; R = Raia del Pedale; T = Tarfaya.

The I/Ca data used for comparison with the model come from 6 sections (Zhou et al., 2015, Figure 3.3, listed in Table 3.5). The pre-OAE2 I/Ca baseline value from each section is estimated through averaging the pre-CIE I/Ca measurements from Table S1 of Zhou et al., (2015). Diagenesis of carbonate hosted I/Ca tends to lower the primary values (Hardisty et al., 2017). However, such an offset is hard to quantitatively predict based on our current knowledge. In addition, according to Zhou et al., (2015), from which we adopted the I/Ca data, most of the sections only suffered minor diagenesis. To simplify the Cretaceous I/Ca-to-IO_3 conversion, we regard the measured I/Ca as primary and acknowledge there is potential uncertainty. For quantitative comparison between the model and the I/Ca data, we create an empirically derived forward proxy model for I/Ca. In this, we took the simulated concentration of IO_3^- and Ca^{2+} in the

ocean surface layer of the model at every ocean grid point, and applied the temperature-dependent linear incorporation relationship derived from inorganic calcite synthesis experiment of Zhou et al., (2014), to estimate I/Ca. Specifically, the distribution coefficient (K_D) between I/Ca and [IO_3] (K_D = (I/Ca)/ [IO_3]) shows linear dependency with temperature (Figure S3 in Zhou et al., 2014). For our Cretaceous model calibration, we apply the K_D based on local temperature (at each grid point associated with a sampling section) simulated by cGENIE. Beyond temperature, we acknowledge that IO_3^- incorporation into carbonate lattice through substitution $IO_3^- + Na^+ \leftrightarrow CO_3^{2-} + Ca^{2+}$ is controlled by [Na^+], [CO_3^{2-}], and [Ca^{2+}] (Podder et al., 2017). However, either quantifying these ions during the Cretaceous seawater or quantitative calculation of ion substitution dynamics requires further constraints. Although uncertainties are inevitable, we assume our temperature-controlled [IO_3^-]-to-I/Ca conversion based on current quantitative knowledge meets the requirement for Cretaceous model-data comparison. We extracted simulated I/Ca values from the model grid points corresponding to the sections reported by Zhou et al., (2015) and calculated the M-score.

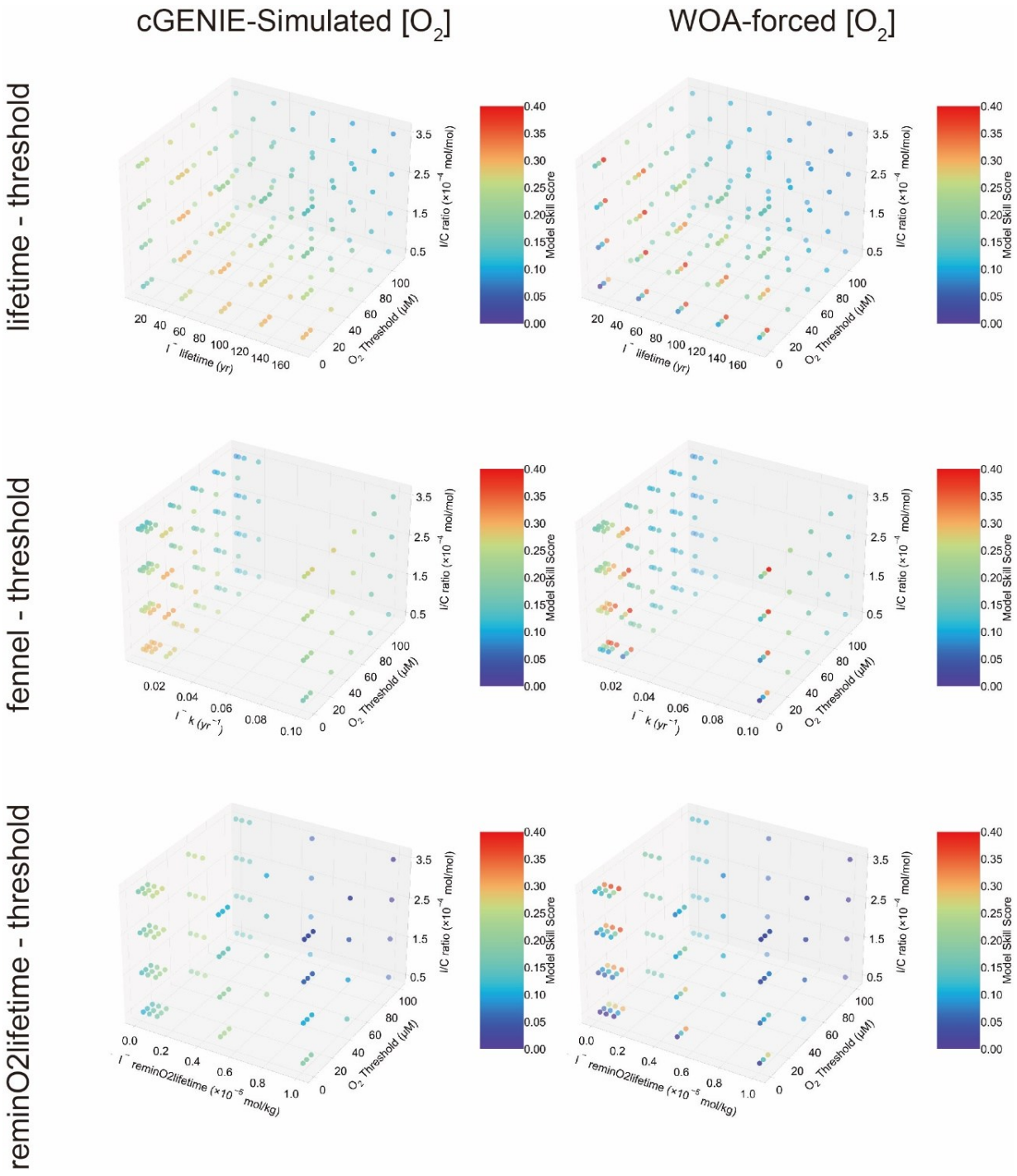

Figure 3.4. The three-dimensional model skill score array of the experiment ensembles.

Table 3.1. The cGENIE iodine redox options and the associated range of parameters of these options. The detailed introduction of each parameter is described in section 3.2.2 and the plausibility of these parameter ranges is discussed in 3.4.1.1. Note that the oxidation rate constant k in 'Fennel' is in unit of $year^{-1}$ in the model configuration, which is the reciprocal of the 'lifetime'. A detailed table containing all considered parameterization ranges can be found in Table 3.3.

Parameterization-combination		Iodine oxidation parameters			Iodine reduction parameters	I:C ratio (× 10^{-4} mol/mol)
		'lifetime' (years)	'reminO2lifetime' (× 10^{-5} mol/kg)	'Fennel' (Inhibition constant/ µM O_2)	'threshold' (µM O_2)	
'lifetime-threshold'	cGENIE O_2	10-170	\	\	1-110	0.5-3.5
	WOA	10-170	\	\	1-110	0.5-3.5
'fennel-threshold'	cGENIE O_2 .	10-170 (1/k)		20	1-110	0.5-3.5
	WOA.	10-170 (1/k)		20	1-110	0.5-3.5
'reminO2lifetime-threshold'	cGENIE O_2	\	0.01-1	\	1-100	0.5-3.5
	WOA	\	0.01-1	\	1-100	0.5-3.5

3.4 Results

In this section, we start by summarizing the overall statistical outcome of the tuning, then present a series of spatial analysis comparisons for each of the highest M-score ensemble members. The spatial analyses progressively reduce in scale, moving from global surface distributions (Section 3.3.2), to global and basin-specific water column profiles (Section 3.3.3), and finally to spatial comparisons for a specific ODZ region (Section 3.3.4). Our final set of results (Section 3.3.5) are of the modeled Cretaceous scenarios using the best parameterizations from the modern, which then are compared to carbonate I/Ca values measured in the rock record.

3.4.1 Model skill score

The M-score values achieved across the complete ensemble for each of the 3 main parameterization-combinations are shown in Figure 3.4 and illustrate how the statistical fit is M-score sensitive to all three of the main parameters. Higher model skill scores are usually reached when 'threshold' is tuned to 10 µM [O_2] for all the ensembles, including both model-simulated

[O_2] and WOA-forced [O_2]. For the ensembles, 'lifetime-threshold' and 'fennel-threshold', the highest M-scores are similar – 0.305 and 0.308, respectively (Table 3.2). Both these ensembles have the highest performance when 'threshold', 'lifetime', and I:C ratio are tuned to 10 μM [O_2], 50 years, and 1.5×10^{-4} mol/mol, respectively, which is generally consistent with observations (Tsunogai, 1971; Elderfield & Truesdale, 1980; Lu et al., 2016, 2020a) (discussed in more detail later). The model performance of 'reminO2lifetime-threshold' is less good than the other two combinations, with the best M-score of 0.266 when 'threshold', 'reminO2lifetime', and I:C ratio are tuned to 10 μM O_2, 1×10^{-6} mol/kg, and 3.5×10^{-4} mol/mol, respectively (Table 3.2, Figure 3.4). We note that for each parameterization-combination, the highest possible M-score achievable by tuning improves when [O_2] is forced to that of the World Ocean Atlas 18 (WOA18) climatology (Garcia et al., 2018).

3.4.2 Meridional surface I^- distribution

Figure 3.5 shows a comparison between the observed latitudinal distribution of [I^-] at the surface and as simulated by the model for each parameterization-combination (for the respective best M-score ensemble member). Note that the observations (Section 3.2.3) are binned to the corresponding model grid cells and as such, reflect averages over the upper-most 80 m of the water column. This represents a reduction from 1338 to 141 surface ocean data points. We find that the surface ocean [I^-] in the model shows a trend of increasing values towards low latitudes, broadly consistent with observations (Chance et al., 2014) (Figure 3.5). The 'lifetime-threshold' and 'fennel-threshold' show similar latitudinal trends, but both overestimate the surface I^- in the mid-low latitudes in the southern hemisphere. The 'reminO2lifetime-threshold' ensemble produces better estimation of meridional surface [I^-] trend, although overestimates [I^-] in the tropical surface ocean compared to the other two ensembles (Figure 3.5).

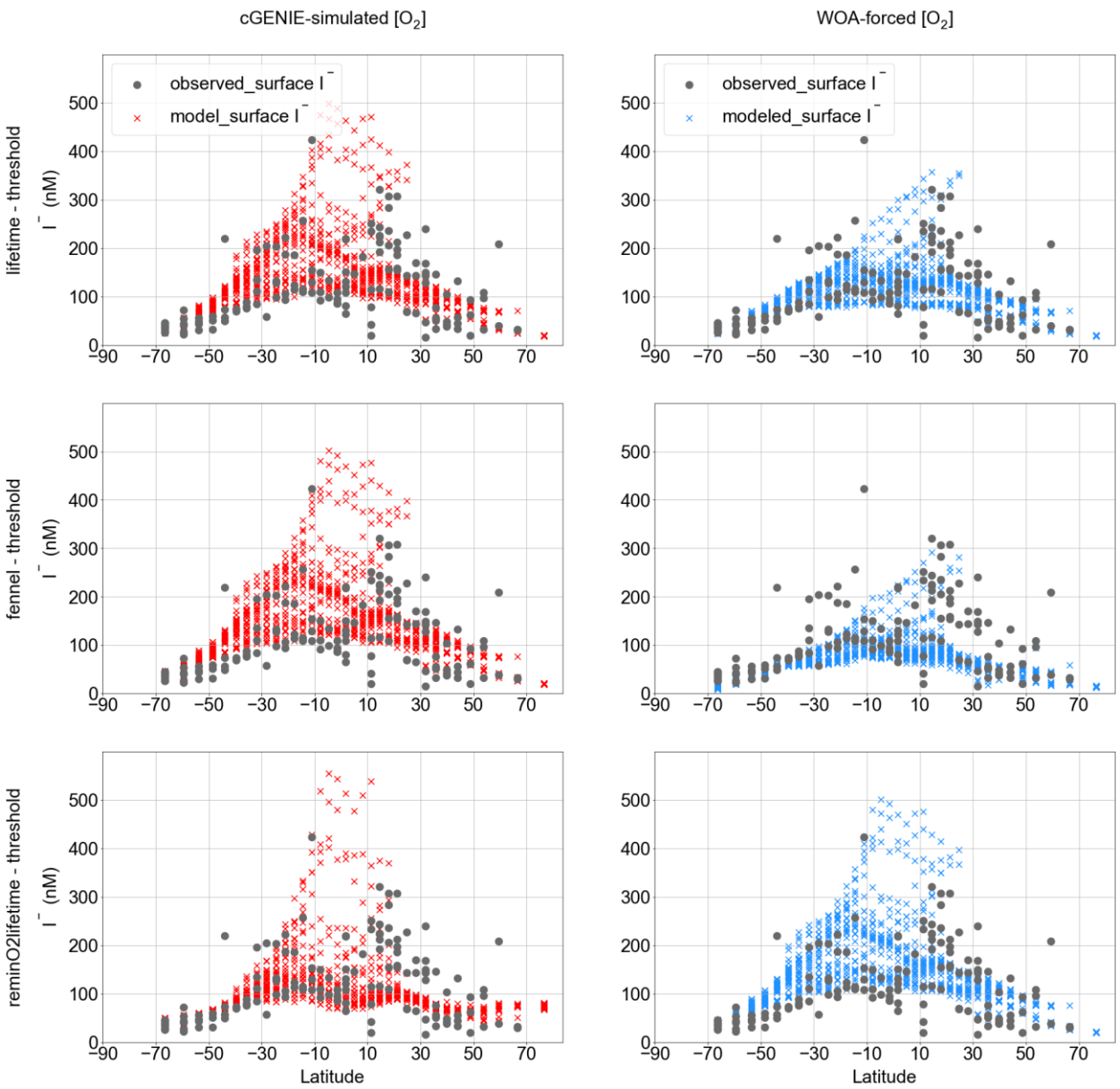

Figure 3.5. Modeled latitudinal surface iodide distribution compared with observation with the cGENIE simulated [O_2] and the [O_2] restoring forcing. The elevated [I^-] observed and modeled in low latitudes is the result of phytoplankton reduction in the surface ocean. Note that the I^- distribution simulated by 'lifetime-threshold' and 'fennel-threshold' are close but not identical.

3.4.3 Global and basin-specific iodine depth distributions

Comparisons between the observed distributions of I^- and IO_3^- seawater concentrations among the global ocean and the Atlantic and Pacific Oceans are presented in Figure 3.6. Again, we gridded the iodine observations (see: Section 3.2.3) and selected sub-sets of the data that lay in either

Atlantic or Pacific basins, contrasting with the corresponding model values at those locations. We find only relatively minor differences between the best M-score ensemble member of each of all three parameterization-combinations, and all show increased [IO_3^-] and decreased [I^-] with increased depth below the euphotic zone in the Atlantic and Pacific basins, as well as globally (Figure 3.6). The modeled depth profile broadly matches with observation in the Atlantic and deep Pacific Ocean, except the underestimated subsurface peak of [I^-] observed in the Pacific and overestimated [IO_3^-] in the deep Pacific (Figure 3.6). This mismatch of subsurface I^- peak is probably the result of sampling bias, with most of the Pacific iodine observations from ODZs in the Eastern Tropical North Pacific (ETNP) and the Eastern Tropical South Pacific (ETSP). For example, in model depth profiles masked to only include grid points with corresponding observations, the modelled Pacific depth profiles show a clear mid-depth ODZ feature (Figure 3.18).

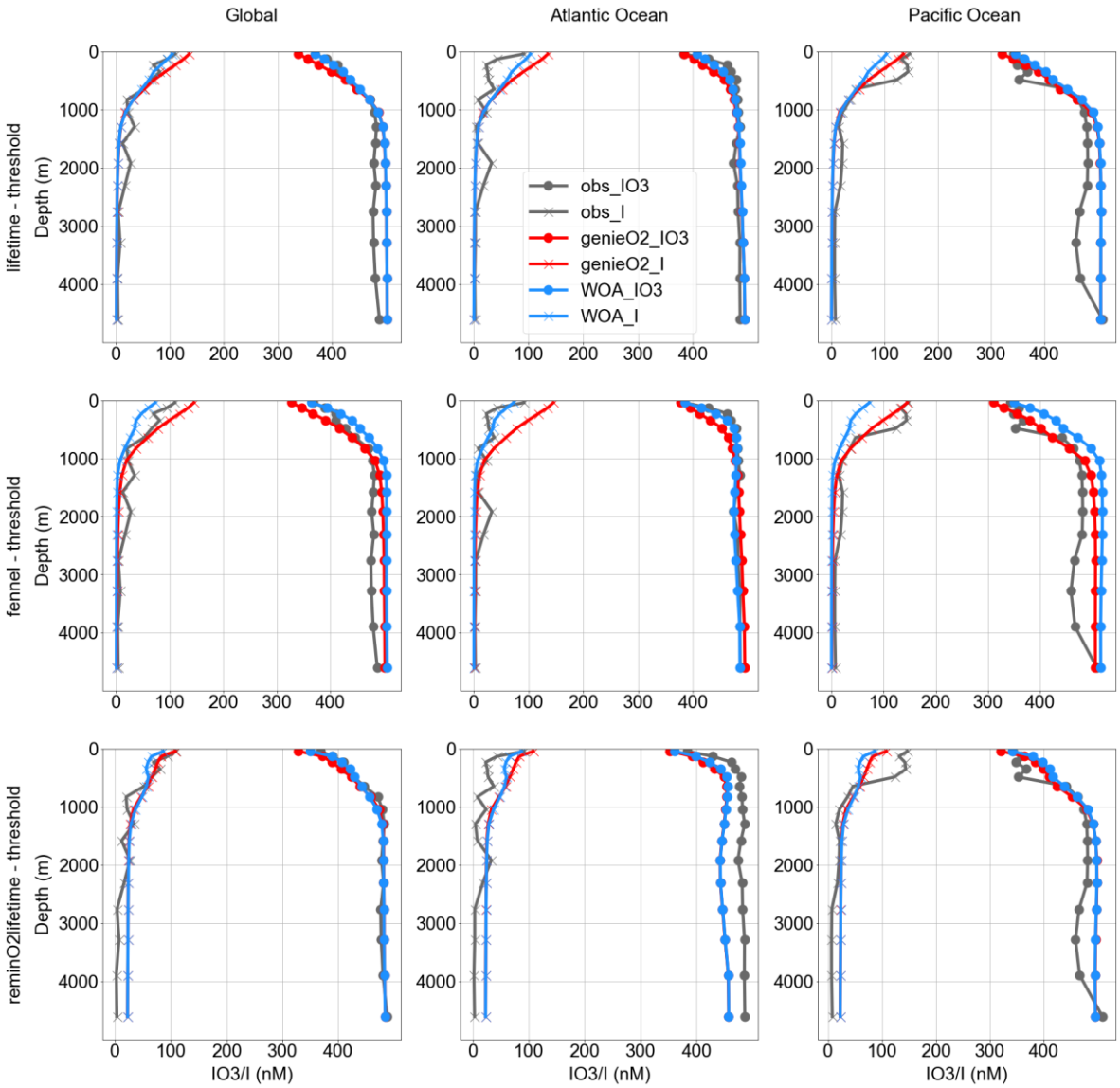

Figure 3.6. Modeled averaged iodine (including iodate and iodide) depth profile among global ocean, the Pacific, and the Atlantic compared with observation. The surface I^- enrichment among the ocean basins is caused by phytoplankton reduction. The subsurface (~500m) I^- enrichment is the result of sampling bias since most of the observations are from the ETNP and ETSP ODZs (see main text for details).

3.4.4 Iodine distribution within ODZs

To assess the model ability to simulate iodine cycling in marine low oxygen environments, we compared distributions of oxygen and iodine species in the ETNP (Figure 3.7). The O_2 transects amongst all model simulations are the same because we only changed the parameterizations of the iodine cycle between ensembles and ensemble members (i.e., they all simulate the same biological

pump in the ocean). All the three chosen best-performance-experiments show similar iodine anomalies (IO_3^- depletion) in the ETNP, fitting the general feature of the observation. Other parameterizations did not replicate the ODZ (Figure 3.13). However, even under the "best-fitting" parameters, compared to the observations, the ODZ feature in the model is underestimated both in intensity and in areal extent compared to the observations (Figure 3.7). Notably, compared to [O_2] measured in the ETNP transect, the model underestimates the extent of the ODZ. Severe deoxygenation below 50 μM [O_2] was observed in relatively shallow depths between 100-200m in the ETNP, and this ODZ extends for more than 3000 km towards off-shore from Mexican coast (Figure 3.7). Although cGENIE simulates the O_2-deficient pattern in the ETNP, the extent of the ODZ is underestimated. The simulated oxycline is ~200 m deeper than the observation and the [O_2] variation is gradual. The ODZ below 20 μM [O_2] in the model is limited to a small spatial extent within 1000 km offshore, which is much smaller than that in the observation (Figure 3.7).

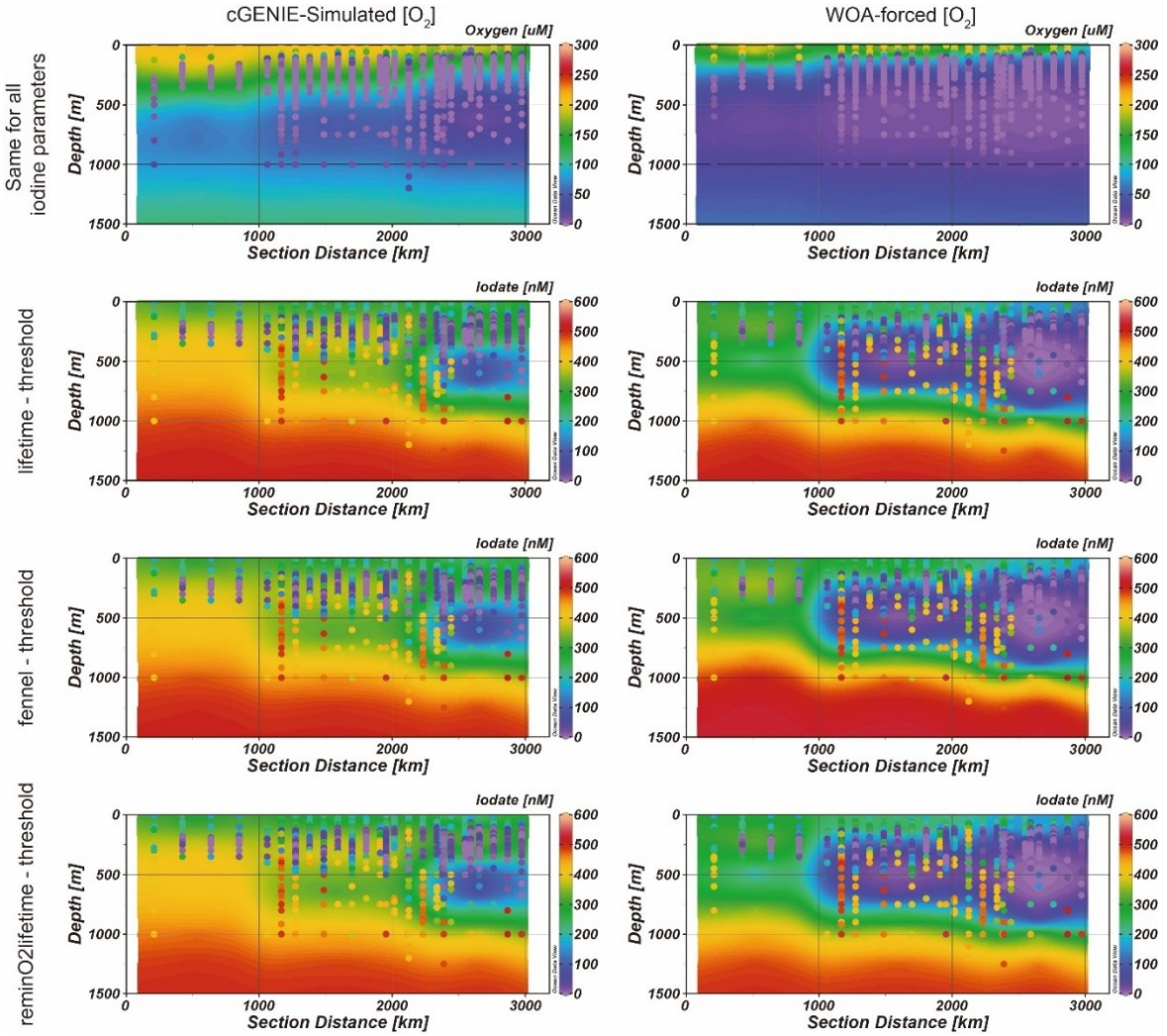

Figure 3.7. Modeled (contour) and observed (colored dots) west-to-east transect (location shown in Figure 3.1) of O_2 (top row) and IO_3^- (bottom rows) in the ETNP. Note that the WOA-forced [O_2] models simulate a larger extent of IO_3^- anomaly, which better matches the observation. The left-hand panel contours are model results based on cGENIE-simulated [O_2] while contours on the right are model results from WOA-forced [O_2].

We also ran model ensembles forcing cGENIE to restore the modern ocean [O_2] annual average climatology to that of the WOA18 (Garcia et al., 2018) (Figure 3.7). Under these conditions, the subsurface IO_3^- depletion zone in the ETNP ODZ in all three ensembles extends ~2000 km offshore and spans across 100-1000 m in depth (Figure 3.7). The shallow and extended ODZ iodine distribution in the ETNP better matches the observation compared to non-O_2 restoration simulations.

Parameterization-combination		Iodine oxidation parameters			Iodine reduction parameters	I:C ratio (× 10^{-4} mol/mol)	Model skill score
		'lifetime' (years)	'reminO2lifetime' (× 10^{-5} mol/kg)	'Fennel' (Inhibition constant/ μM O_2)	'threshold' (μM O_2)		
'lifetime-threshold'	cGENIE O_2	50	\	\	10	1.5	0.305
	WOA	50	\	\	10	1.5	0.385
'fennel-threshold'	cGENIE O_2	50 (1/k)	\	20	10	1.5	0.308
	WOA	10 (1/k)	\	20	10	3.5	0.385
'reminO2lifetime-threshold'	cGENIE O_2	\	0.1	\	10	3.5	0.266
	WOA	\	0.1	\	10	3.5	0.365

Table 3.2. The performance of the cGENIE iodine simulations and associated parameterization when the model reaches the best global M-score. Note that the oxidation rate constant *k* in 'Fennel' is in unit of $year^{-1}$ in the model configuration, which is also the reciprocal of the 'lifetime'. The full model performance is summarized in Table 3.4.

3.4.5 Evaluation against geological observations

The statistical results of the pre-OAE2 evaluation are illustrated in Figure 3.8 for the 3 main parameterization-combinations and for parameter calibrations derived from internally and WOA-forced dissolved oxygen distributions (and in Figure 3.18 for the full set of parameterization-combinations tested). Most of the parameterization-combinations reach their highest M-scores under the assumption of 0.6-0.8 × modern [PO_4] (Figure 3.18). Previous analysis using the same climatological configuration of the cGENIE model indicated a PO_4 inventory of 1.0 x modern was most consistent with geological redox-related observations prior to OAE2 (Monteiro et al., 2012). However, our assumption here of temperature-dependent POM export and remineralization leads to higher export and shallower more intense ODZs compared to temperature-invariant biological scheme (see: Crichton et al., (2021)). Hence, for a similar degree of ocean anoxia, we would expect the need for a slightly lower nutrient inventory, as we indeed find.

In terms of the I/Ca M-score, we find the parameterization-combinations 'reminO2lifetime-threshold' and 'fennel-threshold' better replicate the geological observations compared to the 'lifetime-threshold'. For 'fennel-threshold', the WOA-derived parameter set values differ from those derived from cGENIE-[O_2] (Table 3.2) and perform better. The performance of the scheme 'reminO2lifetime-threshold' is largely independent of the ocean PO_4 inventory assumption for values of 0.6 × modern and higher.

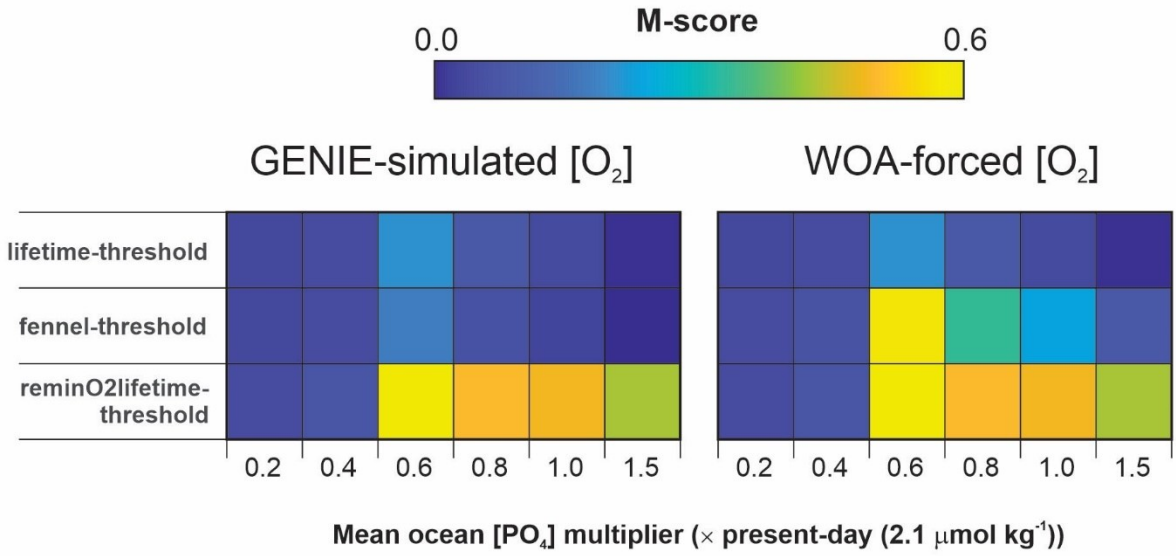

Figure 3.8. The model skill scores of modeled and measured I/Ca during the pre-OAE2. The iodine cycling parameters are derived from modern simulations with cGENIE-simulated [O_2] and WOA-forced [O_2], respectively.

3.5 Discussion

In summary: we presented the results of cGENIE Earth system model ensembles (both with internally calculated and WOA-imposed [O_2] distribution) for 3 parameterization-combinations of iodine cycling that showed the best performance (but summarize a total of 5 different parameterization-combinations in Table 3.4). We analyzed the performance of the ensembles via: (1) M-score for the model-data match of both [I^-] and [IO_3^-] across the entire ocean, (2) qualitative model-observation comparison of latitudinal surface ocean distributions of [I^-], (3) inspection of averaged depth profiles in global and individual ocean basins for both [I^-] and [IO_3^-], (4) inspection

of iodine transects across the across the Eastern Tropical North Pacific (ETNP) ODZ, and (5) M-score for model and carbonate I/Ca observations (Zhou et al., 2015) for the Cretaceous.

3.5.1 Overall model skill score comparison

Two broad observations emerge from the M-score comparison. First, the 1st-order kinetic iodine oxidation associated ensembles ('lifetime-threshold' and 'Fennel-threshold') have the highest M-scores (Table 3.2), under both cGENIE-simulated [O_2] and WOA-forced [O_2]. This is consistent with previous observations of 1st-order kinetics for I^- oxidation (Tsunogai, 1971). Second, the simulations with WOA-forced [O_2] produce significantly higher M-scores than that of the cGENIE-simulated [O_2] field (at least ~0.08 of improvement; Table 3.2). Despite a 1st-order non-O_2 dependent oxidation mechanism providing the highest M-scores, the WOA vs internally model-generated dissolved oxygen distributions comparison highlights the O_2 and related redox dependency of the iodine cycle from the perspective of IO_3^- reduction. Each of these factors are discussed in the following Section 3.4.1.1.

3.5.1.1 Parameter value plausibility

A credible representation of the marine iodine cycle requires not only that observations can be replicated, but that in achieving a fit to observations, tuned parameter values fall within real-world ranges. In this section, we discuss the plausibility of our best-fit (maximized M-score) parameter values. For the iodine cycle, these parameters are: the O_2 threshold, the parameter (depending on the specific parameterization-combination) controlling the I^- oxidation rate, and the cellular I:C ratio.

Our model M-score is highest with an [O_2] reduction threshold of 10 μM (Figure 3.4 and Table 3.2). Although it is generally well accepted that IO_3^- is reduced in low oxygen settings (Wong & Brewer, 1977; Wong et al., 1985; Luther, 1991; Rue et al., 1997; Farrenkopf & Luther, 2002),

the degree of O_2 depletion that triggers IO_3^- reduction is still unclear. A relatively high threshold for triggering IO_3^- reduction has been proposed based on comparison between planktic and benthic foraminiferal I/Ca and ambient [O_2] (20-70 μM O_2; Lu et al., 2016, 2020a). These [O_2] thresholds are similar to that determined in a previous cGENIE-based iodine cycle study (30 μM) (Lu *et al.*, 2018), but it is difficult to directly compare this to our results because of differences in the model representation of the ocean biological pump, the iodine observational dataset, and model-data comparison methods utilized.

Many of the studies suggesting a relatively high [O_2] threshold are based on the relationship of [IO_3^-] and [O_2] within the upper chemocline of ODZs; however, evaluation of [O_2] and [IO_3^-] from ODZs throughout the entire water column suggest the potential for IO_3^- persistence within the low oxygen cores of ODZs. Specifically, IO_3^- accumulation is observed within the ETNP and ETSP at depths where [O_2] is close to or below the detection limit of the sensors which is reported near 1 μM (Hardisty et al., 2021). In addition, it is worth noting that the kinetics of IO_3^- reduction is heterogeneous both within and between ODZs. For example, a transect evaluating IO_3^- reduction rates in the ETNP observed rapid rates in the upper oxycline, where [O_2] was near ~12 μM, but the potential for sluggish rates in the ODZ cores, where [O_2] was below detection. In an early study of the Arabian Sea, IO_3^- was reduced rapidly within the ODZ core. Together, these suggest IO_3^- reduction may be controlled by factors beyond O_2 (Farrenkopf & Luther, 2002; Hardisty et al., 2021). For example, IO_3^- is likely formed in high [O_2], non-ODZ water masses but can be sustained upon transport or mixing within oligotrophic, offshore ODZ regions where organic supplies are more limited (Hardisty et al., 2021). A comparison to the N cycle would also indicate a low [O_2] threshold – for example, denitrification has a sub-μM [O_2] threshold and has a similar redox potential with IO_3^- reduction (Thamdrup et al., 2012; Dalsgaard et al., 2014). A sub-μM [O_2]

threshold for IO_3^- reduction could explain the [IO_3^-] variations observed in ODZ cores with [O_2] below the μM detection limits of sensors; however, iodine speciation has yet to be analyzed alongside [O_2] measurements via sensors with sub-μM detection limits, such as STOX sensors. Regardless, our 10 μM [O_2] threshold based on maximizing the M-score reflects a global average value and clearly falls within the ranges of oceanographic observations.

For both our study and that of Lu et al., (2018), an I^- lifetime of 50 years maximizes model performance. However, Lu et al., (2018) chose to implement a slightly lower value of 40 years for their paleo-application because it reflected the slowest rate observed in the literature at that time (Tsunogai, 1971). Notably, though IO_3^- is the most abundant marine iodine species, its production from I^- has never been unambiguously observed under normal marine conditions. This has acted as a major hinderance on providing direct constraints. That said, our model-based estimate is consistent with a multitude of other constraints that indicate that I^- oxidation to IO_3^- undergoes extremely slow kinetics. The I^- oxidation rates calculated through indirect methods including mass balance and seasonal iodine speciation changes (Tsunogai, 1971; Campos et al., 1996; Edwards & Truesdale, 1997; Truesdale et al., 2001; He et al., 2013; Žic et al., 2013; Moriyasu et al., 2023) or through radiogenic tracer spiked incubations (Hardisty et al., 2020; Schnur et al., 2024; Ştreangă et al., 2024) have a wide range of variation from 1.5 nM/yr to 670 nM/yr. The lifetime in cGENIE is 50 years, which can be approximately converted to the zeroth order rate of <9 nM/yr, falling in the lower end of the previous studies.

Our best-fit I:C ratio is 1.5×10^{-4} mol/mol, which is in agreement with plankton measurements and mass-balance calculations (Elderfield & Truesdale, 1980; Chance et al., 2010). In the euphotic zone, IO_3^- is taken up by phytoplankton and incorporated into their cellular structures followed by subsequent conversion into I^- (Hepach et al., 2020). Due to this, it is

assumed that IO_3^- removal in the surface layer of the ocean is a function of organic carbon fixation during primary productivity according to Redfield-like ratios (Campos et al., 1996; Chance et al., 2010). Of the parameters incorporated into the model, in theory, I:C should probably be the best constrained. However, published I:C ratios based on field and laboratory measurements vary over several orders of magnitude (10^{-5} to 10^{-3}) (Elderfield & Truesdale, 1980; Campos et al., 1996; Chance et al., 2010; Hepach et al., 2020). To limit the number of model simulations and size of the ensembles, we only varied I:C between 5×10^{-5} and 3.5×10^{-4} mol/mol (in increments of 1.0×10^{-4}), which covers the range indicated by previous studies (Elderfield & Truesdale, 1980).

It is unlikely that the I:C value is constant across the global ocean due to differences in phytoplankton composition and other factors, such as temperature (Wadley et al., 2020). In cGENIE, most of the elevated (> 200 nM) surface $[I^-]$ values occur in the ETSP and the northern Indian Ocean, representing the effect of high primary productivity and transformation of IO_3^- to I^- via the rapid recycling DOM 'loss term' in the representation of biological export in the model (Figure 3.15). The overestimation of tropical I^- within the model probably hints that the I:C ratio is not constant in the ocean, as which is also hypothesized by Wadley et al., (2020), although in the absence of an explicit representation of primary productivity in the model and spatially variable f-ratios (Laws et al., 2000) (implicitly, the f-ratio can be considered to be 0.33 everywhere in cGENIE). In testing a fixed, spatially uniform I:C, Wadley et al. (2020) underestimated surface $[I^-]$ in low latitudes and overestimated concentrations in mid-latitudes. Based on their model-observation comparison, they hypothesized that the I:C ratio decreases systematically with sea surface temperature (SST) (Wadley et al., 2020). Until more constraints are developed on spatial variability and associated driving factors for I:C, a generalized approach of a globally uniform I:C

remains the most parsimonious assumption, especially considering cGENIE's intended extrapolation to ancient settings.

3.5.1.2 Comparing alternative iodide oxidation parameterizations in cGENIE

Due to similarity in redox potentials, iodine cycling in the ocean has been hypothesized to be linked to the cycling of nitrogen (Rue et al., 1997). Nitrification promoting I^- oxidation to IO_3^- has been inferred from field studies (Truesdale et al., 2001; Žic et al., 2013), and more recently has been linked via observation of I^- oxidation to IO_3^- by ammonia oxidizing bacteria in laboratory environments (Hughes et al., 2021). We further note that Wadley et al., (2020) explicitly link I^- oxidation to NH_4^+ oxidation in their surface ocean iodine cycle model.

As an alternative to the first-order lifetime oxidation parameterization used here and in Lu et al., (2018) and in the current absence of a full nitrogen cycle (and hence explicit NH_4^+ oxidation) in cGENIE, we also applied a strategy ('reminO2lifetime') which links I^- oxidation to organic carbon remineralization and the consumption rate of dissolved oxygen. The reasoning behind this is that the O_2 consumption rate in the model implicitly reflects bacterial oxidizing activity in the water column and hence the potential for I^- to be oxidized to IO_3^-. We find that the overall model performance involved with the 'reminO2lifetime' is lower than other experiments where I^- oxidation is ubiquitously oxidized according to a parametrized lifetime, or 'lifetime-threshold' (maximum M-score 0.266 vs. 0.305/0.308 under cGENIE simulated [O_2]) (Figure 3.4 and Table 3.2). However, despite slightly lower M-scores, the 'reminO2lifetime' scheme generally replicates the latitudinal surface [I^-] trend, the depth profiles in the ocean basins, and the ODZ transect (Figs. 4-6).

Under the default 'lifetime' scheme, I^- will oxidize in the whole ocean regardless of the concentration (or even presence/absence) of ambient O_2. This scenario might hence not perform

well in replicating the ocean iodine cycling at intervals during the Phanerozoic when ODZs were highly expanded, as it does not account for the possibility for slower I^- oxidation at low O_2 but above the IO_3^- reduction O_2 threshold. Ideally, for application in paleoceanographic studies, I^- oxidation should be linked to ambient [O_2] in some way. Although thermodynamics theory suggests O_2 does not directly drive I^- oxidation (Luther et al., 1995), field studies in ODZs indeed observed low [O_2] inhibits this process (Farrenkopf & Luther, 2002; Moriyasu *et al.*, 2020). We hence developed and tested variable I^- oxidation kinetics, with the ambient dissolved O_2 providing an inhibition of the rate of oxidation based on the enzymatic nitrification scheme of Fennel et al., (2005).

Since most of the ocean is fully oxygenated today, there is little difference in M-scores between 'lifetime' and 'Fennel' oxidation parameterizations (0.305 vs. 0.308, Table 3.2). Despite the very close M-scores, 'Fennel' oxidation under WOA-forcing has a higher optimal I:C ratio (3.5×10^{-4} mol/mol) and faster saturated I^- oxidation kinetics (0.1 yr^{-1} vs. 0.02 yr^{-1} in other ensembles). Such parameter differences between 'Fennel'-WOA and other ensembles reflect compensation between faster oxidation rate (process (2) in Figure 3.1) and increased I^- production through the higher biotic uptake rate (process (3) in Figure 3.1). The pre-OAE2 simulations are particularly illustrative of this tradeoff and are discussed in more detail in section 3.4.3.

In summary, all the three parameterization-combinations produce high and comparable M-scores and similar parameters (oxidation, reduction, and I:C) associated with these M-scores (Table 3.2). Although direct field-based evidence to evaluate the controlling parameters of 'reminO2lifetime' is absent, the parameters controlling the other model scheme are consistent with previous studies.

3.5.2 Beyond the M-score: model-data comparison across iodine gradients

As applied here, the M-score provides a quantitative measure that describes the overall model global performance and allows us to directly compare the implications of parameter value and parameterization choices. However, a M-score based on a global dataset can obscure regional gradients that may be important for both paleo- and modern oceanographic research. Indeed, amongst all the various ensembles we ran as part of this study (Table 3.3), only 'lifetime-threshold', 'lifetime-Fennel', and 'reminO2lifetime-threshold' performed sufficiently well in replicating the modern oceanic iodine gradients (Figures. 3.11-3.12) and we thus decided to focus only on these 3 parameterization-combinations. We now discuss this in more detail below.

3.5.2.1 Meridional surface [I^-] gradient

All the 3 main parameterization-combinations summarized in Table 3.2, as well as the observations, show enrichment of I^- in the surface ocean at low latitudes (Figure 3.5). The pathway of transforming IO_3^- into I^- in these oxidized waters is through primary productivity in the euphotic zone, which results in I^- accumulation within the mixed layer (Chance et al., 2014). In the low latitudinal surface ocean, weaker vertical mixing resulting from warmer surface temperatures allows I^- accumulation in the shallow mixed layer (Chance et al., 2014; Moriyaus et al., 2023). Therefore, the IO_3^- flux from deep waters through seasonal mixing may be an important balance to in situ IO_3^- reduction rate by primary producers in the high latitudes (Chance et al., 2014; Moriyasu et al., 2023). Importantly, this temperature stratification and related vertical mixing trend is also simulated by cGENIE (Figure 3.16). The cGENIE model generates the general pattern of latitudinal surface I^- distribution pattern as well; however, overestimation especially in low latitudes may exist, especially in the tropical surface where [I^-] is close to 500 nM among all the cGENIE-O_2 models (Figure 3.5).

The cGENIE (internally generated oxygen distributions) vs WOA (imposed distributions) O_2 comparison provides evidence that I^- generated in low [O_2] settings may broadly enhance [I^-] in oxygenated euphotic waters, with lower and closer-to-observations [I^-] values in the WOA tunings (Figure 3.5). This includes 'lifetime-threshold', where O_2 only impacts the reductive portion of the iodine cycle, but also the 'Fennel' and 'reminO2lifetime' where rates of I^- oxidation are also [O_2] dependent. More specifically, most of the elevated (> 200 nM) surface [I^-] in cGENIE, occurs in the ETSP and the northern Indian Ocean and corresponds to locations of high primary productivity (Figure 3.15). Since the surface ocean [O_2] in the model is never below 200 μM, O_2-dependent IO_3^- reduction at the ocean surface is unlikely. Instead, ex situ transport from proximal regions of subsurface anoxia is the most probable source of elevated I^-. Indeed, the most prominent regions of I^- enrichment in the model occur near the Peruvian coast and in the Arabian Sea, where ODZs lie below the surface (Figure 3.15). More detailed data-model comparison among these two areas is limited because the observation data are few (e.g., Farrenkopf and Luther, 2002 and Rapp et al., 2020). In contrast, the meridional trend of I^- in the surface Atlantic Ocean, where ODZs are less developed, exhibits better agreement with both the observation and the Wadley et al., (2020) model (Figure 3.15). The overestimation of tropical ocean surface [I^-] by cGENIE is hence likely to be associated with deficiencies in the simulation of ODZ oxygenation.

That said, modeled overestimations of surface ocean [I^-] may be difficult to verify given current observational data densities. In comparing observational data to model-latitudinal trends which have been masked to only include model grid points with corresponding observations, although the same broad trend of increasing [I^-] in the low latitudes exists, there are fewer incidents of apparent model over-estimation (Figure 3.17). More observations in surface ocean [I^-] from low

latitudes are needed to better assess the validity of elevated modelled surface ocean [I^-] in some regions.

3.5.2.2 Global and basin-specific iodine depth profiles

All the iodine cycle schemes (both cGENIE-[O_2] and WOA-forced) generate a decrease in [I^-] and increase in [IO_3^-] from the euphotic zone down to the deep abyssal zone across ocean basins, matching the primary production-driven pattern (Figure 3.6). As discussed in the previous section, this surface maxima of [I^-] in the oxygenated water column is the result of biologically mediated reduction or release during cell senescence of phytoplankton. Below the euphotic zone, [I^-] is close to zero and IO_3^- becomes the dominant species. The deep ocean is mostly oxygenated and has longer water residence times (several millennia, Matsumoto, (2007)) compared to the I^- lifetime (<40 years, Tsunogai, (1971)), thus facilitating I^- oxidation in the absence of IO_3^- reduction in ODZs.

We note that there are multiple general discrepancies between observations and model output as well as differences between the results of WOA vs. cGENIE-[O_2] parameter tuning. In general, all models reproduce the global average better, relative to the basin-specific profiles. We suggest that the global averaged profiles are a better test of the cGENIE simulations because of sampling biases associated with individual basins. For example, the discrepancy between the model and observations are prominent in the Pacific (Figure 3.6). The observed Pacific subsurface [I^-] peak mirrors the [IO_3^-] minima that occurs at depths where ODZs are present. This ODZ feature in the averaged Pacific observation profile is likely the result of sampling bias since most of the observations from the Pacific are from the ETNP (Rue et al., 1997; Moriyasu et al., 2020), and thus do not reflect the overall iodine distribution in the Pacific Ocean (Figure 3.18). This conclusion is supported by depth profiles masked to only include modeled grid points with

corresponding observation data. For example, there is a clear mid-depth ODZ feature in the masked model Pacific depth profiles due to extensive ODZ studies in this region (Figure 3.18). All this said, while the general features of iodine speciation with depth are generally similar, our data compilation indicates the potential for some basin-specific variations which require further research to validate and mechanistically understand.

3.5.2.3 Iodine distribution within ODZs

One of the major goals of calibrating the iodine cycle in cGENIE is to be able to simulate the iodine behavior associated with ancient low oxygen settings. To assess this potential, we analyzed model performance for the ETNP (Rue et al., 1997; Moriyasu et al., 2020) where observational data are abundant and the areal extent of the ODZ is sufficiently large to be reflected in the model grid (Figure 3.6). The simulated reduction in IO_3^- to I^- generally overlaps with the extent of the ODZ (Figure 3.6), which provides support for the use of cGENIE to understand the broad distribution of ancient [IO_3^-] and [O_2]. Non-threshold model parameterization-combinations (not discussed here but shown in Figure 3.13) did not replicate the ODZ feature in iodine speciation.

In all model configurations assuming cGENIE-[O_2], the most prominent discrepancy is an underestimation of the spatial extent and intensity of the IO_3^- depletion zone in the ETNP (Figure 3.6) – a consequence of simulated subsurface O_2 deficient area being notably narrower than WOA climatology (Figure 3.6, Figure 3.14). This is principally a consequence of relatively weak continental margin upwelling and Equatorial divergence, itself a consequence of the low resolution (both horizontally and vertically) model grid that the 3D ocean circulation component is implemented on together with its simplified physics (Marsh et al., 2011). Another consequence of the low-resolution nature of the cGENIE model grid is that the extent of the ETNP is of the order of the size of an individual grid box and the entire ETNP only covers the longitude range of three

grids in the model framework (Figure 3.1). Meanwhile, the depth resolution is ca. 100-200 m per layer in the upper ocean which also limits the finer simulation of ODZ features. Awareness of these limitations highlights the importance of focusing use of the model on regional and global oxygenation features as opposed to overinterpreting local features.

Other data-model misfits may be due to IO_3^--reduction dependencies not explicitly accounted for in the model. As discussed above, shipboard incubation and radiogenic-tracer-spiked rate calculation suggest that IO_3^- reduction is slow in the offshore ETNP ODZ (Hardisty et al., 2021). This could explain why measurable IO_3^- is present in the core of the ETNP ODZ (Figure 3.6). This is further exacerbated in the Eastern Tropical South Pacific ODZ, where [IO_3^-] remains above 250 nM in some studies (Cutter et al., 2018) but near detection limits in in others (Rapp et al., 2020), suggesting extreme spatiotemporal variability related to currently unconstrained factors. Further, while the capability of microbes using IO_3^- as an electron acceptor for oxidizing organic matter has been confirmed in laboratory culture experiments (Councell et al., 1997; Farrenkopf et al., 1997; Amachi et al., 2007; Yamazaki et al., 2020; Reyes-Umana et al., 2021), no study to date has demonstrated non-O_2 dependent controls driving variable IO_3^- reduction rates.

An important factor contributing to elevated [I^-] in ODZs is benthic fluxes and reduction occurring within the uppermost layers of marine sediments (akin to denitrification). To help account for this in our M-score and model calibration (see: methods section), 'excess' iodine (>500 nM total iodine) was filtered from our observational dataset. The excess iodine originated from the sediment flux has been observed in ODZ water columns contacting anoxic sediments (Chapman, 1983; Farrenkopf & Luther, 2002; Cutter et al., 2018; Moriyasu et al., 2020; Scholz et al., 2024). We note that excess iodine occurs explicitly as I^-, reflecting the limited or lack of oxygen within the ODZ, and is a local-regional phenomenon not yet observed to persist beyond ODZ settings.

Future work can focus on understanding the degree, if any, that excess I^- is oxidized to IO_3^-, and hence impacts the I/Ca paleoredox proxy.

3.5.3 Applicability of the cGENIE marine iodine cycle to paleoredox reconstruction

The pre-OAE2 comparison is revealing because the observations encapsulate a strong gradient between high and very low I/Ca (Figure 3.3), reflecting respectively, high and low surface ocean concentrations of IO_3^- in the model. All three of the parameterization-combinations (just focusing on WOA-derived parameter values) are capable of reproducing low I/Ca values in the lower latitudinal sections (Demerara Rise, Tarfaya, and Raia del Pedale; Figure 3.9), although with a tendency to slightly overestimate seawater IO_3^- depletion (cross-plots in Figure 3.9). Low ocean surface [IO_3^-] occurs in the model as a result of the existence of a circum-Equatorial band of intense sub-surface anoxia and short transport time to the surface (and hence limited oxidation). In the higher latitudinal sections, including Newfoundland, Eastbourne, and South Ferriby, I/Ca values tend to be underestimated to varying degrees (Figure 3.9). However, compared to the 'lifetime' parameterization, both 'reminO2lifetime' and 'Fennel' oxidation simulate the I/Ca values in these high latitudinal sections rather better, with the regression closer to the 1:1 line (dotted in Figure 3.9). We find this relationship instructional for understanding controls in the modern iodine cycle.

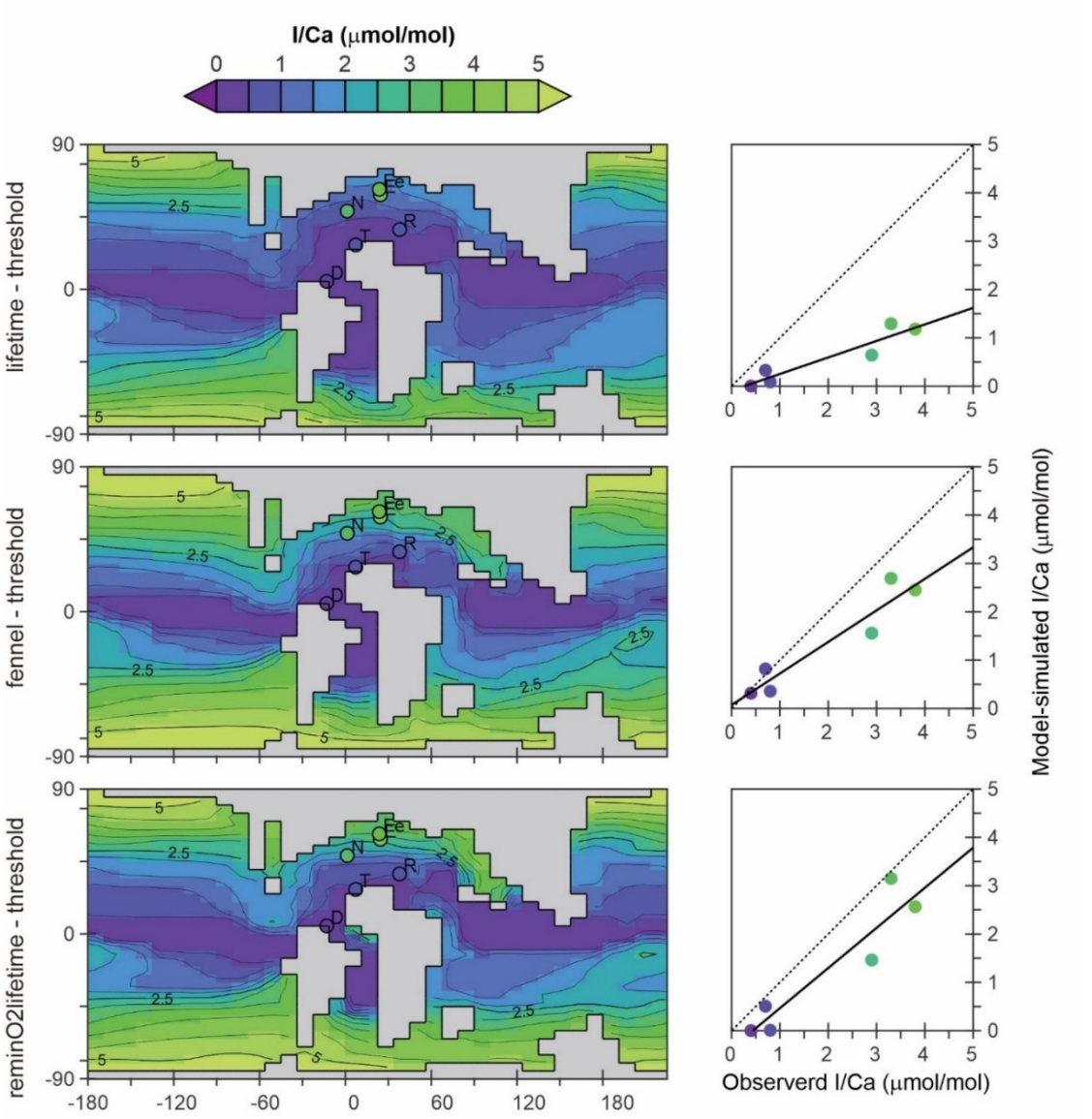

Figure 3.9. The pre-OAE2 I/Ca field derived from cGENIE [IO_3^-] simulations, and the comparison between modeled and observed I/Ca from sections.

We first note that both 'lifetime' and 'fennel' iodine oxidation parameterizations in conjunction with a threshold of IO_3^- reduction and internally generated GENIE-[O_2], give rise to identical parameter values (Table 3.2). We infer that this is because the modern ocean is predominately well-oxygenated and hence there is little inhibition of I^- oxidation in practice. In the Cretaceous environment, although I^- oxidation inhibition should be widespread, the M-scores are similar (Figure 3.8). The rate of I^- oxidation in well oxygenated seawater is likely then critical in

explaining elevated I/Ca values at higher Cretaceous latitudes. However, simply decreasing the lifetime in the modern ocean would result in an under estimation of surface ocean [I^-]. The 'fennel-threshold' combination under WOA-[O_2] reveals a trade-off that solves this – a decreased I^- lifetime compensated for by increased rates of I^- release to the ocean interior directly through the biological pump and elevated cellular I:C (3.5×10^{-4} mol/mol vs. 1.5×10^{-4} mol/mol). In the Cretaceous ocean this combination allows for both sharper latitudinal gradients in [IO_3^-] (and hence I/Ca) to develop, as well as steeper vertical gradients which allow for non-zero I/Ca values at low latitudes to be captured (cross-plot in Figure 3.9). This slight enhancement of the upper ocean [IO_3^-] gradient is also apparent in the present-day analysis (Figure 3.6). The combination of 'reminO2lifetime' with a reduction threshold works similarly – a shorter lifetime for I^- under oxic conditions offset in the modern ocean by elevated cellular I:C (Table 3.2). However, in this case, our gridded parameter search identifies the trade-off as producing the highest M-score for both modelled and WOA oxygen distributions.

What we learn from this is that the cGENIE iodine cycle tuned to modern observations has predictive power under a very different state of ocean oxygenation (and circulation and operation of biological pump). However, this is not true for every choice of parameterization, and the simple 'lifetime-threshold' combination, which when calibrated was statistically almost the best representation of the iodine cycle, was unable to reproduce the latitudinal I/Ca gradients in the Cretaceous ocean. Shortening the lifetime (and adding an inhibition term) together with increasing the assumed cellular I:C, maintains fidelity in simulating the modern ocean whilst much better capturing Cretaceous I/Ca. That even better representations of Cretaceous I/Ca were possible but at the expense of reproducing modern observations adequately hints that improvements in our

mechanistic understanding are needed, although all of the above assumes that the simulation of the Cretaceous redox landscape is plausible.

One caveat to our paleo comparison is that because the residence time of iodine in the ocean is only around 300 kyr, the dissolved iodine inventory of the Cretaceous ocean could have deviated substantially from the modern seawater value that we assume here (500 nM). One possible explanation for the overall underestimation of I/Ca by cGENIE might then be that the Cretaceous iodine inventory was higher than modern (Zhou et al., 2015; Lu et al., 2018). Even a moderate increase (ca. 20-40%) in the ocean iodine inventory (which we did not test here) would presumably act to increase the slope of the regression lines for the parameterization-combinations 'fennel-threshold' and 'reminO2lifetime-threshold' and bring them close to the 1:1 line (Figure 3.9). Another uncertainty concerns the potential impact on carbonate I/Ca ratios of different-from-modern dissolved calcium concentrations in the Cretaceous ocean. The calcite crystal growth experiments of Zhou et al. [2014] on which we base our model-simulated I/Ca values were carried out in synthetic solutions and not seawater. The partition coefficient K_D was calculated as $[I/Ca]/[IO_3^-]$ and as a result our model formulation is independent of the ambient Ca^{2+} concentration. New I/Ca carbonate precipitation experiments that explicitly account for the geological range in seawater composition would help increase confidence in the model-simulated I/Ca values and hence improve the model simulation comparison possible with geological observations.

3.5.4 Choice of marine iodine cycle representation in cGENIE

The risk in tuning model parameters to fit some data target is always that the processes being tuned are distorted to accommodate an underlying structural error with the model. In this paper we illustrated how sub-regional scale ocean oxygenation features such as the Eastern

Tropical North Pacific ODZ (Figure 3.7) are poorly represented at the resolution of the cGENIE Earth system model, and how this can lead to deficiencies in the simulation of the marine iodine cycle in these regions. Indeed, we found an improved statistical fit to observed iodine speciation data when we imposed a dissolved oxygen climatology to the model grid rather than use the internally – general model [O_2] fields (Table 2.2). In the case of the 'Fennel' parameterization-combination, we end up with two different sets of parameter values – one associated with the best fit to iodine speciation data under cGENIE projected [O_2], and one under WOA imposed [O_2]. Selecting this particular scheme for paleo applications would appear to create a conundrum – whether (a) to choose the cGENIE [O_2] derived parameter value set and accept that model deficiencies were being implicitly corrected for in simulating marine iodine cycling and hence imposing a potential bias on paleo I/Ca, or (b) accept WOA [O_2] derived parameter values. The choice would arguably be to accept the less potentially biased parameter value set (b), particularly as the relatively small-scale ODZ features of the modern ocean may be expanded to the regional-to-global scale in deeper time oceans and hence the redox features driving iodate reduction would become much more tractable for a model of the resolution of cGENIE.

However, we note that this choice does not exist for parameterization-combinations 'lifetime-threshold' and 'reminO2lifetime-threshold'. In both cases the sets of optimal parameter values are the same, whether derived from cGENIE projected [O_2] or WOA imposed [O_2] (Table 3.2). This gives us confidence that both these schemes are relatively agnostic to the details of how the modern oxygen cycle is simulated, and that errors in the simulation of sub-regional-scale ocean oxygenation features are not critical. (We note that iodine speciation data is still fitted better under WOA imposed [O_2].) The choice of how to best represent the marine iodine cycle in cGENIE is then a choice between 'lifetime-threshold', which has been used in a similar form previously (Lu

et al., 2018) and is capable of the best fit to modern observations, or 'reminO2lifetime-threshold'. While 'lifetime-threshold' might be preferable for more recent geological time and ocean ODZs similar to the present-day, it fails to account for I/Ca contrasts under more extreme redox gradients (Figure 3.9). Although more difficult to interpret mechanistically, in suppressing the rate of I^- oxidation under low ambient [O_2], 'reminO2lifetime-threshold' appears to be the more appropriate paleo choice.

We note that to achieve improved simulation of sub-regional scale features of the ocean redox landscape, future paleo cGENIE model I/Ca applications could make use of the coupled GENIE-PLASIM climate configuration (Holden et al., 2016) . In this, the ocean circulation model is implemented on a higher resolution grid (64 × 32 with 32 vertical levels) and includes a coupled atmospheric GCM component (hence enabling interannual variability). It is also capable of being configured with different continental configurations for paleo climate questions (e.g. Keery et al., 2018).

3.6 Conclusions

Using the cGENIE Earth system model, we performed a series of ensemble experiments to determine suitable parameterizations to represent the marine iodine cycle and identified the best performing combinations of parameter values in each case. We found that the optimized parameter values associated with, water column IO_3^- reduction and I^- oxidation, plus IO_3^- planktonic uptake (and subsequence I^- release during remineralization), all fell within the range of field and experiment observations and hence could be considered plausible. Three iodine cycling parameterization -combinations, 'lifetime-threshold', 'reminO2lifetime-threshold', and 'fennel-threshold' were considered as viable candidates following our tests of the global ocean model M-score, and model-data comparisons made across specific iodine gradients (euphotic latitudinal

distribution, depth distribution, and ODZ distribution). We further evaluated the plausibility of our parameterizations and their paleo and ocean deoxygenation applicability by contrasting forward-proxy model generated I/Ca values against observations, taking the (pre-OAE2) Cretaceous redox landscape as a case study. While we highlighted the importance of improving the simulation of dissolved oxygen distributions in models, we also found that our conclusions regarding preferred parameterizations and even specific parameter values was not overly dependent on the specific details of the simulated modern ODZs. Overall, while some model-data discrepancies emerge for both modern and paleo, these highlight that future observational and/or experimental work is necessary to better constrain modern iodine cycling mechanisms and related spatiotemporal heterogeneities but that representations of the marine iodine cycle in an Earth system model based on modern observations and mechanistic knowledge appear transferrable to interpreting the geological record of the I/Ca oxygenation proxy.

REFERENCES

Amachi S, Kawaguchi N, Muramatsu Y, Tsuchiya S, Watanabe Y, Shinoyama H, Fujii T (2007) Dissimilatory iodate reduction by marine Pseudomonas sp. strain SCT. *Applied and Environmental Microbiology* **73**, 5725–5730.

Boscolo-Galazzo F, Crichton KA, Ridgwell A, Mawbey EM, Wade BS, Pearson PN (2021) Temperature controls carbon cycling and biological evolution in the ocean twilight zone. *Science* **371**, 1148–1152.

Bowman CN, Lindskog A, Kozik NP, Richbourg CG, Owens JD, Young SA (2020) Integrated sedimentary, biotic, and paleoredox dynamics from multiple localities in southern Laurentia during the late Silurian (Ludfordian) extinction event. *Palaeogeography, Palaeoclimatology, Palaeoecology* **553**, 109799.

Broecker WS, Peng TH (1983) *Tracers in the Sea.* Lamont-Doherty Geological Observatory, Columnbia University, New York.

Campos MLAM, Farrenkopf AM, Jickells TD, Luther GW (1996) A comparison of dissolved iodine cycling at the Bermuda Atlantic Time-series station and Hawaii Ocean Time-series station. *Deep-Sea Research Part II: Topical Studies in Oceanography* **43**, 455–466.

Chance R, Baker AR, Carpenter L, Jickells TD (2014) The distribution of iodide at the sea surface. *Environmental Sciences: Processes and Impacts* **16**, 1841–1859.

Chance R, Tinel L, Sherwen T, Baker A, Bell T, Brindle J, Campos M, Croot P, Ducklow H, He P, Hoogakker B, Hopkins F, Hughes C, Jickells T, Loades D, Reyes Macaya D, Mahajan A, Malin G, Phillips D, Sinha A, Sarkar A, Roberts I, Roy R, Song X, Winklebauer H, Wuttig K, Yang M, Zhou P, Carpenter L (2019) Global sea-surface iodide observations, 1967-2018. *Scientific Data* **286**.

Chance R, Weston K, Baker AR, Hughes C, Malin G, Carpenter L, Meredith MP, Clarke A, Jickells TD, Mann P, Rossetti H (2010) Seasonal and interannual variation of dissolved iodine speciation at a coastal Antarctic site. *Marine Chemistry* **118**, 171–181.

Chapman P (1983) Changes in iodine speciation in the Benguela current upwelling system. *Deep Sea Research Part A, Oceanographic Research Papers* **30**, 1247–1259.

Councell TB, Landa ER, Lovley DR (1997) Microbial reduction of iodate. *Water, Air, and Soil Pollution* **100**, 99–106.

Crichton KA, Wilson JD, Ridgwell A, Pearson PNPN (2021) Calibration of temperature-dependent ocean microbial processes in the cGENIE.muffin (v0.9.13) Earth system model. *Geoscientific Model Development* **14**, 125–149.

Cutter GA, Moffett JG, Nielsdóttir MC, Sanial V (2018) Multiple oxidation state trace elements in suboxic waters off Peru: In situ redox processes and advective/diffusive horizontal transport. *Marine Chemistry* **201**, 77–89.

Dalsgaard T, Stewart FJ, Thamdrup B, Brabandere L De, Revsbech NP, Ulloa O, Canfield DE, Delong EF (2014) Oxygen at nanomolar levels reversibly suppresses process rates and gene expression in anammox and denitrification in the oxygen minimum zone off Northern Chile. *mBio* **5**, 1–14.

Ding Y, Sun W, Liu S, Xie J, Tang D, Zhou X, Zhou L, Li Z, Song J, Li Z, Xu H, Tang P, Liu K, Li W, Chen D (2022) Low oxygen levels with high redox heterogeneity in the late Ediacaran shallow ocean: Constraints from I/(Ca + Mg) and Ce/Ce* of the Dengying Formation, South China. *Geobiology* **20**, 790–809.

Edwards A, Truesdale VW (1997) Regeneration of inorganic iodine species in loch etive, a natural leaky incubator. *Estuarine, Coastal and Shelf Science* **45**, 357–366.

Edwards CT, Fike DA, Saltzman MR, Lu W, Lu Z (2018) Evidence for local and global redox conditions at an Early Ordovician (Tremadocian) mass extinction. *Earth and Planetary Science Letters* **481**, 125–135.

Edwards NR, Marsh R (2005) Uncertainties due to transport-parameter sensitivity in an efficient 3-D ocean-climate model. *Climate Dynamics* **24**, 415–433.

Elderfield H, Truesdale VW (1980) On the biophilic nature of iodine in seawater. *Earth and Planetary Science Letters* **50**, 105–114.

Fang H, Tang D, Shi X, Zhou L, Zhou X, Wu M, Song H, Riding R (2022) Early Mesoproterozoic Ca-carbonate precipitates record fluctuations in shallow marine oxygenation. *Precambrian Research* **373**, 106630.

Farrenkopf AM, Dollhopf ME, Chadhain SN, Luther GW, Nealson KH (1997) Reduction of iodate in seawater during Arabian Sea shipboard incubations and in laboratory cultures of the marine bacterium Shewanella putrefaciens strain MR-4. *Marine Chemistry* **57**, 347–354.

Farrenkopf AM, Luther GW (2002) Iodine chemistry reflects productivity and denitrification in the Arabian Sea: Evidence for flux of dissolved species from sediments of western India into the OMZ. *Deep-Sea Research Part II: Topical Studies in Oceanography* **49**, 2303–2318.

Fennel K, Follows M, Falkowski PG (2005) The co-evolution of the nitrogen, carbon and oxygen cycles in the Proterozoic ocean. *American Journal of Science* **305**, 526–545.

Garcia HE, Weathers K, Paver CR, Smolyar I, Boyer TP, Locarnini RA, Zweng MM, Mishonov A V., Baranova OK, Seidov D, Reagan JR (2018) *Volume 3: Dissolved Oxygen, Apparent Oxygen Utilization, and Oxygen Saturation. A. Mishonov Technical Ed.; NOAA Atlas NESDIS 83. World Ocean Atlas 2018*.

Hardisty DS, Horner TJ, Evans N, Moriyasu R, Babbin AR, Wankel SD, Moffett JW, Nielsen SG (2021) Limited iodate reduction in shipboard seawater incubations from the Eastern Tropical North Pacific oxygen deficient zone. *Earth and Planetary Science Letters* **554**, 116676.

Hardisty DS, Horner TJ, Wankel SD, Blusztajn J, Nielsen SG (2020) Experimental observations of marine iodide oxidation using a novel sparge-interface MC-ICP-MS technique. *Chemical Geology* **532**, 119360.

Hardisty DS, Lu Z, Bekker A, Diamond CW, Gill BC, Jiang G, Kah LC, Knoll AH, Loyd SJ, Osburn MR, Planavsky NJ, Wang C, Zhou X, Lyons TW (2017) Perspectives on Proterozoic surface ocean redox from iodine contents in ancient and recent carbonate. *Earth and Planetary Science Letters* **463**, 159–170.

Hardisty DS, Lu Z, Planavsky NJ, Bekker A, Philippot P, Zhou X, Lyons TW (2014) An iodine record of Paleoproterozoic surface ocean oxygenation. *Geology* **42**, 619–622.

Hashim MS, Burke JE, Hardisty DS, Kaczmarek SE (2022) Iodine incorporation into dolomite: Experimental constraints and implications for the iodine redox proxy and Proterozoic Ocean. *Geochimica et Cosmochimica Acta* **338**, 365–381.

He P, Hou X, Aldahan A (2013) Iodine isotopes species fingerprinting environmental conditions in surface water along the northeastern Atlantic Ocean. *Scientific Reports* **3**, 1–9.

Hepach H, Hughes C, Hogg K, Collings S, Chance R (2020) Senescence as the main driver of iodide release from a diverse range of marine phytoplankton. *Biogeosciences* **17**, 2453–2471.

Holden PB, Edwards NR, Fraedrich K, Kirk E, Lunkeit F, Zhu X (2016) PLASIM-GENIE v1.0: A new intermediate complexity AOGCM. *Geoscientific Model Development* **9**, 3347–3361.

Hughes C, Barton E, Hepach H, Chance R, Wadley MR, Pickering MD, Hogg K, Pommerening-r A, Stevens DP, Jickells TD (2021) Oxidation of iodide to iodate by cultures of marine ammonia-oxidising bacteria. *Marine Chemistry* **234**, 1–7.

Hülse D, Arndt S, Ridgwell A (2019) Mitigation of Extreme Ocean Anoxic Event Conditions by Organic Matter Sulfurization. *Paleoceanography and Paleoclimatology* **34**, 476–489.

Jia-zhong Z, Whitfield M (1986) KINETICS OF INORGANIC REDOX REACTIONS IN SEAWATER I . The reduction of iodate by bisulphide Micro-organisms play a dominant role in the diagenesis of organic-rich sediments . The oxidative breakdown of the organic matter , with the accom- panying reductio. *Science* **19**, 121–137.

Jiang Z, Cui M, Qian L, Jiang Y, Shi L, Dong Y, Li J, Wang Y (2023) Abiotic and Biotic Reduction of Iodate Driven by Shewanella oneidensis MR-1. *Environmental Science & Technology* **57**, 19817–19826.

Keery JS, Holden PB, Edwards NR (2018) Sensitivity of the Eocene climate to CO2 and orbital variability. *Climate of the Past* **14**, 215–238.

Kerisit SN, Smith FN, Saslow SA, Hoover ME, Lawter AR, Qafoku NP (2018) Incorporation Modes of Iodate in Calcite. *Environmental Science and Technology* **52**, 5902–5910.

Laws EA, Falkowski PG, Smith WO, Ducklow H, James J McCarthy (2000) Temperature effects on export production in the open ocean. *Global Biogeochemical Cycles* **14**, 1231–1246.

Liu A, Tang D, Shi X, Zhou X, Zhou L, Shang M, Li Y, Fang H (2020) Mesoproterozoic oxygenated deep seawater recorded by early diagenetic carbonate concretions from the Member IV of the Xiamaling Formation, North China. *Precambrian Research* **341**, 105667.

Lu W, Dickson AJ, Thomas E, Rickaby REM, Chapman P, Lu Z (2020a) Refining the planktic foraminiferal I/Ca proxy: Results from the Southeast Atlantic Ocean. *Geochimica et Cosmochimica Acta* **287**, 318–327.

Lu W, Rickaby REM, Hoogakker BAA, Rathburn AE, Burkett AM, Dickson AJ, Martínez-Méndez G, Hillenbrand CD, Zhou X, Thomas E, Lu Z (2020b) I/Ca in epifaunal benthic foraminifera: A semi-quantitative proxy for bottom water oxygen in a multi-proxy compilation for glacial ocean deoxygenation. *Earth and Planetary Science Letters* **533**, 116055.

Lu W, Ridgwell A, Thomas E, Hardisty DS, Luo G, Algeo TJ, Saltzman MR, Gill BC, Shen Y, Ling HF, Edwards CT, Whalen MT, Zhou X, Gutchess KM, Jin L, Rickaby REM, Jenkyns HC, Lyons TW, Lenton TM, Kump LR, Lu Z (2018) Late inception of a resiliently oxygenated upper ocean. *Science* **361**, 174–177.

Lu Z, Hoogakker BAA, Hillenbrand C-D, Zhou X, Thomas E, Gutchess KM, Lu W, Jones L, Rickaby REM (2016) Oxygen depletion recorded in upper waters of the glacial Southern Ocean. *Nature Communications* **7**, 1–8.

Lu Z, Jenkyns HC, Rickaby REM (2010) Iodine to calcium ratios in marine carbonate as a paleo-redox proxy during oceanic anoxic events. *Geology* **38**, 1107–1110.

Luther GW (2023) Review on the physical chemistry of iodine transformations in the oceans. *Frontiers in Marine Science* **10**, 1–16.

Luther GW, Campbell T (1991) Iodine speciation in the water column of the Black Sea. *Deep Sea Research Part A. Oceanographic Research Papers* **38**, S875–S882.

Luther GW, Wu J, Cullen JB (1995) Redox Chemistry of Iodine in Seawater. *Advances in Chemistry* **244**, 135–155.

Luther W (1991) Iodine Chemistry in the Water the Chesapeake Bay : Evidence Iodine Forms Column of for Organic. *Esruarine, Coastal and Shelf Science* **32**, 267–279.

Marsh R, Müller SA, Yool A, Edwards NR (2011) Incorporation of the C-GOLDSTEIN efficient climate model into the GENIE framework: "eb_go_gs" configurations of GENIE. *Geoscientific Model Development* **4**, 957–992.

Martin TS, Primeau F, Casciotti KL (2019) Modeling oceanic nitrate and nitrite concentrations and isotopes using a 3-D inverse N cycle model. *Biogeosciences* 347–367.

Matsumoto K (2007) Radiocarbon-based circulation age of the world oceans. *Journal of Geophysical Research: Oceans* **112**, 1–7.

Monteiro FM, Pancost RD, Ridgwell A, Donnadieu Y (2012) Nutrients as the dominant control on the spread of anoxia and euxinia across the Cenomanian-Turonian oceanic anoxic event (OAE2): Model-data comparison. *Paleoceanography* **27**, 1–17.

Moriyasu R, Bolster KM, Hardisty DS, Kadko DC, Stephens MP, Moffett JW (2023) Meridional survey of the Central Pacific reveals iodide accumulation in equatorial surface waters and benthic sources in the abyssal plain. *Global Biogeochemical Cycles* **37**, 1–15.

Moriyasu R, Evans N, Bolster KM, Hardisty DS, Moffett JW (2020) The Distribution and Redox Speciation of Iodine in the Eastern Tropical North Pacific Ocean. *Global Biogeochemical Cycles* **34**, 1–23.

Panchuk K, Ridgwell A, Kump LR (2008) Sedimentary response to Paleocene-Eocene thermal maximum carbon release: A model-data comparison. *Geology* **36**, 315–318.

Podder J, Lin J, Sun W, Botis SM, Tse J, Chen N, Hu Y, Li D, Seaman J, Pan Y (2017) Iodate in calcite and vaterite: Insights from synchrotron X-ray absorption spectroscopy and first-principles calculations. *Geochimica et Cosmochimica Acta* **198**, 218–228.

Pohl A, Lu Z, Lu W, Stockey RG, Elrick M, Li M, Desrochers A, Shen Y, He R, Finnegan S, Ridgwell A (2021) Vertical decoupling in Late Ordovician anoxia due to reorganization of ocean circulation. *Nature Geoscience* **14**, 868–873.

Pohl A, Ridgwell A, Stockey RG, Thomazo C, Keane A, Vennin E, Scotese CR (2022) Continental configuration controls ocean oxygenation during the Phanerozoic. *Nature* **608**, 523–527.

Rapp I, Schlosser C, Barraqueta JM, Wenzel B, Lüdke J, Scholten J (2019) Controls on redox-sensitive trace metals in the Mauritanian oxygen minimum zone. *Biogeosciences* **16**, 4157–4182.

Rapp I, Schlosser C, Browning TJ, Wolf F, Moigne FAC Le, Gledhill M, Achterberg EP (2020) El Niño-Driven Oxygenation Impacts Peruvian Shelf Iron Supply to the South Pacific Ocean. *Geophysical Research Letters* **47**.

Reinhard CT, Olson SL, Turner SK, Pälike C, Kanzaki Y, Ridgwell A (2020) Oceanic and atmospheric methane cycling in the cGENIE Earth system model. *Geoscientific Model Development* 1–45.

Reinhard CT, Planavsky NJ (2022) The History of Ocean Oxygenation. *Annual Review of Marine Science* **14**, 331–353.

Reinhard CT, Planavsky NJ, Olson SL, Lyons TW, Erwin DH (2016) Earth's oxygen cycle and the evolution of animal life. *Proceedings of the National Academy of Sciences of the United States of America* **113**, 8933–8938.

Remmelzwaal SRC, Dixon S, Parkinson IJ, Schmidt DN, Monteiro FM, Sexton P, Fehr MA, Peacock C, Donnadieu Y, James RH (2019) Investigating Ocean Deoxygenation During the PETM Through the Cr Isotopic Signature of Foraminifera. *Paleoceanography and Paleoclimatology* **34**, 917–929.

Reyes-Umana V, Henning Z, Lee K, Barnum TP, Coates JD (2021) Genetic and phylogenetic analysis of dissimilatory iodate-reducing bacteria identifies potential niches across the world's oceans. *ISME Journal* **16**, 38–49.

Ridgwell A, Hargreaves JC, Edwards NR, Annan JD, Lenton TM, Marsh R, Yool A, Watson A (2007) Marine geochemical data assimilation in an efficient Earth system model of global biogeochemical cycling. *Biogeosciences* **4**, 87–104.

Rue EL, Smith GJ, Cutter GA, Bruland KW (1997) The response of trace element redox couples to suboxic conditions in the water column. *Deep-Sea Research Part I: Oceanographic Research Papers* **44**, 113–134.

Schnur AA, Sutherland KM, Hansel CM, Hardisty DS (2024) Rates and pathways of iodine speciation transformations at the Bermuda Atlantic Time Series. *Frontiers in Marine Science* **10**, 1–14.

Scholz F, Hardisty DS, Dale AW (2024) Early Diagenetic Controls on Sedimentary Iodine Release and Iodine-To-Organic Carbon Ratios in the Paleo-Record. *Global Biogeochemical Cycles* **38**, e2023GB007919.

Shang M, Tang D, Shi X, Zhou L, Zhou X, Song H, Jiang G (2019) A pulse of oxygen increase in the early Mesoproterozoic ocean at ca. 1.57–1.56 Ga. *Earth and Planetary Science Letters* **527**, 115797.

Ştreangă I-M, Repeta DJ, Blusztajn JS, Horner TJ (2024) Speciation and cycling of iodine in the subtropical North Paci fi c Ocean. *Frontiers in Marine Science* **10**, 1272968.

Tang D, Fang H, Shi X, Liang L, Zhou L, Xie B, Huang K, Zhou X, Wu M, Riding R (2023) Mesoproterozoic Molar Tooth Structure Related to Increased Marine Oxygenation. *Journal of Geophysical Research: Biogeosciences* **128**, 1–18.

Thamdrup B, Dalsgaard T, Revsbech NP (2012) Widespread functional anoxia in the oxygen minimum zone of the Eastern South Pacific. *Deep-Sea Research Part I: Oceanographic Research Papers* **65**, 36–45.

Truesdale VW, Bale AJ, Woodward EMS (2000) The meridional distribution of dissolved iodine in near-surface waters of the Atlantic Ocean. *Progress in Oceanography* **45**, 387–400.

Truesdale VW, Nausch G, Waite TJ (2013) The effects of the 2001 Barotropic intrusion of bottom-water upon the vertical distribution of inorganic iodine in the Gotland Deep. *Continental Shelf Research* **55**, 155–167.

Truesdale VW, Watts SF, Rendell AR (2001) On the possibility of iodide oxidation in the near-

surface of the Black Sea and its implications to iodine in the general ocean. *Deep-Sea Research Part I* **48**, 2397–2412.

Tsunogai S (1971) Iodine in the deep water of the ocean. *Deep-Sea Research* **18**, 913–919.

Uahengo CI, Shi X, Jiang G, Vatuva A (2020) Transient shallow-ocean oxidation associated with the late Ediacaran Nama skeletal fauna: Evidence from iodine contents of the Lower Nama Group, southern Namibia. *Precambrian Research* **343**, 105732.

Wadley MR, Stevens DP, Jickells TD, Hughes C, Chance R, Hepach H, Tinel L, Carpenter LJ (2020) A Global Model for Iodine Speciation in the Upper Ocean. *Global Biogeochemical Cycles* **34**, 0–3.

Watterson IG (1996) Non-dimensional measures of climate model performance. *International Journal of Climatology* **16**, 379–391.

Wei B, Tang D, Shi X, Lechte M, Zhou L, Zhou X, Song H (2021) A Pulsed Oxygenation in Terminal Paleoproterozoic Ocean: Evidence From the Transition Between the Chuanlinggou and Tuanshanzi Formations, North China. *Geochemistry, Geophysics, Geosystems* **22**, 1–23.

Wong GTF, Brewer PG (1977) The marine chemistry of iodine in anoxic basins. *Geochimica et Cosmochimica Acta* **41**, 151–159.

Wong GTF, Piumsomboon AU, Dunstan WM, Wong GTF, Piumsomboon AU, Dunstan WM (2002) The transformation of iodate to iodide in marine phytoplankton cultures. *Marine Geology Progress Series* **237**, 27–39.

Wong GTF, Takayanagi K, Todd JF (1985) Dissolved iodine in waters overlying and in the Orca Basin, Gulf of Mexico. *Marine Chemistry* **17**, 177–183.

Yamazaki C, Kashiwa S, Horiuchi A, Kasahara Y (2020) A novel dimethylsulfoxide reductase family of molybdenum enzyme , Idr , is involved in iodate respiration by Pseudomonas sp . SCT. *Environmental Microbiology* **22**, 2196–2212.

Yu Y, Chen Y, Li D, Su J (2022) A transient oxygen increase in the Mesoproterozoic ocean at ∼1.44 Ga: Geochemical evidence from the Tieling Formation, North China Platform. *Precambrian Research* **369**, 106527.

Zhang S, Xu C, Creeley D, Ho YF, Li HP, Grandbois R, Schwehr KA, Kaplan DI, Yeager CM, Wellman D, Santschi PH (2013) Response to comment on "iodine-129 and iodine-127 speciation in groundwater at hanford site, U.S.: Iodate incorporation into calcite." *Environmental Science and Technology* **47**, 13205–13206.

Zhou X, Jenkyns HC, Owens JD, Junium CK, Zheng XY, Sageman BB, Hardisty DS, Lyons TW, Ridgwell A, Lu Z (2015) Upper ocean oxygenation dynamics from I/Ca ratios during the Cenomanian-Turonian OAE 2. *Paleoceanography* **30**, 510–526.

Zhou X, Thomas E, Rickaby REM, Winguth AME, Lu Z (2014) I/Ca evidence for upper ocean deoxygenation during the PETM. *Paleoceanography* **29**, 964–975.

Žic V, Carić M, Ciglenečki I (2013) The impact of natural water column mixing on iodine and nutrient speciation in a eutrophic anchialine pond (Rogoznica Lake, Croatia). *Estuarine, Coastal and Shelf Science* **133**, 260–27

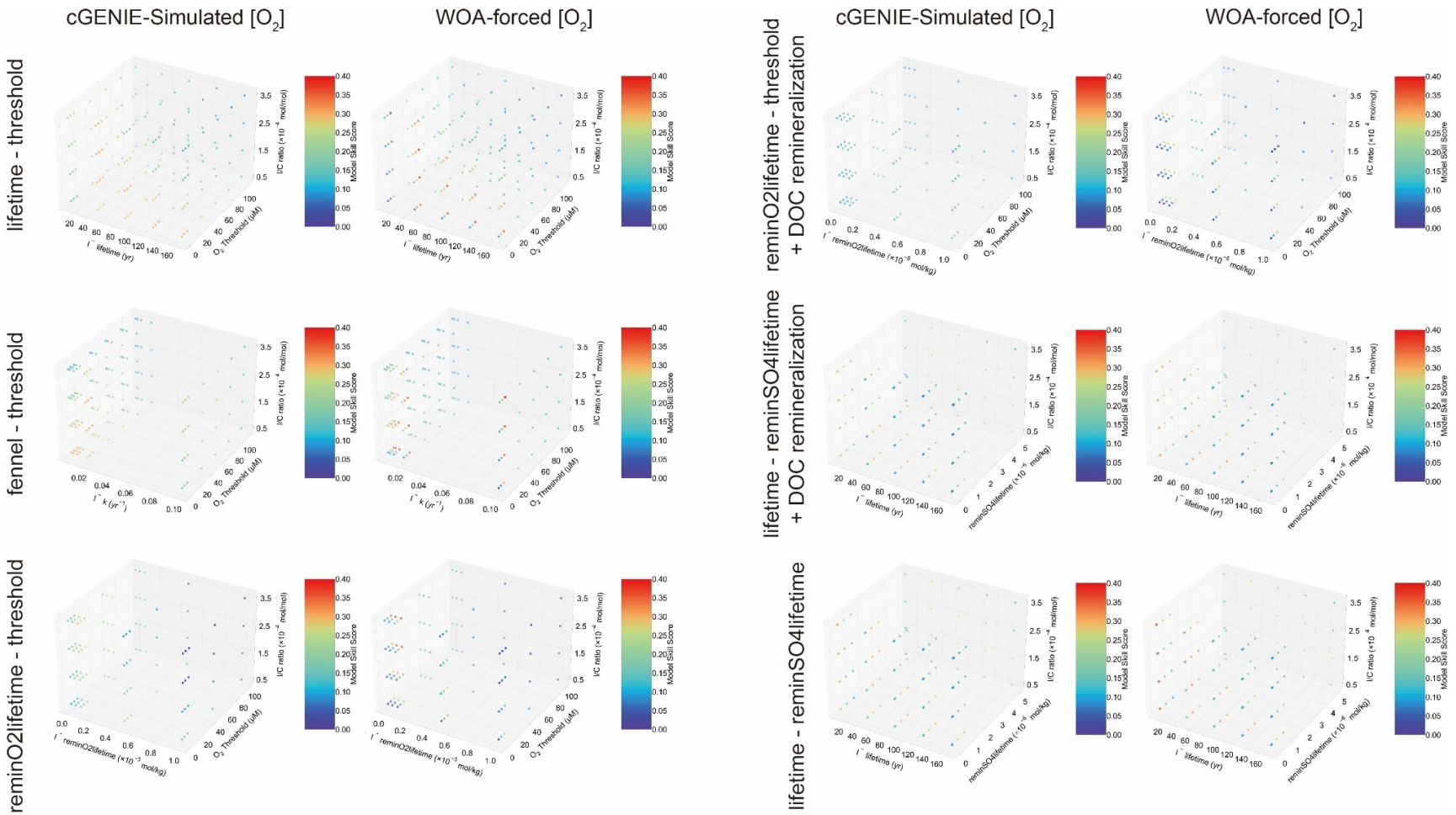

Figure 3.10. The three-dimensional model skill score array of all the experiment ensembles tested in this study.

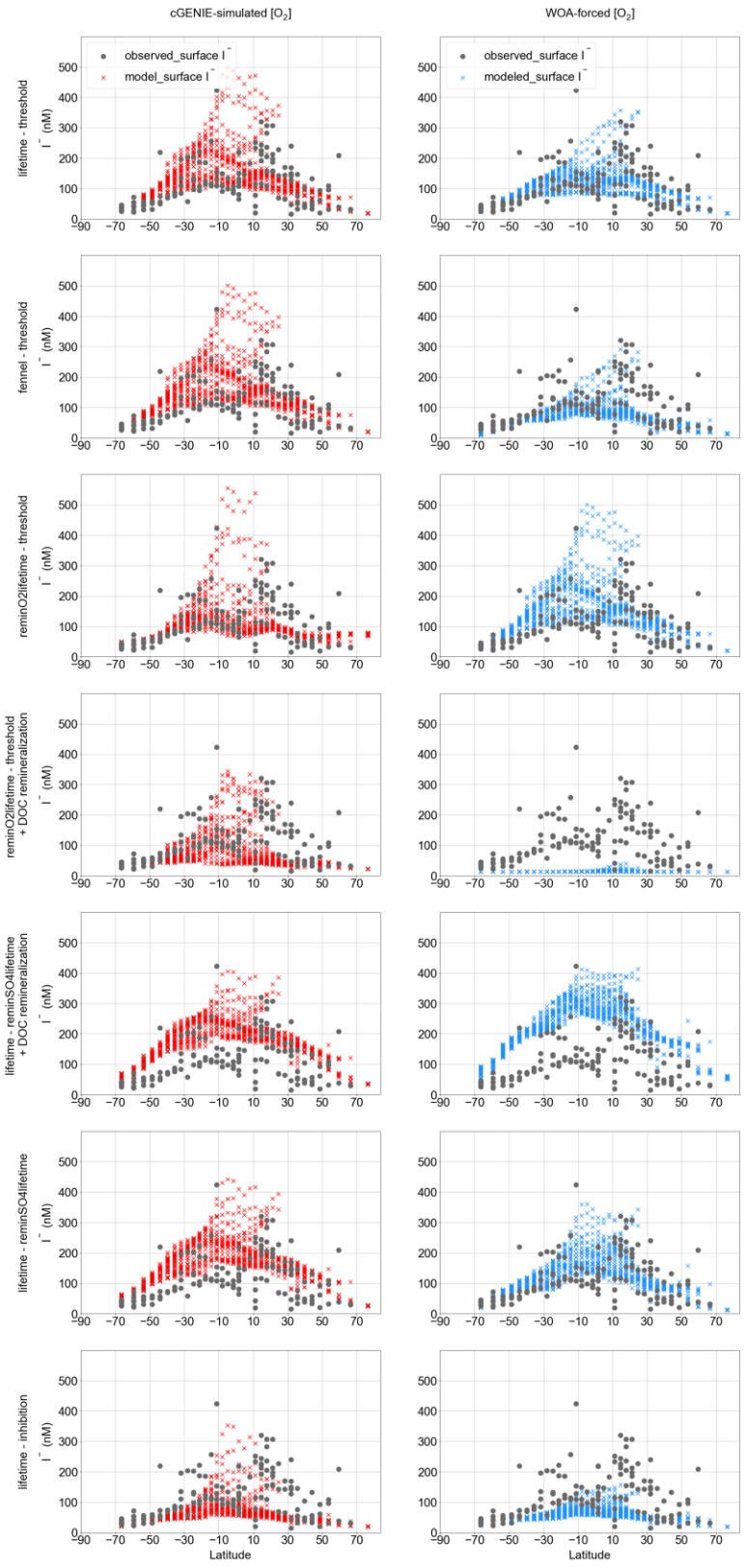

Figure 3.11. Modeled latitudinal surface iodide distribution compared with observation with the cGENIE simulated [O_2] and the WOA-[O_2] restoring forcing.

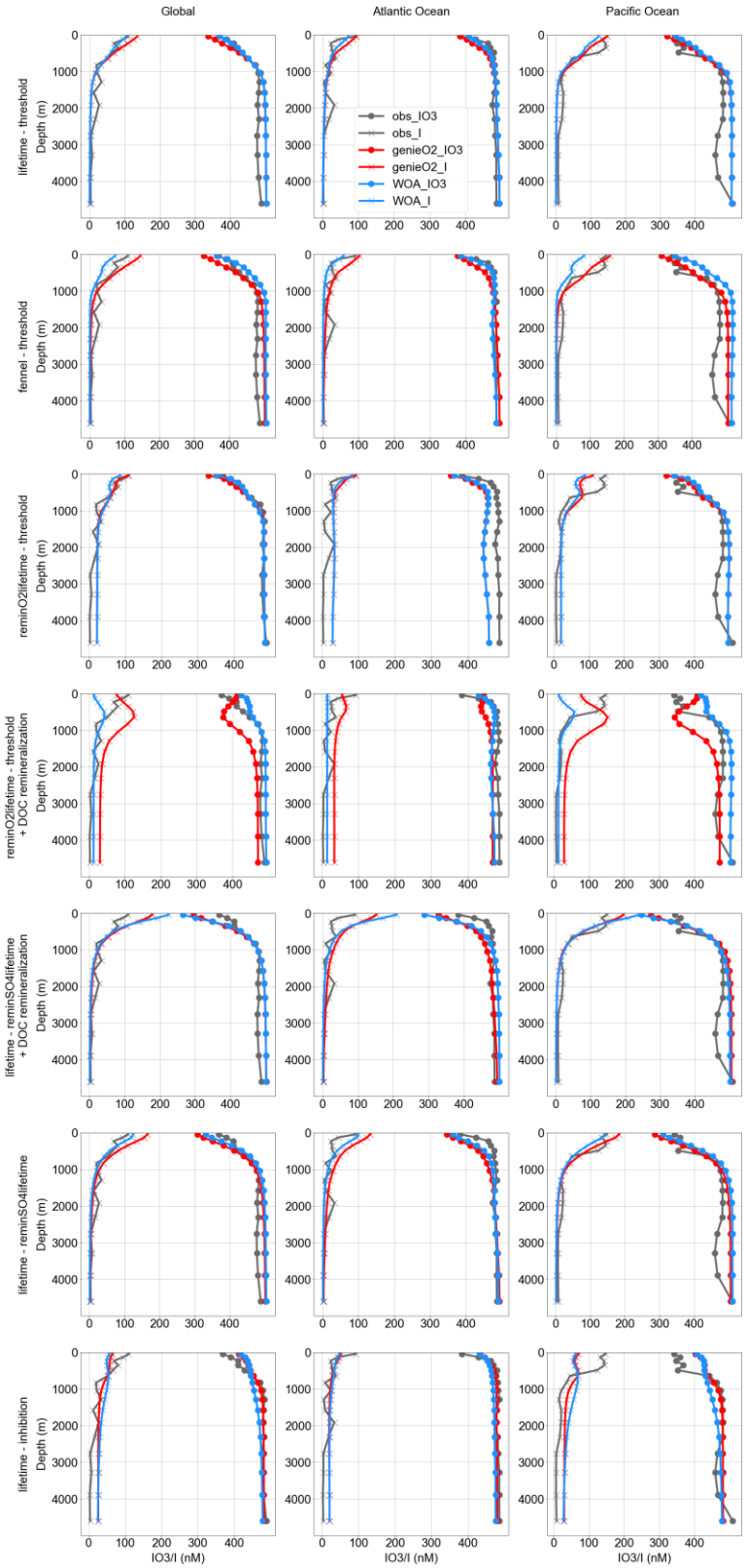

Figure 3.12. Modeled averaged iodine (including iodate and iodide) depth profile among global ocean, the Pacific, the Atlantic compared with observation.

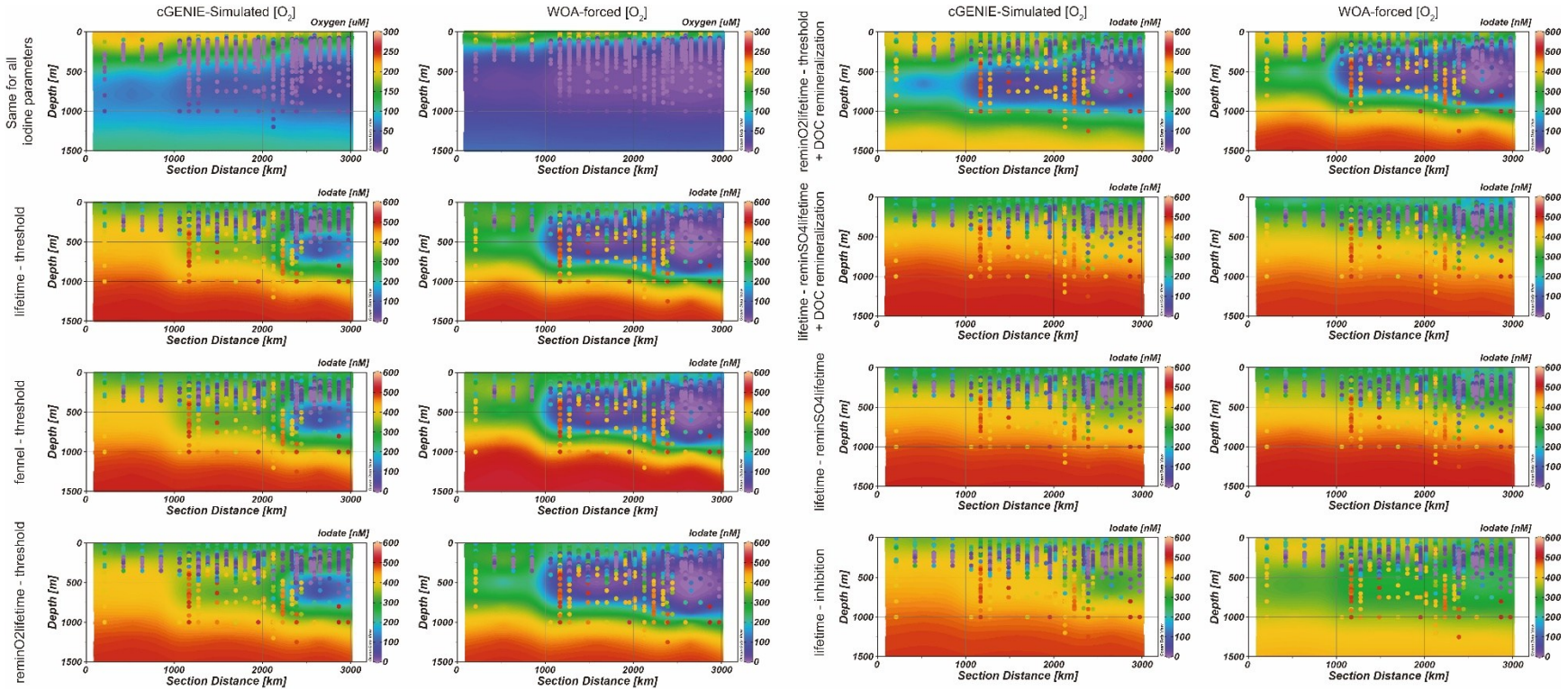

Figure 3.13. Modeled (contour) and observed (colored dots) transects of IO_3^- in the ETNP.

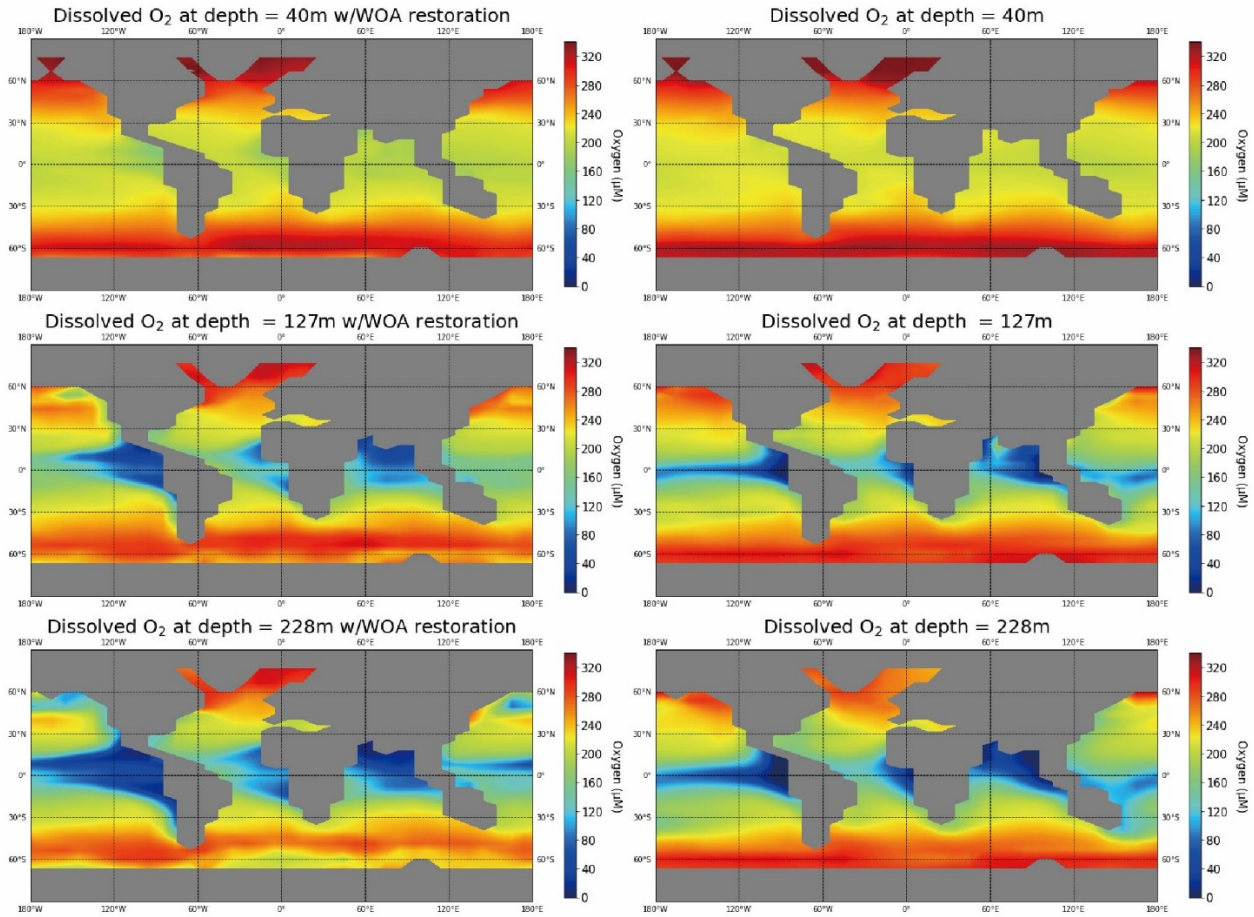

Figure 3.14. The modeled O_2 distribution in the surface and subsurface with [O_2] forced to restore the WOA observation and without forcing.

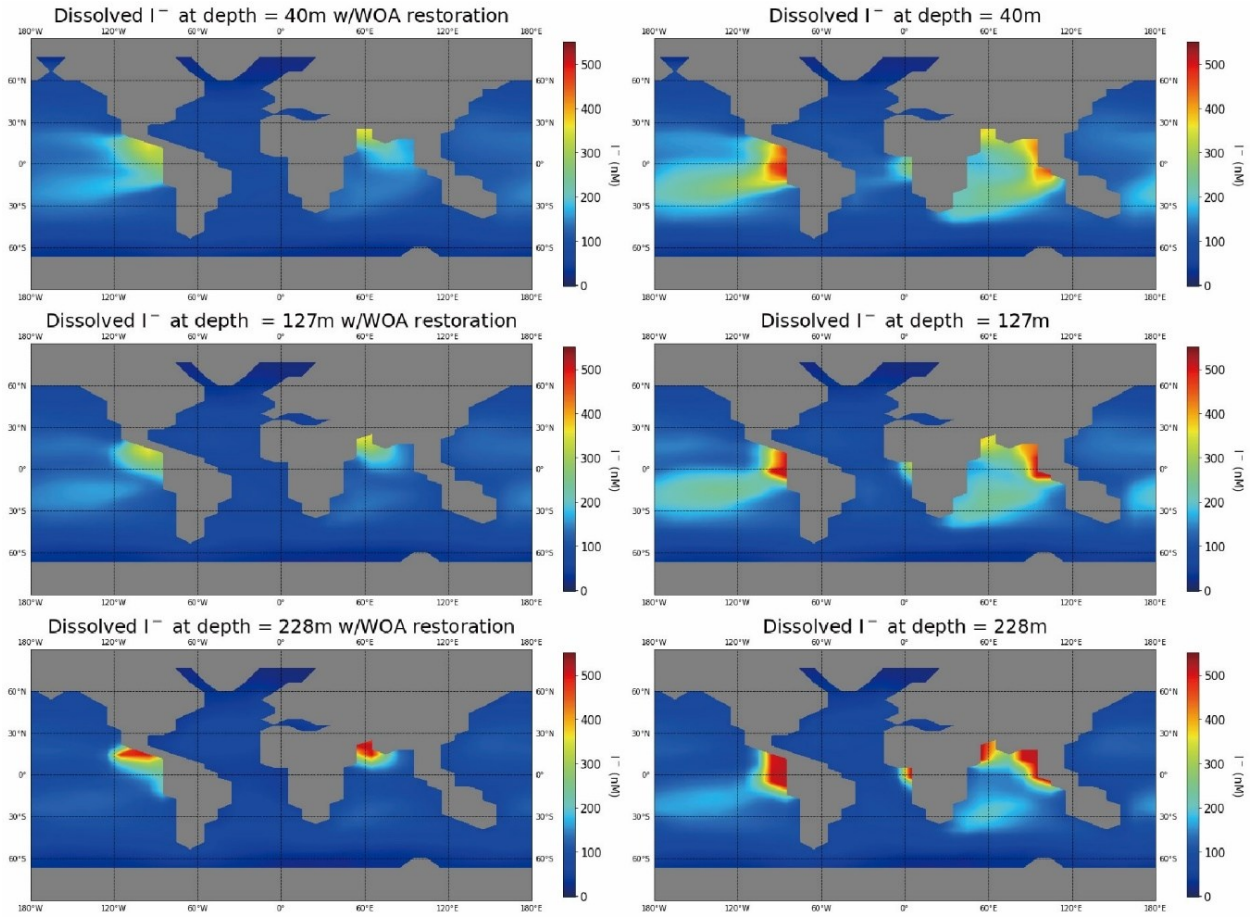

Figure 3.15. The modeled I^- distribution in the surface and subsurface with $[O_2]$ forced to restore the WOA observation and without forcing. Associated iodine cycling parameters: "lifetime" = 50 yrs; "threshold" = 10×10^{-6} mol; I:C ratio = 1.5×10^{-4} mol/mol. This is an example of cGENIE overestimating surface I^- when the overall model performance is tuned to the best.

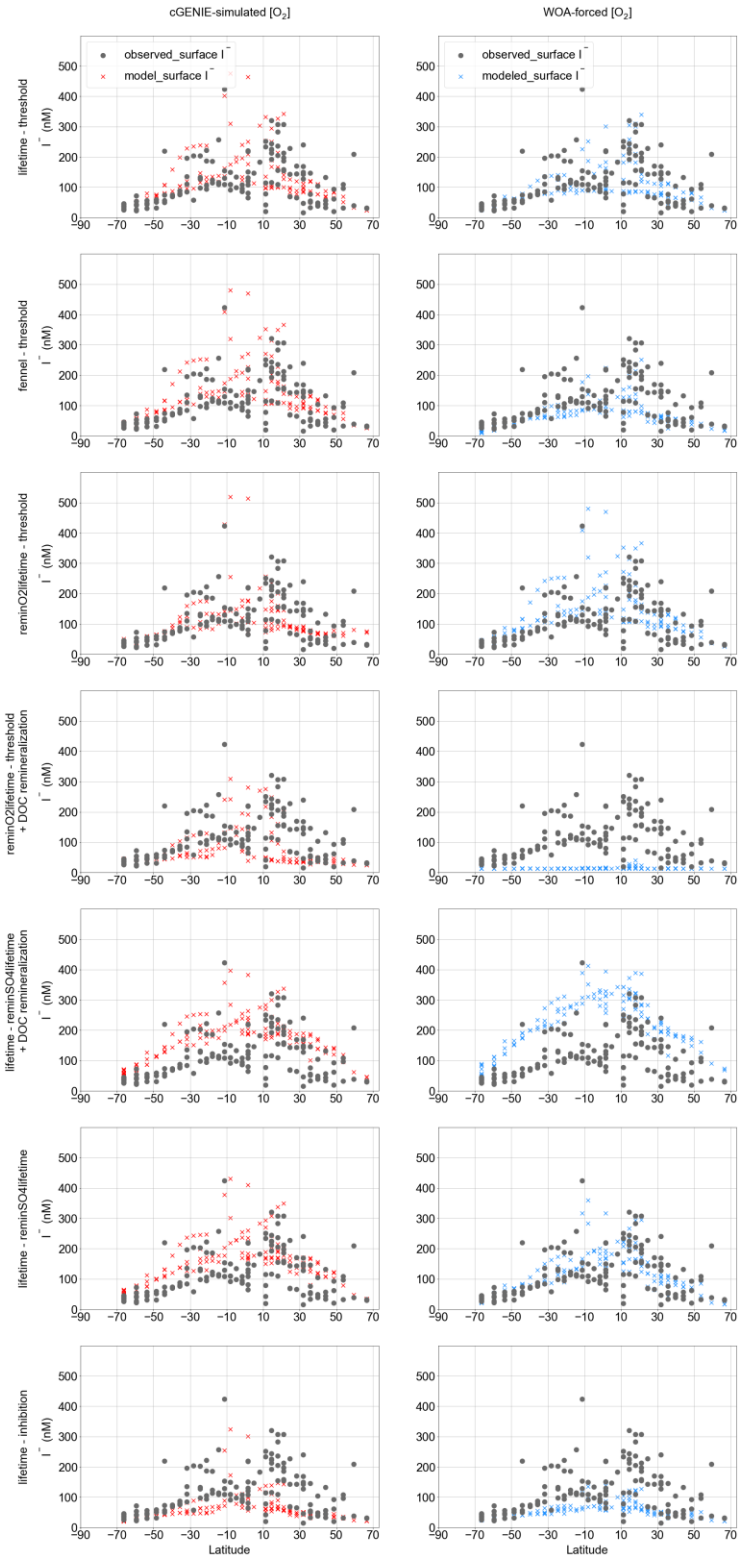

Figure 3.16. Modeled latitudinal surface iodide distribution compared with observation with the cGENIE simulated [O_2] (masked only include grid points with corresponding observations) and the [O_2] restoring forcing.

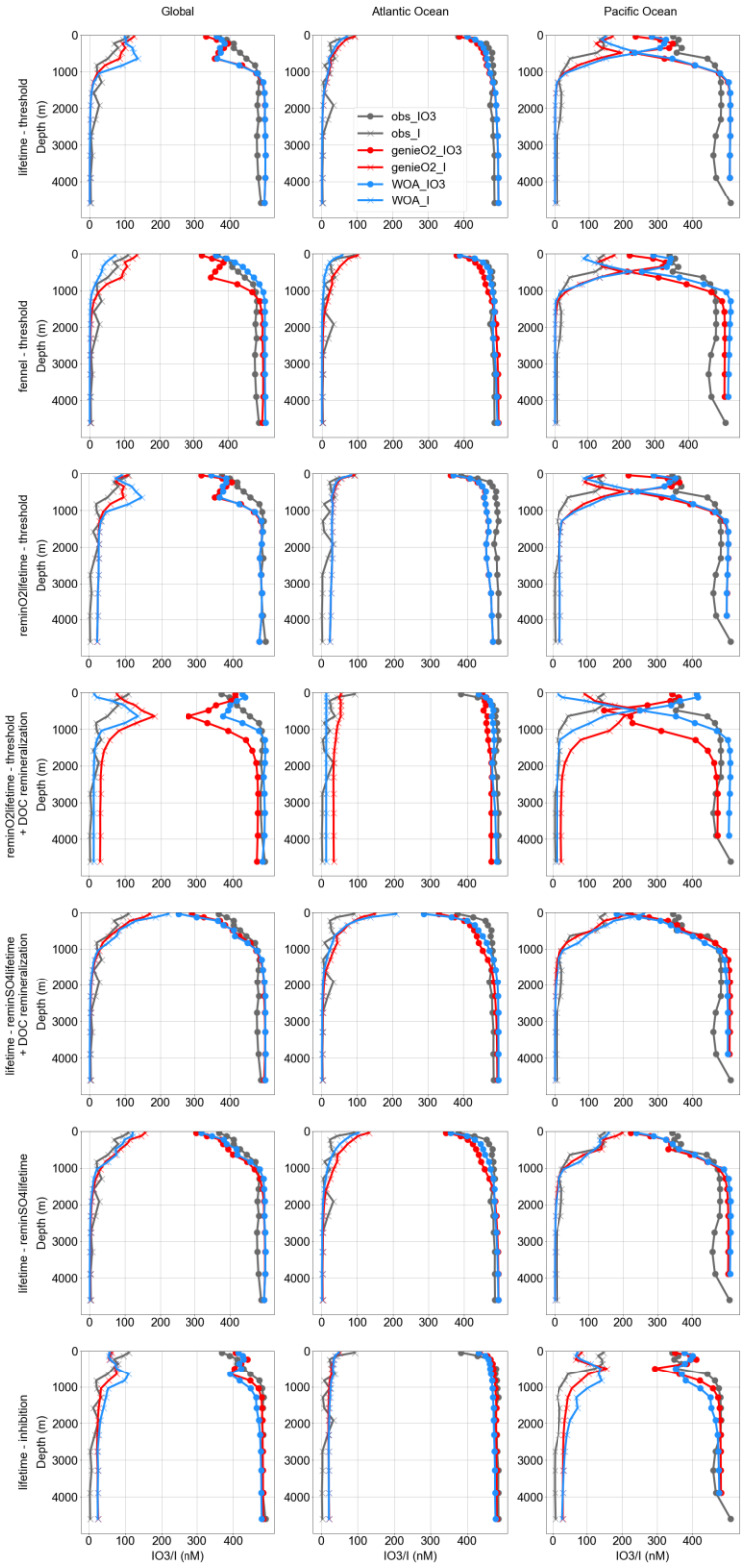

Figure 3.17. Modeled averaged iodine (including iodate and iodide, and masked only include grid points with corresponding observations) depth profile among global ocean, the Pacific, the Atlantic compared with observation.

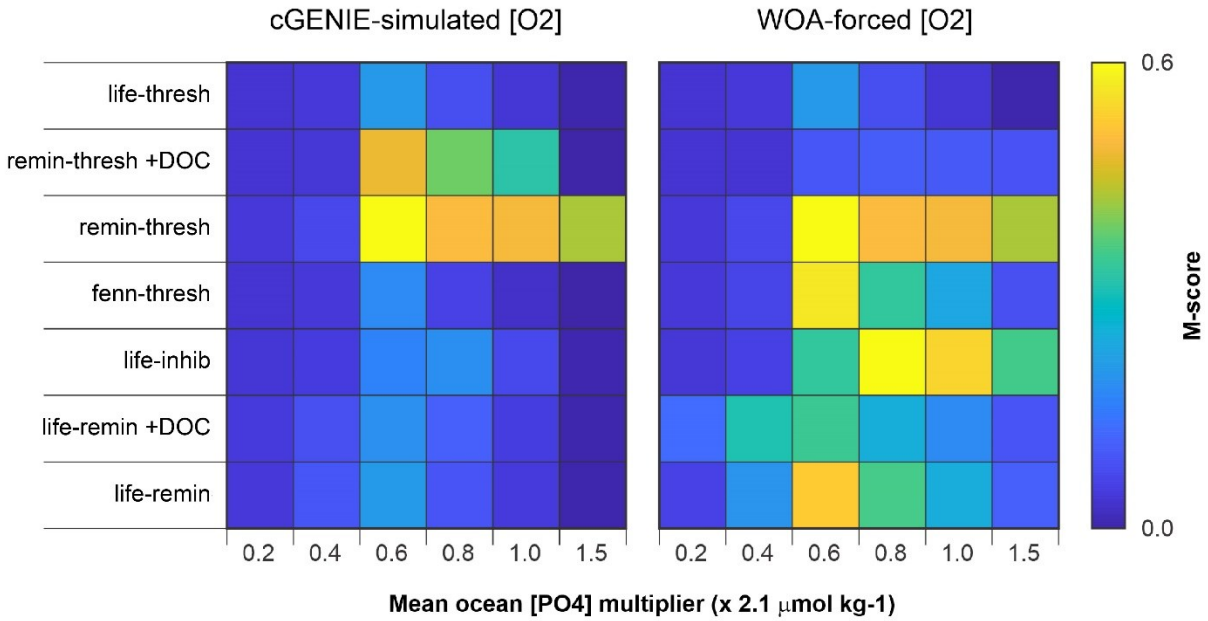

Figure 3.18. The model skill scores between modeled and measured I/Ca during the pre-OAE2. The iodine cycling parameters are derived from modern simulations with cGENIE-simulated [O_2] and WOA-forced [O_2], respectively. lifetime-thresh = lifetime-threshold; remin-thresh +DOC = reminO2lifetime-threshold +DOC remineralization; remin-thresh = reminO2lifetime-threshold; fenn-thresh = fennel-threshold; life-inhib = lifetime-inhibition; life-remin +DOC = lifetime-reminSO4lifetime +DOC remineralization; life-remin = lifetime-reminSO4lifetime.

Table 3.3. The cGENIE iodine redox options and the associated range of parameters of these options in this research. Only simulations 1-3 are chosen for detailed discussion in the manuscript for higher M scores and reasonably replicating iodine ocean gradients (See 2.4).

Parameter description		Iodine oxidation parameters			Iodine reduction parameters			I:C ratio ($\times 10^{-4}$ mol/mol)
		'lifetime' (years)	'reminO2lifetime' ($\times 10^{-5}$ mol/kg)	'Fennel' (Inhibition constant/ μM O_2)	'threshold' (μM O_2)	'inhibition' (μM/ $year^{-1}$)	'reminSO4lifetime' ($\times 10^{-6}$ mol/kg)	
Simulation 1	cGENIE O_2	10-170	\	\	1-110	\	\	0.5-3.5
	WOA	10-170	\	\	1-110	\	\	0.5-3.5
	no excess I^- filtration	10-170	\	\	1-110	\	\	0.5-3.5
	no excess I^- filtration + WOA	10-170	\	\	1-110	\	\	0.5-3.5
Simulation 2	cGENIE O_2	\	0.01-1	\	1-100	\	\	0.5-3.5
	WOA	\	0.01-1	\	1-100	\	\	0.5-3.5
	cGENIE O_2 +DOC remin.	\	0.01-1	\	1-100	\	\	0.5-3.5
	WOA +DOC remin	\	0.01-1	\	1-100	\	\	0.5-3.5
Simulation 3	cGENIE O_2	10-170 (1/k)	\	20	1-110	\	\	0.5-3.5
	WOA	10-170 (1/k)	\	20	1-110	\	\	0.5-3.5
	WOA(alternative)	10-170 (1/k)	\	20	1-110	\	\	0.5-3.5
Simulation 4	cGENIE O_2	0.5-50	\	\	\	10/0.1-10	\	0.5-3.5
	WOA	0.5-50	\	\	\	10/1.0-10	\	0.5-3.5
Simulation 5	cGENIE O_2	10-170	\	\	\	\	0.01-1	0.5-3.5
	WOA	10-170	\	\	\	\	0.01-1	0.5-3.5
	cGENIE O_2 +DOC remin.	10-170	\	\	\	\	0.01-1	0.5-3.5
	WOA +DOC remin	10-170	\	\	\	\	0.01-1	0.5-3.5

Table 3.4. The performance of the cGENIE iodine simulations of all the combinations of parameters in this research and associated parameterization when the model reaches the best global M score.

Parameter description		Iodine oxidation parameters			Iodine reduction parameters				
		'lifetime' (years)	'reminO2lifetime' (× 10^{-5} mol/kg)	'Fennel' (Inhibition constant/ μM O_2)	'threshold' (μM O_2)	'inhibition' (μM/ $year^{-1}$)	'reminSO4lifetime' (× 10^{-6} mol/kg)	I:C ratio (× 10^{-4} mol/mol)	Model skill score (global)
Simulation 1	cGENIE O_2	50	\	\	10	\	\	1.5	0.305
	WOA	50	\	\	10	\	\	1.5	0.385
	no excess I^- filtration	50	\	\	10	\	\	2.5	0.316
	no excess I^- filtration + WOA	50	\	\	10	\	\	2.5	0.393
Simulation 2	cGENIE O_2	\	0.1	\	10	\	\	3.5	0.266
	WOA	\	0.1	\	10	\	\	3.5	0.365
	cGENIE O_2 +DOC remin.	\	1	\	50	\	\	0.5	0.213
	WOA +DOC remin	\	0.1	\	10	\	\	3.5	0.302
Simulation 3	cGENIE O_2	50 (1/k)	\	20	10	\	\	1.5	0.308
	WOA	10 (1/k)	\	20	10	\	\	3.5	0.385
	WOA(alternative)	50 (1/k)	\	20	10	\	\	1.5	0.379
Simulation 4	cGENIE O_2	50	\	\	\	10/0.1	\	1.5	0.289

Table 3.4 (cont'd)

Simulation 4	WOA	10	\	\	\	10/1.0	\	1.5	0.289
Simulation 5	cGENIE O_2	50	\	\	\	\	0.5	1.5	0.307
	WOA	10	\	\	\	\	0.1	2.5	0.363
	cGENIE O_2 +DOC remin.	50	\	\	\	\	1	1.5	0.300
	WOA +DOC remin	10	\	\	\	\	0.1	0.5	0.337

Table 3.5. The Cretaceous OAE2 sections where I/Ca data were measured from for model-data comparison. The d13C from Demerara Rise and Tarfaya are organic data (d13Corg) instead of carbonate data.

Section	Site location	Depth	Pre-CIE d13C	CIE d13C	Post-CIE d13C	Pre-CIE I/Ca	CIE I/Ca	Post-CIE I/Ca
Raia del Pedale	Shallow water	Few meters	-0.353	2.013	0.681	0.688	0.837	1.296
Demerara Rise	Low lat. pelagic	Below storm wave base	-27.616 (org)	-23.816 (org)	-26.345 (org)	0.427	0.530	0.153
Tarfaya	Low lat. pelagic	Below storm wave base	-27.019 (org)	-24.841 (org)	-26.729 (org)	0.836	0.494	0.869
South Ferriby	Mid. lat. Pelagic	Below storm wave base	3.200	3.780	3.260	3.656	4.953	3.344
Eastbourne	Mid. lat. Pelagic	Below storm wave base	2.796	4.335	3.803	2.351	3.005	4.241
Newfoundland	Mid. lat. Pelagic	Below storm wave base	2.803	3.064	2.697	2.883	1.552	2.364

Table 3.6. The literature compilation of IO3- and I- observations from the global ocean that was used for calibrating the iodine cycle in cGENIE model

https://bg.copernicus.org/articles/21/4927/2024/bg-21-4927-2024-supplement.zip

CHAPTER 4: DRIVERS OF SECULAR MARINE IODATE VARIATIONS ACROSS EARTH HISTORY

4.1 Abstract

Most of the ocean during the Mesoproterozoic was anoxic in equilibrium with the coeval atmosphere, which is constrained to have less than 1% of present atmospheric levels (PAL) of oxygen (O_2). However, multiple lines of geochemical evidence indicate the potential for higher levels spatially or temporally in portions of the ocean. For example, the iodine content of carbonates provides evidence for the accumulation of low but present levels of the oxidized iodine species, iodate (IO_3^-) in the Mesoproterozoic surface ocean. However, the redox threshold at which IO_3^- reduction becomes favorable has not been quantified, which limits quantitative constraints from the carbonate-iodine record. Here, we quantify the conditions that allow sustained low level IO_3^- accumulation in the surface ocean. Specifically, we compared two approaches: (1) we cultivated *Shewanella oneidensis* MR-1 under controlled low O_2 environments to determine the O_2 threshold for IO_3^- reduction; (2) determined broader conditions maintaining low but present IO_3^- via an Earth System Model with an active iodine cycle and incorporating atmosphere and ocean biogeochemical and physical processes (cGENIE).

We observed that IO_3^- reduction in the medium did not occur until dissolved O_2 decreased below 0.1μM, which probably represents the molecular threshold triggering activity of IO_3^- reduction enzymes. This threshold provides the minimum estimate of O_2 based on early appearances of measurable IO_3^- before or after the GOE. Following the GOE, our Earth System model simulations at variable O_2 and ocean nutrient conditions indicate the possibility of 2 steady states that could maintain low but present IO_3^-. Specifically, the combination of O_2 <3% PAL with lower PO_4 relative to modern as well as O_2 <30% PAL and modern-like PO_4 both maintain IO_3^-

equivalent to the Proterozoic baseline of 0.5μmol/mol I/Ca (i.e., 50 nM IO_3^-). We suggest that the low O_2-low PO_4 scenario might best describe the mid-Proterozoic low I/Ca baseline. Increases to modern-like I/Ca from the similar I/Ca baseline across Neoproterozoic and into the Paleozoic may reflect combinations of atmospheric O_2 and nutrient dynamics above the second steady state. Together, our model and experimental results indicate that changes in the steady state of carbonate-iodine contents in the Mesoproterozoic and elsewhere in Earth history is sensitive to O_2 variations as well as additional, non-redox factors that were not previously considered.

4.2 Introduction

The Paleo- and Mesoproterozoic Eras represent a critical period hosting milestones in the evolution of life. The first irreversible oxygenation of the atmosphere—known as the Great Oxygenation Event (GOE)—between 2.45 to 2.32 billion years ago (Ga) set the stage for the Proterozoic Eon (Bekker et al., 2004), as well as marked unambiguous advent of oxygenic photosynthesis (Javaux & Lepot, 2018). The earliest appearance of eukaryotes probably took place no later than ~1600 million years ago (Ma) during the Mesoproterozoic, as indicated by micro-scale fossils with complex cell structures identified in shales across multiple ocean basins (Xiao et al., 1997; Javaux et al., 2001; Knoll, 2014; Javaux & Lepot, 2018). Early multicellular macrofossils, which represent more complex life forms, first appear in the sedimentary records between 1.87 to 1.45 Ga (Schneider et al., 2002; Sharma & Shukla, 2009; Zhu et al., 2016). The first appearance or even diversification of early animals happened close to the dusk of the Mesoproterozoic (700-800Ma), as indicated by molecular biological and fossil evidence (Love et al., 2009; Neuweiler et al., 2009; Erwin et al., 2011; Dohrmann & Wörheide, 2017). All of these evolutionary breakthroughs took place within the context an Earth System with only weak and spatiotemporally heterogenous oxygen availability (Reinhard et al., 2016).

Since oxygen is a bio-essential element, it seems intuitive to establish a causal link between the Proterozoic evolutionary events with shallow ocean oxygenation. However, in contrast to this classic view that a certain oxygen thresholds must be reached to support the origin of complex life, some studies suggest that eukaryotic life, especially early animals (e.g. sponges), are capable of withstanding much lower dissolved O_2 levels, likely in sub-μM ranges (Mills & Canfield, 2014). In addition, the delayed occurrence of Neoproterozoic oxygenation event (830-540 Ma) relative to the molecular clock-dated origin of animals (Love et al., 2009; Neuweiler et al., 2009; Erwin et al., 2011; Dohrmann & Wörheide, 2017), points towards a possibility that the evolution of complex life, instead, promoted Proterozoic surface ocean oxygenation. Indeed, shallow ocean oxygenation might be driven by deepened organic matter remineralization in association of recalcitrant organic particles produced by larger eukaryotic cells and animals (Butterfield, 2009; Erwin & Tweedt, 2012; Mills & Canfield, 2014). The resolution of such a debate is therefore hindered by direct comparison between oxygen availability and metabolic demands, as well as the timing of evolutionary appearances. Additional insights come from quantitative geochemical constraints on atmospheric and surface ocean oxygenation across the Proterozoic broadly.

Various geochemical and sedimentological tools, accompanied by Earth System models, have been applied to provide constraints on Proterozoic oxygenation. Discovery of the disappearance of the mass independent fractionation of sulfur (S-MIF) signal after the GOE provides one of the milestones of quantifying atmospheric O_2 ($> 10^{-3}$ present atmospheric levels or PAL) during the Proterozoic (Farquhar & Wing, 2003). The presence of oxidative chromium (Cr) weathering indicated by authigenic $\delta^{53}Cr$ isotopic signal in marine shales indicates 0.1% to 1% PAL O_2 persisted through the Mesoproterozoic atmosphere (Planavsky et al., 2014; Cole et al., 2016; Gilleaudeau et al., 2016; Canfield et al., 2018). The appearance of cerium (Ce) anomaly in

Proterozoic carbonates is also indicative of 10^{-3} to 10^{-2} PAL coeval atmospheric O_2 (Bellefroid et al., 2018; Liu et al., 2021). Earth System models, combining with parameterized constraints of coeval C-N-P-O-S elemental cycles derived from rock records, estimate O_2 increased to 10^{-2} or even to 10^{-1} PAL in the wake of the GOE (Claire et al., 2006; Goldblatt et al., 2006), and maintained several percentages of PAL throughout the mid-Proterozoic (Ozaki et al., 2019). This limited oxygenation in both the ocean and the atmosphere likely spanned into the Early Paleozoic.

Importantly, direct constraints for ocean oxygen levels, as opposed to atmospheric oxygen, during the Paleo- and Mesoproterozoic remain more qualitative instead of quantitative. A widely accepted model of redox structure of the Proterozoic oceans suggests that the majority of the ocean was ferruginous, with interspersed euxinic conditions, and a weakly oxygenated surface layer overlaying these deeper waters (Lyons et al., 2014). Beneath the low Proterozoic atmospheric O_2 levels (close to or below 10^{-2} PAL), such a surface ocean likely maintained spatially limited dissolved O_2 enrichments (> 1 μM) relative to the air-sea equilibrium regime, supported by local productivity (Reinhard et al., 2016; Reinhard & Planavsky, 2022). Such so-called "oxygen oases" might have the potential to be the sanctuary of early multicellular organisms, or even animals, where O_2 levels may be sufficient for metabolic requirements (Reinhard et al., 2016). Beyond geochemical numeric models, the necessity of quantifying local/regional O_2 in Proterozoic oceans arises for the purpose of not only providing ground truthing evidence for oxygen oases but also for understanding the co-evolution between the Earth system and life.

The ratio of iodine to calcium (I/Ca or I/(Ca+Mg) considering dolomitization) in marine carbonates has been regarded as a potential redox proxy for the surface water column within such spatially limited ocean oxygenation (Hardisty et al., 2017). The basic logic behind the application of I/Ca proxy is that the transformation between the two most abundant species of iodine—iodate

(IO_3^-, oxidized) and iodide (I^-, reduced)—is sensitive to the redox state of seawater. Today, in most of the oxygenated regions of the ocean, IO_3^- is the dominant. While in reduced marine environments, such as oxygen deficient zones (ODZ), or anoxic basins, IO_3^- is usually, but not always so, rapidly reduced to I^- and hence is present in low concentrations (Wong & Brewer, 1977; Luther & Campbell, 1991; Rue et al., 1997; Truesdale et al., 2000, 2013; Farrenkopf & Luther, 2002; Cutter et al., 2018; Moriyasu et al., 2020; Rapp et al., 2020). In light of such redox-controlled behavior, IO_3^- is indicative of seawater oxygenation. The formation of carbonates from seawater incorporates IO_3^- instead of I^- into the lattice in proportion to its concentration (Lu et al., 2010; Zhang et al., 2013; Zhou et al., 2014; Podder et al., 2017; Kerisit et al., 2018; Hashim et al., 2022). Meanwhile, post-depositional diagenesis only decreases carbonate-hosted I/Ca by removing iodine from the crystal structure, thereby offering a conservative minimum estimate of oxygenation (Hardisty et al., 2017; Hashim et al., 2022).

While there are already well known secular trends in I/Ca across Earth history (Figure 4.1), the related constrains with respect to ambient O_2 availability remain poorly understood (Hardisty et al., 2014, 2017; Shang et al., 2019; Liu et al., 2020; Fang et al., 2022; Yu et al., 2022; Tang et al., 2023). For example, non-zero I/Ca did not appear in the rock record until the GOE, indicative of first evidence of iodine oxidation and thus accumulation of IO_3^- in association with oxygenation of the atmosphere/ocean (Hardisty et al., 2014, 2017), yet the O_2 threshold at which IO_3^- accumulates is not known, limiting quantitative constraints. Through the Proterozoic, most (~90%) of the I/Ca values during the early through mid-Proterozoic remained below or close to 0.5 μmol/mol, referred to as the "Proterozoic baseline" (Hardisty et al., 2017). This low but present IO_3^- accumulation indicates a redox-stratified surface ocean, but the required O_2 levels still remain unclear. Importantly, this low-I/Ca stasis was interrupted by several events during which higher

values, even those approaching modern levels are reported, including the ones at ~2.2 Ga (Lomagundi Event) (Hardisty et al., 2014), ~1.6 Ga (Shang et al., 2019), ~1.4 Ga (Hardisty et al., 2014, 2017; Yu et al., 2022), and ~1.3 Ga (Liu et al., 2020). If these increases to modern IO_3^- levels indicates highly oxygenated settings, the I/Ca record may have important implications for the evolution of eukaryotic life.

Progress toward quantifying the relationship between O_2 and IO_3^- (hence I/Ca) has been made through the last decade (Glock et al., 2014; Hardisty et al., 2021, 2017, 2014; Lu et al., 2020b, 2020a, 2016; Rue et al., 1997; Shang et al., 2019, summarized in Table 4.1). However, most of the direct comparisons between carbonate I/Ca and dissolved O_2 are based on measurements from foraminifera (Glock et al., 2014; Lu et al., 2016, 2020b, 2020a), thus vital effects may play a role in IO_3^-(Winkelbauer et al., 2023), jeopardizing application of such constraints to Proterozoic carbonate rocks which were formed inorganically. In contrast, the absence of vital effects in such rocks simplifies the constraint on seawater IO_3^- concentration based on I/Ca due to their linear correlation controlled by a temperature-dependent partition coefficient (Zhou et al., 2014). Importantly, since I/Ca tracks IO_3^-, then understanding the role of O_2 on IO_3^- concentrations in seawater is thereby a more direct and necessary prerequisite for quantitatively interpreting the I/Ca proxy. In modern upwelling zones, significant amounts of IO_3^- exist within the low-O_2 water while not being reduced until the core ODZ, suggesting that an O_2 "threshold" may control quantitative IO_3^- reduction (Chapman, 1983; Rue et al., 1997; Farrenkopf & Luther, 2002; Cutter et al., 2018; Rapp et al., 2019, 2020; Moriyasu et al., 2020, 2023; Hardisty et al., 2021). However, this relationship is complicated by the availability of organic matter and water mass mixing, which can either inhibit redox-controlled IO_3^- reduction or introduce *ex situ* signals, respectively (Hardisty et

al., 2021). Due to the lack of mechanistic understanding within the modern iodine cycling, using I/Ca to quantitatively reconstruct Proterozoic surface ocean oxygenation remains challenging.

Table 4.1. Quantitative relationship between dissolved O_2 and seawater IO_3^- (and its derived carbonate I/Ca).

Forms of iodine	Iodine Value	O_2 implication	Citation
carbonate I/(Ca+Mg)	non-zero	> 1 μM	Hardisty et al., 2014
Benthic foraminiferal I/Ca	0.3-2.2 μmol/mol	Linear relationship with benthic O_2	Glock et al., 2014
Surface seawater IO_3^-	< 250 nmol/L (2.5μmol/mol in foraminiferal I/Ca),	< 20-70 μmol/kg minimum O_2	Lu et al., 2016
carbonate I/(Ca+Mg)	> 2.6 μmol/mol	fully oxygenated	Lu et al., 2016
Seawater IO_3^- (cGENIE model)	Reduction threshold	30 μM	Lu et al., 2018
Benthic foraminiferal I/Ca	< 3 μmol/mol	< 50 μmol/kg benthic O_2	Lu et al., 2020a
Planktic foraminiferal I/Ca	< 2.5 μmol/mol	< 70-100 μmol/kg mid- or bottom depths O_2	Lu et al., 2020b
Seawater IO_3^-	< 150 nmol/L	< 7 μM	Hardisty et al., 2021
Seawater IO_3^- (Gene analysis)	Microbial reduction threshold	11.03-65.24 μM	Reyes-Umana et al., 2021
Seawater IO_3^- (cGENIE model)	Reduction threshold	10 μM	Cheng et al., 2024

Here we provide direct O_2 constraints from the secular I/Ca record through 2 approaches: (1) we cultivated *Shewanella oneidensis* MR-1 under controlled low O_2 environments to determine the threshold for IO_3^- reduction; (2) determined broader conditions maintaining low but present IO_3^- via an Earth System Model with an active iodine cycle and incorporating atmosphere and ocean biogeochemical and physical processes (cGENIE). Together, these approaches constrain the conditions required for initial IO_3^- accumulation at the GOE as well as the O_2 and other conditions necessary for I/Ca variations. Importantly, our approaches build off recent observations that IO_3^- reduction is mediated by microbial activities, including genus *Shewanella sp.*, *Roseovarius sp.*, *Notoacmeibacter sp.*, and *Aliiroseovarius sp*. (Farrenkopf et al., 1997; Toporek et al., 2019; Shin et al., 2022; Jiang et al., 2023; Kine et al., 2024) as well as an existing iodine cycling model framework calibrated against the modern ocean (Cheng et al., 2024).

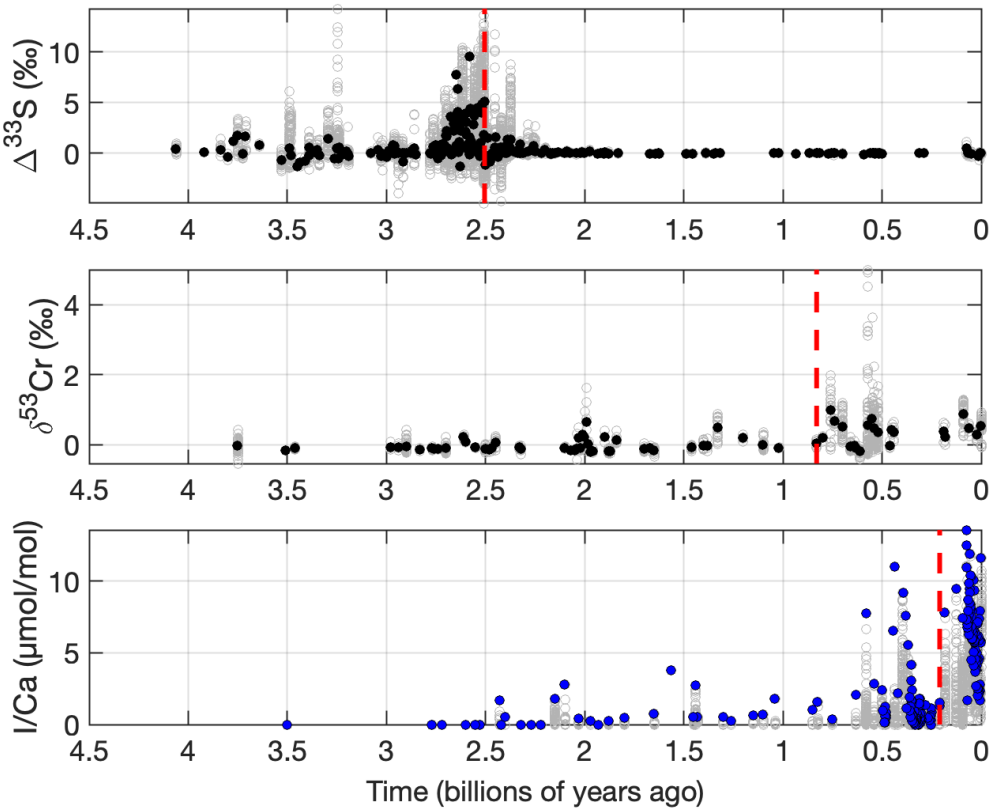

Figure 4.1. Evolution of sulfur mass independent fractionation signal ($\Delta^{33}S$), chromium isotopes signal in shale ($\delta^{53}Cr$), and carbonate I/Ca records through the Earth's history. The ages of the raw data are grouped into bins of 1 million years each. The filled dots represent the overall variation of these redox proxies. The color of filled dots represents the lithology of samples (black = shale, blue = carbonates). The red line is a changepoint analyses finding a significant change in the mean for the proxies from the Precambrian level to the modern level. Taken from Hardisty and Lau, 2025

4.3 Materials and methods

4.3.1 Bacterial growth conditions

We performed *S. oneidensis* MR-1 cultures in Pyrex 250ml flasks as shown in the setup in Figure 4.2, within an 856-HYPO/SP122 hypoxia chamber manufactured by PLAS LABS Inc. The temperature inside the hypoxia chamber was set at 30±1 °C and CO_2 was maintained at 420±40 ppm. We applied varied O_2 partial pressure in the hypoxia chamber from 0.05% atm (500ppm) to 5% atm with precision of 20 ppm (below 0.1% atm) and 0.05% atm (above 0.1% atm). An

additional FireSting TROXROB-10 oxygen probe and a FireSting TDIP-5 temperature sensor were used to monitor and record the dissolved O_2 and temperature in one representative of the triplicate cultures. The oxygen probe was calibrated by deionized (DI) water under room O_2 and with Pyroscience OXCAL O_2 calibration capsule (contains sodium sulphite) for 100% and zero calibration, respectively. Our preliminary experiments showed aerobic metabolism by *S. oneidensis* MR-1 rapidly consumed O_2 in the medium, preventing dissolved O_2 from maintaining a constant equilibrium with the head space (Figure 4.8). We therefore bubbled the medium with a 2μm-poresize airstone and stirred it by a Corning PC-210 magnetic stirrer at approximately 250 rpm. To minimize evaporation of medium, the air was humidified by pumping through a flask with DI water. The whole culture setup was autoclaved except the O_2 and temperature probes (sterilized with ethanol instead), and airflow was sterilized through a Basix 25mm 0.2 μm syringe filter before entering the humidifier flask.

The *S. oneidensis* MR-1 strain was stored frozen at -80°C prior to being inoculated to a lysogeny broth (LB) agar plate and was incubated for ~72 hours at 30°C. A single colony was then selected and isolated for aerobic pre-growth in 5ml LB medium at 30°C and shaking at 150 rpm for ~48 hours until OD_{600} reaches >1. For low-O_2 cultures, The pre-grown cells were then transferred to Pyrex flasks containing 150 ml M5 minimal medium, containing 1.29 mM K_2HPO_4, 1.65 mM KH_2PO_4, 7.87 mM NaCl, 1.70 mM NH_4SO_4, 475 μM $MgSO_4 \cdot 7\ H_2O$, 10 mM HEPES (100mM for experiments <1% atm O_2), 0.01% (w/v) casamino acids, ane then the pH was adjusted to 7.2 with 5 M NaOH. After autoclaving, 100× Wolfe's vitamin solution and 100× Wolfe's mineral solution was added to a final of 1× concentration , and sodium D,L-lactate was added to a final concentration of 20 mM as electron donor (Duhl & TerAvest, 2019; Gruenberg & TerAvest,

2023; Ford & Teravest, 2024). The M5 medium recipe was amended with 250 µM IO_3^- as anerobic electron acceptor. Each experiment includes triplicate cultures and a control with no inoculation.

4.3.2 OD_{600} and IO_3^- measurements

Samples were collected through the experiment every 3-12 hours. From each flask per timestep we collected 1ml sample for OD600 measurement on a VWR UV-3100PC UV-Vis spectrometer. The IO_3^- samples were filtered, and 100µL of aliquots were diluted 25-folds to 2.5ml. We analyzed IO_3^- using the spectrophotometric method of Jickells et al., (1988). To each sample, 62.5 µL of 1.5 M sulfamic acid was added and allowed to react for 2.5 minutes to remove potential nitrite interference, followed by the addition of 187.5 µL of 10% (w/v) potassium iodide and 375 µL of DI water, allowing the formation of triiodide (I_3^-) during a 2-minute reaction. The IO_3^- was quantified by measuring the absorbance at 350 nm.

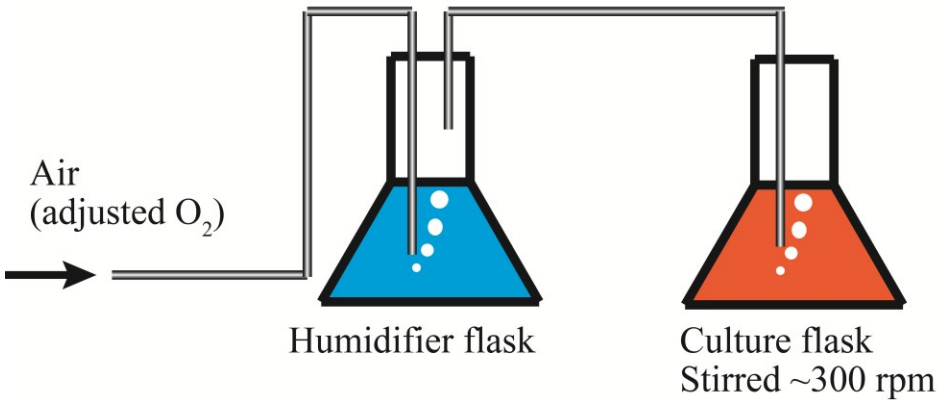

Figure 4.2. Experimental setup of microbial IO_3^- reduction culture. Air was pumped through a 0.2µm *basix* syringe filter prior to the humidifier flask. The whole culture device was in a hypoxia chamber.

4.4 The cGENIE Earth System Model framework

The cGENIE EMIC (Earth system model with intermediate complexity) is a class of model that simulates global ocean biogeochemical cycles under simplified components (such as physical climate, and spatial-temporal resolution) of the Earth system (Ridgwell et al., 2007). The cGENIE

ocean circulation in this study applies to a low-resolution 36×36 equal-areal grid at 16 logarithmically spaced depth levels. Within this Earth surface grid setup, a 3D frictional-geostrophic approximation circulation model (Goldstein)(Edwards & Marsh, 2005) is coupled to a 2D energy-moisture-balance-model (EMBM) and a 2D dynamic-thermodynamic sea-ice model. Due to large uncertainties of current knowledge towards the deep-time oceans—including nutrient levels and redox conditions—sensitivity analyses including large numbers of experiments are required to assist with constraining these factors. cGENIE, as a low-resolution Earth system model, can perform such ensembles at a reasonable efficiency (~10,000 model years/ 24 CPU hours).

The iodine cycle in cGENIE was first introduced and calibrated by Lu et al., (2018), which includes four processes: (1) water column IO_3^- reduction, and reduction, (2) water column I^- oxidation, (3) IO_3^- photosynthetic uptake and assumed intercellular reduction to I^-, and (4) organic-bond I^- release to seawater during remineralization. These processes were further improved by Cheng et al., (2024) by calibration against modern and ancient ocean iodine observations and introducing new mechanisms. In this study, we apply the 'threshold'-'Fennel' combination for IO_3^- reduction and I^- oxidation schemes due to their performance in replicating both modern ocean water dissolved iodine speciation and ancient I/Ca records (Cheng et al., 2024). Specifically, we choose the 'Fennel' oxidation scheme over the classic 'lifetime' because it incorporates variable first-order I^- oxidation kinetics that depend on ambient dissolved O_2 levels. The "Fennel" oxidation is the most suitable option given our goal of simulating the iodine cycle in weakly oxygenated Proterozoic oceans, in which O_2 concentration might be above the threshold triggering IO_3^- reduction, but meanwhile still inhibiting I^- oxidation (Cheng et al., 2024).

We performed a sensitivity analysis by varying atmospheric O_2 from 0.1% to 100% PAL, and nutrients (PO_4) from 0.8% to100% POL (present oceanic level) to quantify the redox and

nutrient conditions that are required to sustain low but present IO_3^- levels. Each simulation was run for 10,000 years to steady state. Additionally, we explore the potential for a larger Proterozoic total iodine reservoir to impact IO_3^- concentration by running an additional cGENIE ensemble where the total iodine inventory is tuned to an arbitrarily higher value of 1.6 POL (800nM). Notably, it is possible that the total iodine inventory was larger in the past than today. For example, modern primary producers, like red algae, contribute to a significant iodine sink from seawater (Muramatsu & Wedepohl, 1998). Given the larger role of cyanobacteria over algae for Proterozoic primary production (Crockford et al., 2023). Such a total iodine inventory might in turn affect the surface ocean IO_3^- concentration, as simulated by Lu et al., (2018).

4.5 Results

4.5.1 Bacterial growth and iodate reduction

We ran the culture under gas phase O_2 at 5% atm, 1% atm, 0.1% atm (1000 ppm), and 0.05% atm (500ppm). O_2 concentration in the medium, bacterial growth, and IO_3^- concentration are presented in Figure 4.3. Bacterial growth was observed in all experiments by the increase of OD_{600}. In experiments under gas-phase O_2 between 1000ppm and 5% atm, the exponential growth stage started immediately after inoculation and lasted for approximately 20 hours, reaching a maximum OD_{600} of 0.125-0.150. The OD_{600} curves in the experiment under 500ppm O_2 show prolonged growth lasting for at least 90 hours, associated with the highest OD_{600} of 0.25.

Bubbling and stirring enhanced air-medium exchange and helped stabilize O_2 in medium in the 5% and 1% atm experiments. The sampling procedure introduces brief disturbances due to inevitable partial exchange between the chamber and the atmosphere, lasting for less than 10 minutes. In these experiments, O_2 levels in the medium remained stable and in equilibrium with the air (50 μM for 5% atm and 10μM for 1% atm) (Figure 4.3). In contrast, in lower O_2 conditions

under 1000 ppm and 500 ppm, metabolic O_2 demand competed with replenishment, causing medium O_2 levels to fluctuate around 0.3 µM and 0.1 µM, respectively. O_2 in the medium also decreased, associated with OD600 increase during the exponential growth stage (Figure 4.3). Notably, during exponential growth in the 500 ppm O_2 experiment, O_2 measurements dropped below the sensor's detection limit, indicating that consumption outpaced replenishment. As noted earlier, in the absence of bubbling, near complete oxygen consumption was observed in experiments below 5% atm pO_2 of the chamber.

No significant IO_3^- reduction is observed in 5% atm, 1% atm, and 1000ppm O_2 experiments. However, under the 500 ppm O_2 condition, IO_3^- in the experimental flasks decreased below the 95% confidential interval of the control flask after 40 hours, in association with increased bacterial growth. At the peak of growth, IO_3^- decreases gradually from 250 µM to 230 µM until the end of the experiment at 100 hours (Figure 4.3).

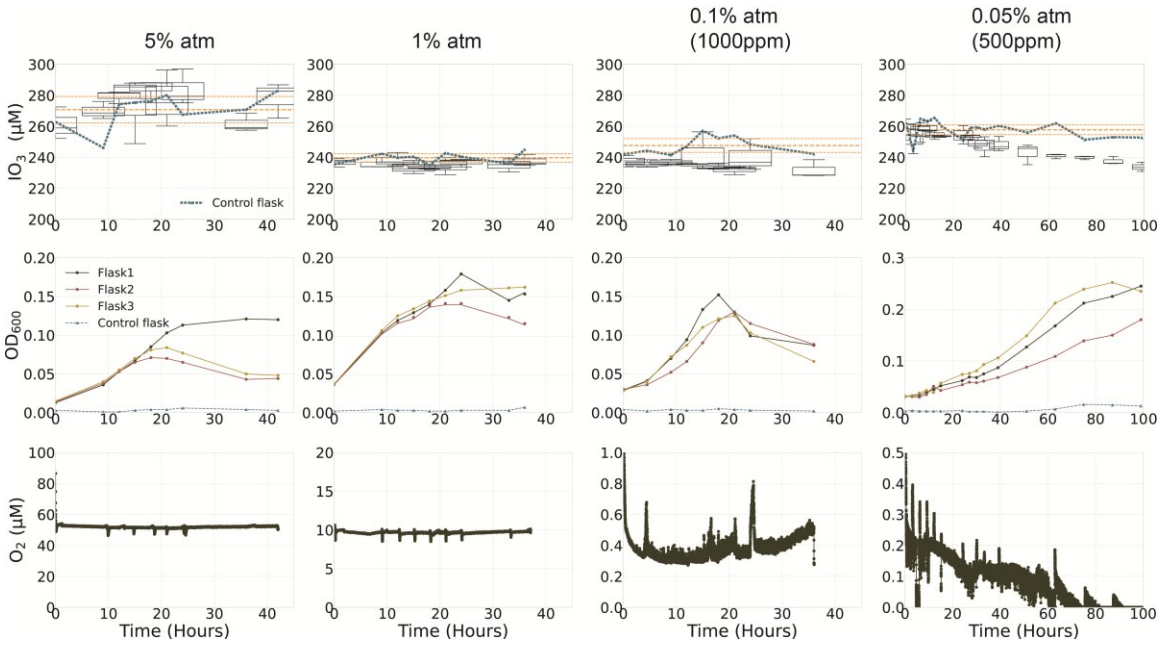

Figure 4.3. Results of microbial culture experiment under different gas-phase O_2 levels. The IO_3^- in experimental flasks are presented as box-whisker plots. Horizontal orange lines demonstrate the average and 95% confidential intervals of IO_3^- concentration in the control flask. The O_2 concentrations below the detection limit are presented as zeros.

4.5.2 Earth System Model results

We present the globally averaged IO_3^- within shallow ocean (above 500m, Figure 4.4A) and deeper ocean (below 500m, Figure 4.4B) simulated by cGENIE sensitivity analysis to explore the O_2 and nutrient conditions that allow IO_3^- accumulation in seawater. The results of the sensitivity analyses are shown in Figure 4.4. The 250 nM IO_3^- (or I/Ca ~2.5 μmol/mol) contour marks the minimum IO_3^- accumulation in modern oxygenated seawater, and the 50 nM IO_3^- (or I/Ca ~0.5 μmol/mol) is the baseline of IO_3^- accumulation measured from Paleozoic and older samples (Hardisty et al., 2017). The high/low nutrient/O_2 scenarios represent constraints on atm pO_2 and marine PO_4 for Mesoproterozoic from the CANOPS model (Ozaki et al., 2019).

In our sensitivity analyses, the general trend of IO_3^- levels in both shallow and deep ocean displays a distinct binary pattern, with ~10% POL PO_4 representing a critical cut off in controlling IO_3^- accumulation. Specifically: (1) under low nutrient conditions, the atm pO_2 threshold for accumulating IO_3^- levels above ODZ levels is relatively low, near 3% PAL; (2) at higher nutrient levels, starting near 10% POL PO_4, there is a linear increase in the amount of O_2 and PO_4 required to accumulate IO_3^- above ODZ levels. In the second scenario, ~30% PAL O_2 is needed for IO_3^- elevated above modern ODZ levels when PO_4 is at modern levels.

The model results also suggest IO_3 in the shallow ocean (<500 m depth) and deep ocean (<500 m depth) are coupled with each other. While subtle differences are seen, the contours of averaged IO_3^- in the deep ocean are similar to that of the shallow ocean (Figures 4.4A and 4.4B), indicating the possibility of IO_3^- accumulation in deeper depths even in a low-O_2 ocean. Close-to-modern depth profiles of IO_3^- are observed at >20 % PAL O_2 and >10% POL PO_4, with deep ocean IO_3^- accumulation at higher levels than the surface (Figure 4.4B). This gradient demonstrates the importance of phytoplankton reduction and assimilation of removing IO_3^- in the photic zone.

To assess the impact of a higher total iodine inventory on IO_3^- levels, we present the model results under 800 nM total iodine inventory (Figures 4.4C and 4.4D). The higher total iodine inventory is associated with steeper gradient between the near-zero and maximum IO_3^- levels, while the O_2 and PO_4 requirements for 50 nM and 250 nM IO_3^- are almost identical to the simulations under 500 nM iodine inventory.

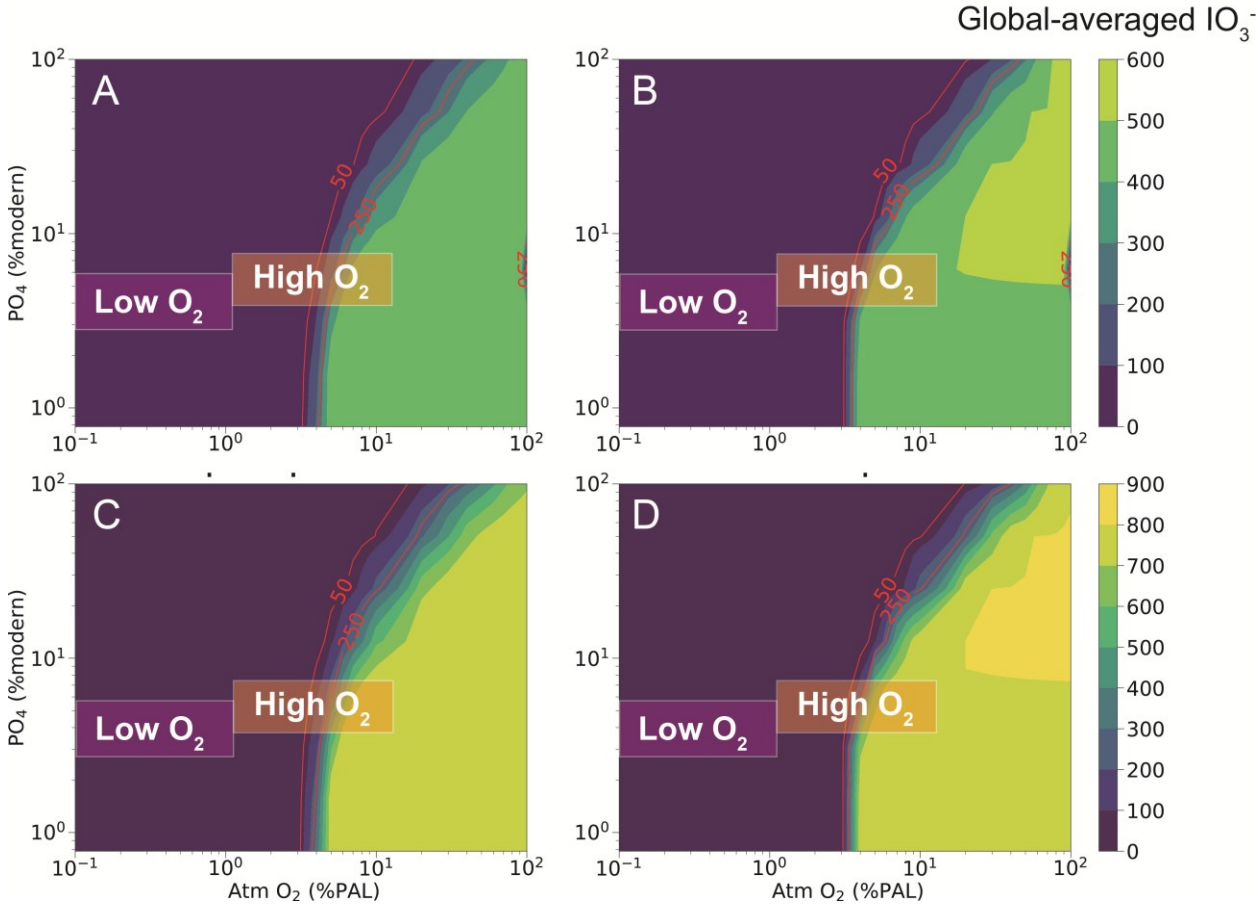

Figure 4.4. Contours of globally averaged IO_3^- above 500m depth (A and C) and below 500m (B and D) simulated by cGENIE under various O_2 and PO_4 levels. Panels A and B show model simulations under modern ocean iodine inventory (500 nM), while C and D show the simulations under higher iodine inventory (800nM). The red lines label the contours of 50 nM and 250 nM IO_3^- accumulation.

4.6 Discussion

4.6.1 Oxygen Threshold of IO_3^- accumulation and implications for the GOE

4.6.1.1 Oxygen Threshold of IO_3^- reduction based on microbial cultures

The occurrence of IO_3^- reduction relative to the control group under 500 ppm O_2 experiments indicates that biotic, instead of abiotic processes contributed to IO_3^- reduction in O_2-depleted medium (Figure 4.3). In the 500ppm O_2 experiment, IO_3^- reduction is not observed until dissolved O_2 decreases to 0.1 μM (~4×10^{-4} PAL), suggesting a low sub-μM threshold required for microbial IO_3^- reduction (Figure 4.3). Meanwhile, however, incomplete reduction through the 100 hours incubation implies that *S. oneidensis* MR-1 were simultaneously using IO_3^- and O_2 as electron acceptors, instead of solely reducing IO_3^-. We therefore hypothesize that the metabolic transition from O_2 to IO_3^- is more likely to be a gradual process while O_2 is present, as IO_3^- reduction kinetics increases with decreasing O_2.

It is not surprising that zonation between terminal electron acceptors of respiration have some extent of overlap on the "redox ladder" (Canfield & Thamdrup, 2009). However, with the O_2 sensor approaching its detection limit, further quantification of IO_3^- reduction kinetics and O_2 becomes difficult. On the microscale, a bulk bacterial culture employing both aerobic and anaerobic metabolisms reflects a "bet hedging" strategy that facilitates the long-term survivability for the entire population (Lycus et al., 2018). For example, when O_2 drops below the level sustaining aerobic metabolism, only a small portion of denitrifying bacteria *Paracoccus denitrificans* switch to nitrite reduction, while the remaining utilize the intermediate N_2O as the electron acceptor, maintaining slow respiratory growth (Lycus et al., 2018). This strategy allows the bulk population to reduce the cost of protein synthesis associated with metabolic transition, in response to potential short-term anoxia (Lycus et al., 2018). In the case of IO_3^- reduction, slow

increase of OD_{600} in the 500ppm O_2 experiment might be explained by the majority of the *S. oneidensis* population utilizing the intermediate (hypoiodous acid, HIO) to maintain slow growth. According to the hypothesized kinetics of microbial denitrification, the fraction of cells that has been recruited to anaerobic respiration is a factor of exposure time to anoxia (Hassan et al., 2014). That is, as anoxia prolongs, the proportion of cells that employed anerobic metabolism progressively increases. Although further experimental and calculational ground truthing is needed, such a hypothesis should be able to explain the delayed IO_3^- reduction, which is most prominent in the later stage of the incubation (Figure 4.3).

During the past decades, incubation experiments to natural and artificial media have proven that microorganisms separated from freshwater, marine, and groundwater conditions, play a key role in reducing IO_3^- to I^- (Tsunogai & Sase, 1969; Farrenkopf et al., 1997; Amachi et al., 2007; Kine et al., 2024; Li et al., 2024). Traditionally, the redox proximity between NO_3^--NO_2^- and IO_3^--I^- has led to the hypothesis that IO_3^- is reduced 'accidentally' by the NO_3^- reductase (Tsunogai & Sase, 1969). However, recent reports of *S. oneidensis* mutants with the genes for dissimilatory and assimilatory NO_3^- reductases deleted shows the cultures still maintain strong IO_3^- reduction capability. This result emphasizes an independent biochemical pathway supporting IO_3^- reduction, instead of a byproduct of NO_3^- reduction (Mok et al., 2018).

The molecular mechanism of IO_3^- reduction driven by *S. oneidensis* was revealed by subsequent studies: two gene clusters, MtrCAB and DmsEFAB contributes to the electron transport from electron donor (e.g. lactate) to IO_3^- (Toporek et al., 2019; Shin et al., 2022). Specifically, the extracellular dimethyl sulfoxide reductase DmsEFAB reduces IO_3^- to intermediate HIO through a four-electron transfer, followed by disproportionation to IO_3^- and I^- (Guo et al., 2022b; Shin et al., 2022). The decaheme c-type cytochromes MtrCAB contributes to either

transferring electrons from the periplasmic space through the outer membrane (Toporek et al., 2019) or detoxifying hydrogen peroxides (H_2O_2)—the byproduct of IO_3^- reduction—to H_2O (Guo et al., 2022b). It is also suggested that in ferric-abundant conditions, MtrCAB catalyzes Fe(III) reduction to biogenic Fe(II), which reduces IO_3^- to I^- abiotically (Jiang et al., 2023). Apart from genus *Shewanella*, another IO_3^- reductase $IdrABP_1P_2$ was identified from Genera *Pseudomonas* and *Denitromonas* (Yamazaki et al., 2020; Reyes-Umana et al., 2021). The IdrA mediated pathway also reduces IO_3^- to HIO, similar to the pathway associated with DmsEFAB enzyme (Reyes-Umana et al., 2021).

These IO_3^- related genes in *S. oneidensis* (MtrCAB and DmsEFAB) are also identified in 26 other *Shewanella* species, as well as three Ferrimonas species, isolated from various environments across the globe including marine water and sediments (Guo et al., 2022a). Similarly, the wide prevalence of the IdrA pathway is also supported by discovery of its gene expression in the marine low oxygen settings, including Eastern Tropical Pacific, Central Pacific, and Arabian Sea ODZs (Reyes-Umana et al., 2021; Saunders et al., 2022). The widespread occurrences of IO_3^- reduction genes clearly point out the environmental significance of microbial process in iodine marine cycling. These IdrA genes are especially present at locations with the median dissolved O_2 <65 μM, providing another approach of estimating IO_3^- reduction threshold (Reyes-Umana et al., 2021). When considering the higher abundance of IdrA expression with more than one hit in gene sequencing, the O_2 threshold is lowered to ~11 μM (Table 4.1).

Importantly, our microbial reduction approach only evaluates IO_3^- accumulation from the perspective of reduction and not from the perspective of oxidation and formation of IO_3^-, which may have higher (or lower) O_2 barriers. Importantly, the mechanisms for IO_3^- production in the ocean is not well understood, but is not driven directly by O_2 (Luther, 2023). Instead, studies

indicate that reactive oxygen species (Li et al., 2012, 2014) or microbial ammonia oxidation (Hughes et al., 2021) may be drivers. From this perspective, evaluating IO_3^- accumulation from the viewpoint of reduction may be more directly tied to oxygen and thus more straightforward. Regardless, future research should consider the O_2 thresholds favoring ammonia oxidation or ROS in order to better understand initial IO_3^- accumulation in modern and ancient oceans.

Ultimately, our experiments and previous culture studies indicate the potential for a low, potentially even sub-μM ambient O_2 requirement for IO_3^- reduction. These results have implications for the GOE and subsequent variations in the I/Ca record, which is discussed in more detail (along with our additional O_2 constraints provided in the following sections) in Section 4.6.1.3.

4.6.1.2 Complimentary constraints on the IO_3^--O_2 relationship

The IO_3^- reduction threshold revealed by our microbial incubation is close to 0.1 μM (~4×10^{-4} PAL), which is the lowest among existing studies. As summarized in Table 4.1, other approaches have defined oxygen thresholds for iodate reduction based on combinations of: 1): indirect implications from foraminiferal I/Ca (Lu et al., 2016, 2020a, 2020b), 2): direct measurements of seawater IO_3^- together with O_2 (Hardisty et al., 2021), and 3) Earth system models (Cheng et al., 2024). Below we summarize these findings and provide additional constraints through statistical analyses of a modern oceanographic iodine database used for model calibrations in recent studies (Wadley et al., 2020; Cheng et al., 2024). Notably, these approaches evaluating IO_3^--O_2 relationships in seawater have the advantage of integrating multiple processes, including oxidation and reduction.

Foraminiferal I/Ca: Studies from planktic and benthic foraminiferal I/Ca ratios yield the highest IO_3^- reduction threshold of 30-100 μM O_2 (Lu et al., 2016, 2020a, 2020b). Such a higher

threshold enables foraminiferal I/Ca as a reliable semiquantitative proxy for hypoxia (Lu et al., 2020a). While revealing, the redox control on iodine cycling based on foraminiferal I/Ca remains challenging due to the potential for vital effects, which are still undercharacterized. For example, distinct inter-species variability in the ability to incorporate iodine relative to calcium has been reported previously (Glock et al., 2014; Winkelbauer et al., 2023), but the mechanisms remain unclear. Moreover, the difference in O_2 thresholds derived from planktic (70-100 μM) vs. benthic (50 μM) foraminifera indicates that biological processes between clades, rather than redox factors alone, also exert influences on I/Ca in carbonate tests (Lu et al., 2020a, 2020b). For these reasons, the foraminferal I/Ca-O_2 constraints are not considered hereafter for inorganic carbonates on the I/Ca record through early Earth history.

Seawater measurements of IO_3^- and O_2: Compared to foraminiferal I/Ca, direct measurements from water column O_2 and IO_3^- avoid the complications from vital effects, and are therefore are more likely to reflect redox controls on iodine cycling and hence I/(Ca+Mg) in abiotic carbonates. The prevalence of ocean transect projects (e.g., GEOTRACES) enables the collection of abundant seawater samples using Niskin bottles from global ODZs for IO_3^- analysis, along with *in situ* O_2 measured by CTD-mounted sensors, as compiled in Figure 4.5 (Chapman, 1983; Rue et al., 1997; Farrenkopf & Luther, 2002; Cutter et al., 2018; Rapp et al., 2019, 2020; Moriyasu et al., 2020). These compilations yield a few key observations. First, it is clear that elevated IO_3^- exists in the core ODZ especially in the Pacific ODZs, which complicates the identification of a threshold for IO_3^- reduction. Indeed, limited access of organic matter likely inhibits IO_3^- reduction rates in the ODZ core in oligotrophic open regions, even with ambient O_2 below 10 μM (Hardisty et al., 2021). Such elevated IO_3^- in low O_2 settings is likely an *ex situ* signal that has been transported from oxygenated waters, reflecting a regional water mass mixing and slow reduction kinetics

instead of strictly local redox controls (Hardisty et al., 2021). However, low IO_3^- (<150 nM) is rarely observed beyond low O_2 regions with local dissolved O_2 below ~7 μM (Hardisty et al., 2021)(Figure 4.5). This interpretation is reliable based on the fact that although primary producers in the euphotic zone assimilate and reduce IO_3^- to I^-, its concentrations below 250 nM are rarely observed in oxygenated seawater (Chance et al., 2014).

To be more quantitative in identifying the IO_3^- reduction threshold, we applied the receiver operating characteristic (ROC) curve to a literature compilaton of dissolved IO_3^- and O_2 from the same samples. The ROC is a method that has been used to find the cutoff value of benthic foraminiferal I/Ca and its associated O_2 threshold (Lu et al., 2020b). To conduct the ROC test, we first assume a given O_2 threshold and classify the data into binary "high O_2" and "low O_2" categories. Then, IO_3^- measurements associated with each of the O_2 categories are separated for true positive (correctly interpreting high IO_3^- reflecting high O_2 in seawater, TPR) and false positive (incorrectly classify high IO_3^- as positive out of actual low O_2, FPR) rates for calculation of ROC. The effectiveness of a given O_2 threshold for separating high and low IO_3^- is determined by a parameter called the area under curve (AUC), where a higher value represents better separation. The highest AUC (0.92), representing the best separation, is achieved when the O_2 threshold is set to ~0.9 μM (Figures 4.5, S1). This sub-μM O_2 level supports the sub-μM O_2 threshold established from our culture experiments.

Although the ROC test suggests the optimum water column IO_3^- reduction threshold is near 0.9 μM, such interpretation is associated with significant FPR (measuring high IO_3^- formed in low O_2 water, Figure 4.9A). We note that the high IO_3^- in the core of the ODZs of the ETNP and the ETSP caused an inevitable FPR which even rises above 30% when the IO_3^- cutoff value is below 50nM. In the light of the possibility that the source of unreduced IO_3^- in the ODZ core may be

from transport from regional oxygenated water masses (Hardisty et al., 2021), such high FPR is not concerning. This is because the formation of IO_3^- requires oxygenated areas somewhere in the ocean, which nevertheless supports interpretations of ancient ocean oxygenation when I/Ca is above detection limits. On the other hand, the scenario of low IO_3^- yet in high O_2 (false negative, FNR)—which fails to capture signals of oxygenation events—is more concerning. If we increase the IO_3^- reduction threshold to 7 μM as proposed by (Hardisty et al., 2021), near 100% of TPR (i.e., 0% FNR), could be achieved when the IO_3^- cutoff value is set to 150nM (Figure 4.9D). That is, based on the modern ocean IO_3^--O_2 relationship, non-zero I/Ca values below ~1.5 μmol/mol are highly likely to indicate regional O_2 below 7 μM. This statistical test also implies that, IO_3^- reduction can take place below 7 μM O_2 yet above the sub-μM O_2 threshold.

Importantly, since the O_2 detection limit of most CTD sensors is near 1 μM, our ROC results indicating 0.9 μM O_2 with the highest AUC are best interpreted to indicate that critical O_2 thresholds for IO_3^- may occur at currently uncharacterized sub-μM levels. In addition to mixing processes, a sub-μM O_2 threshold may also explain the prevalence of IO_3^- in the ODZ cores where CTD measurements of O_2 are at the detection limit (typically ~1 μM). In this scenario, internal ODZ IO_3^- variations reflect sub-μM variations in O_2 that are not discernable with standard CTD O_2 sensors. Indeed, every elemental cycle (N, C, Mn) that has been evaluated within ODZs alongside sub-μM O_2 sensors (e.g., STOX) has revealed important lower O_2 thresholds for triggering oxidative vs reductive processes (Clement et al., 2009; Thamdrup et al., 2012; Bristow et al., 2016). For example, N and Mn redox cycling has been demonstrated to be sensitive to O_2 at levels of 5–30 and 100 nmol kg^{-1}, respectively (Clement et al., 2009; Thamdrup et al., 2012; Dalsgaard et al., 2014; Bristow et al., 2016). The same is likely true for iodine. That said, we

recommend that mixing factors and non-O_2 parameters that may be rate limiting for IO_3^- reduction (e.g., nutrients, organic matter) also likely impact internal ODZ IO_3^- variability.

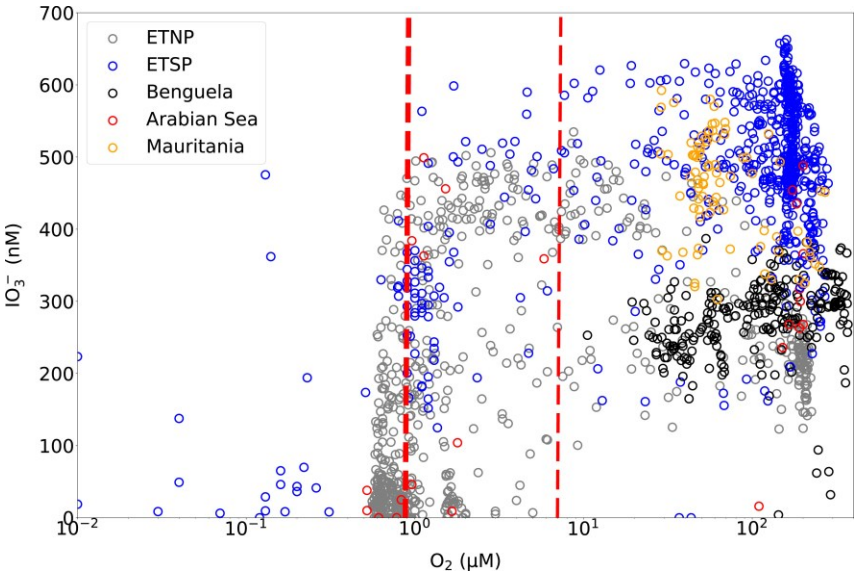

Figure 4.5. Compilation of IO_3^- and O_2 from global ODZs, including ETNP (Rue et al., 1997; Moriyasu et al., 2020), ETSP (Cutter et al., 2018; Rapp et al., 2020), Benguela upwelling system (Chapman, 1983), Arabian Sea (Farrenkopf & Luther, 2002), and Mauritania (Rapp et al., 2019). The thick dashed line highlights the O_2 threshold of 0.9 µM for best IO_3^- separation (AUC = 0.92). The thin dashed line represents the 'empirical' O_2 threshold proposed by Hardisty et al., (2021) and supported here when AUC and TPR are both optimized.

Earth System modelling: The cGENIE Earth System model has an iodine cycling module including: 1) water column IO_3^- reduction, 2) water column I^- oxidation, 3) photosynthetic uptake of IO_3^-, and 4) release of biogenic iodine as I^- during remineralization (Lu et al., 2018; Cheng et al., 2024). Tuning the iodine cycling parameterization in such a process-based model, together with comparing the simulated iodine distribution against abundant observations, offers an alternative method of comprehensively quantifying these parameters in the real world. Based on independent biological pump scenarios (non-temperature vs. temperature-dependent remineralization), real-ocean iodine compilations, and methods of model-data comparison (frequency distribution vs. model skill score M), two IO_3^- reduction thresholds were proposed: 30 µM (Lu et al., 2018) and 10 µM (Cheng et al., 2024). While both match with other independent

interpretations of IO_3^- reduction (Table 4.1), we note that the model calibration in Cheng et al., (2024) considered a more expanded modern iodine database and broader spatiotemporal statistical tests to define the O_2 threshold for IO_3^- reduction.

The limitation of such an approach is, however, that it is largely dependent on model uncertainties, even including factors beyond the iodine cycling. As an intermediate complexity model designed for paleoceanography studies, the spatial resolution of cGENIE is coarse so that detailed structures of the modern ocean are likely to be omitted. By dividing the global ocean in to 36×36 equal-area grids with 16 depth layers, the ODZs, such as the ETNP, are only represented as several grids, with very limited representation of complex oxygen gradients seen in the real ocean (Cheng et al., 2024). The uncertainties of simulation of other tracers in the model, such as oxygen, also impacts the model-data comparison of iodine. As discussed by Cheng et al., (2024), forcing the model O_2 to replicate the World Ocean Atlas 2018 (WOA18) observations enhances the simulation of iodine distribution, while in conjunction with changes in iodine cycling parameters. This observation demonstrated some uncertainty but also bolstered the importance of O_2 availability on data-model best fit. Further, although the IO_3^- threshold remains constant in the aforementioned study, we do not rule out the possibility that it could change with further model improvements or additional data.

4.6.1.3 Implications for the earliest appearance of I/Ca at the GOE

Our analyses of the conditions allowing for IO_3^- accumulation in seawater have direct implications for marine O_2 availability at the GOE when a shift from ubiquitous IO_3^- absence to widespread low, but present, IO_3^- accumulation is first observed for I/Ca (Hardisty et al., 2014). No matter whether in microenvironments or in bulk water, IO_3^- reduction appears to be regulated by certain O_2 thresholds below which the process is triggered. Therefore, certain I/Ca levels in

carbonate sediments, reflecting coeval seawater IO_3^-, should be able to provide constraints on the minimum degree of seawater oxygenation. Our microbial incubation experiment suggests that the O_2 level that triggers synthesis of IO_3^- reduction enzymes is probably close to 0.1 μM (~4×10^{-4} PAL). Importantly, the combination of the loss of S-MIF and maintenance of low Cr isotope fractionations constrains atmospheric pO_2 at the GOE at 10^{-5}-10^{-3} PAL, or 2.5nM to 0.25 μM O_2 in ambient waters via equilibrium with the atmosphere. Given that O_2 oases hosting *in situ* oxygen production above equilibrium thresholds may have occurred both before and after the GOE (Reinhard et al., 2016; Oslon et al., 2013), we suggest that widespread IO_3^- production starting at the GOE may most likely represent a change in the air-sea equilibrium value of O_2. As such, our results of 0.1 μM O_2 (~4×10^{-4} PAL) for IO_3^- reduction may be applied to discern atmospheric pO_2 at the GOE, which relates to pO_2 of ~0.4×10^{-3} PAL. Thus, the I/Ca record compliments the S-MIF and Cr isotope records and raises the minimum constraint on the pO_2 starting at the GOE.

There is some evidence of spatiotemporally isolated pre-GOE iodate accumulation (circa 2.9 to 2.8 Ga), potentially within oxygen oases (Fang et al., 2024). The presence of the S-MIF prior to the GOE requires the atmospheric pO_2 was $<10^{-3}$ PAL, which sets the equilibrium value for seawater. Our constraints on IO_3^- accumulation requiring higher O_2 marine oxygen than the equilibrium value may then in this case be best interpreted to reflect locally elevated O_2 accumulation via *in situ* photosynthesis in oxygen oases (Olson et al., 2013). Earth System modelling has demonstrated that local dissolved O_2 could maintain several micromoles, exceeding air-sea equilibrium, in high productivity areas when atmospheric O_2 is as low as 10^{-7} PAL (Olson et al., 2013; Reinhard et al., 2016; Reinhard & Planavsky, 2022). The likelihood of such oxygen oases has also been supported by elemental and isotopic signals indicating weakly oxygenated pre-GOE environments (Riding et al., 2014; Ossa et al., 2019). That said, our modeled iodate

distributions in Section 5.1.2 indicate that it is difficult to accumulate IO_3^- in simulated oxygen oases (Figure 4.6), thus more work is needed to understand the origin of pre-GOE IO_3^-.

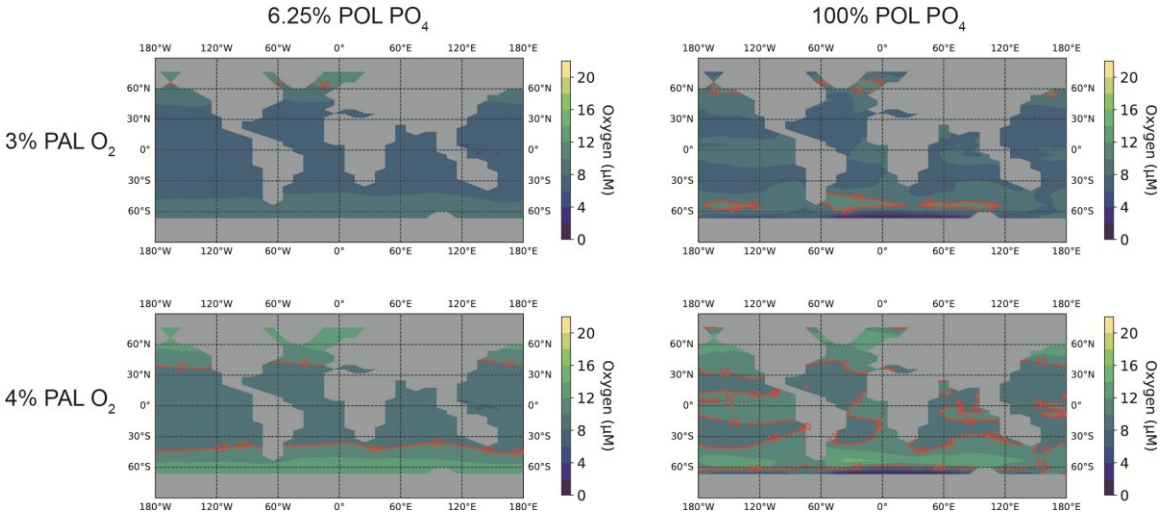

Figure 4.6. Surface dissolved O_2 distribution simulated by cGENIE. The red line contours 10 μM O_2, the proposed IO_3^- reduction threshold in the model. Under low PO_4 levels, oxygen oases do not develop.

The approaches evaluating O_2 thresholds that lead to low IO_3^- in modern ODZs provide upper constraints (~7 μM) on IO_3^- accumulation at the GOE, corresponding to pO_2 of ~3% PAL. However, these constraints may be more applicable toward estimating the conditions preventing elevated modern-like IO_3^-, and thus the maintenance of low but present IO_3^- once conditions allow for its initial accumulation. This topic is discussed in more detail in the following sections.

4.6.2 Constraints on post-GOE secular iodate variations from an Earth system model

Following the initial formation of ubiquitous iodate at the GOE, a low but stable I/Ca baseline around 0.5 μmol/mol prolongs during the long stasis period of the Proterozoic and into the Paleozoic—punctuated to higher values limited to discreet events (Hardisty et al., 2014, 2017; Lu et al., 2018; Shang et al., 2019). The conditions driving these secular variations are therefore a combination of O_2, primary productivity, and physical mixing, instead of redox alone. We attempt to explore the redox and nutrient conditions that are required to maintain low but present IO_3^-

accumulation in the Proterozoic surface ocean and thereafter with the aid from the cGENIE Earth system model.

We use the modern continental and bathymetric configuration, acknowledging that Proterozoic continents likely differed significantly from those of today (e.g., Olson et al., 2013; Reinhard et al., 2016). We discuss the merits of alternative continental configurations later, but the basic components driving the large-scale horizontal and vertical circulation—including Hadley-cell convergence driven equatorial westward current and its induced mid-low latitudes at the western size of the continents and high latitudinal deep-water formation—are well represented in the modern continental setting (Reinhard et al., 2016). Therefore, to better constrain the general conditions of broad secular IO_3^- variations over billions of years, a single, constant continental configuration appears to be more practical and limits uncertainty. The size of the total iodine inventory itself also has the potential to alter IO_3^- distributions (Lu et al., 2018). Due to the lack of certain evidence of a different oceanic iodine inventory, we also use the modern value of 500 nM total dissolved iodine. However, previous studies hypothesized that a larger iodine inventory might be possible, due to the absence of a remarkable sedimentary sink through biological assimilation by red and other algal clades, which did not evolve until the late Mesoproterozoic at the earliest (Muramatsu & Wedepohl, 1998; Hardisty et al., 2017). By running an alternative scenario by tuning the total iodine inventory to 800 nM, we evaluate total iodine inventory relationships with IO_3^- in the surface ocean (Figure 4.4 C,D).

The averaged IO_3^- in the surface ocean exhibits a distinct binary pattern in response to varying atmospheric O_2 and PO_4: (1) a low pO_2 threshold for the transition from low to high IO_3^- at PO_4 <10% POL; and (2) a linear increase in the pO_2 and PO_4 threshold at elevated PO_4 (Figure 4.4). Under low PO_4 conditions, as little as ~3% PAL pO_2 may be needed to increase IO_3^- from

ODZ-like levels to that observed in modern oxygenated settings. At higher PO_4, this value varies, but is 30% PAL pO_2 when PO_4 is at 100% POL. The implication is that secular I/Ca variations may have had a strict O_2 response in time periods with lower PO_4 (e.g., the Proterozoic), while some combination of nutrients and pO_2 may have impacted I/Ca in other periods. Notably, the 30% PAL pO_2 requirement for elevated IO_3^- at modern PO_4 is similar to the pO_2 required for ocean ventilation (Reinhard & Planavsky, 2022), implying that the increase in the IO_3^- baseline near the Paleozoic-Mesozoic may have required a restructuring of the ocean redox stratification and large swaths of oxygenated deep waters. These interpretations are discussed in more detail below.

4.6.2.1 Maintaining low IO_3^- levels in deoxygenated early oceans

Widespread ferruginous conditions in the Proterozoic may have supported a low PO_4 ocean (e.g., Lyons et al., 2014), making the lowest pO_2 requirements for increased I/Ca relevant for this interval. Nutrient levels, represented by PO_4 concentration in cGENIE, largely control the biological assimilation of IO_3^- as well as subsurface redox landscape through export productivity. As a consequence, when the PO_4 level increases above 10% POL, it influences the surface IO_3^- through biological reduction and assimilation together with reduction regulated by ambient O_2 levels (Figure 4.4). Recent model reconstruction supports a severely P-limited ocean, since widespread ferruginous deep ocean effectively remove PO_4 from the surface (Reinhard et al., 2017). Indeed, under the modern PO_4 level, at least 10% PAL is required to reach the Proterozoic baseline of 50 nM IO_3^- (Figure 4.4). Such prevalent high atmospheric O_2 levels throughout the mid-Proterozoic period was nevertheless inconsistent with current knowledge (e.g., reviewed by Lyons et al., 2021). The low productivity independently reconstructed from triple oxygen isotopes also supports that mid-Proterozoic ocean was probably nutrient limited (Crockford et al., 2018; Hodgskiss et al., 2019).

Under productivity below 10% POL, surface IO_3^- is therefore almost solely dependent on redox conditions (Figure 4.4A). Only several percentages of increase in atmospheric O_2 could raise the averaged surface IO_3^- beyond the 50 nM baseline to 250 nM, or the level at and above which is observed in modern well-oxygenated waters. We hypothesize that such a sharp gradient of IO_3^- in low atmospheric O_2 is mainly influenced by the threshold-controlled reduction mechanism in cGENIE (Cheng et al., 2024). Under low PO_4 levels, productivity might not support the development of oxygen oases (Figure 4.7). In this case, the surface O_2 is in equilibrium with the atmosphere and is controlled by temperature, and hence accumulates at high latitudes. The 3% PAL O_2, consequently, is required to allow high latitudinal dissolved O_2 to exactly reach the 10 μM threshold for IO_3^- accumulation in the model (Figures 4.6 and 4.7). Under these conditions, even subtle increases in atmospheric O_2 could remarkably expand the polar oxygenated region, enabling IO_3^- accumulation above 250 nM before it is physically transported into anoxic areas and reduced (Figure 4.4). Under even higher O_2 above this threshold (while maintaining low PO_4), IO_3^- will continue to expand into mid- and low latitude regions.

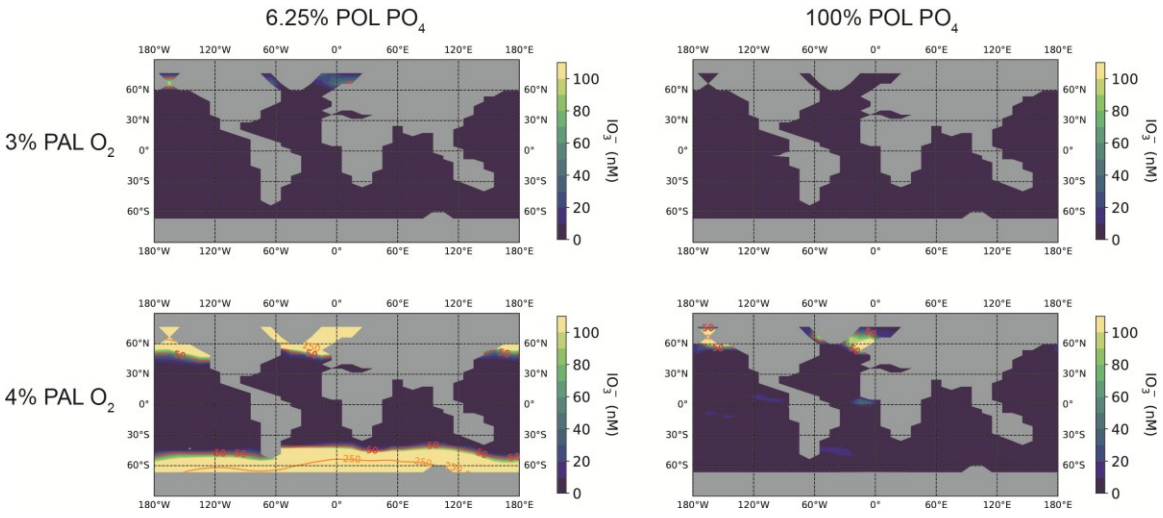

Figure 4.7. Surface seawater IO_3^- distribution simulated by cGENIE. The red and orange lines highlights 50 nM and 250 nM IO_3^- respectively, which representing the Proterozoic baseline and maximum I/Ca levels.

Our modeling results can be constrain conditions allowing Proterozoic increases in I/Ca ratios. Importantly the strata from the Xiamaling, Tieling, and Gaoyuzhuang Formations that host these highest mid-Proterozoic I/Ca values were formed in mid-low latitudes (Zhang et al., 2012). These observations require that higher O_2 beyond 7% PAL may have occurred during these intervals or that O_2 was generally higher across the Proterozoic and these increases in I/Ca then indicate decreases in nutrient levels.

Of course, there are limitations to the model that should be considered as well. For example, a plausible explanation is primary productivity in our cGENIE simulations are underestimated. Such underestimation could be caused by overestimating the PO_4 requirements by organism in a P-limited environment, since the maximum hypothesized Proterozoic C/P stoichiometry is four times of the present value (Reinhard et al., 2017). Additionally, we do not exclude the possibility of relatively localized enrichment of PO_4 from continental weathering (Föllmi et al., 2009) contributing to the formation of low-latitudinal oxygen oases. Indeed, the similar scenario also took place during the Neoproterozoic, followed by the expansion of marine productivity and oxygenation (Planavsky et al., 2010).

We emphasize that, no matter if it is in high latitudes in overall oligotrophic ocean, or in productive oxygen oases, modern-like accumulation of IO_3^- might requires atmospheric O_2 at levels above 3-7%. Basically, the mid-Proterozoic 'whiffs' highlighted by elevated I/Ca (Hardisty et al., 2014, 2017; Shang et al., 2019) might only represent several percentages of increase in atmospheric O_2. This reinforces the idea that the Earth's middle age was characterized by a prolonged stasis in atmospheric oxygenation, with only minor fluctuations failing to break through the low-O_2 ceiling that persisted for over a billion years (Liu et al., 2021).

4.6.2.2 Implications for the evolution of early animals

A prolonged and continuing debate has been focused on whether eukaryotic diversification was internally driven by evolution, or was triggered by O_2 availability (e.g., Mills & Canfield, 2014). The broad temporal coincidence between ocean and atmospheric oxygenation and diversification in fossil records leads to the classic point of view that O_2 played an essential role on evolution of complex life forms (Canfield et al., 2007; Sahoo et al., 2012). Also, indeed, some of the highest I/Ca values reported in ~1.56Ga Gaoyuzhuang Formation coincides with evolution of decimeter-scale multicellular eukaryotic fossils (Zhu et al., 2016; Shang et al., 2019). In contrast, early eukaryotes, even simple animals like demosponges, can survive under low O_2 of 0.5-4% PAL (Mills et al., 2014), therefore the low but prevalent O_2 throughout the mid-Proterozoic was unlikely to have inhibited diversification of early eukaryotes that dwelled in shallow nearshore settings (Sperling et al., 2013). Our model suggests that accumulation of elevated IO_3^- in local seawater does not—at least at low nutrient levels—necessarily require significant increases in atmospheric O_2. Under the prolonged stasis of atmospheric O_2 levels, the ocean redox landscape during the mid-Proterozoic was likely dynamic and highly heterogeneous (Luo et al., 2014; Gilleaudeau & Kah, 2015). Locally oxygenated oases, of which the extent was controlled by nutrient availability, were able to accumulate higher levels of dissolved O_2 but their instability likely made them difficult refuges for early animals to evolve (Reinhard et al., 2016).

4.6.2.3 Increase in iodate baseline to modern-like levels

Although I/Ca records information of surface ocean oxygenation, its secular transition from the Proterozoic level to modern-like levels also likely reflects deep ocean oxygenation since persistence of high near-surface IO_3^- requires replenishment from deep water masses (Hardisty & Lau, 2025). The low Proterozoic I/Ca baseline persisted into the Neoproterozoic, even with the

onset of the second major oxygenation event (Neoproterozoic oxygenation event, NOE) (Figure 4.1). Indeed, events of transient high I/Ca values breakthrough this low baseline temporally correlate to carbon isotopes ($\delta^{13}C$) excursions (e.g., Bitter Springs Anomally and Shuram Anomally) (Hardisty et al., 2017; Lu et al., 2017; Ding et al., 2022). We note that, during these events, the maximum I/Ca values exceeded ~5 μmol/mol, which reaches the modern levels. This is in contrast to the mid-Proterozoic maximum values (Figure 4.1). Such an increase in maximum accumulation IO_3^- in seawater probably reflects higher dissolved O_2 as well as wider oxygenated areas in equilibrium with the increased atmospheric O_2 in association with the NOE (as summarized by Cole et al., 2020 and Lyons et al., 2021). Independent of PO_4 levels, the minimum atmospheric O_2 that is required to support modern-level IO_3^- accumulation varies from 5%-30% PAL. These Neoproterozoic oxygenation events were, however, transient and in limited duration. Like their mid-Proterozoic predecessors, these oxygenation events failed to permanently maintain IO_3^- in the surface ocean at modern levels. Meanwhile, widespread anoxia, especially mid-depth euxinia laying below the shallow chemocline suppressed the formation of IO_3^- (Li et al., 2010; Sperling et al., 2015), as with its modern analogues in the Black Sea and the Baltic Sea (Wong & Brewer, 1977; Luther & Campbell, 1991; Truesdale et al., 2013; Cheng et al., unpublished). The redox interpretation from I/Ca matches with that based on thallium, uranium, as well as iron geochemical data, supporting a scenario that oxygenation during the Neoproterozoic was rather limited (Sperling et al., 2015; Zhang et al., 2018; Ostrander, 2023; Ostrander et al., 2023). The lack of fundamental changes in ocean redox structure is represented by a prolonged low I/Ca baseline (0.5-1 μmol/mol) throughout the whole Proterozoic Eon, which extended into the Early Paleozoic (Figure 4.1).

The Early Paleozoic oxygenation of atmosphere and ocean was more likely represented by a series stepwise process over a protracted period than a single event (Krause et al., 2018). Multiple lines of evidence have suggested that this period is characterized by low but dynamic redox conditions in the ocean (Gill et al., 2011; Sperling et al., 2015, 2021; Wei et al., 2021), which possibly applied evolutionary pressure for radiation of biodiversity (Pruss & Gill, 2024). This Early Paleozoic redox dynamo was recorded by frequent appearances of high I/Ca above the ODZ level (~2.5 μmol/mol) raising up from the low baseline (Lu et al., 2018; Wei et al., 2024).

Our model results suggest that atmospheric O_2 above ~30% PAL should support near-modern IO_3^- accumulation in the surface ocean (Figure 4.4A). This ~30% threshold also coincides with the modeled requirements for deep ocean ventilation (Reinhard & Planavsky, 2022). This milestone of fundamental change in the global ocean redox state probably was reached between the Middle Devonian through the Early Carboniferous (398-318 Ma), as recorded by near-modern baseline of Ce anomaly (Wallace et al., 2017) and uranium isotopes (Song et al., 2017; Cheng et al., 2020; Elrick et al., 2022). Biogeochemical models (e.g., GEOCARBSULFOR and COPSE) proposed an even earlier transition back to Silurian-Devonian (~416 Ma) (Krause et al., 2018; Lenton et al., 2018). If increases in atmospheric oxygen fully ventilated the ocean, similar to modern time, the transition of carbonate I/Ca record to the modern baseline would be expected to have occurred no later than the Carboniferous period.

A temporal inconsistency arises as, however, the early Paleozoic ocean redox state transition is only marked by a transient increase in I/Ca, followed by returning to the low baseline during the Late Carboniferous and Permian (Lu et al., 2018). Instead, the I/Ca in carbonates did not shift to a higher baseline approximate to the modern-like levels until ~200 Ma in the Early Mesozoic (Figure 4.1), which indicates a relatively delayed establishment of the modern iodine

cycle (Lu et al., 2018). Previous work has suggested that plant colonization and the associated increase in nutrient flux during the Late Paleozoic may have enhanced primary productivity, leading to intensified shallow ocean stratification even as atmospheric oxygen concentrations rose to modern levels. This redox stratification hence likely interrupted the transition of I/Ca to the modern baseline (Lu et al., 2018). The modern I/Ca baseline was not achieved until deepening of remineralization depths, a consequence proliferation of eukaryotic planktons (Lu et al., 2018).

We present a new perspective on the secular variation of the I/Ca baseline. Recent Earth System Model simulations have demonstrated that oxygenation of the deep ocean did not simply require an increase in O_2 above some threshold, but was also driven by changes of ocean circulation as a consequence of redistribution of continents (Pohl et al., 2022). Continental configurations conducive to ocean stratification and anoxia were particularly pronounced during the Paleozoic (Pohl et al., 2022). An analogy for this scenario are Mesozoic Oceanic Anoxic Events, where the atmosphere was fully oxygenated, but I/Ca and multiple other proxies indicate the ocean maintained widespread hypoxia due to continental configuration and other compounding conditions (e.g., Zhou et al., 2015; Clarkson et al., 2018; Reershemius & Planavsky, 2021). In this view, similar sensitivity analyses as those presented in Figure 4.4 may have different outcomes for the atmospheric pO_2 thresholds for elevated IO_3^- accumulation if alternative continental configurations were considered. We propose that, the final establishment of modern-like I/Ca baseline in Mesozoic therefore reflects a combination of factors that led to decreases in ocean stratification with a baseline in ocean redox more similar to today. This transition provides the latest constraint on the timing of the transition of an Oceanic Oxygenation Event world—i.e., increases in O_2 against a low O_2 baseline—to an Earth System characterized by Ocean Anoxic Events—i.e., decreases in O_2 against a backdrop of elevated O_2 (Hardisty & Lau, 2025).

4.7 Conclusion

We determined the O_2 threshold for triggering IO_3^- reduction through incubation of facultative anaerobic bacteria *S. oneidensis* MR-1. When dissolved O_2 in the medium decreased to ~0.1 μM (~4×10^{-4} PAL), IO_3^- reduction was observed. Incomplete IO_3^- reduction through the 72-hours experiment and slow growth indicates the *S. oneidensis* population utilizes the "bet-hedging" strategy, which only partially switch to anaerobic metabolism to reduce the energy cost of synthesizing proteins for electron-acceptor transformation. This O_2 threshold provides a new constraint on atmospheric pO_2 starting at the GOE when ubiquitous IO_3^- first appeared in the ocean at low but present levels.

Our cGENIE Earth system model simulation, which synthesizes a complete redox and biology induced iodine cycle, suggests that under low nutrient conditions only ~3% PAL O_2 is needed to accumulate 50 nM IO_3^- , which equivalent to the 0.5 μmol/mol I/Ca baseline of the Proterozoic. Reaching the level of 250 nM IO_3^-—that indicative of well oxygenated settings in the modern—in the Proterozoic ocean under the same low nutrient conditions, however, only requires a slight increase of atmospheric O_2 by less than 1% PAL. Our model results thus support the long-term stasis of atmospheric oxygenation <4% PAL during the mid-Proterozoic.

Accumulation of modern-like levels of IO_3^- in the surface ocean during the Paleozoic reflected deep ocean oxygenation, likely by a combination of increasing atmospheric O_2 above 30% PAL (if nutrients levels were more similar to today) or rearrangement of continental distribution. The final transition of I/Ca to the modern baseline indicates oxygenation through the water column, including surface, mid-depth, and deep ocean. This transition hence marks the estimation of the ocean redox baseline transitioning to that more similar to the modern.

REFERENCES

Amachi, S., Kawaguchi, N., Muramatsu, Y., Tsuchiya, S., Watanabe, Y., Shinoyama, H., and Fujii, T.: Dissimilatory iodate reduction by marine Pseudomonas sp. strain SCT, Appl. Environ. Microbiol., 73, 5725–5730, https://doi.org/10.1128/AEM.00241-07, 2007.

Bekker, A., Holland, H. D., Wang, P. L., Rumble, D., Stein, H. J., Hannah, J. L., Coetzee, L. L., and Beukes, N. J.: Dating the rise of atmospheric oxygen, Nature, 427, 117–120, https://doi.org/10.1038/nature02260, 2004.

Bellefroid, E. J., Hood, A. V. S., Hoffman, P. F., Thomas, M. D., Reinhard, C. T., and Planavsky, N. J.: Constraints on paleoproterozoic atmospheric oxygen levels, Proc. Natl. Acad. Sci. U. S. A., 115, 8104–8109, https://doi.org/10.1073/pnas.1806216115, 2018.

Bristow, L. A., Dalsgaard, T., Tiano, L., Mills, D. B., Bertagnolli, A. D., Wright, J. J., Hallam, S. J., Ulloa, O., Canfield, D. E., Peter, N., and Thamdrup, B.: Ammonium and nitrite oxidation at nanomolar oxygen concentrations in oxygen minimum zone waters, Proc. Natl. Acad. Sci., 113, 10601–10606, https://doi.org/10.1073/pnas.1600359113, 2016.

Butterfield, N. J.: Oxygen, animals and oceanic ventilation: An alternative view, Geobiology, 7, 1–7, https://doi.org/10.1111/j.1472-4669.2009.00188.x, 2009.

Canfield, D. E. and Thamdrup, B.: Towards a consistent classification scheme for geochemical environments, or, why we wish the term “suboxic” would go away: Editorial, Geobiology, 7, 385–392, https://doi.org/10.1111/j.1472-4669.2009.00214.x, 2009.

Canfield, D. E., Poulton, S. W., and Narbonne, G. M.: Late-Neoproterozoic deep-ocean oxygenation and the rise of animal life, Science (80-.)., 315, 92–95, https://doi.org/10.1126/science.1135013, 2007.

Canfield, D. E., Zhang, S., Frank, A. B., Wang, X., Wang, H., Su, J., Ye, Y., and Frei, R.: Highly fractionated chromium isotopes in Mesoproterozoic-aged shales and atmospheric oxygen, Nat. Commun., 9, 1–11, https://doi.org/10.1038/s41467-018-05263-9, 2018.

Chance, R., Baker, A. R., Carpenter, L., and Jickells, T. D.: The distribution of iodide at the sea surface, Environ. Sci. Process. Impacts, 16, 1841–1859, https://doi.org/10.1039/c4em00139g, 2014.

Chapman, P.: Changes in iodine speciation in the Benguela current upwelling system, Deep Sea Res. Part A, Oceanogr. Res. Pap., 30, 1247–1259, https://doi.org/10.1016/0198-0149(83)90083-3, 1983.

Cheng, K., Elrick, M., and Romaniello, S. J.: Early mississippian ocean anoxia triggered organic carbon burial and late paleozoic cooling: Evidence from uranium isotopes recorded in marine limestone, Geology, 48, 363–367, https://doi.org/10.1130/G46950.1, 2020.

Cheng, K., Ridgwell, A., and Hardisty, D. S.: Characterizing the marine iodine cycle and its relationship to ocean deoxygenation in an Earth System model, Biogeosciences, 21, 4927–4949, 2024.

Claire, M. W., Catling, D. C., and Zahnle, K. J.: Biogeochemical modelling of the rise in atmospheric oxygen, Geobiology, 4, 239–269, https://doi.org/10.1111/j.1472-4669.2006.00084.x, 2006.

Clarkson, M. O., Stirling, C. H., Jenkyns, H. C., Dickson, A. J., Porcelli, D., Moy, C. M., Von Strandmann, P. P. A. E., Cooke, I. R., and Lenton, T. M.: Uranium isotope evidence for two episodes of deoxygenation during Oceanic Anoxic Event 2, Proc. Natl. Acad. Sci. U. S. A., 115, 2918–2923, https://doi.org/10.1073/pnas.1715278115, 2018.

Clement, B. G., Luther, G. W., and Tebo, B. M.: Rapid, oxygen-dependent microbial Mn(II) oxidation kinetics at sub-micromolar oxygen concentrations in the Black Sea suboxic zone, Geochim. Cosmochim. Acta, 73, 1878–1889, https://doi.org/10.1016/j.gca.2008.12.023, 2009.

Cole, D. B., Reinhard, C. T., Wang, X., Gueguen, B., Halverson, G. P., Gibson, T., Hodgskiss, M. S. W., Mckenzie, N. R., Lyons, T. W., and Planavsky, N. J.: A shale-hosted Cr isotope record of low atmospheric oxygen during the Proterozoic, Geology, 44, 555–558, 2016.

Cole, D. B., Mills, D. B., Erwin, D. H., Sperling, E. A., Porter, S. M., Reinhard, C. T., and Planavsky, N. J.: On the co-evolution of surface oxygen levels and animals, Geobiology, 18, 260–281, https://doi.org/10.1111/gbi.12382, 2020.

Crockford, P. W., Hayles, J. A., Bao, H., Planavsky, N. J., Bekker, A., Fralick, P. W., Halverson, G. P., Bui, T. H., Peng, Y., and Wing, B. A.: Triple oxygen isotope evidence for limited mid-Proterozoic primary productivity, Nature, 559, 613–616, https://doi.org/10.1038/s41586-018-0349-y, 2018.

Crockford, P. W., On, Y. M. B., Ward, L. M., Milo, R., Halevy, I., Crockford, P. W., On, Y. M. B., Ward, L. M., Milo, R., and Halevy, I.: The geologic history of primary productivity, Curr. Biol., 33, 4741-4750.e5, https://doi.org/10.1016/j.cub.2023.09.040, 2023.

Cutter, G. A., Moffett, J. G., Nielsdóttir, M. C., and Sanial, V.: Multiple oxidation state trace elements in suboxic waters off Peru: In situ redox processes and advective/diffusive horizontal transport, Mar. Chem., 201, 77–89, https://doi.org/10.1016/j.marchem.2018.01.003, 2018.

Dalsgaard, T., Stewart, F. J., Thamdrup, B., De Brabandere, L., Revsbech, N. P., Ulloa, O., Canfield, D. E., and Delong, E. F.: Oxygen at nanomolar levels reversibly suppresses process rates and gene expression in anammox and denitrification in the oxygen minimum zone off Northern Chile, MBio, 5, 1–14, https://doi.org/10.1128/mBio.01966-14, 2014.

Ding, Y., Sun, W., Liu, S., Xie, J., Tang, D., Zhou, X., Zhou, L., Li, Z., Song, J., Li, Z., Xu, H., Tang, P., Liu, K., Li, W., and Chen, D.: Low oxygen levels with high redox heterogeneity in the late Ediacaran shallow ocean: Constraints from I/(Ca + Mg) and Ce/Ce* of the

Dengying Formation, South China, Geobiology, 20, 790–809, https://doi.org/10.1111/gbi.12520, 2022.

Dohrmann, M. and Wörheide, G.: Dating early animal evolution using phylogenomic data, Sci. Rep., 7, 1–6, https://doi.org/10.1038/s41598-017-03791-w, 2017.

Duhl, K. L. and TerAvest, M. A.: Shewanella oneidensis NADH Dehydrogenase Mutants Exhibit an Amino Acid Synthesis Defect, Front. Energy Res., 7, 1–12, https://doi.org/10.3389/fenrg.2019.00116, 2019.

Edwards, N. R. and Marsh, R.: Uncertainties due to transport-parameter sensitivity in an efficient 3-D ocean-climate model, Clim. Dyn., 24, 415–433, https://doi.org/10.1007/s00382-004-0508-8, 2005.

Elrick, M., Gilleaudeau, G. J., Romaniello, S. J., Algeo, T. J., Morford, J. L., Sabbatino, M., Goepfert, T. J., Cleal, C., Cascales-miñana, B., and Chernyavskiy, P.: Major Early-Middle Devonian oceanic oxygenation linked to early land plant evolution detected using high-resolution U isotopes of marine limestones, Earth Planet. Sci. Lett., 581, 117410, https://doi.org/10.1016/j.epsl.2022.117410, 2022.

Erwin, D. H. and Tweedt, S.: Ecological drivers of the Ediacaran-Cambrian diversification of Metazoa, Evol. Ecol., 26, 417–433, https://doi.org/10.1007/s10682-011-9505-7, 2012.

Erwin, D. H., Laflamme, M., Tweedt, S. M., Sperling, E. A., Pisani, D., and Peterson, K. J.: The Cambrian conundrum: Early divergence and later ecological success in the early history of animals, Science (80-.)., 334, 1091–1097, https://doi.org/10.1126/science.1206375, 2011.

Fang, H., Tang, D., Shi, X., Zhou, L., Zhou, X., Wu, M., Song, H., and Riding, R.: Early Mesoproterozoic Ca-carbonate precipitates record fluctuations in shallow marine oxygenation, Precambrian Res., 373, 106630, https://doi.org/10.1016/j.precamres.2022.106630, 2022.

Fang, H., Fralick, P., Ramsay, B., Tang, D., and Riding, R.: Non-zero I/(Ca + Mg) recorded in Archean and Paleoproterozoic shallow marine Ca-carbonate sediments, Precambrian Res., 405, 107350, https://doi.org/10.1016/j.precamres.2024.107350, 2024.

Farquhar, J. and Wing, B. A.: Multiple sulfur isotopes and the evolution of the atmosphere, 213, 1–13, https://doi.org/10.1016/S0012-821X(03)00296-6, 2003.

Farrenkopf, A. M. and Luther, G. W.: Iodine chemistry reflects productivity and denitrification in the Arabian Sea: Evidence for flux of dissolved species from sediments of western India into the OMZ, Deep. Res. Part II Top. Stud. Oceanogr., 49, 2303–2318, https://doi.org/10.1016/S0967-0645(02)00038-3, 2002.

Farrenkopf, A. M., Dollhopf, M. E., Chadhain, S. N., Luther, G. W., and Nealson, K. H.: Reduction of iodate in seawater during Arabian Sea shipboard incubations and in laboratory cultures of the marine bacterium Shewanella putrefaciens strain MR-4, Mar. Chem., 57, 347–354, https://doi.org/10.1016/S0304-4203(97)00039-X, 1997.

Föllmi, K. B., Hosein, R., Arn, K., and Steinmann, P.: Weathering and the mobility of phosphorus in the catchments and forefields of the Rhône and Oberaar glaciers, central Switzerland: Implications for the global phosphorus cycle on glacial-interglacial timescales, Geochim. Cosmochim. Acta, 73, 2252–2282, https://doi.org/10.1016/j.gca.2009.01.017, 2009.

Ford, K. C. and Teravest, M. A.: operate bidirectionally to enable microbial electrosynthesis, 90, 2024.

Gill, B. C., Lyons, T. W., Young, S. A., Kump, L. R., Knoll, A. H., and Saltzman, M. R.: Geochemical evidence for widespread euxinia in the Later Cambrian ocean, Nature, 469, 80–83, https://doi.org/10.1038/nature09700, 2011.

Gilleaudeau, G. J. and Kah, L. C.: Heterogeneous redox conditions and a shallow chemocline in the Mesoproterozoic ocean: Evidence from carbon-sulfur-iron relationships, Precambrian Res., 257, 94–108, https://doi.org/10.1016/j.precamres.2014.11.030, 2015.

Gilleaudeau, G. J., Frei, R., Kaufman, A. J., Kah, L. C., Azmy, K., Bartley, J. K., Chernyavskiy, P., and Knoll, A. H.: Oxygenation of the mid-Proterozoic atmosphere: Clues from chromium isotopes in carbonates, Geochemical Perspect. Lett., 2, 178–187, https://doi.org/10.7185/geochemlet.1618, 2016.

Glock, N., Liebetrau, V., and Eisenhauer, A.: I/Ca ratios in benthic foraminifera from the Peruvian oxygen minimum zone: Analytical methodology and evaluation as a proxy for redox conditions, Biogeosciences, 11, 7077–7095, https://doi.org/10.5194/bg-11-7077-2014, 2014.

Goldblatt, C., Lenton, T. M., and Watson, A. J.: Bistability of atmospheric oxygen and the Great Oxidation, Nature, 443, 683–686, https://doi.org/10.1038/nature05169, 2006.

Gruenberg, M. C. and TerAvest, M. A.: A common inducer molecule enhances sugar utilization by Shewanella oneidensis MR-1, J. Ind. Microbiol. Biotechnol., 50, https://doi.org/10.1093/jimb/kuad018, 2023.

Guo, J., Jiang, J., Peng, Z., Zhong, Y., Jiang, Y., Jiang, Z., Hu, Y., Dong, Y., and Shi, L.: Global occurrence of the bacteria with capability for extracellular reduction of iodate, Front. Microbiol., 13, 1–10, https://doi.org/10.3389/fmicb.2022.1070601, 2022a.

Guo, J., Jiang, Y., Hu, Y., Jiang, Z., Dong, Y., and Shi, L.: The roles of DmsEFAB and MtrCAB in extracellular reduction of iodate by Shewanella oneidensis MR-1 with lactate as the sole electron donor, Environ. Microbiol., 24, 5039–5050, https://doi.org/10.1111/1462-2920.16130, 2022b.

Hardisty, D. S. and Lau, K. V: Ocean redox evolution past and present, in: Treatise on geochemistry (3rd Edition), edited by: Anbar, A. D. and Weis, D., Elsevier Science, 245–296, 2025.

Hardisty, D. S., Lu, Z., Planavsky, N. J., Bekker, A., Philippot, P., Zhou, X., and Lyons, T. W.: An iodine record of Paleoproterozoic surface ocean oxygenation, Geology, 42, 619–622, https://doi.org/10.1130/G35439.1, 2014.

Hardisty, D. S., Lu, Z., Bekker, A., Diamond, C. W., Gill, B. C., Jiang, G., Kah, L. C., Knoll, A. H., Loyd, S. J., Osburn, M. R., Planavsky, N. J., Wang, C., Zhou, X., and Lyons, T. W.: Perspectives on Proterozoic surface ocean redox from iodine contents in ancient and recent carbonate, Earth Planet. Sci. Lett., 463, 159–170, https://doi.org/10.1016/j.epsl.2017.01.032, 2017.

Hardisty, D. S., Horner, T. J., Evans, N., Moriyasu, R., Babbin, A. R., Wankel, S. D., Moffett, J. W., and Nielsen, S. G.: Limited iodate reduction in shipboard seawater incubations from the Eastern Tropical North Pacific oxygen deficient zone, Earth Planet. Sci. Lett., 554, 116676, https://doi.org/10.1016/j.epsl.2020.116676, 2021.

Hashim, M. S., Burke, J. E., Hardisty, D. S., and Kaczmarek, S. E.: Iodine incorporation into dolomite: Experimental constraints and implications for the iodine redox proxy and Proterozoic Ocean, Geochim. Cosmochim. Acta, 338, 365–381, https://doi.org/10.1016/j.gca.2022.10.027, 2022.

Hassan, J., Bergaust, L. L., Wheat, I. D., and Bakken, L. R.: Low Probability of Initiating nirS Transcription Explains Observed Gas Kinetics and Growth of Bacteria Switching from Aerobic Respiration to Denitrification, PLoS Comput. Biol., 10, https://doi.org/10.1371/journal.pcbi.1003933, 2014.

Hodgskiss, M. S. W., Crockford, P. W., Peng, Y., Wing, B. A., and Horner, T. J.: A productivity collapse to end Earth ' s Great Oxidation, 116, 10–15, https://doi.org/10.1073/pnas.1900325116, 2019.

Hughes, C., Barton, E., Hepach, H., Chance, R., Wadley, M. R., Pickering, M. D., Hogg, K., Pommerening-r, A., Stevens, D. P., and Jickells, T. D.: Oxidation of iodide to iodate by cultures of marine ammonia-oxidising bacteria, Mar. Chem., 234, 1–7, https://doi.org/10.1016/j.marchem.2021.104000, 2021.

Javaux, E. J. and Lepot, K.: The Paleoproterozoic fossil record: Implications for the evolution of the biosphere during Earth's middle-age, Earth-Science Rev., 176, 68–86, https://doi.org/10.1016/j.earscirev.2017.10.001, 2018.

Javaux, J., Knoll, A., and Walter, M.: Morphological and ecological complexicity in early eukaryotic ecosystem, Nature, 412, 2001.

Jiang, Z., Cui, M., Qian, L., Jiang, Y., Shi, L., Dong, Y., Li, J., and Wang, Y.: Abiotic and Biotic Reduction of Iodate Driven by Shewanella oneidensis MR-1, Environ. Sci. Technol., 57, 19817–19826, https://doi.org/10.1021/acs.est.3c06490, 2023.

Jickells, T. D., Boyd, S. S., and Knap, A. H.: Iodine Cycling in the Sargasso Sea and the B e r m u d a Inshore Waters, Mar. Chem., 24, 61–82, 1988.

Johnson, J. E., Gerpheide, A., Lamb, M. P., and Fischer, W. W.: O2 constraints from Paleoproterozoic detrital pyrite and uraninite, Bull. Geol. Soc. Am., 126, 813–830, https://doi.org/10.1130/B30949.1, 2014.

Kerisit, S. N., Smith, F. N., Saslow, S. A., Hoover, M. E., Lawter, A. R., and Qafoku, N. P.: Incorporation Modes of Iodate in Calcite, Environ. Sci. Technol., 52, 5902–5910, https://doi.org/10.1021/acs.est.8b00339, 2018.

Kine, K., Yamamura, S., and Amachi, S.: Iodate reduction by marine aerobic bacteria, Front. Microbiol., 15, 1–8, https://doi.org/10.3389/fmicb.2024.1446596, 2024.

Knoll, A. H.: Paleobiological perspectives on early microbial evolution, Cold Spring Harb. Perspect. Biol., 7, 1–17, https://doi.org/10.1101/cshperspect.a018093, 2014.

Krause, A. J., Mills, B. J. W., Zhang, S., Planavsky, N. J., Lenton, T. M., and Poulton, S. W.: Stepwise oxygenation of the Paleozoic atmosphere, Nat. Commun., 9, 1–10, https://doi.org/10.1038/s41467-018-06383-y, 2018.

Lenton, T. M., Daines, S. J., and Mills, B. J. W.: Earth-Science Reviews Invited review COPSE reloaded : An improved model of biogeochemical cycling over Phanerozoic time, Earth-Science Rev., 178, 1–28, https://doi.org/10.1016/j.earscirev.2017.12.004, 2018.

Li, C., Love, G. D., Lyons, T. W., Fike, D. A., Sessions, A. L., and Chu, X.: A stratified redox model for the ediacaran ocean, Science (80-.)., 328, 80–83, https://doi.org/10.1126/science.1182369, 2010.

Li, C., Hardisty, D. S., Luo, G., Huang, J., Algeo, T. J., Cheng, M., Shi, W., An, Z., Tong, J., Xie, S., Jiao, N., and Lyons, T. W.: Uncovering the spatial heterogeneity of Ediacaran carbon cycling, Geobiology, 15, 211–224, https://doi.org/10.1111/gbi.12222, 2017.

Li, H., Yeager, C. M., Brinkmeyer, R., Zhang, S., Ho, Y., Xu, C., Jones, W. L., Schwehr, K. A., Otosaka, S., Roberts, K. A., Kaplan, D. I., and Santschi, P. H.: Bacterial Production of Organic Acids Enhances H 2 O 2 -Dependent Iodide Oxidation, Environ. Sci. Technol., 46, 4837–4844, 2012.

Li, H., Daniel, B., Creeley, D., Grandbois, R., Zhang, S., Xu, C., Ho, Y., and Schwehr, K. A.: Superoxide Production by a Manganese-Oxidizing Bacterium Facilitates Iodide Oxidation, Appl. Environ. Microbiol., 80, 2693–2699, https://doi.org/10.1128/AEM.00400-14, 2014.

Li, J., Fang, W., Li, C., Cui, M., Qian, L., Jiang, Z., Jiang, Y., Shi, L., Xie, X., Guo, H., Li, P., Dong, Y., Xiu, W., Wang, Y., and Wang, Y.: Dissimilatory Iodate-Reducing Microorganisms Contribute to the Enrichment of Iodine in Groundwater, Environ. Sci. Technol., 58, https://doi.org/10.1021/acs.est.4c04455, 2024.

Liu, A., Tang, D., Shi, X., Zhou, X., Zhou, L., Shang, M., Li, Y., and Fang, H.: Mesoproterozoic oxygenated deep seawater recorded by early diagenetic carbonate concretions from the Member IV of the Xiamaling Formation, North China, Precambrian Res., 341, 105667, https://doi.org/10.1016/j.precamres.2020.105667, 2020.

Liu, X. M., Kah, L. C., Knoll, A. H., Cui, H., Wang, C., Bekker, A., and Hazen, R. M.: A persistently low level of atmospheric oxygen in Earth's middle age, Nat. Commun., 12, 1–7, https://doi.org/10.1038/s41467-020-20484-7, 2021.

Love, G. D., Grosjean, E., Stalvies, C., Fike, D. A., Grotzinger, J. P., Bradley, A. S., Kelly, A. E., Bhatia, M., Meredith, W., Snape, C. E., Bowring, S. A., Condon, D. J., and Summons, R. E.: Fossil steroids record the appearance of Demospongiae during the Cryogenian period, Nature, 457, 718–721, https://doi.org/10.1038/nature07673, 2009.

Lu, W., Wörndle, S., Halverson, G. P., Zhou, X., Bekker, A., Rainbird, R. H., Hardisty, D. S., Lyons, T. W., and Lu, Z.: Iodine proxy evidence for increased ocean oxygenation during the Bitter Springs Anomaly, Geochemical Perspect. Lett., 5, 53–57, https://doi.org/10.7185/geochemlet.1746, 2017.

Lu, W., Ridgwell, A., Thomas, E., Hardisty, D. S., Luo, G., Algeo, T. J., Saltzman, M. R., Gill, B. C., Shen, Y., Ling, H. F., Edwards, C. T., Whalen, M. T., Zhou, X., Gutchess, K. M., Jin, L., Rickaby, R. E. M., Jenkyns, H. C., Lyons, T. W., Lenton, T. M., Kump, L. R., and Lu, Z.: Late inception of a resiliently oxygenated upper ocean, Science (80-.)., 361, 174–177, https://doi.org/10.1126/science.aar5372, 2018.

Lu, W., Rickaby, R. E. M., Hoogakker, B. A. A., Rathburn, A. E., Burkett, A. M., Dickson, A. J., Martínez-Méndez, G., Hillenbrand, C. D., Zhou, X., Thomas, E., and Lu, Z.: I/Ca in epifaunal benthic foraminifera: A semi-quantitative proxy for bottom water oxygen in a multi-proxy compilation for glacial ocean deoxygenation, Earth Planet. Sci. Lett., 533, 116055, https://doi.org/10.1016/j.epsl.2019.116055, 2020a.

Lu, W., Dickson, A. J., Thomas, E., Rickaby, R. E. M., Chapman, P., and Lu, Z.: Refining the planktic foraminiferal I/Ca proxy: Results from the Southeast Atlantic Ocean, Geochim. Cosmochim. Acta, 287, 318–327, https://doi.org/10.1016/j.gca.2019.10.025, 2020b.

Lu, Z., Jenkyns, H. C., and Rickaby, R. E. M.: Iodine to calcium ratios in marine carbonate as a paleo-redox proxy during oceanic anoxic events, Geology, 38, 1107–1110, https://doi.org/10.1130/G31145.1, 2010.

Lu, Z., Hoogakker, B. A. A., Hillenbrand, C.-D., Zhou, X., Thomas, E., Gutchess, K. M., Lu, W., Jones, L., and Rickaby, R. E. M.: Oxygen depletion recorded in upper waters of the glacial Southern Ocean, Nat. Commun., 7, 1–8, https://doi.org/10.1038/ncomms11146, 2016.

Luo, G., Junium, C. K., Kump, L. R., Huang, J., Li, C., Feng, Q., Shi, X., Bai, X., and Xie, S.: Shallow stratification prevailed for ~ 1700 to ~ 1300 Ma ocean : Evidence from organic carbon isotopes in the North China Craton, Earth Planet. Sci. Lett., 400, 219–232, https://doi.org/10.1016/j.epsl.2014.05.020, 2014.

Luther, G. W.: Review on the physical chemistry of iodine transformations in the oceans, Front. Mar. Sci., 10, 1–16, https://doi.org/10.3389/fmars.2023.1085618, 2023.

Luther, G. W. and Campbell, T.: Iodine speciation in the water column of the Black Sea, Deep Sea Res. Part A. Oceanogr. Res. Pap., 38, S875–S882, https://doi.org/10.1016/s0198-0149(10)80014-7, 1991.

Lycus, P., Soriano-Laguna, M. J., Kjos, M., Richardson, D. J., Gates, A. J., Milligan, D. A., Frostegård, Å., Bergaust, L., and Bakken, L. R.: A bet-hedging strategy for denitrifying

bacteria curtails their release of N2O, Proc. Natl. Acad. Sci. U. S. A., 115, 11820–11825, https://doi.org/10.1073/pnas.1805000115, 2018.

Lyons, T. W., Reinhard, C. T., and Planavsky, N. J.: The rise of oxygen in Earth's early ocean and atmosphere, Nature, 506, 307–315, https://doi.org/10.1038/nature13068, 2014.

Lyons, T. W., Diamond, C. W., Planavsky, N. J., Reinhard, C. T., and Li, C.: Oxygenation, Life, and the Planetary System during Earth's Middle History: An Overview, Astrobiology, 21, 906–923, https://doi.org/10.1089/ast.2020.2418, 2021.

Mills, D. B. and Canfield, D. E.: Oxygen and animal evolution: Did a rise of atmospheric oxygen "trigger" the origin of animals?, BioEssays, 36, 1145–1155, https://doi.org/10.1002/bies.201400101, 2014.

Mills, D. B., Ward, L. M., Jones, C. A., Sweeten, B., Forth, M., Treusch, A. H., and Canfield, D. E.: Oxygen requirements of the earliest animals, Proc. Natl. Acad. Sci. U. S. A., 111, 4168–4172, https://doi.org/10.1073/pnas.1400547111, 2014.

Mok, J. K., Toporek, Y. J., Shin, H. D., Lee, B. D., Lee, M. H., and DiChristina, T. J.: Iodate Reduction by Shewanella oneidensis Does Not Involve Nitrate Reductase, Geomicrobiol. J., 35, 570–579, https://doi.org/10.1080/01490451.2018.1430189, 2018.

Moriyasu, R., Evans, N., Bolster, K. M., Hardisty, D. S., and Moffett, J. W.: The Distribution and Redox Speciation of Iodine in the Eastern Tropical North Pacific Ocean, Global Biogeochem. Cycles, 34, 1–23, https://doi.org/10.1029/2019GB006302, 2020.

Moriyasu, R., Bolster, K. M., Hardisty, D. S., Kadko, D. C., Stephens, M. P., and Moffett, J. W.: Meridional Survey of the Central Pacific Reveals Iodide Accumulation in Equatorial Surface Waters and Benthic Sources in the Abyssal Plain Global Biogeochemical Cycles, Global Biogeochem. Cycles, 37, 1–15, https://doi.org/10.1029/2021GB007300, 2023.

Muramatsu, Y. and Wedepohl, K. H.: The distribution of iodine in the Earth's crust, Chem. Geol., 147, 201–216, https://doi.org/10.1016/S0009-2541(98)00013-8, 1998.

Neuweiler, F., Turner, E. C., and Burdige, D. J.: Early Neoproterozoic origin of the metazoan clade recorded in carbonate rock texture, Geology, 37, 475–478, https://doi.org/10.1130/G25621A.1, 2009.

Olson, S. L., Kump, L. R., and Kasting, J. F.: Quantifying the areal extent and dissolved oxygen concentrations of Archean oxygen oases, Chem. Geol., 362, 35–43, https://doi.org/10.1016/j.chemgeo.2013.08.012, 2013.

Ossa, F. O., Hofmann, A., Spangenberg, J. E., Poulton, S. W., Stüeken, E. E., Schoenberg, R., Eickmann, B., Wille, M., Butler, M., and Bekker, A.: Limited oxygen production in the Mesoarchean ocean, Proc. Natl. Acad. Sci. U. S. A., 116, 6647–6652, https://doi.org/10.1073/pnas.1818762116, 2019.

Ostrander, C. M.: Mulling and nulling the coeval rise of Ediacaran oxygen and animals, Earth Planet. Sci. Lett., 614, 118187, https://doi.org/10.1016/j.epsl.2023.118187, 2023.

Ostrander, C. M., Bjerrum, C. J., Ahm, A. S. C., Stenger, S. R., Bergmann, K. D., El-Ghali, M. A. K., Harthi, A. R., Aisri, Z., and Nielsen, S. G.: Widespread seafloor anoxia during generation of the Ediacaran Shuram carbon isotope excursion, Geobiology, 1–15, https://doi.org/10.1111/gbi.12557, 2023.

Ozaki, K., Reinhard, C. T., and Tajika, E.: A sluggish mid-Proterozoic biosphere and its effect on Earth's redox balance, Geobiology, 17, 3–11, https://doi.org/10.1111/gbi.12317, 2019.

Planavsky, N. J., Rouxel, O. J., Bekker, A., Lalonde, S. V., Konhauser, K. O., Reinhard, C. T., and Lyons, T. W.: The evolution of the marine phosphate reservoir, Nature, 467, 1088–1090, https://doi.org/10.1038/nature09485, 2010.

Planavsky, N. J., Reinhard, C. T., Wang, X., Thomson, D., McGoldrick, P., Rainbird, R. H., Johnson, T., Fischer, W. W., and Lyons, T. W.: Low mid-proterozoic atmospheric oxygen levels and the delayed rise of animals, Science (80-.)., 346, 635–638, https://doi.org/10.1126/science.1258410, 2014.

Podder, J., Lin, J., Sun, W., Botis, S. M., Tse, J., Chen, N., Hu, Y., Li, D., Seaman, J., and Pan, Y.: Iodate in calcite and vaterite: Insights from synchrotron X-ray absorption spectroscopy and first-principles calculations, Geochim. Cosmochim. Acta, 198, 218–228, https://doi.org/10.1016/j.gca.2016.11.032, 2017.

Pohl, A., Ridgwell, A., Stockey, R. G., Thomazo, C., Keane, A., Vennin, E., and Scotese, C. R.: Continental configuration controls ocean oxygenation during the Phanerozoic, Nature, 608, 523–527, https://doi.org/10.1038/s41586-022-05018-z, 2022.

Pruss, S. B. and Gill, B. C.: Life on the Edge : The Cambrian Marine Realm and Oxygenation, Annu. Rev. Earth Planet. Sci., 52, 109–132, 2024.

Rapp, I., Schlosser, C., Barraqueta, J. M., Wenzel, B., Lüdke, J., and Scholten, J.: Controls on redox-sensitive trace metals in the Mauritanian oxygen minimum zone, Biogeosciences, 16, 4157–4182, 2019.

Rapp, I., Schlosser, C., Browning, T. J., Wolf, F., Le Moigne, F. A. C., Gledhill, M., and Achterberg, E. P.: El Niño-Driven Oxygenation Impacts Peruvian Shelf Iron Supply to the South Pacific Ocean, Geophys. Res. Lett., 47, 0–3, https://doi.org/10.1029/2019GL086631, 2020.

Reershemius, T. and Planavsky, N. J.: Earth-Science Reviews What controls the duration and intensity of ocean anoxic events in the Paleozoic and the Mesozoic ?, Earth-Science Rev., 221, 103787, https://doi.org/10.1016/j.earscirev.2021.103787, 2021.

Reinhard, C. T. and Planavsky, N. J.: The History of Ocean Oxygenation, Ann. Rev. Mar. Sci., 14, 331–353, https://doi.org/10.1146/annurev-marine-031721-104005, 2022.

Reinhard, C. T., Planavsky, N. J., Olson, S. L., Lyons, T. W., and Erwin, D. H.: Earth's oxygen cycle and the evolution of animal life, Proc. Natl. Acad. Sci. U. S. A., 113, 8933–8938, https://doi.org/10.1073/pnas.1521544113, 2016.

Reinhard, C. T., Planavsky, N. J., Gill, B. C., Ozaki, K., Robbins, L. J., Lyons, T. W., Fischer, W. W., Wang, C., Cole, D. B., and Konhauser, K. O.: Evolution of the global phosphorus cycle, Nature, 541, 386–389, https://doi.org/10.1038/nature20772, 2017.

Reyes-Umana, V., Henning, Z., Lee, K., Barnum, T. P., and Coates, J. D.: Genetic and phylogenetic analysis of dissimilatory iodate-reducing bacteria identifies potential niches across the world's oceans, ISME J., 16, 38–49, https://doi.org/10.1038/s41396-021-01034-5, 2021.

Ridgwell, A., Hargreaves, J. C., Edwards, N. R., Annan, J. D., Lenton, T. M., Marsh, R., Yool, A., and Watson, A.: Marine geochemical data assimilation in an efficient Earth system model of global biogeochemical cycling, Biogeosciences, 4, 87–104, https://doi.org/10.5194/bg-4-87-2007, 2007.

Riding, R., Fralick, P., and Liang, L.: Identification of an Archean marine oxygen oasis, Precambrian Res., 251, 232–237, https://doi.org/10.1016/j.precamres.2014.06.017, 2014.

Rue, E. L., Smith, G. J., Cutter, G. A., and Bruland, K. W.: The response of trace element redox couples to suboxic conditions in the water column, Deep. Res. Part I Oceanogr. Res. Pap., 44, 113–134, https://doi.org/10.1016/S0967-0637(96)00088-X, 1997.

Sahoo, S. K., Planavsky, N. J., Kendall, B., Wang, X., Shi, X., Scott, C., Anbar, A. D., Lyons, T. W., and Jiang, G.: Ocean oxygenation in the wake of the Marinoan glaciation, Nature, 489, 546–549, https://doi.org/10.1038/nature11445, 2012.

Saunders, J. K., McIlvin, M. R., Dupont, C. L., Kaul, D., Moran, D. M., Horner, T., Laperriere, S. M., Webb, E. A., Bosak, T., Santoro, A. E., and Saito, M. A.: Microbial functional diversity across biogeochemical provinces in the central Pacific Ocean, Proc. Natl. Acad. Sci. U. S. A., 119, 1–12, https://doi.org/10.1073/pnas.2200014119, 2022.

Schneider, D. A., Bickford, M. E., Cannon, W. F., Schulz, K. J., and Hamilton, M. A.: Age of volcanic rocks and syndepositional iron formations, Marquette Range Supergroup: Implications for the tectonic setting of Paleoproterozoic iron formations of the Lake Superior region, Can. J. Earth Sci., 39, 999–1012, https://doi.org/10.1139/e02-016, 2002.

Shang, M., Tang, D., Shi, X., Zhou, L., Zhou, X., Song, H., and Jiang, G.: A pulse of oxygen increase in the early Mesoproterozoic ocean at ca. 1.57–1.56 Ga, Earth Planet. Sci. Lett., 527, 115797, https://doi.org/10.1016/j.epsl.2019.115797, 2019.

Sharma, M. and Shukla, Y.: Taxonomy and affinity of Early Mesoproterozoic megascopic helically coiled and related fossils from the Rohtas Formation, the Vindhyan Supergroup, India, Precambrian Res., 173, 105–122, https://doi.org/10.1016/j.precamres.2009.05.002, 2009.

Shin, H. D., Toporek, Y., Mok, J. K., Maekawa, R., Lee, B. D., Howard, M. H., and DiChristina, T. J.: Iodate Reduction by Shewanella oneidensis Requires Genes Encoding an

Extracellular Dimethylsulfoxide Reductase, Front. Microbiol., 13, 1–11, https://doi.org/10.3389/fmicb.2022.852942, 2022.

Song, H., Song, H., Algeo, T. J., Tong, J., Romaniello, S. J., Zhu, Y., Chu, D., Gong, Y., and Anbar, A. D.: Uranium and carbon isotopes document global-ocean redoxproductivity relationships linked to cooling during the Frasnian- Famennian mass extinction, Geology, 45, 887–890, https://doi.org/10.1130/G39393.1, 2017.

Sperling, E. A., Halverson, G. P., Knoll, A. H., MacDonald, F. A., and Johnston, D. T.: A basin redox transect at the dawn of animal life, 143–155 pp., https://doi.org/10.1016/j.epsl.2013.04.003, 2013.

Sperling, E. A., Wolock, C. J., Morgan, A. S., Gill, B. C., Kunzmann, M., Halverson, G. P., Macdonald, F. A., Knoll, A. H., and Johnston, D. T.: Statistical analysis of iron geochemical data suggests limited late Proterozoic oxygenation, Nature, 523, 3–6, https://doi.org/10.1038/nature14589, 2015.

Sperling, E. A., Melchin, M. J., Fraser, T., Stockey, R. G., Farrell, U. C., Bhajan, L., Brunoir, T. N., Cole, D. B., Gill, B. C., Lenz, A., Loydell, D. K., Malinowski, J., Miller, A. J., Plaza-torres, S., Bock, B., Rooney, A. D., Tecklenburg, S. A., Vogel, J. M., Planavsky, N. J., and Strauss, J. V: GEOCHEMISTRY A long-term record of early to mid-Paleozoic marine redox change, Sci. Adv., 7, 1–12, 2021.

Tang, D., Fang, H., Shi, X., Liang, L., Zhou, L., Xie, B., Huang, K., Zhou, X., Wu, M., and Riding, R.: Mesoproterozoic Molar Tooth Structure Related to Increased Marine Oxygenation, J. Geophys. Res. Biogeosciences, 128, 1–18, https://doi.org/10.1029/2022jg007077, 2023.

Thamdrup, B., Dalsgaard, T., and Revsbech, N. P.: Widespread functional anoxia in the oxygen minimum zone of the Eastern South Pacific, Deep. Res. Part I Oceanogr. Res. Pap., 65, 36–45, https://doi.org/10.1016/j.dsr.2012.03.001, 2012.

Toporek, Y. J., Mok, J. K., Shin, H. D., Lee, B. D., Lee, M. H., and DiChristina, T. J.: Metal Reduction and Protein Secretion Genes Required for Iodate Reduction by Shewanella oneidensis, Appl. Environ. Microbiol., 85, 1–13, https://doi.org/10.1128/AEM.02115-18, 2019.

Truesdale, V. W., Bale, A. J., and Woodward, E. M. S.: The meridional distribution of dissolved iodine in near-surface waters of the Atlantic Ocean, Prog. Oceanogr., 45, 387–400, https://doi.org/10.1016/S0079-6611(00)00009-4, 2000.

Truesdale, V. W., Nausch, G., and Waite, T. J.: The effects of the 2001 Barotropic intrusion of bottom-water upon the vertical distribution of inorganic iodine in the Gotland Deep, Cont. Shelf Res., 55, 155–167, https://doi.org/10.1016/j.csr.2013.01.005, 2013.

Tsunogai, S. and Sase, T.: Formation of iodide-iodine in the ocean, Deep. Res., 16, 489–496, 1969.

Wadley, M. R., Stevens, D. P., Jickells, T. D., Hughes, C., Chance, R., Hepach, H., Tinel, L., and Carpenter, L. J.: A Global Model for Iodine Speciation in the Upper Ocean, Global Biogeochem. Cycles, 34, 0–3, https://doi.org/10.1029/2019GB006467, 2020.

Wallace, M. W., Hood, A., Shuster, A., Greig, A., Planavsky, N. J., and Reed, C. P.: Oxygenation history of the Neoproterozoic to early Phanerozoic and the rise of land plants, Earth Planet. Sci. Lett., 466, 12–19, https://doi.org/10.1016/j.epsl.2017.02.046, 2017.

Wei, G., Li, D., Lu, Z., Jiang, G., and Ling, H.: Shallow-water redox evolution from the Ediacaran to the early Cambrian : Linkages to the early animal innovations, Glob. Planet. Change, 240, 1–11, https://doi.org/10.1016/j.gloplacha.2024.104522, 2024.

Wei, G. Y., Planavsky, N. J., He, T., Zhang, F., Stockey, R. G., Cole, D. B., Lin, Y. B., and Ling, H. F.: Global marine redox evolution from the late Neoproterozoic to the early Paleozoic constrained by the integration of Mo and U isotope records, Earth-Science Rev., 214, 103506, https://doi.org/10.1016/j.earscirev.2021.103506, 2021.

Winkelbauer, H. A., Hoogakker, B. A. A., Chance, R. J., Davis, C. V, Anthony, C. J., Bischoff, J., Carpenter, L. J., Chenery, S. R. N., Hamilton, E. M., Holdship, P., Peck, V. L., Poulton, A. J., Stinchcombe, M. C., and Wishner, K. F.: Planktic foraminifera iodine/calcium ratios from plankton tows, Front. Mar. Sci., 10, 1–11, https://doi.org/10.3389/fmars.2023.1095570, 2023.

Wong, G. T. F. and Brewer, P. G.: The marine chemistry of iodine in anoxic basins, Geochim. Cosmochim. Acta, 41, 151–159, https://doi.org/10.1016/0016-7037(77)90195-8, 1977.

Xiao, S., Knoll, A. H., Kaufman, A. J., Yin, L., and Zhang, Y.: Neoproterozoic fossils in Mesoproterozoic rocks? Chemostratigraphic resolution of a biostratigraphic conundrum from the North China Platform, Precambrian Res., 84, 197–220, https://doi.org/10.1016/s0301-9268(97)00029-6, 1997.

Yamazaki, C., Kashiwa, S., Horiuchi, A., and Kasahara, Y.: A novel dimethylsulfoxide reductase family of molybdenum enzyme , Idr , is involved in iodate respiration by Pseudomonas sp . SCT, Environ. Microbiol., 22, 2196–2212, https://doi.org/10.1111/1462-2920.14988, 2020.

Yu, Y., Chen, Y., Li, D., and Su, J.: A transient oxygen increase in the Mesoproterozoic ocean at ∼1.44 Ga: Geochemical evidence from the Tieling Formation, North China Platform, Precambrian Res., 369, 106527, https://doi.org/10.1016/j.precamres.2021.106527, 2022.

Zhang, F., Xiao, S., Kendall, B., Romaniello, S. J., Cui, H., Meyer, M., Gilleaudeau, G. J., Kaufman, A. J., and Anbar, A. D.: Extensive marine anoxia during the terminal ediacaran period, Sci. Adv., 4, https://doi.org/10.1126/sciadv.aan8983, 2018.

Zhang, S., Li, Z. X., Evans, D. A. D., Wu, H., Li, H., and Dong, J.: Pre-Rodinia supercontinent Nuna shaping up: A global synthesis with new paleomagnetic results from North China, Earth Planet. Sci. Lett., 353–354, 145–155, https://doi.org/10.1016/j.epsl.2012.07.034, 2012.

Zhang, S., Xu, C., Creeley, D., Ho, Y. F., Li, H. P., Grandbois, R., Schwehr, K. A., Kaplan, D. I., Yeager, C. M., Wellman, D., and Santschi, P. H.: Iodine-129 and iodine-127 speciation in groundwater at hanford site, U.S.: Iodate incorporation into calcite", Environ. Sci. Technol., 47, 13205–13206, https://doi.org/10.1021/es4046132, 2013.

Zhou, X., Thomas, E., Rickaby, R. E. M., Winguth, A. M. E., and Lu, Z.: I/Ca evidence for upper ocean deoxygenation during the PETM, Paleoceanography, 29, 964–975, https://doi.org/10.1002/2014PA002702, 2014.

Zhou, X., Jenkyns, H. C., Owens, J. D., Junium, C. K., Zheng, X. Y., Sageman, B. B., Hardisty, D. S., Lyons, T. W., Ridgwell, A., and Lu, Z.: Upper ocean oxygenation dynamics from I/Ca ratios during the Cenomanian-Turonian OAE 2, Paleoceanography, 30, 510–526, https://doi.org/10.1002/2014PA002741, 2015.

Zhu, S., Zhu, M., Knoll, A. H., Yin, Z., Zhao, F., Sun, S., Qu, Y., Shi, M., and Liu, H.: Decimetre-scale multicellular eukaryotes from the 1.56-billion-year-old Gaoyuzhuang Formation in North China, Nat. Commun., 7, https://doi.org/10.1038/ncomms11500, 2016.

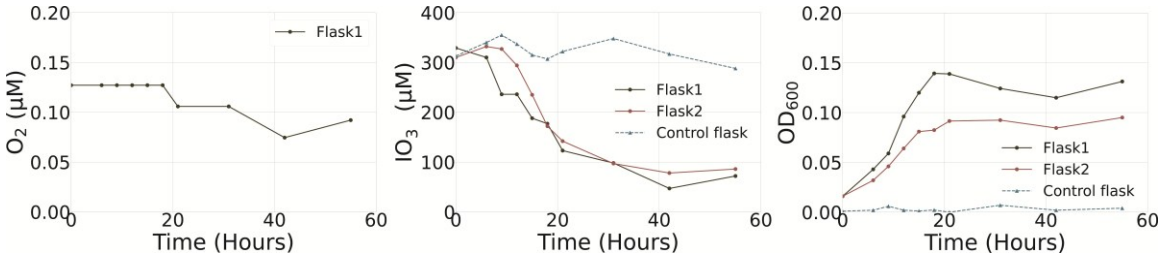

Figure 4.8. Preliminary results of *Shewanella oneidensis* MR-1 incubation under 5% atm O_2 but without bubbler. Note that medium-dissolved O_2 in equilibrium under such gas-phase O_2 partial pressure (~40μM) is much higher than the measured data.

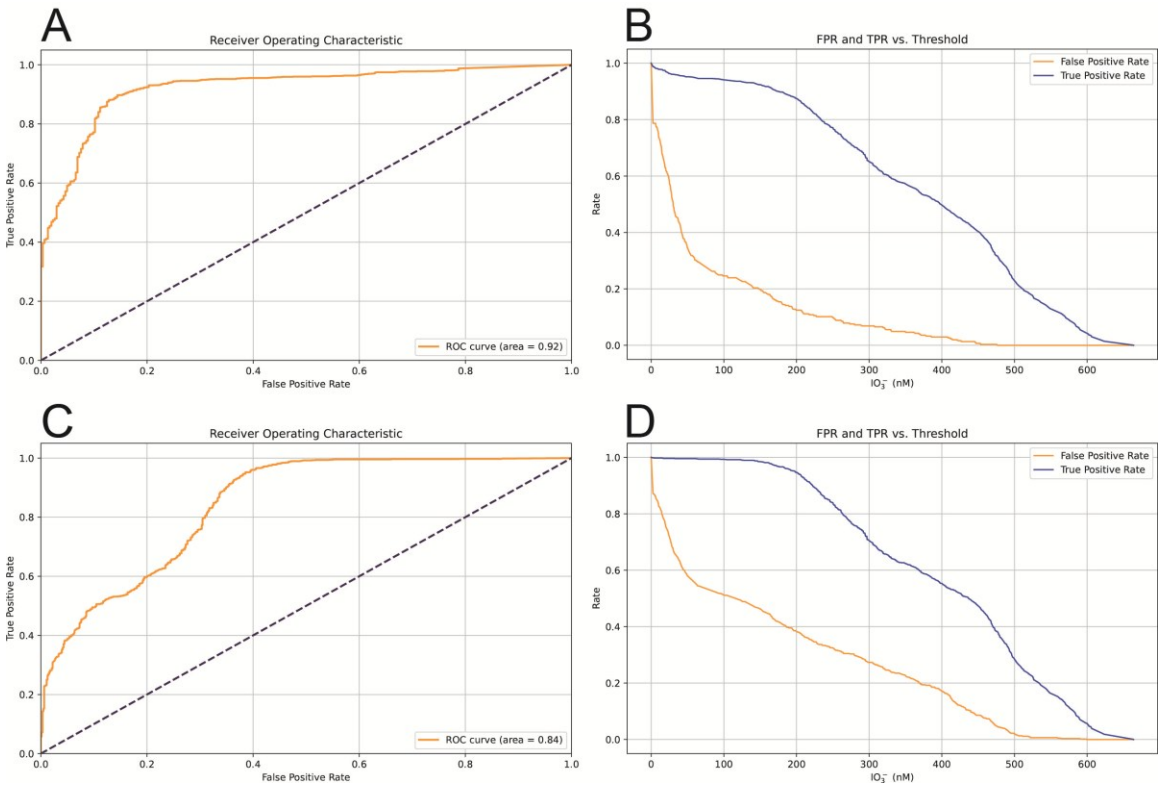

Figure 4.9. A: the ROC curve when the O_2 threshold is set to 0.9 μM. **B:** under the same O_2 threshold, the true positive rate (TPR, high IO_3^- in high O_2 seawater) and the false positive rate (FPR, high IO_3^- in low O_2 seawater) changes as the 'threshold parameter' of IO_3^- changes. **C:** the ROC curve when the O_2 threshold is set to 7 μM. **D:** under the same O_2 threshold of 7 μM, the true positive rate (TPR, high IO_3^- in high O_2 seawater) and the false positive rate (FPR, high IO_3^- in low O_2 seawater) change as the 'threshold parameter' of IO_3^- changes.

Table 4.2. Measurements of IO_3^- and cell density (OD_{600}) of samples from *Shewanella oneidens* MR-1 incubation experiments.

pO_2 headspace/ DO medium (atm)/(μM)	Time from T0 (hr)	IO_3^- _flask1 (μM)	IO_3^- _flask2 (μM)	IO_3^- _flask3 (μM)	IO_3^- _control (μM)	OD_{600} _flask1	OD_{600} _flask2	OD_{600} _flask3	OD_{600} _control
5%/50	0	252.22	258.94	272.55	262.88	0.013	0.014	0.015	0.003
	9	265.06	276.10	268.68	246.24	0.036	0.038	0.040	0.001
	12	282.01	281.45	274.76	274.31	0.053	0.053	0.055	0.001
	15	248.85	285.45	287.95	275.40	0.067	0.065	0.070	0.003
	18	277.89	288.23	288.02	276.31	0.085	0.071	0.081	0.004
	21	275.22	260.17	296.57	280.14	0.103	0.070	0.084	0.004
	24	275.22	279.41	296.92	267.62	0.113	0.065	0.077	0.006
	36	268.54	257.50	259.25	270.86	0.121	0.043	0.050	0.004
	42	265.20	282.68	286.83	283.17	0.120	0.044	0.048	0.003
1%/10	0	233.65	239.21	237.22	235.47	0.037	0.038	0.037	0.002
	9	240.00	234.03	233.93	242.36	0.103	0.103	0.106	0.004
	12	243.12	234.65	237.01	239.83	0.119	0.117	0.125	0.003
	15	238.08	229.54	232.66	240.44	0.129	0.123	0.134	0.003
	18	235.20	233.34	232.45	234.85	0.140	0.138	0.144	0.002
	21	228.78	240.07	235.16	242.74	0.158	0.141	0.151	0.002
	24	233.79	238.69	237.84	240.48	0.179	0.141	0.158	0.003
	33	230.56	235.30	239.76	235.92	0.145	0.123	0.161	0.003
	36	234.78	236.33	241.64	245.11	0.155	0.115	0.162	0.007
0.1%/0.4	0	233.93	237.69	241.18	241.83	0.029	0.030	0.028	0.004
	4.5	233.69	235.37	238.48	244.33	0.041	0.036	0.040	0.002
	9	234.71	236.97	238.62	241.52	0.070	0.052	0.072	0.004
	12	235.47	235.67	236.02	247.07	0.094	0.066	0.087	0.003
	15	235.81	233.14	256.44	257.16	0.133	0.090	0.110	0.003
	18	232.42	236.25	232.94	252.34	0.152	0.119	0.121	0.005

Table 4.2 (cont'd).

0.1%/0.4	21	233.89	233.00	228.73	254.12	0.129	0.130	0.125	0.004
	24	236.87	252.03	232.29	248.27	0.099	0.115	0.103	0.003
	36	238.48	228.62	228.28	242.21	0.087	0.088	0.066	0.002
0.05%/0.1	0	251.10	264.71	258.34	262.48	0.031	0.032	0.032	0.003
	3	254.41	261.14	242.35	244.37	0.033	0.031	0.033	0.004
	6	249.59	262.15	257.80	265.00	0.033	0.03	0.038	0.003
	9	256.79	257.36	263.38	263.41	0.04	0.035	0.043	0.003
	12	254.16	251.68	257.51	265.54	0.045	0.051	0.039	0.003
	15	254.02	253.76	252.97	260.06	0.052	0.043	0.057	0.003
	24	248.69	253.84	260.35	251.28	0.062	0.054	0.074	0.004
	27	254.34	254.09	251.82	259.13	0.069	0.059	0.076	0.002
	30	245.95	253.01	248.76	259.34	0.068	0.058	0.081	0.002
	33	240.34	248.87	253.26	258.05	0.075	0.061	0.093	0.002
	39	244.26	253.44	246.92	260.39	0.087	0.068	0.106	0.001
	51	247.82	245.70	235.26	256.03	0.127	0.088	0.149	0.003
	63	239.11	241.92	241.60	262.04	0.168	0.109	0.212	0.007
	75	240.48	240.70	238.46	251.39	0.212	0.139	0.239	0.016
	87	235.94	236.23	240.59	253.04	0.225	0.15	0.252	0.015
	99	233.64	236.88	230.94	252.76	0.245	0.18	0.235	0.013

CONCLUSIONS AND PERSPECTIVES

This dissertation provides new insights into the modern marine iodine cycle in low-O_2 conditions, as well as constrains secular evolution of O_2 in the atmosphere and the ocean through Earth's history.

The introduction provides the motivation of this dissertation: quantitative reconstruction of atmospheric and ocean oxygenation using I/Ca in ancient carbonates, and hence providing insights into the co-evolution of Earth's environment and biological evolution. Here, I emphasize the irreplaceable role of I/Ca proxy in recording the broad stepwise feature of atmospheric and ocean oxygenation. I also pointed out the limitations in our current understanding of marine iodine cycle which hinders quantitative redox reconstruction with the I/Ca proxy.

In Chapter 2, I collected and measured iodine speciation from two redox stratified basins: Siders Pond and the Baltic Sea. Two distinct features are observed from the iodine depth profiles: (1) salinity-normalized IO_3^- is depleted in the surface layer in both the basins, even under near saturated dissolved O_2, and (2) non-conservative I^- concentrations within and below the chemocline. I interpret that the depletion of IO_3^- in the surface water has resulted from a combination of factors including freshwater fluxes rich in I^-, the introduction of IO_3^- rich seawater below the chemocline due to density stratification, reduction by phytoplankton, and reduction by dissolved organic matter (DOM). The non-conservative, excessive I^- relative to average seawater in the euxinic portion of Siders Pond is likely the consequence from benthic fluxes. The understanding the net removal of I^- observed near chemocline in the Baltic Sea requires further investigation. By comparing to the hydrographic features of the Baltic Sea between periods of 2001-2002 and 2021, I suggest that intense stratification during the stagnant period likely enhanced IO_3^- reduction in the surface of the Baltic Sea. The iodine species observed in modern anoxic basins

therefore has important implications to mechanisms of IO_3^- accumulation in the past. I propose that oligotrophic open ocean might serve as hotspots for IO_3^- accumulation, subsequently supporting its concentrations in near-shore areas through ventilation. I also emphasize the possibility of decoupling between surface ocean IO_3^- and O_2 in the ancient ocean should be considered in paleoredox reconstruction. Therefore I/Ca proxy application requires careful examination of local water column stratification.

Chapter 3 introduced new iodine oxidation/reduction scenarios into an Earth System Model. Together with parameterization from previous work, I evaluated their representation of the marine iodine cycling through model-data comparison against my updated dissolved iodine compilation in the modern ocean. The best parameter values associated with IO_3^- reduction, I^- oxidation, as well as IO_3^- photosynthetic uptake fell within the range of field and experiment observation and thus could be considered plausible. Three parameters' combinations, 'lifetime-threshold', 'reminO2lifetime-threshold' and 'Fennel-threshold' performed well in replicating specific iodine gradients (euphotic latitudinal distribution, depth distribution, and ODZ distribution), in addition to achieving overall global scale model-data match. I further evaluated the performance of these three combinations in simulating an ancient ocean deoxygenation event using the Cretaceous pre-OAE2 redox landscape as a case study. I note that, 'lifetime-threshold' might be more preferable for simulating iodine cycle in recent geological times, while 'reminO2lifetime-threshold' and 'Fennel-threshold' perform better in simulating an ocean with more extreme redox gradients, such as an anoxia-dominated ocean.

In Chapter 4, I determined the O_2 threshold for triggering IO_3^- reduction by Shewanella oneidensis MR-1. When dissolved O_2 in the medium decreases to ~0.1 μM, IO_3^- reduction was observed. Importantly, only a small portion of IO_3^- was reduced in the experiment, suggesting that

bacteria only partially switch to anaerobic metabolism even under the existence of trace amounts of O_2. I also performed a receiver operating characteristic (ROC) curve method to existing compilation of bulk seawater measurements of IO_3^- and O_2 in the modern ocean. I identify that IO_3^- above 150 nM indicates seawater O_2 higher than 7 μM locally or in adjacent regions. Combining microbial experiment and the modern ocean IO_3^--O_2 data, I therefore estimate the minimum O_2 in seawater supporting the first IO_3^- accumulation during the GOE is between 0.1 to 7 μM.

My cGENIE Earth system model simulations show that at least 3% PAL of atmospheric O_2 is necessary to maintain 50 nM IO_3^- in the Proterozoic surface ocean, equivalent to the observed 0.5 μmol/mol baseline. This minimum requirement for IO_3^- accumulation increases when ocean nutrient level (PO_4) rises. When PO_4 is above 10% of the present level, the PO_4 controls IO_3^- accumulation together with redox. The model sensitivity analysis indicates that transiently higher I/Ca (above 2.5 μmol/mol) currently interpreted as Ocean Oxygenation Evenrt signals can be either reached by minor increase of O_2 by less then 1% PAL, or decrease of nutrient level in higher atmospheric O_2 (above ~10% PAL) scenario. The shift of I/Ca from Proterozoic low baseline to the modern high baseline initiated in the Middle Paleozoic, reflecting deep ocean oxygenation, was either caused by rising atmospheric O_2 above 30% PAL or reorganization of ocean circulation driven by continental repositioning. The final completion of I/Ca baseline transition to the modern state during the Early Mesozoic around 200 Ma indicates the surface, middle, and deep parts of the ocean water column were pervasively oxygenated.

Based on the results of this dissertation, I propose several topics that are worth exploring in the future, including:

(1) In Chapter 2, I identified net depletion in I^- close to or within the chemocline in the Baltic Sea. The mechanism causing I^- removal below the euphotic zone is however very poorly understood. As laboratory experiments have demonstrated that Mn-oxides can adsorb I^- (Fox et al., 2009), could this process also take place in the Baltic water? If Mn-oxides absorbs I^-, what is the stoichiometry of this reaction? Are there other compounds, like organic particles, or clay particles that also absorb I^-?

(2) Also in Chapter 2, IO_3^- depletion has been interpreted as the result of reduction and photosynthetic uptake in the isolated surface layer, but the detailed mechanism as well as kinetics are unknown. Can we use isotope tracers (^{129}I) to quantify the reduction or oxidation kinetics of IO_3^- and I^- in the Baltic Sea? Do N and Mn species, such as NO_2^-, NH_4, Mn(III), and Mn-oxides inhibit or promote redox reactions of iodine? What is the Redfield ratio of IO_3^- uptake in the surface Baltic Sea? Combining the fluxes such as IO_3^- reduction, I^- oxidation, I^- upwelling, can we build a numeric model that describes iodine cycling in the Baltic Sea?

(3) In Chapter 3, the iodine cycle parameters constrained from simulations under model-generated O_2 fields and real-world oxygen (WOA)-forced O_2 fields are different. In addition, the parameters derived from WOA-forced simulations exhibit better overall replication of iodine observation in the real ocean, as well as iodine gradients (euphotic latitudinal distribution, depth distribution, and ODZ distribution). These differences highlight the importance of simulating dissolved O_2 in models. Meanwhile, under low spatial resolution (36×36 equal areal grids plus 16 depth layers), each grid in cGENIE spans across 1000 km, hence some important ocean redox structures (like Eastern Tropical Pacific ODZs) are represented as only a few grids. How can we improve the quality of the oxygen cycle simulation in cGENIE and hence improve

the simulation of the iodine cycle? Can we improve the iodine cycle simulation by applying higher-resolution grids?

(4) Also in Chapter 3, the I^- oxidation parameter 'reminO2lifetime' links I^- oxidation with O_2 consumption during remineralization. The logic behind this parameterization is the recent observation of I^- oxidation to IO_3^- catalyzed by bacteria, perhaps in association with NH_4^+ oxidation (Hughes et al., 2021). Since the nitrogen cycle is not currently included in cGENIE, an alternative is to scale NH_4^+ oxidation to OM remineralization (Martin et al., 2019) and hence link to I^- oxidation. Notably, this oxidation scheme performed the best in replicating both modern and ancient iodine distributions. What is the link between kinetics of I^- oxidation with NH_4^+ oxidation or OM remineralization in the ocean?

(5) In Chapter 4, the IO_3^- reduction threshold under low O_2 was found to be around 0.1 μM, which is relatively low compared to preliminary experiments in which bacterial consumption reduced O_2 levels below the sensor's detection limit. This result implies that IO_3^- reduction kinetics is dependent on O_2 concentration. Variable IO_3^- reduction kinetics are also proposed in Chapter 3 as represented by the 'inhibition' scheme in cGENIE. Therefore, the question arises: how does O_2 control microbial IO_3^- reduction? Can marine iodine cycle simulations be improved if the correct kinetics are incorporated into the 'inhibition' scheme?

(6) The cGENIE simulations in Chapter 4 apply modern boundary conditions that might not accurately represent the Precambrian oceans. These conditions are, for example, absence of deep ocean redox buffer (large Fe(II) and sulfide reservoirs), remineralization depth, continental configuration, I:C stoichiometry, etc. In addition, like previously mentioned in question (5), the 'threshold' reduction scheme assumes IO_3^- is quantitatively reduced when O_2 drops below a threshold regardless of microbial activity. This scheme appears to be inaccurate, given the inhibited

IO_3^- reduction observed in oligotrophic ocean environments (Hardisty et al., 2021) and in control media without inoculation. If these boundary conditions match the Precambrian ocean, can secular O_2 be constrained more accurately? Can cGENIE simulate IO_3^- accumulation in mid-latitudes more consistent with geochemical observation?

REFERENCES

Fox, P. M., Davis, J. A., and Luther, G. W.: The kinetics of iodide oxidation by the manganese oxide mineral birnessite, Geochim. Cosmochim. Acta, 73, 2850–2861, https://doi.org/10.1016/j.gca.2009.02.016, 2009.

Hardisty, D. S., Horner, T. J., Evans, N., Moriyasu, R., Babbin, A. R., Wankel, S. D., Moffett, J. W., and Nielsen, S. G.: Limited iodate reduction in shipboard seawater incubations from the Eastern Tropical North Pacific oxygen deficient zone, Earth Planet. Sci. Lett., 554, 116676, https://doi.org/10.1016/j.epsl.2020.116676, 2021.

Hughes, C., Barton, E., Hepach, H., Chance, R., Wadley, M. R., Pickering, M. D., Hogg, K., Pommerening-r, A., Stevens, D. P., and Jickells, T. D.: Oxidation of iodide to iodate by cultures of marine ammonia-oxidising bacteria, Mar. Chem., 234, 1–7, https://doi.org/10.1016/j.marchem.2021.104000, 2021.

Martin, T. S., Primeau, F., and Casciotti, K. L.: Modeling oceanic nitrate and nitrite concentrations and isotopes using a 3-D inverse N cycle model, Biogeosciences, 347–367, 2019.